

OTHER TITLES IN THE SERIES IN THE SCIENCE OF THE SOLID STATE

- VOL. 1. GREENAWAY AND HARBEKE—Optical Properties and Band Structures of Semiconductors.
- VOL. 2. RAY—II-VI Compounds.
- VOL. 3. NAG—Theory of Electrical Transport in Semiconductors.
- VOL. 4. JARZEBSKI—Oxide Semiconductors.
- VOL. 5. SHARMA and PUROHIT—Semiconductor Heterojunctions.
- VOL. 6. PAMPLIN—Crystal growth.

TERNARY CHALCOPYRITE SEMICONDUCTORS: GROWTH, ELECTRONIC PROPERTIES, AND APPLICATIONS

J. L. SHAY

BELL TELEPHONE LABORATORIES, INCORPORATED
HOLMDEL, NEW JERSEY 07733

AND

J. H. WERNICK

BELL TELEPHONE LABORATORIES, INCORPORATED
MURRAY HILL, NEW JERSEY 07974



PERGAMON PRESS

OXFORD · NEW YORK · TORONTO · SYDNEY · PARIS · BRAUNSCHWEIG

U.K. Pergamon Press Ltd., Headington Hill Hall, Oxford OX3 0BW,
England

U.S.A. Pergamon Press Inc., Maxwell House, Fairview Park,
Elmsford, New York 10523, U.S.A.

CANADA Pergamon of Canada Ltd., 207 Queen's Quay West,
Toronto 1, Canada

AUSTRALIA Pergamon Press (Aust.) Pty. Ltd., 19a Boundary Street,
Rushcutters Bay, N.S.W. 2011, Australia

FRANCE Pergamon Press SARL, 24 rue des Ecoles,
75240 Paris, Cedex 05, France

WEST GERMANY Pergamon Press GmbH-3300 Braunschweig, Postfach 2923,
Burgplatz 1, West Germany

Copyright © 1975 Bell Telephone Laboratories Incorporated

*All Rights Reserved. No part of this publication may be
reproduced, stored in a retrieval system or transmitted in
any form or by any means: electronic, electrostatic,
magnetic tape, mechanical, photocopying, recording or
otherwise, without permission in writing from the
publishers*

First edition 1975

Library of Congress Cataloging in Publication Data

Shay, Joseph Leo, 1942-

Ternary chalcopyrite semiconductors growth,
electronic properties, and applications.

(International series of monographs in the science
of the solid state, v. 7)

Includes bibliographies.

1. Semiconductors. 2. Chalcopyrite crystals.
3. Crystals—Growth. 4. Energy-band theory of solids.

I. Wernick, Jack Harry, 1923—joint author.

II. Title.

QC611.8.C45S52 1975 537.6'22 74-5763

ISBN 0-08-017883-9

ACKNOWLEDGMENTS

This book probably would never have been written without the efforts of several individuals over the last few years. P. A. Wolff, A. G. Chynoweth and C. K. N. Patel have encouraged and supported our own research, and provided helpful suggestions and advice. Our colleagues, K. Bachmann, E. Buehler, G. Boyd, H. Kasper and B. Tell, have contributed enormously to our understanding of ternary chalcopyrite semiconductors. The cooperation of our secretaries, Miss Susan Feyerabend and Miss M. P. Reitter, in typing the several drafts of the manuscript is gratefully appreciated.

EDITORS PREFACE

THE diamond structure is one of the simplest and most symmetrical arrangements of atoms known in crystallography. Only the two important semiconducting elements, Si and Ge, habitually crystallize in this structure and their commercial importance can be traced back to this fact. The four electron per site rule, which can be deduced from the Grimm-Sommerfeld rule of chemical bonding, can account for their semiconducting and doping properties and the strength of the bonding down from diamond through Si and Ge to grey Sn can account for the change in energy gap and thermal conductivity. The rule can also be used to predict semiconductivity in a vast family of compounds related to diamond which is variously called the tetrahedral or adamantine or simply diamond-like family. The latter name does not strictly include the structures derived from wurtzite which I feel are in this family, because every anion is bonded tetrahedrally to four cations and every cation to four anions.

As one proceeds from the group IV elements to the III-V and II-VI compounds new properties become available for study and exploitation. A wider choice of energy gaps and band structure enables devices depending on larger and sometimes direct energy gaps (like light-emitting diodes and heterojunction lasers) or on high mobilities (like Hall effect and magnetoresistance devices) to be made which cannot be made with the elements. Some completely new devices like those based on the Gunn Effect also become possible. Moving on to ternary compounds the choice becomes wider still and the drop in symmetry due to superlattice formation opens the way for non-linear devices and interesting optical properties.

This book deals with the two most interesting ternary cousins of the tetrahedral family. The I-III-VI₂ and the II-IV-V₂ compounds, when they form, usually have the chalcopyrite structure and fifty such compounds are now known. It is interesting to note that no antichalcopyrite compounds (e. g. of the families III₂-IV-VI II₂-V-VII) have been found to exist in spite of many attempts to make them. These materials are now perhaps in the same state that the III-V compounds reached ten years ago. The preliminary work has been done on many of them and the door is open for applications, but a great deal of scientific and technological development particularly in crystal growth, characterization, detailed band structure studies and device exploitation remains to be done. I welcome this book which provides a timely and thorough summary of the work done and pointers to the future.

Chalcopyrite itself was known many years before semiconductor in the elements was discovered. Its crystal structure was the subject of an early controversy in crystallography. Burdick and Ellis (1917) proposed a unit cell based on a tetragonally distorted diamond unit cell. Fifteen years later Pauling and Brockway using single crystals confirmed the now generally accepted body centred tetragonal structure with a unit cell twice the size. The Burdick and Ellis structure is a possible superlattice structure for a tetrahedral A-B-C₂ compound and may yet be found to exist if people will look for it. Chalcopyrite is antiferromagnetic and is one of only a very small number of magnetic tetrahedral semiconductors.

Early work on these compounds was performed out of purely scientific interest, this was spurred on in the early sixties by the hope of thermoelectric applications. These materials have very low lattice thermal conductivities, which for many devices is a disadvantage. Some, like CdSnAs_2 , have remarkably high mobilities. It was hoped that one member of the family would be found, chemically stable and cheap to produce, which might have a sufficiently high figure of merit to enable it to be developed for the one-in-every-home or one-in-every-car mass market for refrigerators or battery chargers. However it soon became clear that this dream was not to be realized and some steam went out of the drive for new compounds.

Careful scientific work continued and application-minded scientists watched the development of work in the III-V and II-VI compounds on light-emitting junctions and heterojunctions, Gunn effect devices and acoustooptical effects, and on magnetic semiconductors and amorphous materials. As this book reports, all these topics can be studied in the ternary compounds. But pessimists will argue that such studies are admirable topics to amuse academic workers and PhD students but unlikely to prove of commercial interest because of the technological difficulties inherent in three element semiconductors. They said the same about GaAs-AlAs alloys ten years ago!

The authors have drawn out the present state of possible applications of these compounds for optical communications systems as infrared- or visible light-emitting materials and for use with other lasers as pumps or up convertors. There may be a break-through in the far infrared by down conversion or spin flip action or in the blue or ultraviolet region using some of the newly discovered nitrides. Again the peculiar non-linear properties of these compounds may have an application round the corner in some electrical device—who knows what hot electron effects may be found in tetragonal materials with pseudo-direct gaps or how phonon interactions may be affected.

The First International Conference on Ternary Chalcopyrite Semiconductors was held at Bath in November 1973. Over seventy participants from eight countries reported on and discussed these compounds and their properties. I hope this book will be available for participants at the Second Conference in Strasbourg in 1975. I am writing these notes a few days after returning from a six-week lecture and study tour of Japanese semiconductor laboratories under the auspices of the Royal Society. I can report great interest in these materials both in Japan and at the international conference and school on crystal growth held there this spring. I am sure that this admirable book by two eminent workers in the field, who make such a splendid matched pair in their diverse yet overlapping interests, and who work at the leading semiconductor research laboratory in the world, will be read with close interest by a wide variety of scientific workers and used as a Bible by workers in the fields of ternary compounds and non-linear optics. I am sure it will stimulate much further work.

B.R.P.

CHAPTER 1

INTRODUCTION

ALTHOUGH many binary and ternary naturally occurring compounds were known to exhibit behavior now associated with semiconductors long before the invention of the transistor, it was this development that stimulated systematic searches for new semiconductors in the early 1950s. The first materials investigated in this manner were the III-V compounds which exhibit the diamond structure. Blum *et al.* (1950) and Goryunova and Obukhov (1950) reported InSb to be a semiconductor, but it appears that Welker (1952) was the first to appreciate the importance of the III-V compounds as a class of new semiconductors. High carrier mobilities and the ability to dope *n*- and *p*-type were properties investigators strived for.

A natural extension in the search for new semiconductors was to examine ternary compounds exhibiting diamond-like or tetrahedral coordination, and Goodman and Douglas (1954) discussed the possibility of semiconductivity in the I-III-VI₂ compounds synthesized a year earlier by Hahn *et al.* (1953). Goodman (1957) further showed that by ordered substitution of Groups II and IV atoms for the Group III atoms in the III-V compounds, new ordered semiconducting II-IV-V₂ compounds could be prepared.

Although only two or three of the II-IV-V₂ compounds exhibited electron mobilities of a few thousand, the II-IV-V₂ and I-III-VI₂ compounds, and in particular, solid solutions of them with their III-V and II-VI analogs, were investigated from the thermoelectric standpoint. For utility as practical thermoelectric materials, high-quality single crystals generally are not required.

The discovery of the laser and the interest in light-emitting materials in the late 1950s and early 1960s stimulated renewed effort in these materials, particularly by the Russian workers. Studies aimed towards understanding the electronic structure and elucidating the nonlinear optical properties of these materials, with the hope of producing a technological material, require high quality single crystals. Many of these materials are difficult to grow in the form of large, high quality crystals, and it has only been within the past few years that researchers have been successful in this effort.

Ternary chalcopyrite crystals are currently of technological interest since they show promise for application in the areas of visible and infrared light-emitting diodes, infrared detectors, optical parametric oscillators, upconverters, and far infrared generation. It has been discovered that several ternary compounds can be obtained both *p*- and *n*-type. In addition it has been found that two of them, CuGaS₂ and CuAlS₂, can be made *p*-type and have direct bandgaps in the visible and ultraviolet respectively. They are unique in this respect, and have generated activity in the area of heterojunctions with large bandgap II-VI compounds, which can only be obtained *n*-type. Infrared light-emitting diodes have been prepared by epitaxial growth of CdSnP₂ on InP.

By virtue of the noncubic crystal structure, these compounds are optically birefringent, and therefore nonlinear optical interactions can be phase-matched. Further-

TERNARY CHALCOPYRITE SEMICONDUCTORS

more, these compounds are covalently bonded to a large extent, so that they have large nonlinear coefficients, a measure of their usefulness as nonlinear optical materials.

These compounds are also of interest from a fundamental point of view since the chalcopyrite structure is the simplest, noncubic ternary analog of the well-understood binary zincblende structure. It has been found that the energy band structure of ternary crystals differs from that of binary compounds in several nontrivial ways by virtue of the noncubic structure. Degeneracies are lifted, and forbidden electronic transitions become allowed. Whereas the valence bands of most zincblende crystals are composed of *s*- and *p*-like orbitals, the noble metal *d*-levels in I-III-VI₂ compounds hybridize with the otherwise *s*- and *p*-like orbitals, and lead to several anomalous features of the energy band structure.

In Chapter 2 we review the crystal growth of II-IV-V₂ and I-III-VI₂ single crystals. In Chapters 3 and 4 we review studies of the electronic structure of II-IV-V₂ and I-III-VI₂ compounds respectively. And in Chapters 5-8 we review the luminescence, nonlinear optical, electrical properties, and miscellaneous physical properties of chalcopyrite crystals.

References

- BLUM, A. N., MOKROVSKI, N. P., and REGEL, A. R. (1950) *Seventh All-union Conference on the Properties of Semiconductors, Kiev*.
- GOODMAN, C. H. L. (1957) *Nature* **179**, 828.
- GOODMAN, C. H. L., and DOUGLAS, R. W. (1954) *Physica* **20**, 1107.
- GORYUNOVA, N. A., and OBUKHOV, A. P. (1950) *Seventh All-union Conference on the Properties of Semiconductors, Kiev*.
- HAHN, H., FRANK, G., KINGLER, W., MEYER, A., and STORGER, G. (1953) *Z. anorg. Chem.* **271**, 153.
- WELKER, H. (1952) *Z. Naturforsch.* **11**, 744.

CHAPTER 2

THE CHALCOPYRITE STRUCTURE AND CRYSTAL GROWTH

2.1 The Chalcopyrite Structure

The I–III–VI₂ and II–IV–V₂ (ABC₂) phases possess the tetragonal E1₁ structure-type space group $I\bar{4}2d$, with four formula units per cell.[†] The known phases exhibiting this structure are tabulated in Tables 2.1 and 2.2. Each A- and B-atom is tetrahedrally coordinated to four C-atoms, while each C-atom is tetrahedrally coordinated to two A- and two B-atoms in an ordered manner (Fig. 2.1). The atomic distribution is as follows:

equivalent position $(000; \frac{111}{222})^{\ddagger}$

4A in (a) positions, $000; 0 \frac{11}{24}$

4B in (b) positions, $00 \frac{1}{2}; 0 \frac{13}{24}$

8C in (d) positions, $x \frac{11}{48}; \bar{x} \frac{31}{48}; \frac{3}{4} x \frac{7}{8}; \frac{1}{3} \bar{x} \frac{7}{8}$

If the cations A and B were distributed at random, the cubic zincblende structure would result. Thus the chalcopyrite structure is a superlattice of the zincblende structure with the c/a ratio approximately equal to 2. The tetrahedral coordination implies that the bonding is primarily covalent with sp^3 hybrid bonds prevalent, although there is some ionic character present because the atoms are different.

The I–III–VI₂ and II–IV–V₂ compounds can be regarded as the ternary analogs of the II–VI and III–V binary compounds respectively. They can be derived from the binary phases by ordered substitution of other group atoms so as to maintain an electron-to-atom ratio of 4. The derivation of these phases from the pure covalent crystals, Si and Ge, is schematically illustrated in Fig. 2.2. The ordered arrangement of the metal atoms (or cations) leads to the formation of the tetragonal superlattice.

The quantity $2-c/a$ is a measure of the tetragonal distortion which may occur as a result of ordering. The x -parameter which precisely locates the C-atom position, depends on the difference between the A–C and B–C interactions. Since $2-c/a$ is greater than zero for most II–IV–V₂ compounds, x greater than 0.25 (the value for the cubic zincblende structure) represents a motion of the V-atom toward the IV-atom and away from the column II atom.

[†] The prototype phase is the mineral chalcopyrite, CuFeS₂.

[‡] Add the coordinates of the equivalent positions to the coordinates of the *a*, *b*, and *d* sites to obtain the coordinates of all of the atoms.

TERNARY CHALCOPYRITE SEMICONDUCTORS

 TABLE 2.1. *Lattice Parameters for I-III-VI₂ Compounds*

	<i>a</i> (Å)	<i>c</i> (Å)	<i>c/a</i>	References
CuAlS ₂	5.323	10.44	1.96	a
	5.312	10.42	1.96	b
	5.31	10.41	1.96	e
	5.336	10.444	1.958	l
CuAlSe ₂	5.617	10.92	1.94	a
	5.60	10.90	1.95	b
	5.60	10.86	1.94	e
	5.6035	10.977	1.959	m
CuAlTe ₂	5.967	11.80	1.97	a
	5.96	11.74	1.97	e
CuGaS ₂	5.34741	10.47429	1.9588	j
	5.360	10.49	1.96	a
	5.35	10.48	1.96	c
	5.34	10.47	1.96	e
	5.351	10.484	1.959	f, g
	5.328	10.462	1.964	f, h
	5.349	10.480	1.959	i
CuGaSe ₂	5.618	11.01	1.96	a
	5.602	11.00	1.964	d
	5.60	10.98	1.96	e
	5.6159	11.0182	1.962	m
CuGaTe ₂	6.006	11.93	1.98	a
	5.99	11.92	1.99	e
	6.025	11.948	1.983	k
CuInS ₂	5.528	11.08	2.00	a
	5.51	11.02	2.00	e
	5.524	11.13	2.01	f
	5.52279	11.13295	2.0158	j
CuInSe ₂	5.785	11.57	2.00	a
	5.77	11.54	2.00	e
CuInTe ₂	6.179	12.36	2.00	a
	6.16	12.32	2.00	e
CuTlS ₂	5.58	11.16	2.00	e
CuTlSe ₂	5.83	11.60	1.99	e
AgAlS ₂	5.707	10.28	1.80	a
	5.69	10.24	1.80	e
AgAlSe ₂	5.968	10.77	1.80	a
	5.95	10.71	1.89	e
AgAlTe ₂	6.309	11.85	1.88	a
	6.29	11.83	1.88	e
AgGaS ₂	5.755	10.28	1.79	a
	5.74	10.27	1.79	e
	5.75	10.305	1.79	f
	5.75722	10.3036	1.7897	j
AgGaSe ₂	5.985	10.90	1.82	a
	5.97	10.87	1.82	e
	5.9920	10.8863	1.817	m
AgGaTe ₂	6.301	11.96	1.90	a
	6.29	11.95	1.90	e

THE CHALCOPYRITE STRUCTURE AND CRYSTAL GROWTH

TABLE 2.1. *continued*

	<i>a</i> (Å)	<i>c</i> (Å)	<i>c/a</i>	References
AgInS_2	5.829	11.19	1.92	a
	5.81	11.16	1.92	e
AgInSe_2	6.102	11.69	1.92	a
	6.092	11.64	1.91	d
	6.09	11.69	1.92	e
	6.0913	11.7122	1.923	m
AgInTe_2	6.419	12.58	1.96	a
	6.40	12.54	1.96	e
	6.446	12.634	1.960	k

^a Hahn *et al.* (1953).^b Honeyman (1969); Cu, Al, and S in atomic proportions 1 : 1 : 1.9.^c Strunz *et al.* (1968); mineral sample.^d Lerner (1966).^e Goryunova (1965).^f Kasper (1972).^g Dark crystals.^h Orange crystals.ⁱ Belova *et al.* (1967).^j Abrahams and Bernstein (1973a, b); CuGaS_2 and CuInS_2 slightly nonstoichiometric.^k Wooley and Williams (1966); samples quenched in water after melting. Annealing experiments suggested that CuGaTe_2 and AgInTe_2 are nonstoichiometric (precipitation occurred). *a* for AgInTe_2 after annealing at 440°C was 6.455 Å.^l Brandt *et al.* (1973).^m Boyd *et al.* (1972).

Abrahams and Bernstein (1971) have shown, on the basis of a detailed structure investigation of ZnSiP_2 and CdSiP_2 , that the Group IV atom (Si) nearly forms a perfect tetrahedron with its Group V nearest neighbors and it appears that this is the key structural feature of these materials. This is not surprising in view of the fact that the Group IV atoms have a strong tendency to form sp^3 hybrid bonds. Assuming a regular tetrahedral location of the C-atoms about the B-sites, the *x*-parameter is no longer an independent variable but is fixed by the lattice parameters (Table 2.3). For ZnSiP_2 , the predicted *x*-value (0.2671) compares very favorably with the experimental value (0.2691). For CdSiP_2 , the predicted and experimental values of *x* are 0.2929 and 0.2967 respectively. On this basis, Abrahams and Bernstein computed the *x*-parameters for several other members of this family. Their calculated A-C and B-C distances are also shown in Table 2.3 and compared with the values obtained by use of the tetrahedral radii given by Van Vechten and Phillips (1970) (Table 2.4) which are derived on the basis of their dielectric theory of covalent bonding (see also Phillips, 1970). Based on the recent lattice constants for ZnGeP_2 (Buehler *et al.*, 1973; Lind and Grant, 1973), *x* (meas.) and *x* (calc.) are 0.2582 and 0.2597 respectively (Abrahams and Bernstein, 1973a, b). Abrahams and Bernstein give *x* (meas.) and *x* (calc.) for ZnSiAs_2 as 0.2658 and 0.2645 respectively. Thus it appears that the A- and C-atom tetrahedra are distorted so as to conform to the regular B-atom tetrahedron and result in the tetragonal distortion.

TERNARY CHALCOPYRITE SEMICONDUCTORS

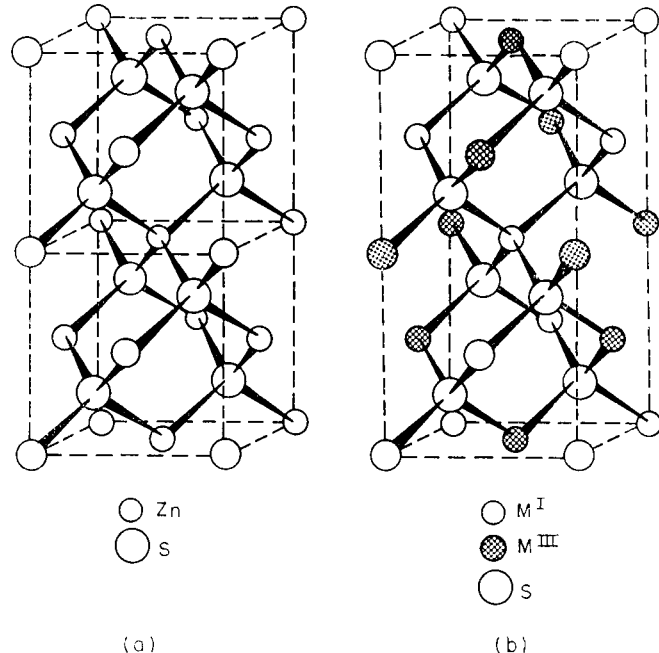


FIG. 2.1. The tetragonal chalcopyrite structure illustrated for the I-III-VI₂ compounds. Two cubic zincblende structures are illustrated on the left.

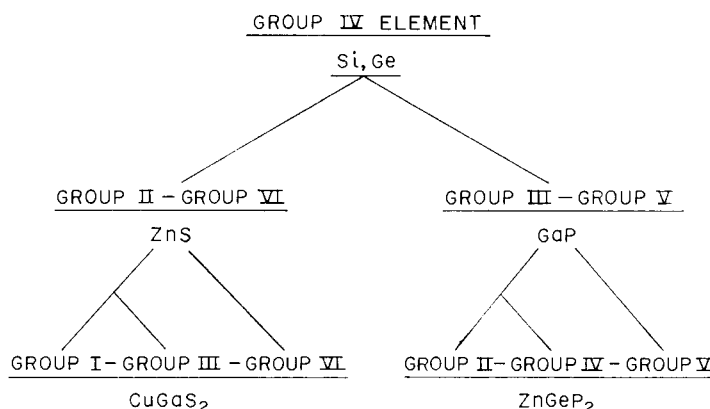


FIG. 2.2. Schematic illustration of the formation of I-III-VI₂ and II-IV-V₂ compounds from tetrahedrally coordinated Group IV elements by substitution of elements so as to maintain the electron-atom ratio equal to 4.

From the Abrahams–Bernstein equations (Table 2.3) the B–C distance is related to the c -dimension by

$$c = (8/\sqrt{3}) (B-C),$$

and Lind and Grant (1973) have shown that the II-IV-V₂ compounds, except ZnSnAs₂,

THE CHALCOPYRITE STRUCTURE AND CRYSTAL GROWTH

 TABLE 2.2. *Lattice Parameters for II-IV-V₂ Compounds (see also Table 2.3)*

	<i>a</i> (Å)	<i>c</i> (Å)	<i>c/a</i>	References
BeSiN ₂	Orthorhombic, wurtzite-like			t
ZnGeN ₂	Monoclinic			n
MgSiP ₂	5.718	10.144	1.769	o
	5.721	10.095	1.764	p
MgGeP ₂	5.652 (cubic ZnS)			a
ZnSiP ₂	5.400	10.441	1.934	b
	5.399	10.435	1.932	c
ZnSiAs ₂	5.606	10.890	1.943	b
	5.608	10.89	1.94	a
	5.60	10.88	1.94	w
	5.611	10.886	1.940	z
ZnGeP ₂	5.46	10.76	1.97	d
	5.465	10.771	1.971	k
	5.466	10.719	1.961	l
	5.465	10.707	1.959	m, x
	5.466	10.722	1.961	v
	5.46	10.71	1.96	w
ZnGeAs ₂	5.670	11.153	1.967	d
	5.672	11.153	1.966	k
ZnSnP ₂	5.651	11.302	2.00	q
	5.651	11.302	2.00	r
	5.651	11.302	2.00	u
	5.652	11.307	2.00	z
ZnSnAs ₂	5.852	11.705	2.000	e
	5.851	11.702	2.000	d
	5.8515	11.703	2.000	f
ZnSnSb ₂	6.273	12.546	2.00	s
CdSiP ₂	5.678	10.431	1.837	b
	5.680	10.431	1.836	g
CdSiAs ₂	5.884	10.882	1.849	k
	5.885	10.881	1.849	z
CdGeP ₂	5.738	10.776	1.878	a
	5.741	10.775	1.877	k
	5.740	10.775	1.877	y
	5.740	10.777	1.878	z
CdGeAs ₂	5.9427	11.2172	1.8875	h
	5.942	11.224	1.889	d
	5.943	11.217	1.888	z
CdSnP ₂	5.900	11.518	1.952	k
	5.900	11.513	1.951	y
	5.902	11.512	1.951	z
CdSnAs ₂	6.084	11.916	1.957	i
	6.092	11.922	1.957	d
	6.093	11.936	1.959	e, j
	6.0937	11.9184	1.955	k

TERNARY CHALCOPYRITE SEMICONDUCTORS

- ^a Folberth and Pfister (1961).
- ^b Vaipolin *et al.* (1964 a,b)
- ^c Abrahams and Bernstein (1970).
- ^d Pfister (1958).
- ^e Gasson *et al.* (1962); sphalerite above $\sim 635^\circ\text{C}$, $a = 5.880 \text{ \AA}$ at 640°C , 5.851 \AA at room temperature.
- ^f Goryunova *et al.* (1964).
- ^g Abrahams and Bernstein (1971).
- ^h Goryunova *et al.* (1963 a).
- ⁱ Rosenberg and Strauss (1960).
- ^j Phase transformation slightly below melting point for CdSnAs_2 may be a disordering to zincblende structure.
- ^k Borshchevskii *et al.* (1967).
- ^l Masumoto *et al.* (1966).
- ^m Buehler *et al.* (1973). From Bi-Pb eutectics, $a = 5.465 \pm 0.001 \text{ \AA}$, $c = 10.704 \pm 0.001 \text{ \AA}$. Bertoti and Somogyi (1971) give $a = 5.465 \pm 0.001 \text{ \AA}$, $c = 10.707 \pm 0.001 \text{ \AA}$.
- ⁿ Maunaye and Lang (1970); related to wurtzite.
- ^o Trykozko and Goryunova (1968).
- ^p Springthorpe and Harrison (1969; prepared from Sn solution and probably saturated with Sn).
- ^q Goryunova *et al.* (1969).
- ^r Rubenstein and Ure (1968).
- ^s Vaipolin *et al.* (1971); As zincblende, $a = 6.281 \text{ \AA}$ (Goryunova *et al.*, 1968a, b).
- ^t Rabenau and Eckerlin (1959); Eckerlin (1961).
- ^u Vaipolin *et al.* (1968); $x = 0.239$.
- ^v Ray *et al.* (1969).
- ^w Lind and Grant (1973). For ZnGeP_2 $x = 0.25816$ and for ZnSiAs_2 $x = 0.2658$.
- ^x Ivanova *et al.* (1970).
- ^y Buehler *et al.* (1972).
- ^z Valov *et al.* (1973).

TABLE 2.3. *Atomic position parameters and predicted A-C and B-C interatomic distances in the chalcopyrite family $A^{\text{II}}B^{\text{IV}}C^{\text{V}}$. (After Abrahams and Bernstein, 1971)*

	$a (\text{\AA})^\dagger$	$c (\text{\AA})^\dagger$	Predicted x and A-C (\AA) and B-C (\AA) distances \ddagger			A-C and B-C distances from covalent radii of Van Vechten and Phillips \S	
			x	A-C	B-C	A-C	B-C
ZnSiP_2	5.399	10.435	0.2671	2.367	2.259	2.353	2.301
CdSiP_2	5.680	10.431	0.2929	2.546	2.258	2.533	2.301
ZnSiAs_2	5.606	10.890	0.2646	2.453	2.358	2.450	2.398
CdSiAs_2	5.884	10.882	0.2893	2.629	2.356	2.630	2.398
ZnGeP_2	5.465	10.771	0.2573	2.378	2.332	2.353	2.353
CdGeP_2	5.741	10.775	0.2819	2.548	2.333	2.533	2.353
ZnGeAs_2	5.672	11.153	0.2585	2.471	2.415	2.450	2.450
CdGeAs_2	5.9427	11.2172	0.2790	2.631	2.429	2.630	2.450
CdSnP_2	5.900	11.518	0.2621	2.577	2.494	2.533	2.533
CdSnAs_2	6.0937	11.9184	0.2612	2.659	2.580	2.630	2.630

\dagger Lattice constants used for these computations.

$\ddagger x = 0.5 - (c^2/32a^2 - 1/16)^{1/2}$; (A-C) = $[a^2x^2 + (4a^2 + c^2)/64]^{1/2}$; (B-C) = $[a^2(1/2 - x)^2 + (4a^2 + c^2)/64]^{1/2}$.

\S Van Vechten and Phillips (1970) (Table 2.4).

THE CHALCOPYRITE STRUCTURE AND CRYSTAL GROWTH

TABLE 2.4. Tetrahedral covalent radii. (After Van Vechten and Phillips, 1970)

Be		B	C	N	O	F
0.975		0.853	0.774	0.719	0.678	0.672
Mg		Al	Si	P	S	Cl
1.301		1.230	1.173	1.128	1.127	1.127
Ca	Cu	Zn	Ga	Ge	As	Se
1.333	1.225	1.225	1.225	1.225	1.225	1.225
Sr	Ag	Cd	In	Sn	Sb	Te
1.689	1.405	1.405	1.405	1.405	1.405	1.405

and several I-III-VI₂ compounds (based on early lattice constant data) conform to this relation and confirms that the BC₄ tetrahedra are regular.

The Abrahams-Bernstein analysis was subsequently carried out for many of the I-III-VI₂ compounds (Abrahams and Bernstein, 1973a, b) on the basis of a detailed structural investigation of AgGaS₂, CuGaS₂, and CuInS₂ (CuGaS₂ and CuInS₂ were slightly nonstoichiometric). For AgGaS₂ they show that the value of x predicted from $2 - c/a$ is 0.3061 compared with a measured value of 0.2908. For CuGaS₂, x (calc.) = 0.2604 and x (meas.) = 0.2539. For CuInS₂, x (calc.) = 0.2461 and x (meas.) = 0.2296. In contrast to the II-IV-V₂ compounds, the measured values are significantly different from that expected for a geometrically regular B-atom tetrahedron.

Robbins *et al.* (1973) have examined the experimental value of x for the I-III-VI₂ compounds in the light of the Abrahams and Bernstein equations and suggest that there is stronger bonding of the C-atom with its two nearest A-atom neighbors presumably because of A-atom *d*-electron contribution to the bonding.[†]

For the II-IV-V₂ compounds, Folberth discussed the formation, stability, and tetragonal compression of the chalcopyrite structure in terms of the polarizabilities and thus relative electronegativities of the Group II and Group IV atoms., i.e. relative polarization of the A-C and B-C bonds (Folberth, 1959; Folberth and Pfister, 1960, 1961). It is suggested that the tetragonal compression will be small or only the zinc-blende phase will form (ex: MgGeP₂) when the polarization of these bonds are approximately equal, and this will occur when

$$\left[\left(\frac{r_{II}}{r_{IV}} \right)_{\text{ionic}} - \left(\frac{r_{II}}{r_{IV}} \right)_{\text{covalent}} \right] \text{ is small;}$$

r is the radius of the ion or atom.

The observation of $2 - c/a \cong 0$ for the ZnSnC₂ compounds has recently been discussed (Robbins *et al.*, 1973) on the basis of the difference in number of valence electrons for the Zn-C bonds and the number of valence electrons for the Sn-C bonds (Zn-C atom pairs have seven valence electrons and Sn-C atom pairs have nine valence electrons; the latter will thus have a shorter bond length than the former even though the sum of the covalent radii is greater). It is suggested that this difference in interatomic distances just compensates for the difference in tetrahedral radii of the A- and B-atoms. In general, with increasing atomic radii (or atomic number) of the A-atoms

[†] See Section 4.1 concerning the role of Cu and Ag *d*-states on the valence band structure of these materials.

TERNARY CHALCOPYRITE SEMICONDUCTORS

and decreasing atomic number of the B-atoms, one finds increasing values of $2 - c/a$ because the contraction of B-C bonds due to stronger bonds (B-C atom pairs have nine valence electrons) reinforce the difference in atomic size. Thus the largest value of $2 - c/a$ is found in CdSiP₂ (0.163), AgAlS₂, and AgGaS₂ (~ 0.20).

Phillips (1973) has discussed the trends in the tetragonal distortion of II-IV-V₂ compounds in terms of nearest-neighbor electronegativities that were obtained from his dielectric electronegativity scale developed to treat A^NB^{8-N} compounds with diamond and wurtzite structures (Table 2.5). Note, for example, that the Pauling electronegativities for Si, Ge, and Sn are all the same, yet for the CdBP₂ phases the tetragonal distortions decrease with increasing atomic number of the B-atom. Only the dielectric electronegativities can explain the observed trends, and Phillips finds good quantitative agreement for the observed values of $2 - c/a \lesssim 0.05$ with those calculated on the basis of $2 - c/a$ linearly related to the electronegativities X_A, X_B, and X_C. ($2 - c/a = -0.60 X_A + 0.25 X_B + 0.15 X_C + 0.01$.) For larger values of $2 - c/a$, the linear theory underestimates the observed distortion, and it is concluded that the tetragonal distortion is determined by charge redistribution. Atoms B and C gain charge, while atom A loses charge.

TABLE 2.5. Comparison of scales of electronegativity for non-transition elements

For each element values are taken from the Phillips dielectric scale (sp^3 hybridized crystalline bonds) in line 1, from Pauling's (1960) thermochemical molecular scale in line 2 (in parentheses), and from Gordy's (1956) (based on work functions at surfaces and on molecular thermochemical data) in line 3 [(in double parentheses)]. (After Phillips, 1973)

Li	Be	B	C	N	O	F
1.00	1.50	2.00	2.50	3.00	3.50	4.00
(1.0)	(1.5)	(2.0)	(2.5)	(3.0)	(3.5)	(4.0)
[(0.95)]	[(1.5)]	[(2.0)]	[(2.5)]	[(3.0)]	[(3.5)]	[(3.95)]
Na	Mg	Al	Si	P	S	Cl
0.72	0.95	1.18	1.41	1.64	1.87	2.10
(0.9)	(1.2)	(1.5)	(1.8)	(2.1)	(2.5)	(3.0)
[(0.9)]	[(1.2)]	[(1.5)]	[(1.8)]	[(2.1)]	[(2.5)]	[(3.0)]
Cu	Zn	Ga	Ge	As	Se	Br
0.79	0.91	1.13	1.35	1.57	1.79	2.01
(1.9)	(1.6)	(1.6)	(1.8)	(2.0)	(2.4)	(2.8)
[(1.8)]	[(1.5)]	[(1.5)]	[(1.8)]	[(2.0)]	[(2.4)]	[(2.8)]
Ag	Cd	In	Sn	Sb	Te	I
0.67	0.83	0.99	1.15	1.31	1.47	1.63
(1.9)	(1.7)	(1.7)	(1.8)	(1.9)	(2.1)	(2.5)
[(1.8)]	[(1.5)]	[(1.5)]	[(1.7)]	[(1.8)]	[(2.0)]	[(2.55)]
Au	Hg	Tl	Pb	Bi		
0.64	0.79	0.94	1.09	1.24		
(2.4)	(1.9)	(1.8)	(1.8)	(1.9)		
[(2.3)]	[(1.8)]	[(1.5)]	[(1.9)]	[(1.8)]		

2.2 Phase Transitions in Chalcopyrite Crystals

The close relation between the cubic zincblende and ordered ternary tetragonal phases results in the existence of disordered ternary phases exhibiting the zincblende structure for several of the chalcopyrites, particularly at elevated temperatures, and

THE CHALCOPYRITE STRUCTURE AND CRYSTAL GROWTH

TABLE 2.6. *Melting points and solid state transition temperatures for the II-IV-V₂ compounds*

Compound	Melting temperature (°C)	Transition temperature (°C)	Structure of transition phase	References
BeSiN ₂	Unknown			
MgSiP ₂	Unknown			
MgGeP ₂	Unknown			
ZnSiP ₂	~1370			
	1250			a, e
ZnSiAs ₂	1096			c
ZnGeP ₂	1025	952		
	1027 ± 3	950 ± 5	Unknown	b, c, d, e
ZnGeAs ₂	850		Zincblende	a, g, h
	875	812?		
ZnSnP ₂	Peritectic, 930	720	Zincblende	f, j, k, e
ZnSnAs ₂	775	650	Zincblende	h, g, i, m
	772	635		
	778	632		
ZnSnSb ₂	Unknown	Unknown	Zincblende	v
CdSiP ₂	<1200			a, e, w
	1120			
CdSiAs ₂	>850			u
CdGeP ₂	776			a, i, l, e
	800			
	790 ± 5			
	779			
CdGeAs ₂	670	630?	Zincblende?	g, h, p, q, r, s, t
	645			
	665			
CdSnP ₂	570			o
CdSnAs ₂	593	567		
	596	587	Zincblende	b, h, m, n
	595	554		

^a Vaipolin *et al.* (1964 a, b, 1965 a, b).

^b Vaipolin *et al.* (1965 a, b).

^c Masumoto *et al.* (1966).

^d Buehler *et al.* (1973).

^e Mughal *et al.* (1969).

^f Goryunova *et al.* (1969); crystals grown slowly from liquid Sn exhibit the chalcopyrite structure (5–10/hr). Faster cooling rates give zincblende structure.

^g Borchers and Maier (1963 a, b).

^h Leroux-Hugon (1963); the transition at 812°C reported by this author (see also Fig. 2.43).

ⁱ Masumoto and Isomura (1965).

^j Borshchevskii *et al.* (1968).

^k Berkovskii *et al.* (1968).

^l Buehler and Wernick (1972).

^m Gasson *et al.* (1962); see also Fig. 2.35.

ⁿ Goryunova *et al.* (1962).

^o Buehler and Wernick (1971); peritectic.

^p Osmanov *et al.* (1968); quenching of CdGeAs₂ produced a glass.

^q Borshchevskii and Roenkov (1969) did not corroborate the solid state transformation (see also Fig. 2.39), and show that solidification is complicated by supercooling phenomena.

TERNARY CHALCOPYRITE SEMICONDUCTORS

^a Vaipolin *et al.* (1964 a,b).

^b Goryunova (1965).

^c Cervenka and Kasper (1970) did not observe a phase transition.

^d Averkieva *et al.* (1970 a,b); peritectic.

^e Goryunova *et al.* (1968 a,b); forms peritectically.

^w Valov *et al.* (1973); the melting point of CdSiP₂ is suggested to be underestimated.

TABLE 2.7. *Melting points for the I-III-VI₂ compounds*

Compound	Melting temperature (°C)	References
CuAlS ₂	~1300	f
CuAlSe ₂	~1200	f
CuAlTe ₂	—	
CuGaS ₂	1280	e, g, h
	>1200	
CuGaSe ₂	1040	a, b
	~1070	
CuGaTe ₂	870	a
CuInS ₂	1000–1050	f
CuInSe ₂	990	a
CuInTe ₂	780	a
CuTlS ₂	—	
CuTlSe ₂	405	a
AgAlS ₂	—	
AgAlSe ₂	—	
AgAlTe ₂	—	
AgGaS ₂	1040	d, e, f
	980	
	~950	
AgGaSe ₂	850	a
AgGaTe ₂	720	a
AgInS ₂	—	i
AgInSe ₂	773	a, b, c
	~770	
	780	
AgInTe ₂	680	a
CuFeS ₂	950	j

^a Zhuze *et al.* (1958). A phase transition is suggested for CuTlSe₂.

^b Lerner (1966).

^c Mason and O'Kane (1960).

^d Cound *et al.* (1970).

^e Belova *et al.* (1967).

^f Kasper (1972).

^g Apple (1958).

^h Fischer (1959).

ⁱ Hahn *et al.* (1953) reported a tetragonal to hexagonal (wurtzite) phase transition at ~700°C.

^j Frueh (1950) and Schlegel and Schuller (1952). Pankratz and King (1970); tetragonal-to-cubic zinc-blende transformation at 557°C; second order transition at ~657°C.

THE CHALCOPYRITE STRUCTURE AND CRYSTAL GROWTH

several can be retained to room temperature by fast cooling. The melting points of the chalcopyrite phases and transition temperatures, if a particular phase undergoes a transition, are given in Tables 2.6 and 2.7. MgGeP_2 (Table 2.6) exhibits only the cubic zincblende structure. This structure is the equilibrium phase at elevated temperatures for ZnSnP_2 , ZnSnAs_2 , CdSnAs_2 , and CuFeS_2 . ZnGeP_2 undergoes a transformation to an unknown phase at 950°C which has not been retained by quenching (Buehler *et al.*, 1973). CdGeP_2 has been reported to undergo a phase change to a presumed zincblende structure, but recent phase diagram work on the CdP_2 -Ge system does not support this (Buehler *et al.*, 1973). ZnSnAs_2 only exists as a single phase in the zincblende structure at elevated temperatures (Gasson *et al.*, 1962, see Section 2.8.3), and Folberth and Pfister (1960) discuss the existence of the zincblende form in terms of the greater similarity of Zn-As and Sn-As bonds compared to the other II-IV-V₂ compounds. Confirmation of a phase change in ZnGeAs_2 has not been directly confirmed, but alloying InAs with ZnGeAs_2 appears to stabilize a cubic phase (Voitsekhovsky, 1964; see Section 2.10).

The possible existence of zincblende modifications of the I-III-VI₂ phases has not been determined to the same degree as for the II-IV-V₂ compounds. Complete cubic zincblende solid solutions exist in the $(\text{CuInTe}_2)_x(2 \text{InAs})_{1-x}$ and $(\text{CuInTe}_2)_x(2 \text{CdTe})_{1-x}$ systems, suggesting that a zincblende phase of CuInTe_2 is stabilized by InAs and CdTe (Voitsekhovsky, 1964; see also Section 2.7).

2.3 Tetrahedrally Coordinated Compounds with more than Three Components

Although ternary chalcopyrite structure materials are primarily discussed in this book, we wish to discuss briefly tetrahedrally coordinated compounds containing more than three components in the light of the scheme depicted in Fig. 2.2 for the formation of phases which are analogs of the III-V and II-VI compounds. By cross-substitution of other atoms while maintaining an average electron-to-atom ratio of 4, it is possible to derive or think in terms of new tetrahedrally coordinated phases containing more than three components, and this approach has been used in the search for new materials (see, for example, Goodman and Douglas, 1954; Goodman, 1958; Pamplin, 1960, 1964; Parthé, 1963, 1964, 1972; Goryunova and Parthé, 1967). If, indeed, a new tetrahedrally coordinated phase forms and all of the lattice sites are occupied, the phase is referred to as a *normal* tetrahedral compound. *Defect* tetrahedral phases can exist, i.e. some of the lattice sites are unoccupied, and, on first glance, the formula of the compound would suggest e/a to be greater than 4. However, if the number of vacant sites per formula unit are counted, but assigned zero valence, e/a is equal to 4 (Pamplin, 1960). Pamplin's original general formula is

$$\frac{\sum n_i v_i}{\sum n_i} = 4,$$

where n_i is the number of atoms of the i th kind per formula and v_i the number of outer valence electrons. Vacant sites are counted but assigned zero valence. For example, consider Ga_2S_3 which can be written as $\text{Ga}_2\square\text{S}_3$, where \square is a vacant site on the Ga sublattice. Thus $\sum n_i v_i = (2)(3) + (1)(0) + (3)(6) = 24$ and $\sum n_i = 2 + 1 + 3 = 6$. Another example is CdIn_2Se_4 , which is a cubic-ordered structure related to zincblende. If the vacancy on the cation sublattice is not considered, e/a > 4. However, considering this compound as $\text{CdIn}_2\square\text{Se}_4$, e/a = 4. The reader is referred to Parthé (1964, 1972) for a fuller discussion and all-embracing definition of defect tetrahedral structures.

TERNARY CHALCOPYRITE SEMICONDUCTORS

TABLE 2.8. Some tetrahedral systems involving I-III-VI₂ and II-IV-V₂ compounds

Phase or System	Remarks	Ref.
Cu ₁₆ Zn ₃₃ Ga ₁₁₃ Ge ₁₇ As ₁₃₁ Se ₄₈	Z†, $a = 5.65 \text{ \AA}$	a
Cu ₅₇ Zn ₃₃ Ga ₂₄₃ Ge ₅₁ As ₂₈₈ Se ₉₆	Z, $a = 5.65 \text{ \AA}$	a
Cu ₁₉ Zn ₉₉ Ga ₂₂₅ Ge ₄₁ As ₂₈₈ Se ₉₆	Z, $a = 5.65 \text{ \AA}$	a
InSb-AgInTe ₂	Incomplete solid solubility	a
CuZn ₂ AlSe ₄ (CuAlSe ₂ + 2 ZnSe)	Z, not ordered, $a = 5.624 \text{ \AA}$	b
CuZn ₂ AlTe ₄ (CuAlTe ₂ + 2 ZnTe)	Z, not ordered, $a = 6.043 \text{ \AA}$	b
CuZn ₂ GaSe ₄ (CuGaSe ₂ + 2 ZnSe)	Z, order cannot be determined, $a = 5.653 \text{ \AA}$	b
CuZn ₂ GaFe ₄ (CuGaTe ₂ + 2 ZnTe)	Z, order cannot be determined, $a = 6.057 \text{ \AA}$	b
CuZn ₂ InS ₄ (CuInS ₂ + 2 ZnS)	Z, not ordered, $a = 5.475 \text{ \AA}$	b
CuZn ₂ InSe ₄ (CuInSe ₂ + 2 ZnSe)	Z, not ordered, $a = 5.733 \text{ \AA}$	b
CuZn ₂ InTe ₄ (CuInTe ₂ + 2 ZnTe)	Z, not ordered, $a = 6.153 \text{ \AA}$	b
CuCd ₂ InSe ₄ (CuInSe ₂ + 2 CdSe)	Z, not ordered, $a = 5.934 \text{ \AA}$	b
CuCd ₂ InTe ₄ (CuInTe ₂ + 2 CdTe)	Z, not ordered, $a = 6.335 \text{ \AA}$	b
AgZn ₂ InTe ₄ (AgInTe ₂ + 2 ZnTe)	Z, not ordered, $a = 6.253 \text{ \AA}$	b
AgCd ₂ GaTe ₄ (AgGaTe ₂ + 2 CdTe)	Z, not ordered, $a = 6.375 \text{ \AA}$	b
AgCd ₂ InTe ₄ (AgInTe ₂ + 2 CdTe)	Z, order cannot be determined, $a = 6.438 \text{ \AA}$	b
CuCd ₂ AlSe ₄ (CuAlSe ₂ + 2 CdSe)	W†, not ordered, $a = 4.106 \text{ \AA}$, $c = 6.752 \text{ \AA}$	b
CuCd ₂ InS ₄ (CuInS ₂ + 2 CdS)	W, not ordered, $a = 4.047 \text{ \AA}$, $c = 6.617 \text{ \AA}$	b
AgZn ₂ AlS ₄ (AgAlS ₂ + 2 ZnS)	W, not ordered, $a = 3.846 \text{ \AA}$, $c = 6.313 \text{ \AA}$	b
AgZn ₂ InS ₄ (AgInS ₂ + 2 ZnS)	W, not ordered, $a = 3.944 \text{ \AA}$, $c = 6.459 \text{ \AA}$	b
AgCd ₂ AlS ₄ (AgAlS ₂ + 2 CdS)	W, not ordered, $a = 4.13 \text{ \AA}$, $c = 6.723 \text{ \AA}$	b
AgCd ₂ GaSe ₄ (AgGaSe ₂ + 2 CdSe)	W, not ordered, $a = 4.251 \text{ \AA}$, $c = 6.956 \text{ \AA}$	b
AgCd ₂ InS ₄ (AgInS ₂ + 2 CdS)	W, order cannot be determined, $a = 4.112 \text{ \AA}$, $c = 6.709 \text{ \AA}$	b
AgCd ₂ InSe ₄ (AgInSe ₂ + 2 CdSe)	W, order cannot be determined, $a = 4.277 \text{ \AA}$, $c = 6.988 \text{ \AA}$	b
ZnCdIn ₄ Sn ₂ As ₈ (ZnSnAs ₂ + CdSnAs ₂ + 4 InAs)	Z, $a = 6.005 \text{ \AA}$	c
Zn ₂ CdIn ₂ Sn ₃ As ₈ (2ZnSnAs ₂ + CdSnAs ₂ + 2InAs)	Z, $a = 5.949 \text{ \AA}$	c
ZnCd ₂ In ₂ Sn ₃ As ₈ (ZnSnAs ₂ + 2 CdSnAs ₂ + 2InAs)	Z, $a = 6.006 \text{ \AA}$	c

† Z = zincblende related structure.

‡ W = wurtzite related structure.

^a Goryunova (1965).

^b Parthé *et al.* (1969).

^c Pamplin and Shah (1965); annealed at 595°C for a few days.

An example of an ordered quaternary normal tetrahedral material is Cu₂FeSnS₄ (the mineral stannite). It is tetragonal and the ordered quaternary analog of the zinc-blende structure; $a \approx a_z$ and $c \approx 2a_z$. Cu₂FeSnSe₄ and Cu₂ZnSnS₄ are two compounds isostructural to stannite. On the other hand, Cu₂CdGeS₄ (a₁₂₄₆ in the Parthé notation) is an ordered normal tetrahedral phase with an orthorhombic structure which is a superstructure of wurtzite ($a \sim 2a_w$, $b \sim a_w\sqrt{3}$, and $c \sim c_w$) (Parthé *et al.*, 1969).

THE CHALCOPYRITE STRUCTURE AND CRYSTAL GROWTH

Counting atoms, vacancies, and electrons to formulate new ordered phases does not necessarily lead to the formation of new phases. For example, Pamplin (1970) formulated a large number of I–III–IV₂–V₄ compositions (ex: CuGaGe₂As₄), which can be derived by cross-substitution in the II–IV–V₂ phases. However, no such phases could be synthesized. Similarly, twenty formulations of general composition 12₂36₄ (ex: CuZn₂InS₄) did not form *ordered* superstructures but yielded simple zincblende or wurtzite diffraction patterns (Parthé *et al.*, 1969, see also Table 2.8).

It is important to distinguish between ordered and disordered phases in discussing the formation of new phases; the latter can be considered as solid solutions of one phase in another. For example, CuSn₂GaSe₄ (zincblende, $a = 5.653 \text{ \AA}$) can be considered a solid solution of tetragonal CuGaSe₂ in 2 ZnSe (Parthé *et al.*, 1969). Similarly, the zincblende phase Cu₁₆Zn₃₃Ga_{11.3}Ge₁₇As_{13.1}Se_{4.8} (Goryunova, 1965; and Table 2.8) can be considered as a solid solution of 17 ZnGeAs₂, 16 CuGaSe₂, and 16ZnSe in 97 GaAs with $a = 5.65 \text{ \AA}$ and “sharp” diffraction lines. The disordered phase Cu_{11.5}Zn₂₃Ga_{7.5}Ge₈As₁₆Se₃₀Br₄ appears to have the same lattice constant as Ge (Parthé, 1972). Now the lattice constants for ZnSe, GaAs, and Ge are 5.65 \AA , 5.6533 \AA , and 5.6575 \AA respectively. The near identity of the lattice constants of the above multi-component disordered solid solutions (*sharp diffraction lines*) with ZnSe, GaAs, and Ge can only be reconciled on the basis of the Van Vechten–Phillips tetrahedral radii (Table 2.4) because the tetrahedral radii of Cu, Zn, Ga, As, Se, and Br are identical. No other listing of tetrahedral radii is consistent with this result.

2.4 DISSOCIATION PRESSURES OF CHALCOPYRITE COMPOUNDS

Quantitative estimates of total dissociation pressures for the chalcopyrite phases are sparse. No such data exists at the present time for the I–III–VI₂ compounds, although, as discussed below, caution is generally given by various authors regarding the possibilities of explosions during preparation and subsequent crystal growth of these materials.

The situation is somewhat better for the II–IV–V₂ compounds. Two techniques have been used for determining dissociation pressures. The first, a so-called bulb technique (Buehler and Wernick, 1971), consists of maintaining a presynthesized powder sample of the compound at various temperatures in the “cold zone” of an evacuated quartz ampoule (Fig. 2.3) and the other end, the thin-wall “bulb,” at a temperature at which the quartz is plastic (~1250°C), and the total decomposition pressure (P_T) determined for various fixed lower temperatures by determining the external pressure required to

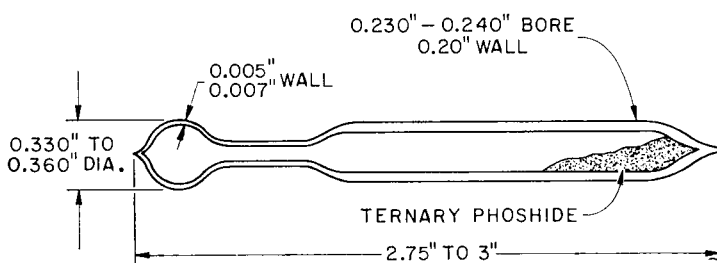


FIG. 2.3. Quartz ampoule having a thin-wall bulb for determining total decomposition pressure. (After Buehler and Wernick, 1971.)

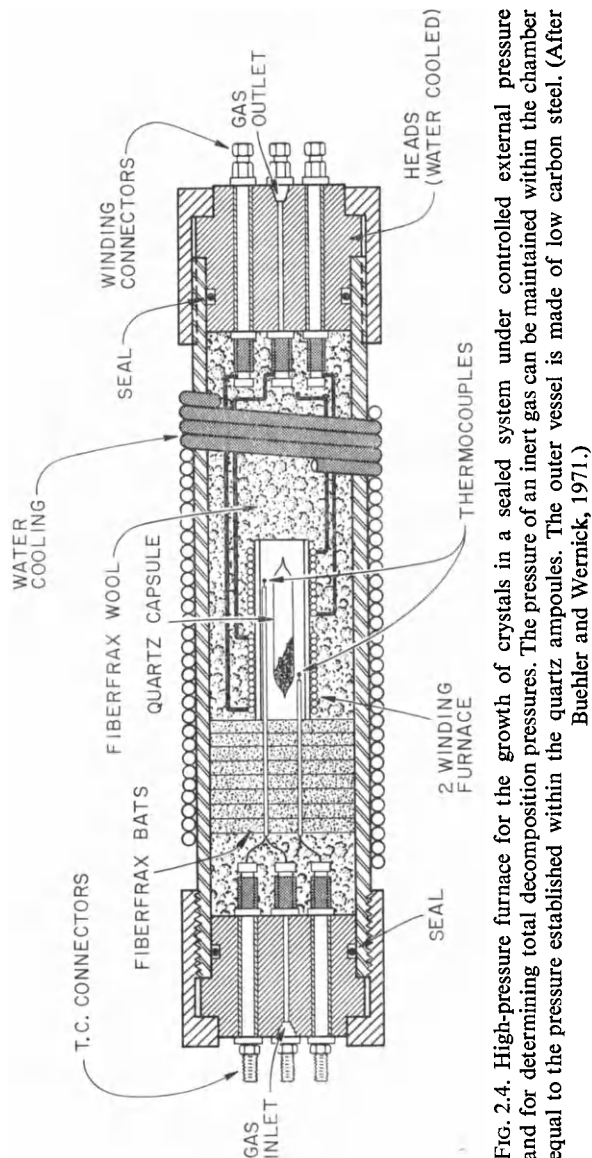


FIG. 2.4. High-pressure furnace for the growth of crystals in a sealed system under controlled external pressure and for determining total decomposition pressures. The pressure of an inert gas can be maintained within the chamber equal to the pressure established within the quartz ampoules. The outer vessel is made of low carbon steel. (After Buehler and Wernick, 1971.)

THE CHALCOPYRITE STRUCTURE AND CRYSTAL GROWTH

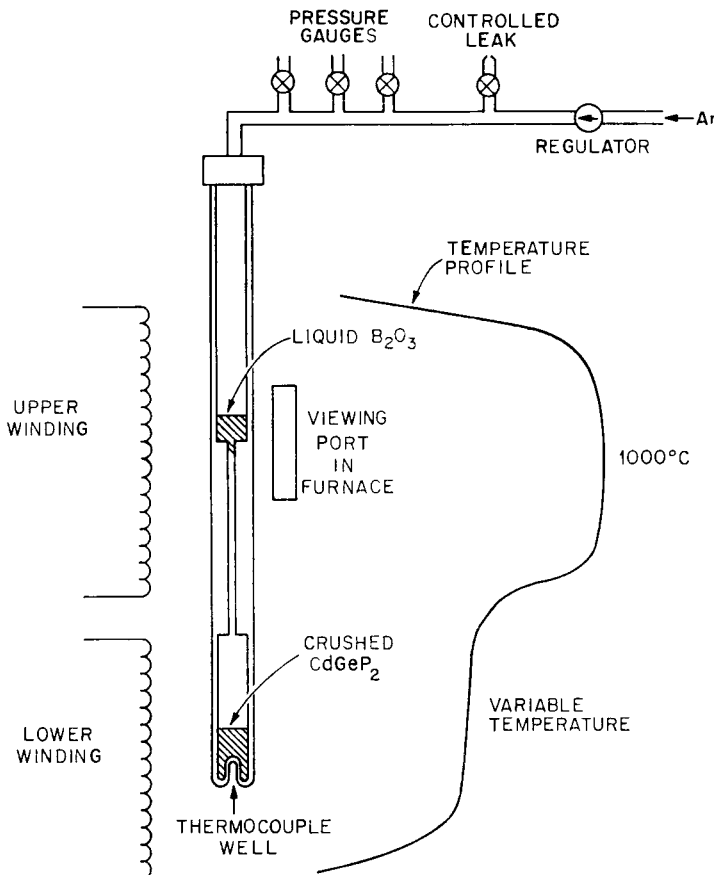


FIG. 2.5. Liquid B_2O_3 meniscus technique for determining total dissociation pressures. Modification of that used by Borshchevskii *et al.* (1971). (After Wiley *et al.*, 1973.)

prevent either expansion or collapse of that portion of the quartz ampoule in the plastic range. A pressurized two-zone furnace for performing such experiments is depicted in Fig. 2.4. At least four experiments were necessary to determine an experimental point, and this requires the use of a new ampoule for each experiment. Equilibration times in most cases were of the order of 3 hr. For checks, several were as long as 24 hr.

A second technique is the one described by Borshchevskii and Roenkov (1971). A modification of their apparatus is shown on Fig. 2.5. It consists of a two-chamber quartz tube with a capillary joining the two chambers. The lower chamber contains the sample in the form of a crushed powder which surrounds a thermocouple well. The upper chamber contains a small quantity of high-purity vacuum cast B_2O_3 . The tube is flushed with Ar and positioned, as shown, in a two-zone furnace which contains a viewing port for observing the B_2O_3 . During a run, the B_2O_3 is melted and the meniscus observed through the port. The temperature of the lower furnace is then slowly increased. The B_2O_3 meniscus is held at a constant position by applying a counter-pressure of Ar to the upper chamber to balance the rising pressure in the lower chamber. The effect of temperature on the pressure of Ar in the lower chamber can be easily corrected.

TERNARY CHALCOPYRITE SEMICONDUCTORS

Of the above two methods, the latter is better in terms of accuracy, ease with which the measurements can be made, and ease of establishing reversibility on heating and cooling. In general, it appears that liquid-vapor equilibrium at a given temperature is established relatively rapidly, but caution is expressed for such an interpretation of the solid-vapor data. It should be realized that in establishing a given total pressure, the composition of the condensed phase will change as material is lost to the vapor phase and that the condensed phase is no longer stoichiometric. The larger the ratio of sample weight to lower chamber volume, the smaller the change in stoichiometry.

Borshchevskii and Roenkov determined the equilibrium dissociation pressures of ZnSiAs_2 , ZnGeAs_2 , ZnSnAs_2 , CdSiAs_2 , CdGeAs_2 , and CdSnAs_2 as a function of temperature. For the liquids above the melting points, the pressure P_T in torr is given by the following equations ($T = \text{K}$):

$$\text{ZnSiAs}_2: \log P_T = 6.667 - 5175/T.$$

$$\text{ZnGeAs}_2: \log P_T = 5.360 - 3392/T.$$

$$\text{ZnSnAs}_2: \log P_T = 4.505 - 2445/T.$$

$$\text{CdSiAs}_2: \log P_T = 6.91 - 4730/T.$$

$$\text{CdGeAs}_2: \log P_T = 6.622 - 4380/T.$$

$$\text{CdSnAs}_2: \log P_T = 6.976 - 4770/T.$$

The vapor phase over liquid CdGeAs_2 consists primarily of Cd and As, while for ZnSnAs_2 and ZnGeAs_2 , As is primarily present.

Decomposition pressure data for solid ZnSiP_2 , CdSiP_2 and solid and liquid ZnGeP_2 , obtained by use of the bulb technique, are shown in Fig. 2.6 and 2.7 (Buehler and Wernick, 1971). Similar data for solid and liquid CdGeP_2 , obtained by use of the liquid B_2O_3 meniscus technique, are shown in Figs. 2.8 and 2.9 and, in contrast to ZnGeP_2 , do not show an abrupt change at the melting point (Wiley *et al.*, 1973). The data of Fig. 2.9 is given by

$$\log P_T(\text{atm}) = 8.826 - 9023/T.$$

For ZnSiP_2 and CdSiP_2 the vapor phase consists of essentially Zn and/or Cd and P,

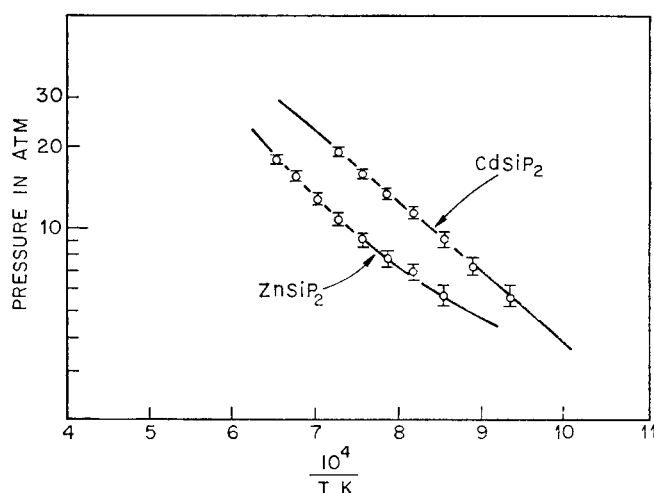


FIG. 2.6. Plot of $\ln P_T$ versus $1/T$ for ZnSiP_2 and CdSiP_2 . Data obtained by the bulb technique. (After Buehler and Wernick, 1971.)

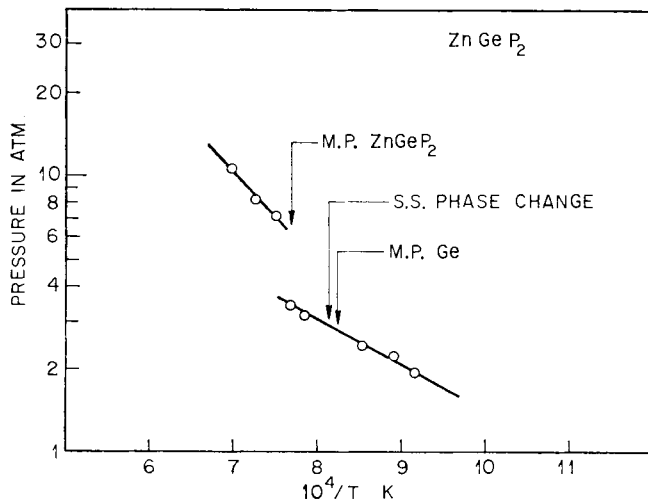


FIG. 2.7. Plot of $\ln P_T$ versus $1/T$ for ZnGeP_2 . Data obtained by the bulb technique. (After Buehler and Wernick, 1971.)

while for ZnGeP_2 and CdGeP_2 , the vapor phase consists essentially of P , although detectable amounts of Zn and Cd are present as determined by analysis of condensate. Comparison of the pressure data for the arsenides and phosphides reveals that the latter exhibit much higher dissociation pressures.

Experience as regards the preparation and purification of sulfides, selenides, and tellurides suggests that the dissociation pressure will generally be the largest for the sulfides, followed by the selenides and tellurides. During the preparation of sulfides and phosphides from the elements, slow heating rates are required to prevent explosions until all of the sulfur and phosphorus have reacted.

2.5 Phase Relationships in I-III-VI Systems

Some information apropos phase relations in the I-III-VI systems are contained in Table 2.7, but in general the information presently known about the high energy gap materials, i.e. sulfides, which exhibit high dissociation pressures, are qualitative and based essentially on observations made during crystal growth studies. For example, Kasper (1972) has shown that AgGaS_2 exhibits a narrow homogeneity range. Ingots obtained from slow-cooled stoichiometric melts consisted of a light yellow portion, which crystallized first, blending into a green portion, which crystallized last. Growth experiments showed that when the initial melt stoichiometry was $\text{Ag}_{0.97}\text{Ga}_{1.01}\text{S}_2$, only completely yellow material was obtained. On the other hand, when the ampoule was contaminated with oxygen, green crystals were obtained. It is suggested that, in addition to the optical properties depending on defect concentration, AgGaS_2 does not melt congruently. The reported differences in melting points perhaps also suggest the existence of incongruency.

Kasper's results for CuGaS_2 also suggest that stoichiometric CuGaS_2 melts (or freezes) incongruently, while crystals of CuInS_2 grown from stoichiometric melts did not indicate strong stoichiometry variation as observed in CuGaS_2 . The results of a room temperature X-ray study of alloys in the $\text{CuGaS}_2\text{-Ga}_2\text{S}_3$ system by Belova *et al.*

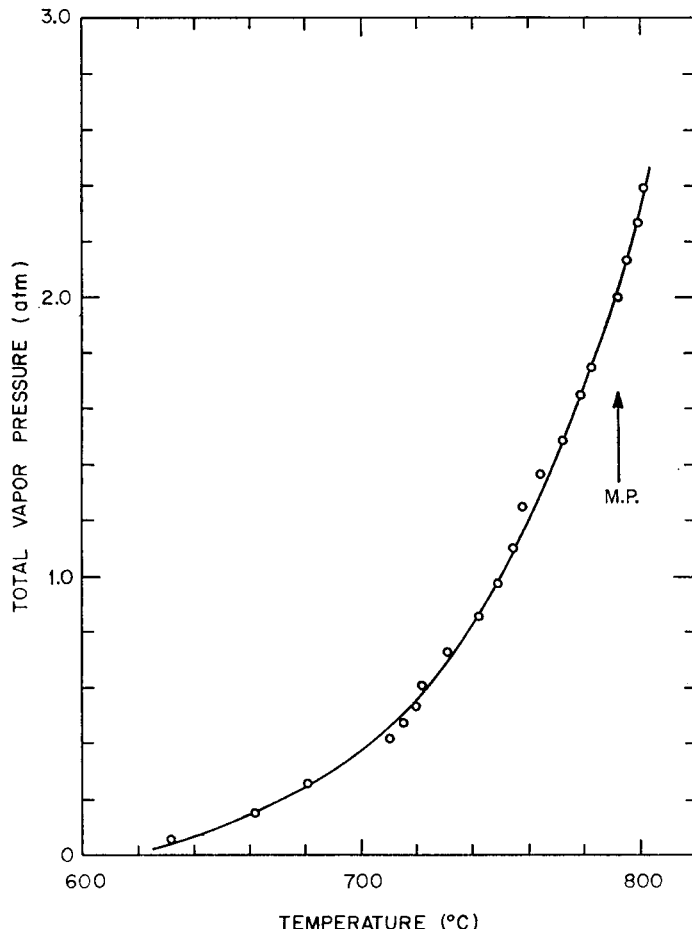


FIG. 2.8. Total dissociation pressure P_T of CdGeP_2 as a function of temperature. Data obtained by the liquid B_2O_3 meniscus technique.
(After Wiley *et al.*, 1973.)

(1967) are shown in Fig. 2.10. With increasing concentration of Ga_2S_3 , a and c decrease due to cation defect formation in the tetragonal structure. The chalcopyrite structure extends to about 15 mol % 2 Ga_2S_3 , and it was noted that their polycrystalline CuGaS_2 ingots, red-brown in color, were always nonuniform. Ga_2S_3 is pale yellow. A two-phase region exists between 10–55 mol % 2 Ga_2S_3 . A single-phase region exists between 55–80 mol % 2 Ga_2S_3 , and the structure of this phase appears to be of the zincblende type and related to the ordered phase CuGa_5S_8 .

2.5.1 The $\text{Cu}_2\text{Se}-\text{Ga}_2\text{Se}_3$ System

The phase relations in a portion of this system were determined by Palatnik and Belova (1967), and their proposed diagram covering the range 40–100 mol % Ga_2Se_3 is shown in Fig. 2.11. Note that CuGaSe_2 forms peritectically. Lerner's (1966) single crystal growth, via zone-leveling of stoichiometric melts suggested that the $\text{Cu}_2\text{Se}-\text{Ga}_2\text{Se}_3$ join was not strictly pseudobinary and that CuGaSe_2 formed incongruently.

THE CHALCOPYRITE STRUCTURE AND CRYSTAL GROWTH

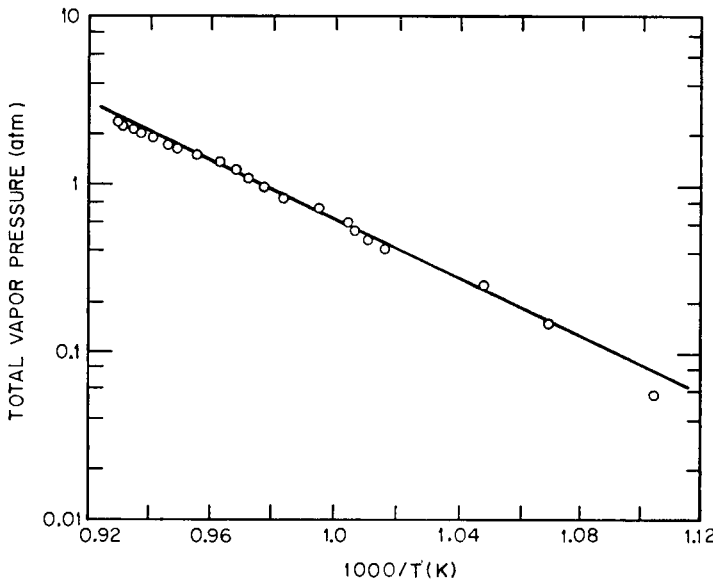


FIG. 2.9. Total dissociation pressure P_T of CdGeP_2 as a function of temperature. Data obtained by the liquid B_2O_3 meniscus technique.
(After Wiley *et al.*, 1973.)

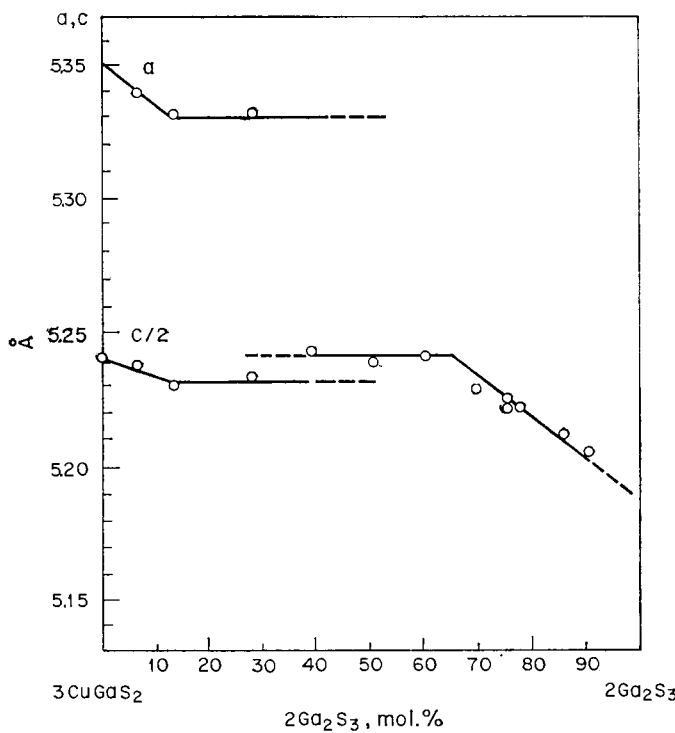


FIG. 2.10. Lattice constants as a function of composition in the $\text{CuGaS}_2-\text{Ga}_2\text{S}_3$ join of the Cu-Ga-S system. (After Belova *et al.*, 1967.)

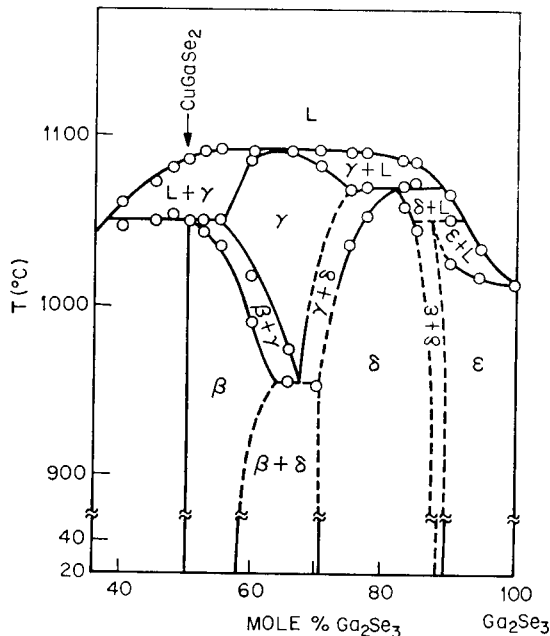


FIG. 2.11. The system $\text{Cu}_2\text{Se}-\text{Ga}_2\text{Se}_3$ in the range 40–100 mol.% Ga_2Se_3 . (After Palatnik and Belova, 1967.)

2.5.2 The $\text{Ag}_2\text{Se}-\text{Ga}_2\text{Se}_3$ System

The phase relations in this system were determined by Palatnik and Belova (1967), and their proposed diagram is shown in Fig. 2.12. AgGaSe_2 forms congruently and can exist over a homogeneity range (Ga_2Se_3 -rich) at elevated temperatures.

2.5.3 The $\text{Ag}_2\text{Se}-\text{In}_2\text{Se}_3$ System

No diagram is available for this system. Lerner's single crystal growth via zone-leveling of AgInSe_2 suggests that the $\text{Ag}_2\text{Se}-\text{In}_2\text{Se}_3$ join is not strictly pseudobinary and that AgInSe_2 freezes incongruently.

2.5.4 The $\text{Cu}_2\text{Te}-\text{Ga}_2\text{Te}_3$ System

Phase diagrams for this system have been proposed by Palatnik and Belova (1967), Fig. 2.13, and by Congiu *et al.* (1973), Fig. 2.14. In the diagram of the former, the chalcopyrite phase β or CuGaTe_2 does not exist at the stoichiometric composition below about 780°C and forms from the β -solid solution (based on Ga_2Te_3) on cooling. The β -phase can exist over a fairly broad Ga_2Te_3 -rich composition range; 10 mol% Ga_2Te_3 is soluble in the β -phase at room temperature. On the other hand, the diagram of Congiu *et al.* shows that CuGaTe_2 forms peritectoidally and exists over a narrow composition range encompassing the stoichiometric composition. In any case, the growth of large homogeneous crystals by ordinary methods will be difficult.

2.5.5 The $\text{Ag}_2\text{Te}-\text{Ga}_2\text{Te}_3$ System

The phase diagram for this system, determined by Palatnik and Belova (1967), is shown in Fig. 2.15. The β -Phase (chalcopyrite) forms incongruently. It exhibits a broad

THE CHALCOPYRITE STRUCTURE AND CRYSTAL GROWTH

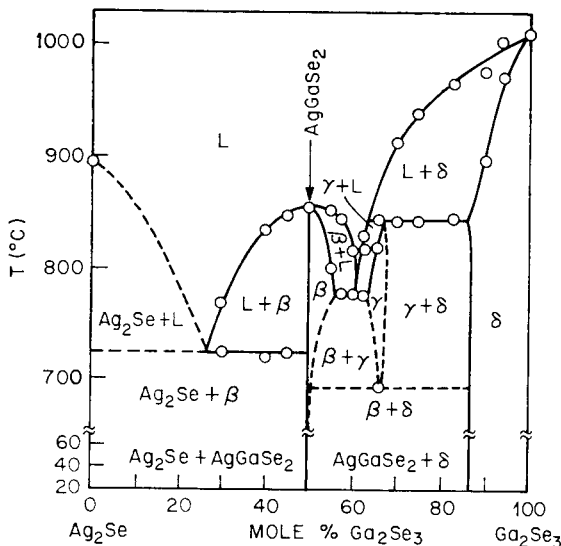


FIG. 2.12. The system $\text{Ag}_2\text{Se}-\text{Ga}_2\text{Se}_3$. (After Palatnik and Belova, 1967.)

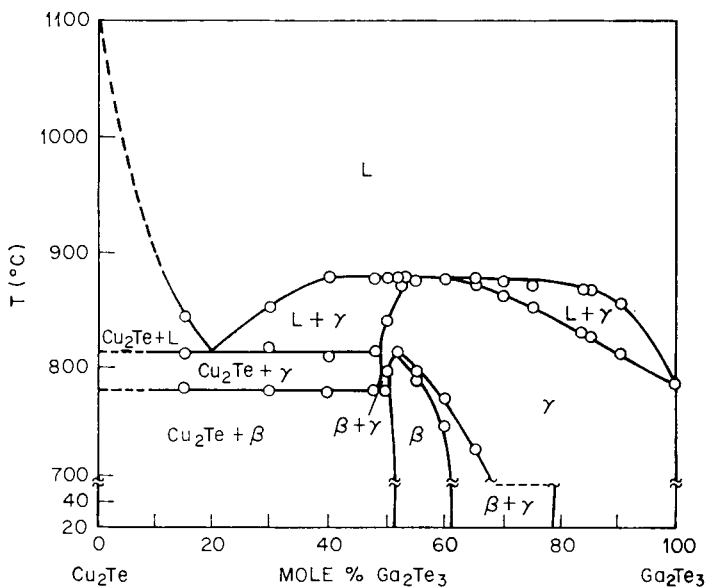
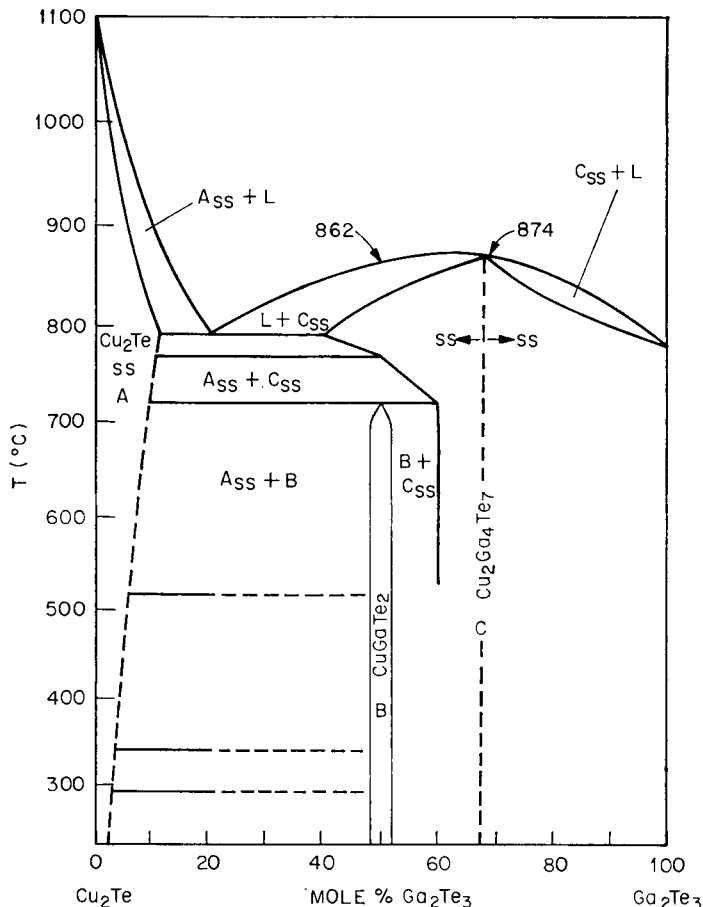


FIG. 2.13. The system $\text{Cu}_2\text{Te}-\text{Ga}_2\text{Te}_3$. (After Palatnik and Belova, 1967.)

FIG. 2.14. The system $\text{Cu}_2\text{Te}-\text{Ga}_2\text{Te}_3$. (After Congiu *et al.*, 1973.)

homogeneity region at elevated temperatures and does not encompass the stoichiometric composition at low temperatures.

2.6 Phase Relationships in Mixed I-III-VI₂-Systems

Information regarding the phase relationships in several mixed I-III-VI₂ systems has been reported by Robbins *et al.* (1973) in the form of lattice constants as a function of composition (Figs. 2.16 and 2.17). Limited solid solubility occurs in the $\text{Cu}_{1-x}\text{Ag}_x\text{AlX}_2$ and $\text{Cu}_{1-x}\text{Ag}_x\text{GaX}_2$ systems (Fig. 2.16a and b) and the extent of the terminal solid solubilities appears to be greater for the selenides than for the sulfides. Complete solid solubility exists in the $\text{Cu}_{1-x}\text{Ag}_x\text{InX}_2$ system (Fig. 2.16c). The c/a ratios for the above three systems are shown in Table 2.9. Complete solid solubility exists in the $\text{M}^{\text{I}}\text{M}^{\text{III}}\text{S}_{2-x}\text{Se}_x$ systems, where $\text{M}^{\text{I}} = \text{Cu}$ and Ag and $\text{M}^{\text{III}} = \text{Al}$, Ga , and In (Fig. 2.17). The melting points for $\text{CuGaS}_{1.5}\text{Se}_{0.5}$ and CuGaSSe are $\sim 1150^\circ\text{C}$. For $\text{CuGaS}_{0.5}\text{Se}_{1.5}$ and CuInSSe , they are $\sim 1100^\circ\text{C}$ and $\sim 1200^\circ\text{C}$ respectively.

For the $\text{Cu}_{1-x}\text{Ag}_x\text{AlX}_2$, $\text{Cu}_{1-x}\text{Ag}_x\text{GaX}_2$, and $\text{Cu}_{1-x}\text{Ag}_x\text{InX}_2$ systems (Fig. 2.16 and Table 2.9), the difference in $2 - c/a$ from one end member to the other are 0.15, 0.16,

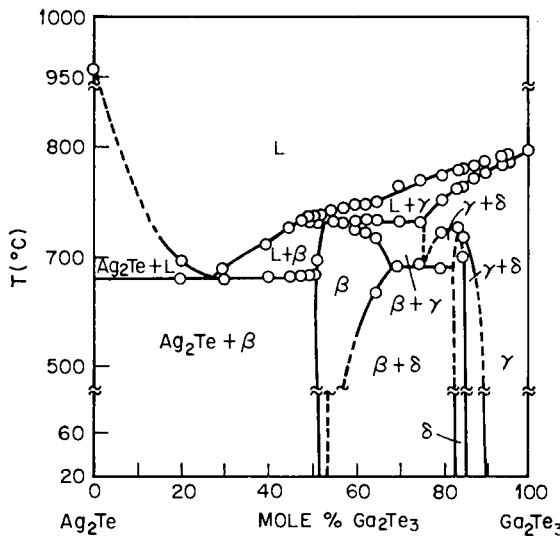


FIG. 2.15. The system $\text{Ag}_2\text{Te}-\text{Ga}_2\text{Te}_3$. (After Palatnik and Belova, 1967.)

and 0.08, respectively (Robbins *et al.*, 1973). Only in the $\text{Cu}_{1-x}\text{Ag}_x\text{InX}_2$ systems is complete solid solubility observed. The trends in the miscibility gap are discussed in terms of the difference Δ in $2 - c/a$ and for $\Delta_{\text{Cu}-\text{Ag}} \lesssim 0.13$ the alloys are miscible in all proportions and the miscibility gap increases with increasing Δ . It is expected that $2 - c/a (\text{M}^{\text{I}}\text{M}^{\text{III}}\text{S}_2) > 2 - c/a (\text{M}^{\text{I}}\text{M}^{\text{III}}\text{Se}_2)$ because Se atoms are more polarizable and screen $\text{M}^{\text{III}}-\text{M}^{\text{III}}$ interactions more effectively than S atoms.

Yamamoto and Miyauchi (1972) showed that a continuous series of solid solutions form in the $\text{CuGa}_{1-x}\text{In}_x\text{S}_2$ system. Room temperature lattice constants as a function of composition are shown in Fig. 2.18.

2.7 Phase Relationships in $(\text{I-III-VI}_2)-(\text{II-VI})$ and $(\text{I-III-VI}_2)-(\text{III-V})$ Systems

Systematic investigations of the large number of such systems possible have not been carried out. Some information relevant to phase equilibria in these mixed systems are shown in Table 2.8. Apple (1958) reported large solid solution existence regions in the $\text{CuGaS}_2-\text{ZnS}$ system, and his room temperature lattice constant data are shown in Fig. 2.19. The chalcopyrite phase extends to over 50 mol% CuGaS_2 in ZnS . Apple also reported only ~ 5 mol% AgGaS_2 soluble in ZnS .

Robbins has performed crystallographic studies on a large number of $(\text{I-III-VI}_2)-(\text{II-VI})$ systems, and his results are summarized in Figs. 2.20-2.29. In the $\text{CuInS}_2-\text{ZnS}$ and $\text{CuAlS}_2-\text{ZnS}$ systems, large, solid solution existence regions are formed, as shown in Fig. 2.19. In the $\text{CuIIIS}_2-\text{CdS}$ systems (Figs. 2.21-2.23), limited terminal solid solubility exists, the amount increasing with increasing atomic number of the Group III ion (or with increasing polarizability). In the $\text{AgIIIS}_2-\text{ZnS}$ systems (Figs. 2.24-2.26) it is noted that a quaternary disordered wurtzite phase appears or is stabilized to room temperature. Wide composition-temperature regions of immiscibility exist. On the other hand, for the $\text{AgIIIS}_2-\text{CdS}$ systems (Fig. 2.27-2.29) no new quaternary phase is sta-

TERNARY CHALCOPYRITE SEMICONDUCTORS

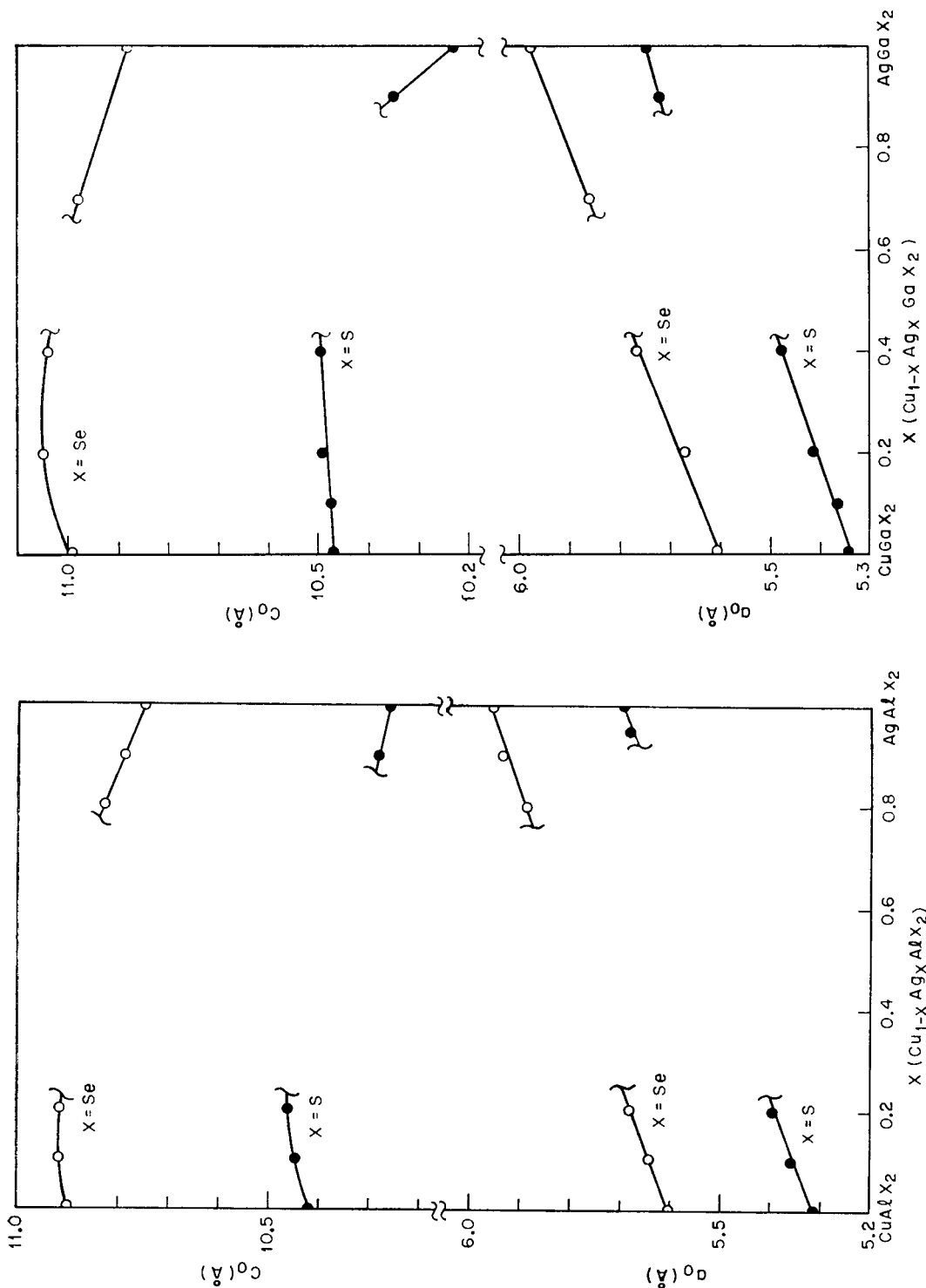


Fig. 2.16

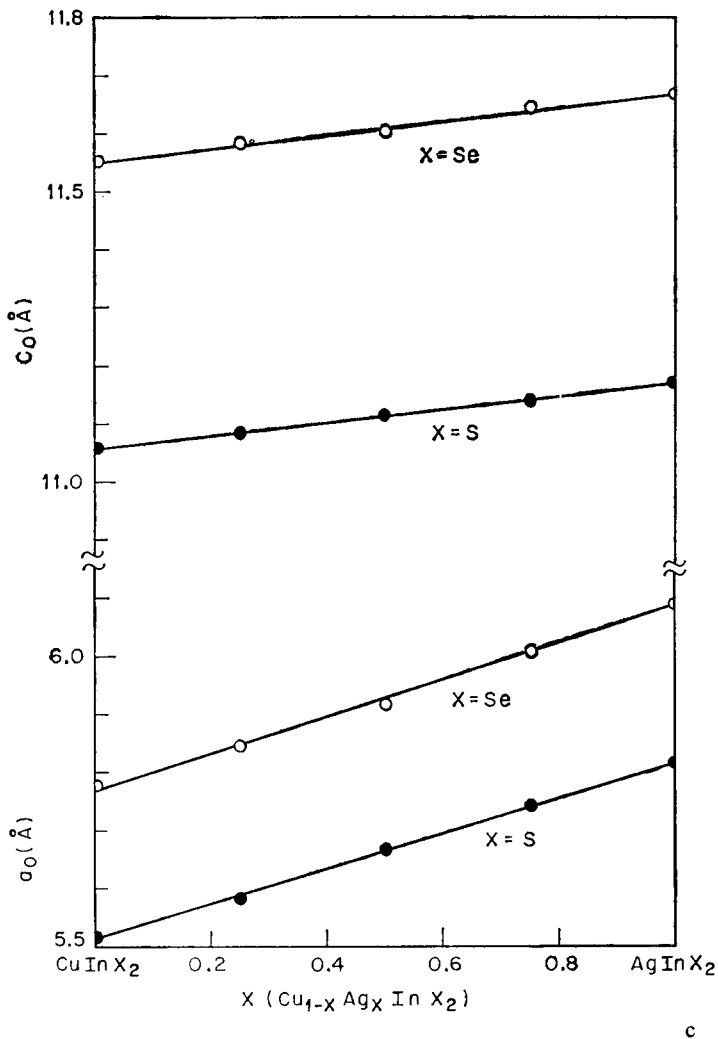


FIG. 2.16. Unit cell parameters as a function of composition for several mixed I-III-VI₂ systems. Approximate room temperature solid-solubility limits are shown. (a) The CuAlS₂-AgAlS₂ and CuAlSe₂-AgAlSe₂ systems. (b) The CuGaS₂-AgGaS₂ and CuGaSe₂-AgGaSe₂ systems. (c) The CuInS₂-AgInS₂ and CuInSe₂-AgInSe₂ systems.
(After Robbins *et al.*, 1973.)

TERNARY CHALCOPYRITE SEMICONDUCTORS

TABLE 2.9. *c/a ratios for compositions in the pseudo-binary systems CuM^{III}X₂-AgM^{III}X₂, Where M^{III} = Al, Ga, In, and X = S, Se. (After Robbins et al., 1973.)*

Nominal composition (mol%)		<i>c/a</i>	Nominal composition (mol%)	<i>c/a</i>
CuAlS ₂ -AgAlS ₂			CuAlSe ₂ -AgAlSe ₂	
100	0	1.96	100	0
90	10	1.95	90	10
80	20	1.94	80	20
10	90	1.81	20	80
0	100	1.80	10	90
			0	100
CuGaS ₂ -AgGaS ₂			CuGaSe ₂ -AgGaSe ₂	
100	0	1.96	100	0
90	10	1.95	80	20
80	20	1.94	60	40
60	40	1.92	30	70
10	90	1.81	0	100
0	100	1.78		
CuInS ₂ -AgInS ₂			CuInSe ₂ -AgInSe ₂	
100	0	2.00	100	0
75	25	1.99	75	25
50	50	1.96	50	50
25	75	1.93	25	75
0	100	1.92	0	100

bilized. Robbin's results are in agreement with Parthé's (Table 2.8) for the single compositions CuInS₂ + 2 ZnS, CuInS₂ + 2 CdS, and AgInS₂ + 2 CdS. They differ for the compositions AgAlS₂ + 2 ZnS, AgInS₂ + 2 ZnS, and AgAlS₂ + 2 CdS, and this may be related to the different methods employed in preparing the samples.

Voitsekhovsky (1964) reported complete solid solubility in the CuInTe₂-CdTe and CuInTe₂-InAs systems, and this suggests the possible existence of a zincblende form of CuInTe₂ at elevated temperatures (see also Fig. 2.45). Solid solution formation in the AgInTe₂-CdTe and AgInTe₂-HgTe systems were reported by Rodot (1960). Woolley and Williams (1966) determined the extent of solid solution formation and variation of optical energy gaps in the AgInTe₂-CdTe and CuGaTe₂-CdTe systems, and their room temperature lattice constant results are summarized in Figs. 2.30 and 2.31. Their alloys were prepared by melting, followed by quenching in water and annealing at various temperatures and times (as much as 60 days for some of the CuGaTe₂-CdTe alloys) to sharpen the X-ray reflections, i.e. to reach equilibrium. For the AgInTe₂-CdTe system (Fig. 2.30), the cubic zincblende phase exists up to ~60 mol% AgInTe₂, followed by the formation of a chalcopyrite phase, which is stable between 60–70 mol% AgInTe₂, and a two-phase region. For the CuGaTe₂-CdTe system (Fig. 2.31), the cubic zincblende phase is stable to ~60 mol% CuGaTe₂, and a two-phase region exists beyond this composition. The solid solubility of CdTe in CuGaTe₂ at room temperature appears to be less than 5 mol%. Their annealing studies suggest that CuGaTe₂ and AgInTe₂ are nonstoichiometric compounds at room temperature.

THE CHALCOPYRITE STRUCTURE AND CRYSTAL GROWTH

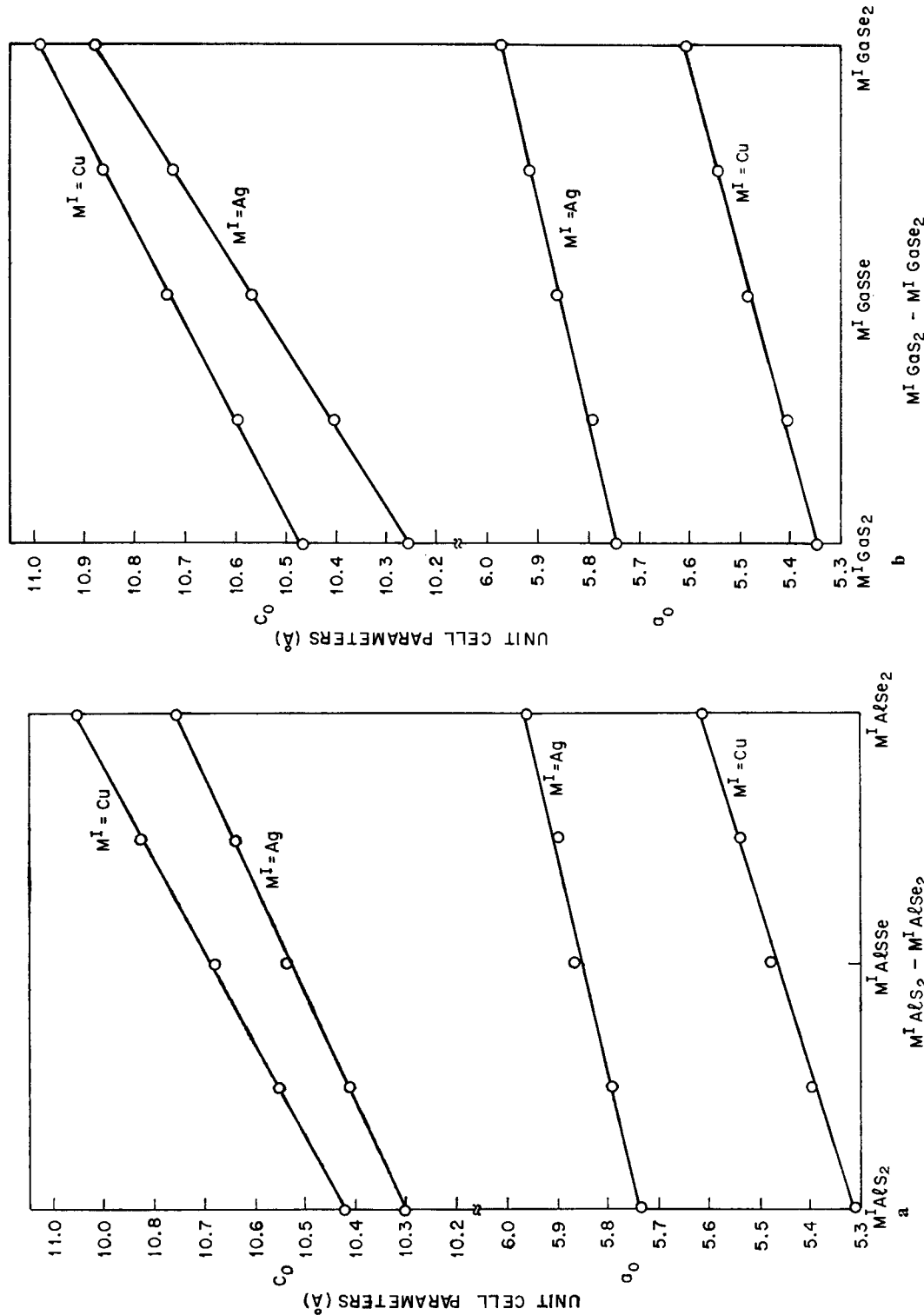


Fig. 2.17

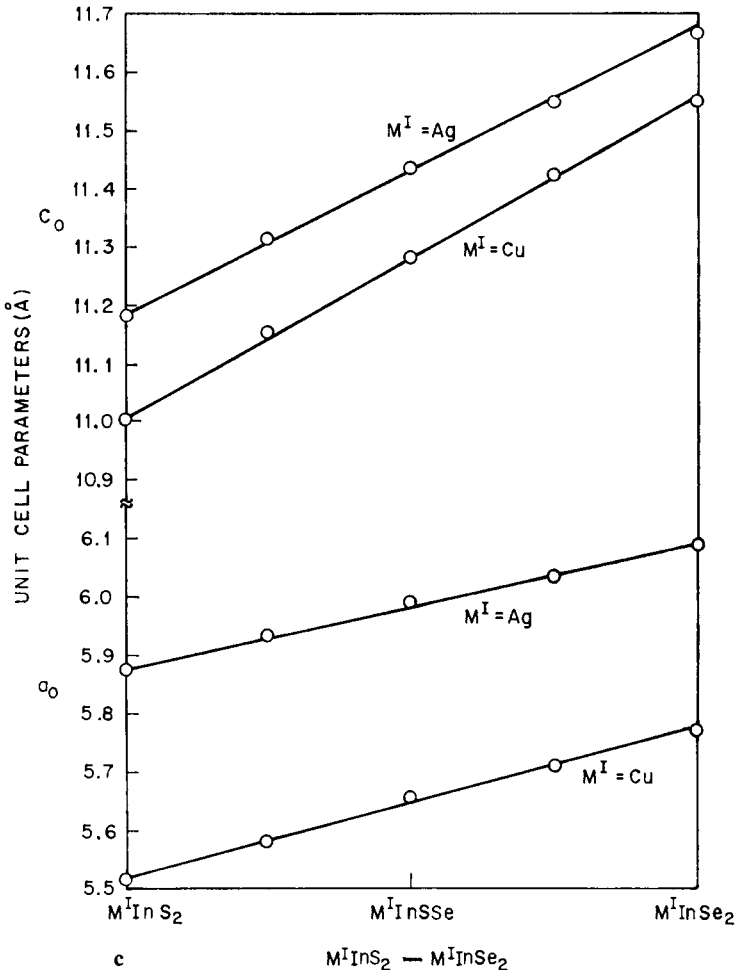


FIG. 2.17. Unit cell parameters as a function of composition for several mixed I-III-VI₂ systems. (a) CuAlS₂-CuAlSe₂ and AgAlS₂-AgAlSe₂ systems. (b) CuGaS₂-CuGaSe₂ and AgGaS₂-AgGaSe₂ systems. (c) CuInS₂-CuInSe₂ and AgInS₂-AgInSe₂ systems. (After Robbins and Lambrecht, 1973.)

THE CHALCOPYRITE STRUCTURE AND CRYSTAL GROWTH

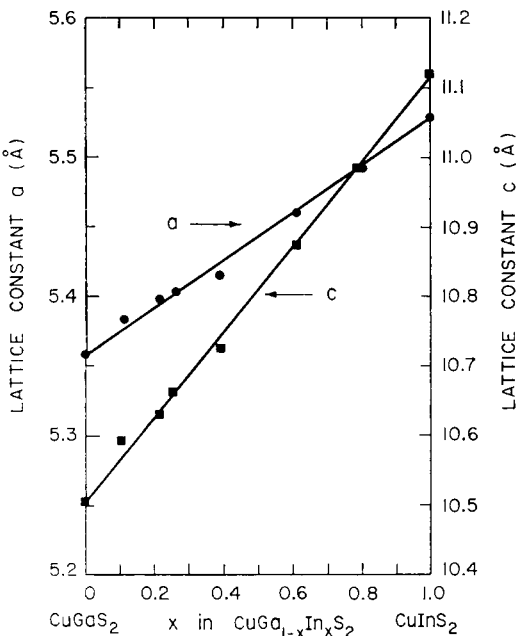


FIG. 2.18. Lattice constants as a function of composition in the $\text{CuGa}_{1-x}\text{In}_x\text{S}_2$ systems. (After Yamamoto and Miyauchi, 1972.)

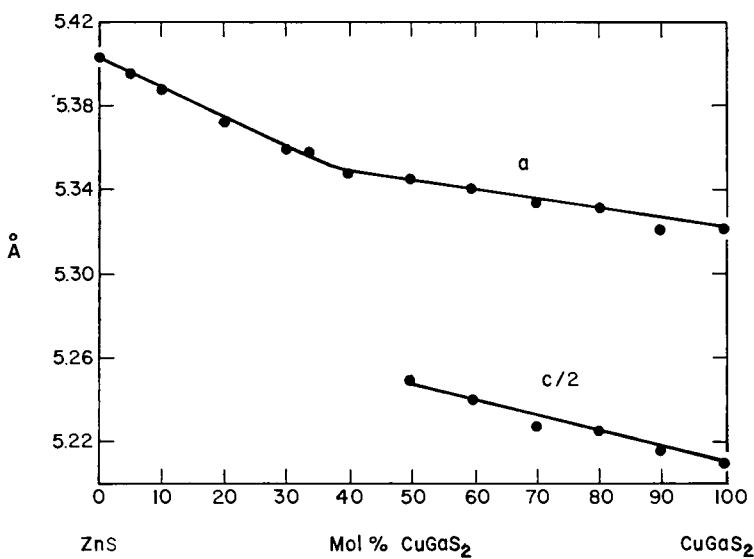


FIG. 2.19. Unit cell dimensions in the systems $\text{ZnS}-\text{CuGaS}_2$. (After Apple, 1958.)

TERNARY CHALCOPYRITE SEMICONDUCTORS

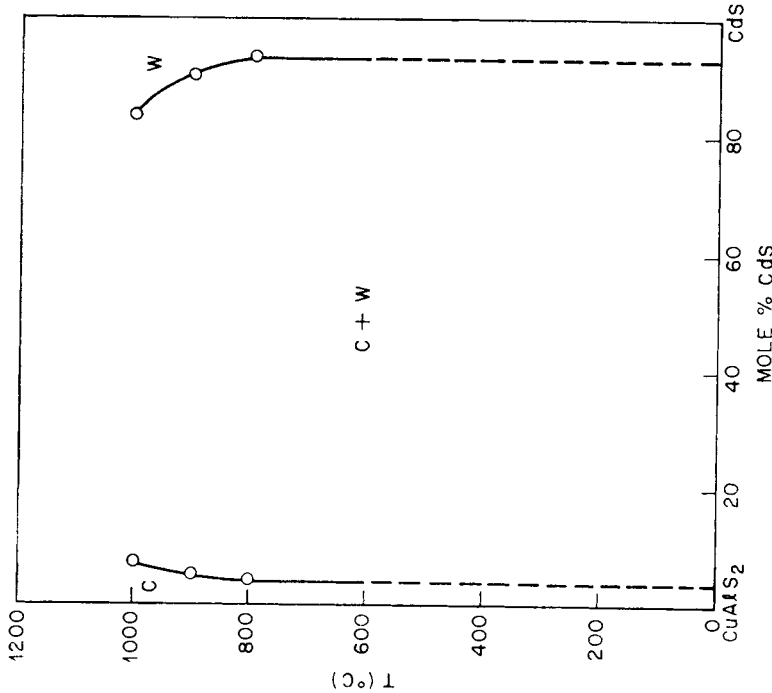


FIG. 2.21. Proposed partial phase diagram for the CuAlS₂-CdS system; C = chalcopyrite and W = wurtzite. (After Robbins and Lambrecht, 1973.)

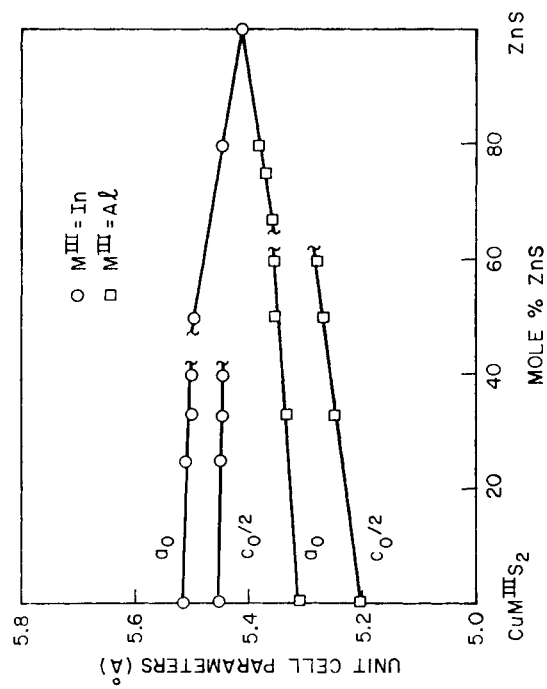


FIG. 2.20. Lattice constants as a function of composition in the CulnS₂-ZnS systems. (After Robbins and Mikovsky, 1972.)

THE CHALCOPYRITE STRUCTURE AND CRYSTAL GROWTH

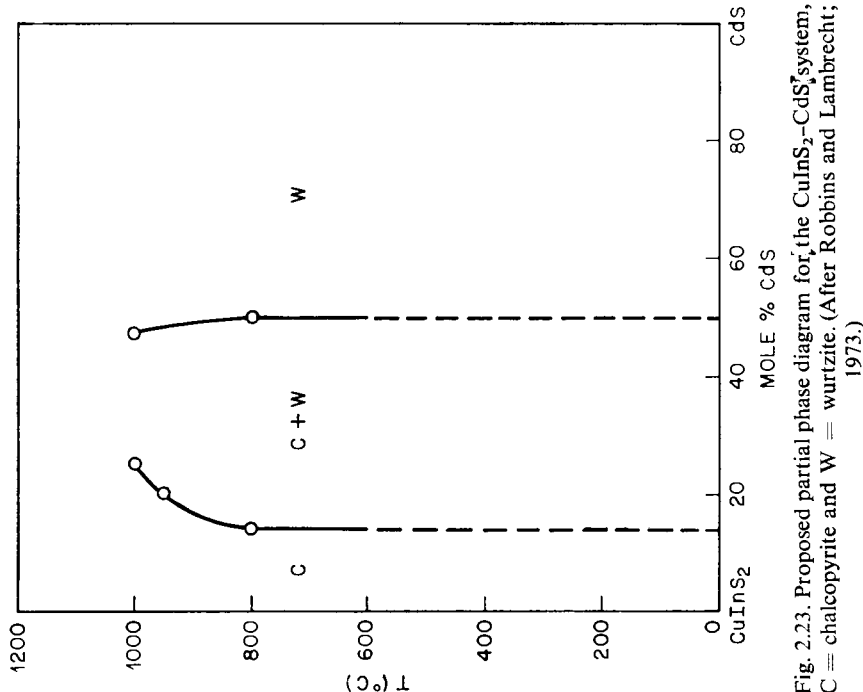


Fig. 2.23. Proposed partial phase diagram for the CuInS₂-CdS system, C = chalcopyrite and W = wurtzite. (After Robbins and Lambrecht, 1973.)

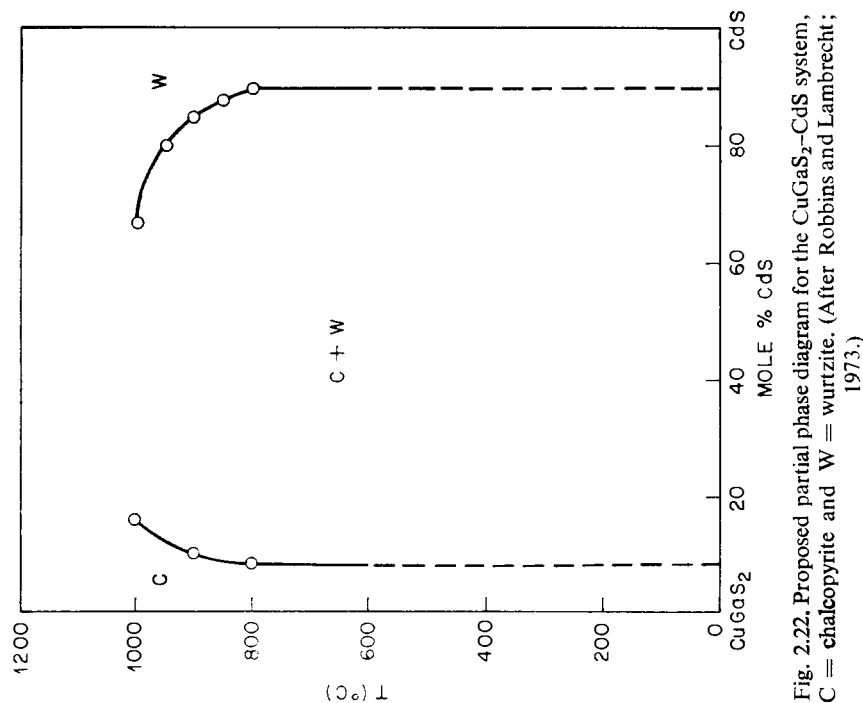


Fig. 2.22. Proposed partial phase diagram for the CuGaS₂-CdS system, C = chalcopyrite and W = wurtzite. (After Robbins and Lambrecht, 1973.)

TERNARY CHALCOPYRITE SEMICONDUCTORS

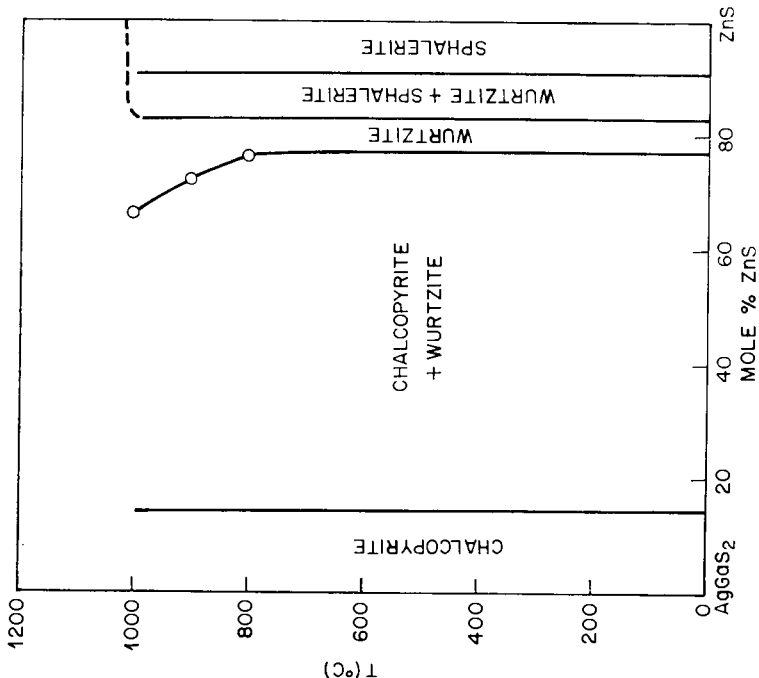


FIG. 2.25. Proposed partial phase diagram for the AgGaS_2 - ZnS system below 1020°C. Diagram based on powder X-ray data only. (After Robbins and Mikovsky, 1972.)

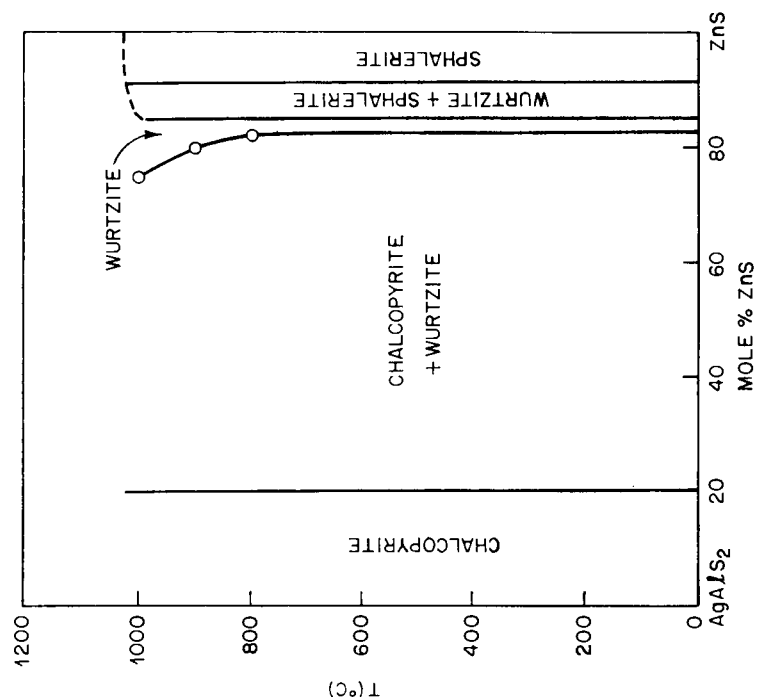


FIG. 2.24. Proposed partial phase diagram for the AgAlS_2 - ZnS system below 1020°C. Diagram based on powder X-ray data only. (After Robbins and Mikovsky, 1972.)

THE CHALCOPYRITE STRUCTURE AND CRYSTAL GROWTH

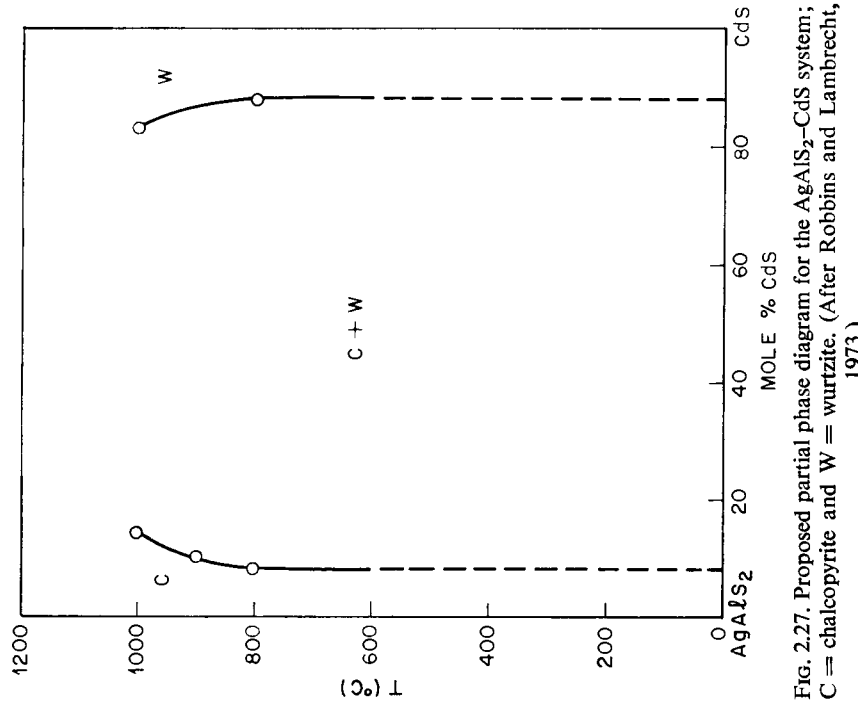


FIG. 2.27. Proposed partial phase diagram for the $\text{AgAlS}_2\text{-CdS}$ system; C = chalcopyrite and W = wurtzite. (After Robbins and Lambrecht, 1973.)

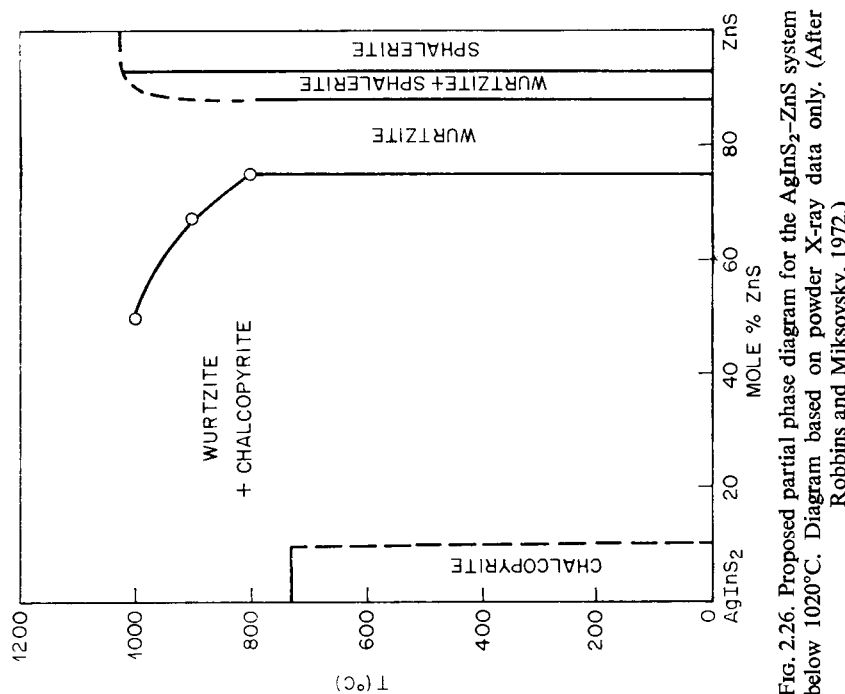


FIG. 2.26. Proposed partial phase diagram for the $\text{AgInS}_2\text{-ZnS}$ system below 1020°C. Diagram based on powder X-ray data only. (After Robbins and Mirkovsky, 1972.)

TERNARY CHALCOPYRITE SEMICONDUCTORS

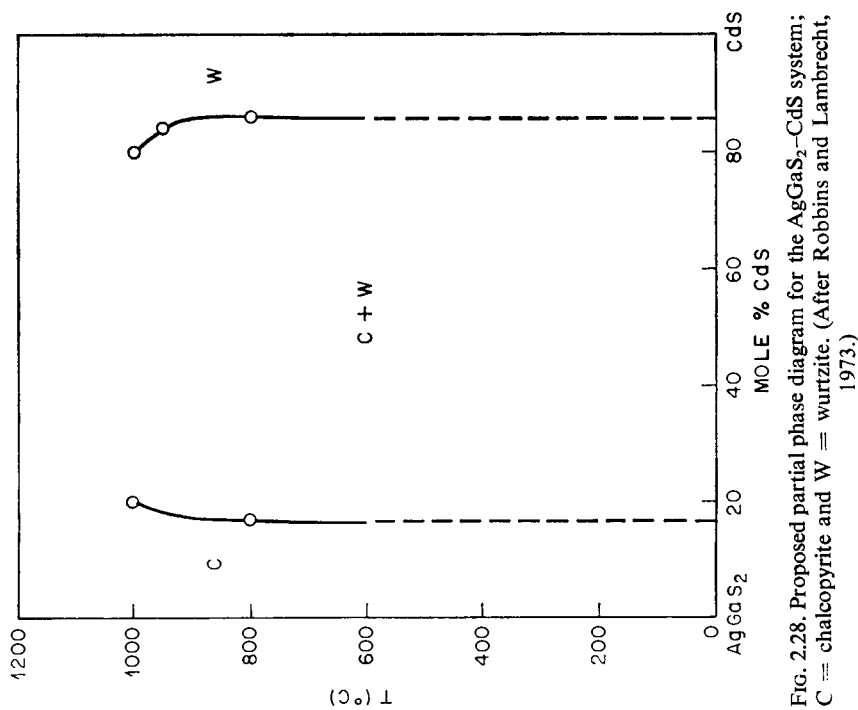


FIG. 2.28. Proposed partial phase diagram for the $\text{AgGaS}_2\text{-CdS}$ system;
 C = chalcopyrite and W = wurtzite. (After Robbins and Lambrecht,
 1973.)

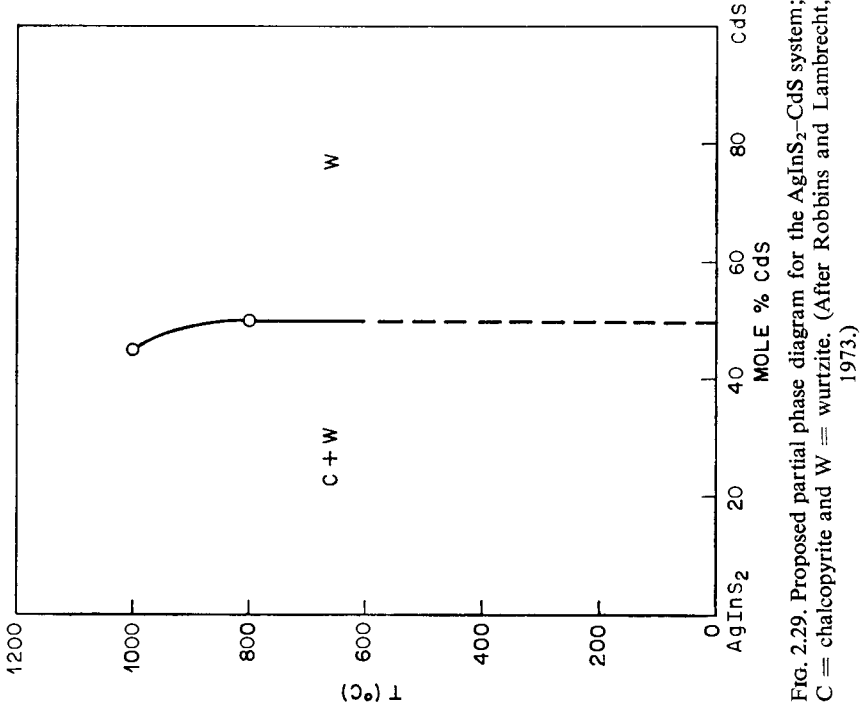


FIG. 2.29. Proposed partial phase diagram for the $\text{AgInS}_2\text{-CdS}$ system;
 C = chalcopyrite and W = wurtzite. (After Robbins and Lambrecht,
 1973.)

THE CHALCOPYRITE STRUCTURE AND CRYSTAL GROWTH

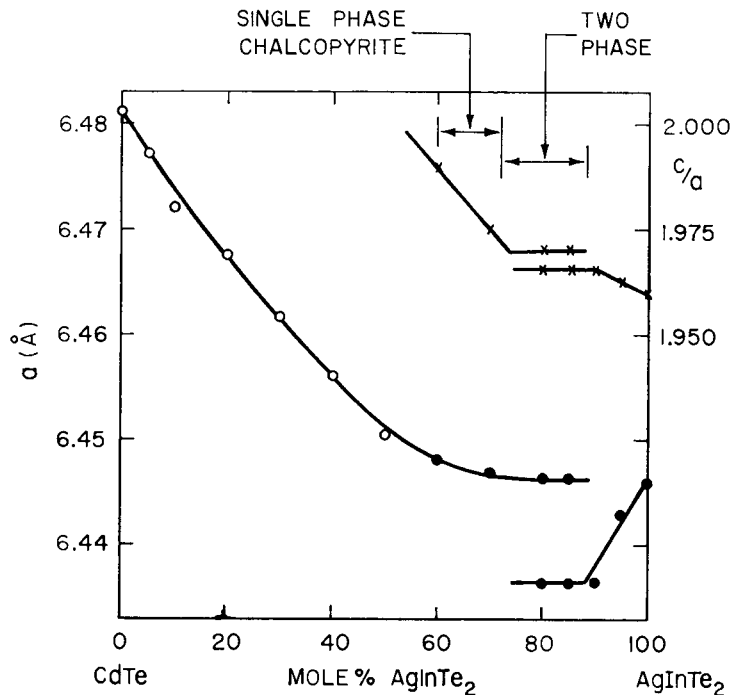


FIG. 2.30. Variation of lattice parameters with composition in the $\text{AgInTe}_2\text{-CdTe}$ system. Open circles = zincblende; closed circles = a for chalcopyrite; x = chalcopyrite c/a . (After Woolley and Williams, 1966.)

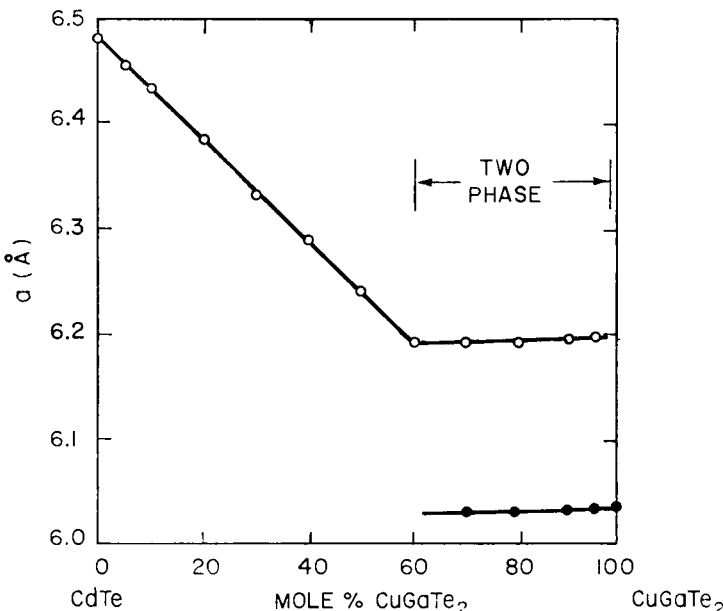


FIG. 2.31. Variation of lattice parameters with composition in the $\text{CuGaTe}_2\text{-CdTe}$ system. Open circles = zincblende; closed circles = chalcopyrite. (After Woolley and Williams, 1966.)

2.8 Phase Relationships in II-IV-V Systems

Some information pertinent to phase equilibria in II-IV-V systems is given in Table 2.6. In the following sections we discuss those individual systems for which additional information is known.

2.8.1 The Zn-Ge-P System

The phase relations in the ZnP_2 -Ge join have been determined by Buehler *et al.* (1973) by DTA in closed systems, X-ray, and metallurgical studies,[†] and these results are shown in Fig. 2.32.

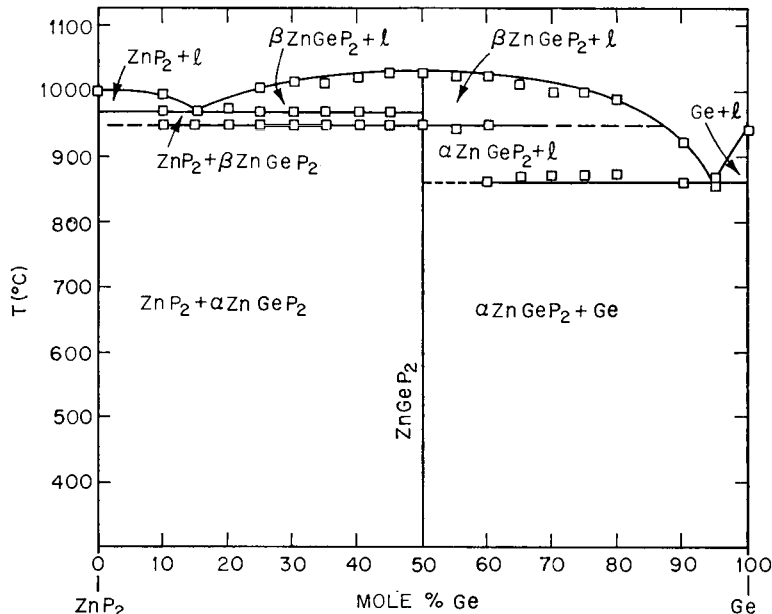


FIG. 2.32. The ZnP_2 -Ge pseudobinary phase diagram. (After Buehler *et al.*, 1973.)

The DTA experiments were carried out by adding an excess of phosphorus to provide sufficient phosphorus pressure so that the original charge stoichiometry could be assumed to be relatively unchanged. (This was also done for the CdP_2 -Ge and CdP_2 -Sn systems discussed in Sections 2.8.5 and 2.8.7 respectively.) To be a more significant diagram for understanding the *fine details* of crystal growth, each point on the liquidus curve should be determined for the vapor pressure in equilibrium with the condensed phase. For the ZnP_2 -Ge system enough phosphorus was added to the compositions from 30 mol % Ge to 100 mol % Ge to give a phosphorus pressure as P_4 over the melt of 5 atm at 1025°C. For compositions from 0 to 20 mol % Ge, enough excess phosphorus was added to give 10 atm of P_4 over the melt. The total equilibrium decompo-

[†] A suitable etching reagent for ZnGeP_2 is a solution of Br in methanol (1 : 50 by volume). Borshchevskii *et al.* (1967) report that some of the II-IV-V₂ compounds can be chemically polished in an HF : HNO_3 (1 : 3) solution and the microstructure of CdGeAs_2 , ZnSnAs_2 , and ZnSiAs_2 revealed by use of H_2O_2 : NH_4OH : H_2O (1 : 2 : 4), CH_3COOH : $\text{C}_3\text{H}_5(\text{OH})_3$: HNO_3 (1 : 1 : 1), and CH_3COOH : $\text{C}_3\text{H}_5(\text{OH})_3$: HNO_3 (3 : 3 : 1) respectively.

THE CHALCOPYRITE STRUCTURE AND CRYSTAL GROWTH

sition pressure of ZnP_2 at 1000°C is close to 10 atm (Buehler *et al.*, 1973). In general, each composition was heated to $\sim 1060^\circ\text{C}$ prior to cooling. Cooling rates were 0.7°/min. For cooling rates in excess of $\sim 1^\circ/\text{min}$, supercooling effects were noted for the ZnP_2 -rich melts.

The congruent nature of $ZnGeP_2$ (melting point $1027 \pm 3^\circ\text{C}$) and the solid state transformation at $950 \pm 5^\circ\text{C}$ were confirmed (Masumoto *et al.*, 1966; Mughal *et al.*, 1969). $\alpha ZnGeP_2$ is the low-temperature chalcopyrite phase while the structure of the β -phase is unknown. Quenching experiments were unsuccessful in retaining the high-temperature form to room temperature, and it appears that identification of $\beta ZnGeP_2$ will require the use of high-temperature X-ray diffraction under conditions of zero dissociation, or alloying studies, for example, studies of the $ZnGeP_2$ -GaP system. If $\beta ZnGeP_2$ is disordered zincblende as has been suggested, GaP should stabilize this phase to room temperature if sufficient solid solution occurs. The solid solubility of Ge in $ZnGeP_2$, (as well as Si in $ZnSiP_2$), has been reported to be large (Borshchevskii *et al.*, 1967), and this is probably the reason for the lack of observation of a eutectic arrest for the composition 55 mol% Ge, 45 mol% ZnP_2 .

The phase transformation is not an impediment to the growth of large crack-free single crystals by directional solidification of stoichiometric melts (see below).

2.8.2 The Zn-Ge-As System

The Zn-Ge-As system has been examined by Goryunova *et al.* (1963b) (see also Borshchevskii *et al.*, 1967), and the $ZnGeAs_2$ -Ge section is shown in Fig. 2.33. There is a large solid solubility of Ge in $ZnGeAs_2$, and it has been reported that Ge can substitute for both the Zn and As atoms.

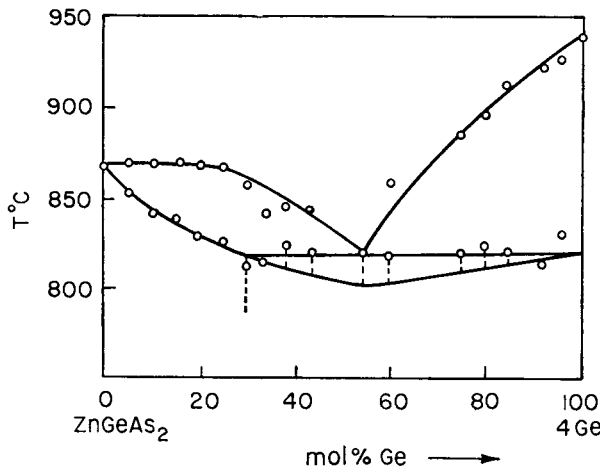


Fig. 2.33. The $ZnGeAs_2$ -Ge join in the Zn-Ge-As system. (As given by Borshchevskii *et al.*, 1967.)

2.8.3 The Zn-Sn-As System

Phase diagram information are summarized in Fig. 2.34, 2.35, and 2.36. $ZnSnAs_2$ forms incongruently and $\alpha ZnSnAs_2$ (Fig. 2.34) exhibits the zincblende structure and corresponds to the α' notation of Gasson *et al.* (1962). Incongruency, of course, com-

TERNARY CHALCOPYRITE SEMICONDUCTORS

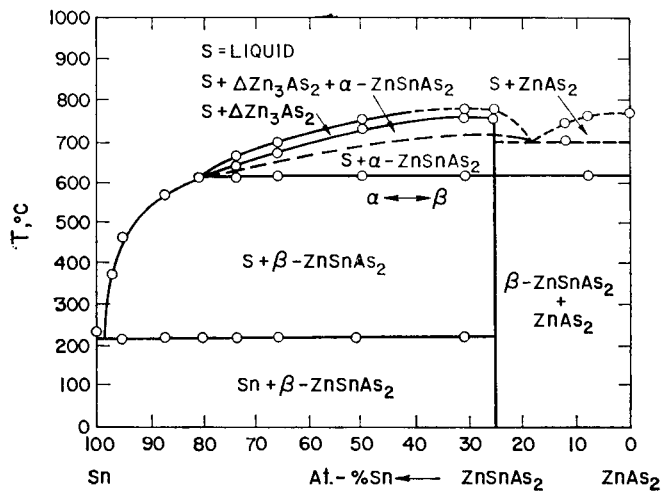


Fig. 2.34. The Sn-ZnAs₂ join in the Zn-Sn-As system. (After Borchers and Maier, 1963 a,b.)

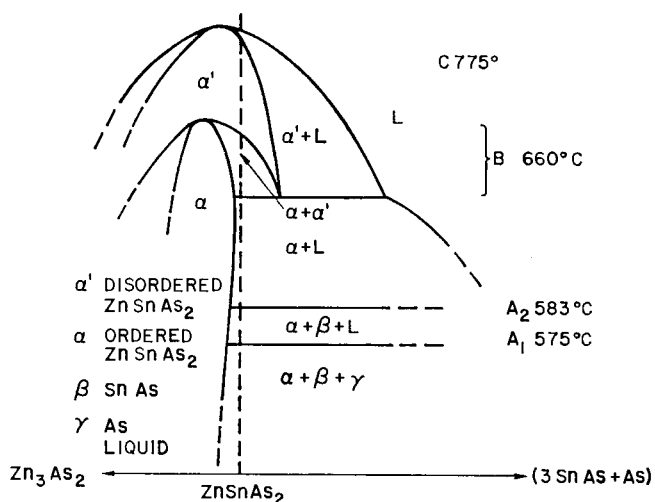


Fig. 2.35. Proposed phase diagram along a certain join in the neighborhood of ZnSnAs₂. Note that single phase ordered stoichiometric ZnSnAs₂ does not exist at low temperatures. (After Gasson *et al.*, 1962.)

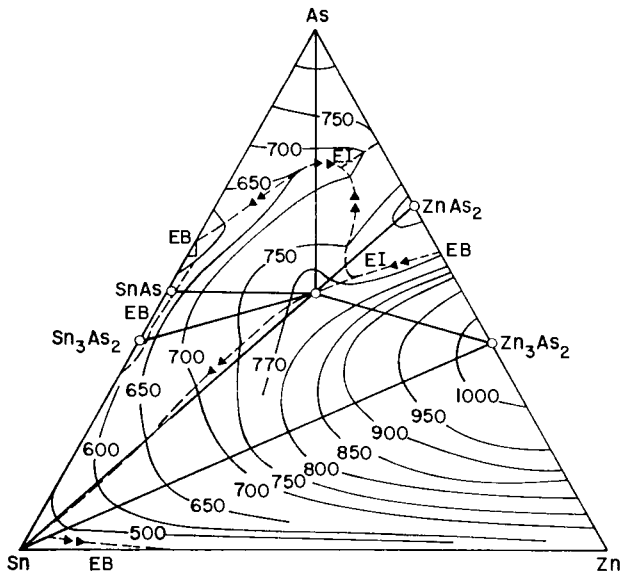


FIG. 2.36. The liquidus surface of the Zn–Sn–As system. (After Borchers and Maier, 1963.)

plicates the crystal growth process for obtaining large, single phase stoichiometric crystals.

2.8.4 The Zn–Sn–Sb System

As noted earlier (Table 2.6), ZnSnSb_2 forms peritectically and can exist in two forms. A portion of the Sn– ZnSnSb_2 join is shown in Fig. 2.37. Single crystals are grown from saturated Sn solutions, and the zincblende phase, rather than the chalcopyrite phase, forms during fast cooling (Goryunova *et al.*, 1968a, b, see also Section 2.11.2.6).

2.8.5 The Cd–Ge–P System

The phase relationships in the pseudobinary CdP_2 –Ge system are shown in Fig. 2.38 (Buehler and Wernick, 1972).† CdGeP_2 forms congruently at $790 \pm 5^\circ\text{C}$, in substantial agreement with Masumoto *et al.* (1966) and Mughal *et al.* (1969). A homogeneity region for CdGeP_2 , of undetermined width, is indicated at elevated temperatures and based on the metallographic observation of coring in off-stoichiometric ingots. A solution of Br in methanol (1:1000 by volume) was found to be a sensitive etching reagent for CdGeP_2 . The features of the liquidus (also in the case of ZnGeP_2) would suggest, from thermodynamic arguments, the existence of a homogeneity region. Borshchevskii *et al.* (1967) report that CdGeP_2 possesses a “remarkable homogeneity region,” but no temperature information was given.

No evidence of a solid-state transformation for CdGeP_2 was detected, although the occurrence of one close to the melting point is not ruled out.

† See discussion in Section 2.8.1 and indicated reference for details of this study.

TERNARY CHALCOPYRITE SEMICONDUCTORS

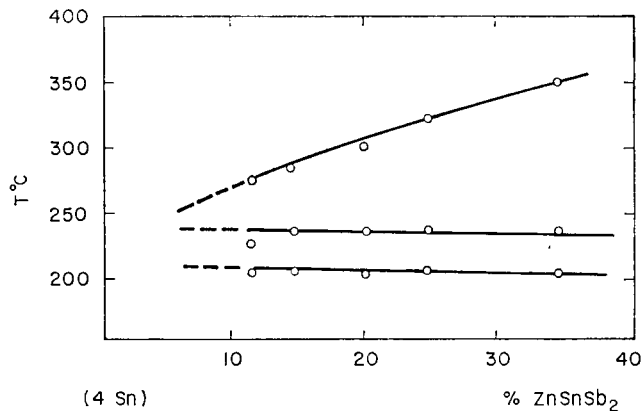


FIG. 2.37. The liquidus for a portion of the Sn-ZnSnSb₂ join in the Zn-Sn-Sb system. (After Goryunova *et al.*, 1968a.)

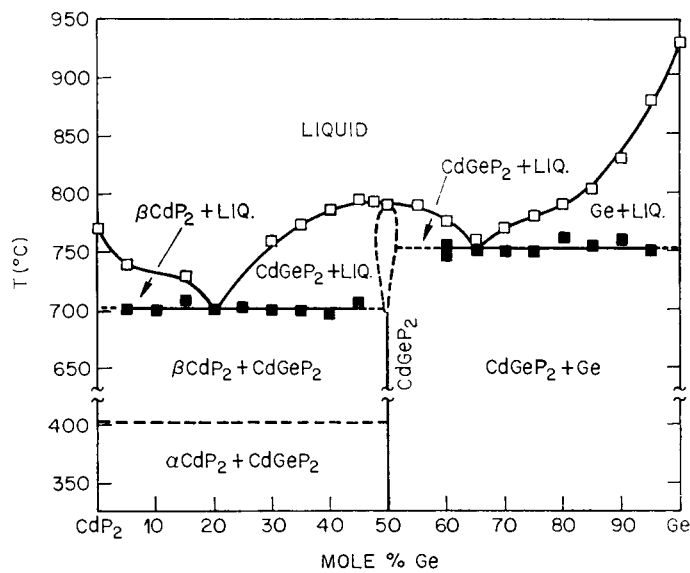


FIG. 2.38. The CdP₂-Ge system. (After Buehler and Wernick, 1972.)

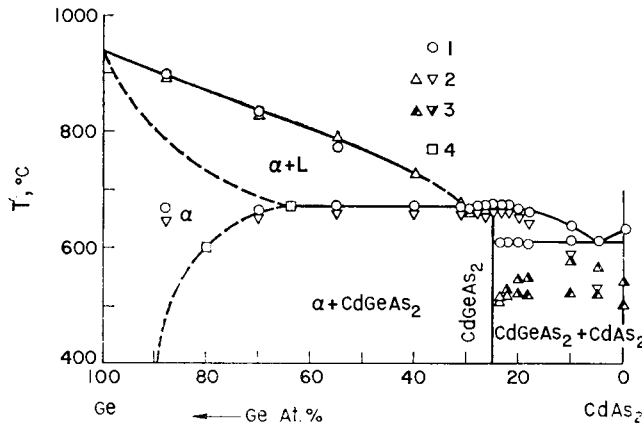


FIG. 2.39. The CdAs₂-Ge system. (1) DTA (on heating); (2) DTA (on cooling); (3) DTA (cooling), onset of heat evolution and maximum temperature respectively for the same thermal effect; (4) microprobe analysis. (After Borshchevskii and Roenkov, 1969.)

2.8.6 The Cd-Ge-As System

Borshchevskii and Roenkov (1969) have studied the Cd-Ge-As system in some detail. Their results for the CdAs₂-Ge section are shown in Fig. 2.39 and suggests that CdGeAs₂ is congruent, although it is conceivable that CdGeAs₂ is slightly incongruent. Borshchevskii *et al.* (1967) report a large homogeneity region for CdGeAs₂.

2.8.7 The Cd-Sn-P System

The CdP₂-Sn system† (Fig. 2.40) shows that CdSnP₂ forms peritectically and that single crystals can be grown from Sn-rich solutions below $\sim 570^\circ\text{C}$. The extent of solid solubility of Sn in CdSnP₂ is not known.

† See discussion in Section 2.8.1 and indicated reference for details of this study.

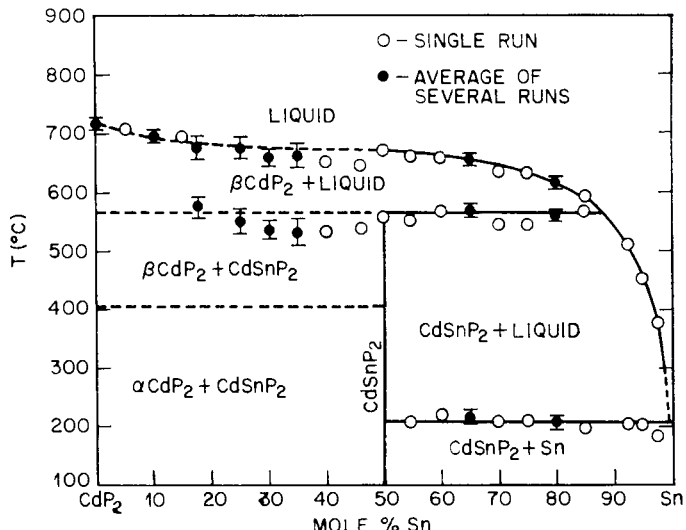


Fig. 2.40. The CdP₂-Sn system. (After Buehler *et al.*, 1971.)

2.8.8 The Cd-Sn-As and Zn-Si-As Systems

Borshchevskii *et al.* (1967) reported that CdSnAs₂ and ZnSiAs₂ exhibit narrow homogeneity regions, but no details were given.

2.9 Phase Relationships in Mixed II-IV-V Systems

Very little has been done on phase equilibria in mixed II-IV-V systems. Springthorpe and Pamplin (1968) showed that a complete series of chalcopyrite solid solutions formed in the ZnSiAs_xP_{2-x} system (Fig. 2.41), and Pamplin and Shah (1969) showed this to be the case for the Zn_xCd_{1-x}SnAs₂ system (Fig. 2.42).

Karymshakov and Radul (1970) reported that in the CdSnAs_{2-x}P_x system, CdSnP₂ is soluble in CdSnAs₂ to the extent of 40 mol% CdSnP₂ at room temperature. No other details were given.

Complete solid solubility in the CdGe_{1-x}Sn_xP₂ system was reported by Valov *et al.* (1973).

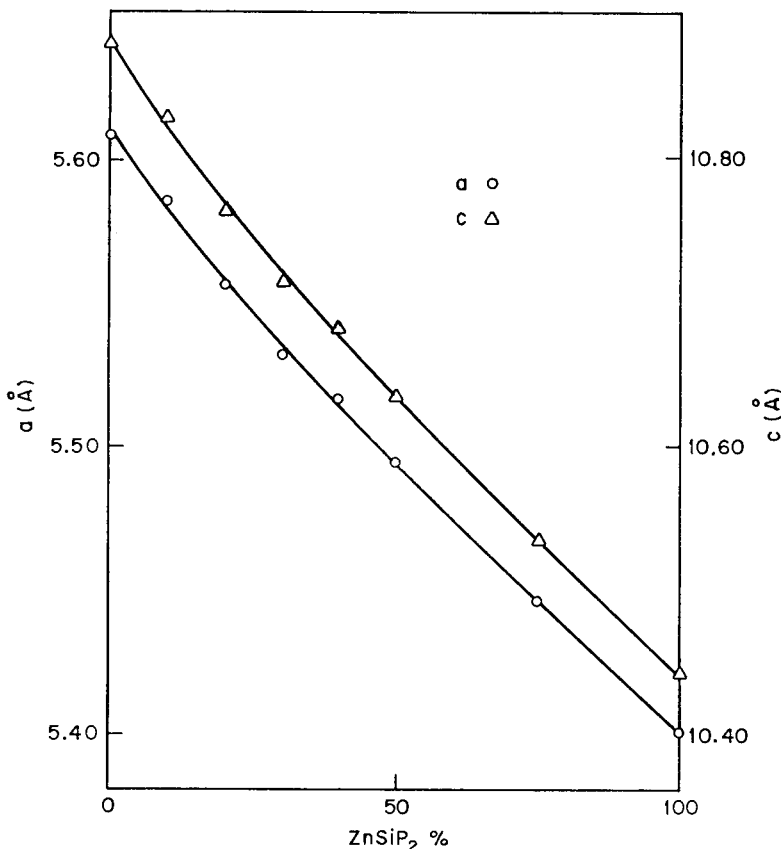


FIG. 2.41. Variation of lattice constants with composition in the $\text{ZnSiAs}_x\text{P}_{2-x}$ system. (After Springthorpe and Pamplin, 1968.)

2.10 Phase Relationships in Mixed (II-IV-V₂)(III-V) Systems

The main impetus for the study of mixed systems was for the discovery of new thermoelectric materials because alloying, which results in atomic disorder, will give rise to a lowering in the lattice contribution to the thermal conductivity. One reason a III-V endmember was used in this search was to capitalize on the higher carrier mobilities exhibited by several of them, even though lattice disorder will reduce mobilities and lower electrical conductivity. Thus the amount of phase equilibria information regarding these systems is somewhat larger in comparison to the mixed II-IV-V systems.

In the ZnGeAs_2 -InAs system (Figs. 2.43 and 2.44), large solid solubility of ZnGeAs_2 in InAs occurs. The existence of a two-phase region at room temperature in this system in the neighborhood of ~ 20 mol% InAs in ZnGeAs_2 is not indicated in the lattice constant data of Voitsekhovsky (1964) (Fig. 2.45).

InAs forms a complete series of zincblende solid solutions with ZnSnAs_2 (Figs. 2.45 and 2.46) at elevated temperatures. InAs stabilizes the zincblende form of ZnSnAs_2 to room temperature.

TERNARY CHALCOPYRITE SEMICONDUCTORS

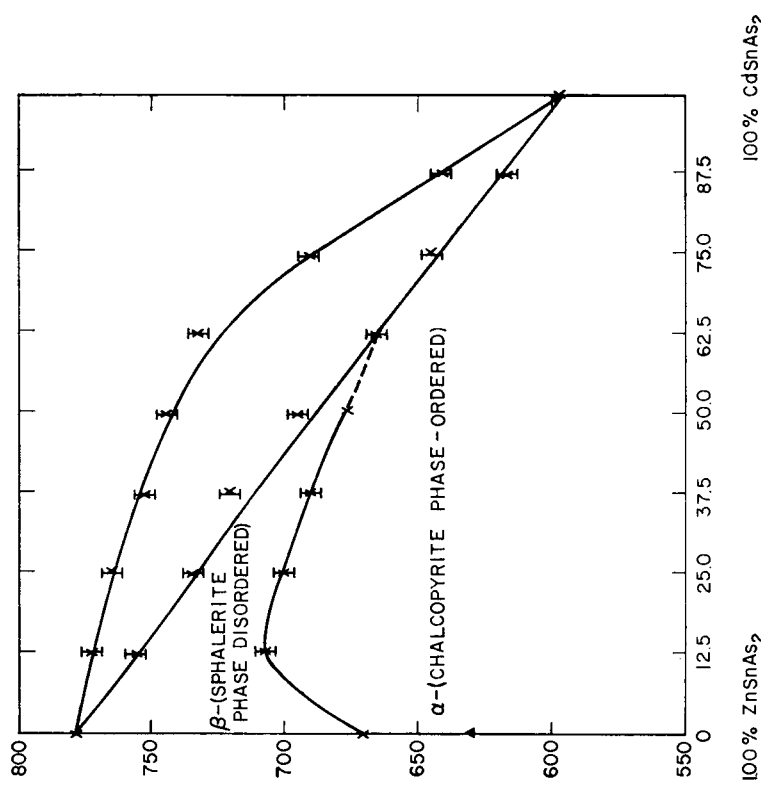


Fig. 2.42. Proposed phase diagram for the $Zn_xCd_{1-x}SnAs_2$ system.
(After Pamplin and Shah, 1969.)

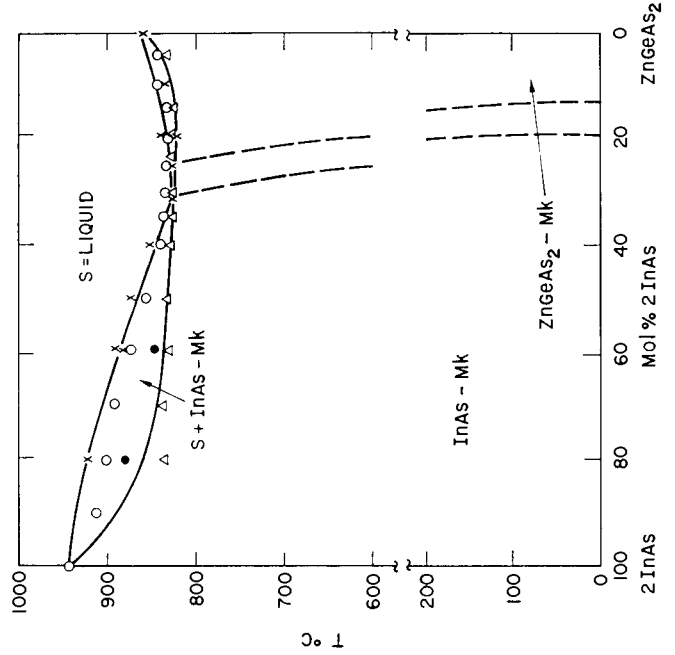


Fig. 2.43. The $ZnGeAs_2$ -InAs system. (After Borchers and Maier, 1963b.)

THE CHALCOPYRITE STRUCTURE AND CRYSTAL GROWTH

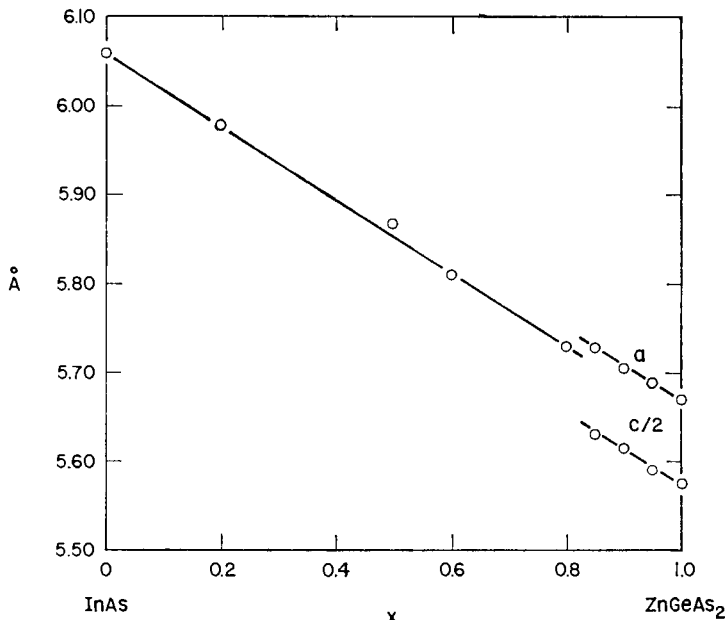


FIG. 2.44. Lattice parameters of alloys lying along the ZnGeAs_2 -InAs join as a function of composition. Zincblende structure on left and chalcopyrite on right. (After Giesecke and Pfister, 1961.)

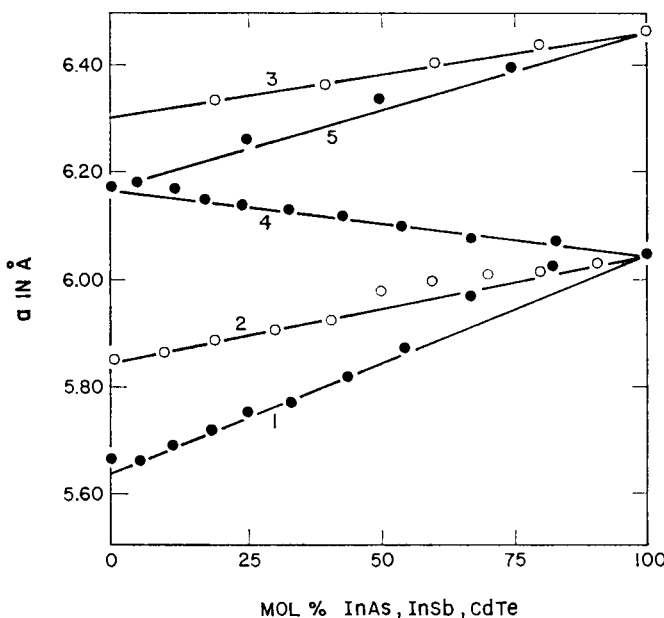


FIG. 2.45. Lattice parameters as a function of composition in the following systems: 1, $(\text{ZnGeAs}_2)_x(2\text{InAs})_{1-x}$; 2, $(\text{ZnSnAs}_2)_x(2\text{InAs})_{1-x}$; 3, $(\text{ZnSnSb}_2)_x(2\text{InSb})_{1-x}$; 4, $(\text{CuInTe}_2)_x(2\text{InAs})_{1-x}$; 5, $(\text{CuInTe}_2)_x(2\text{CdTe})_{1-x}$. (After Voitsekhovsky, 1964.)

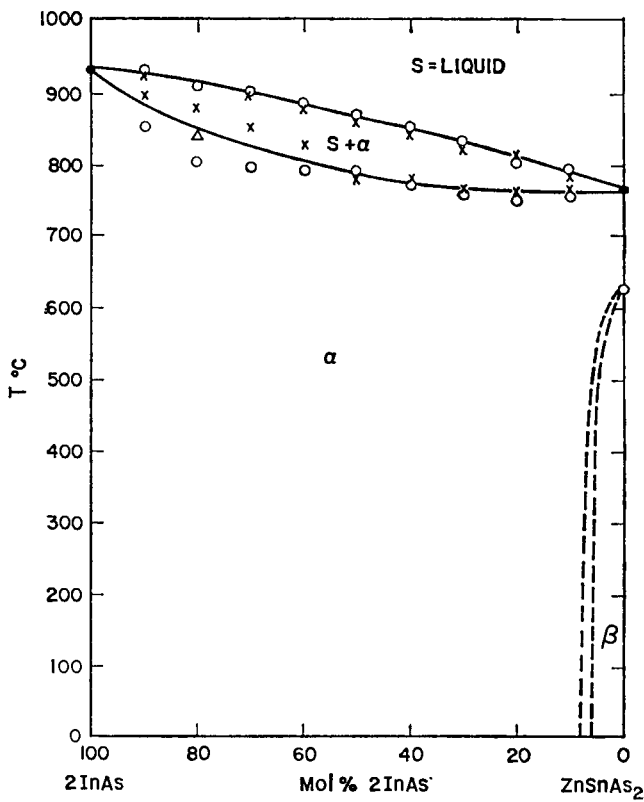


FIG. 2.46. The ZnSnAs₂-InAs system. (After Borchers and Maier, 1963a).

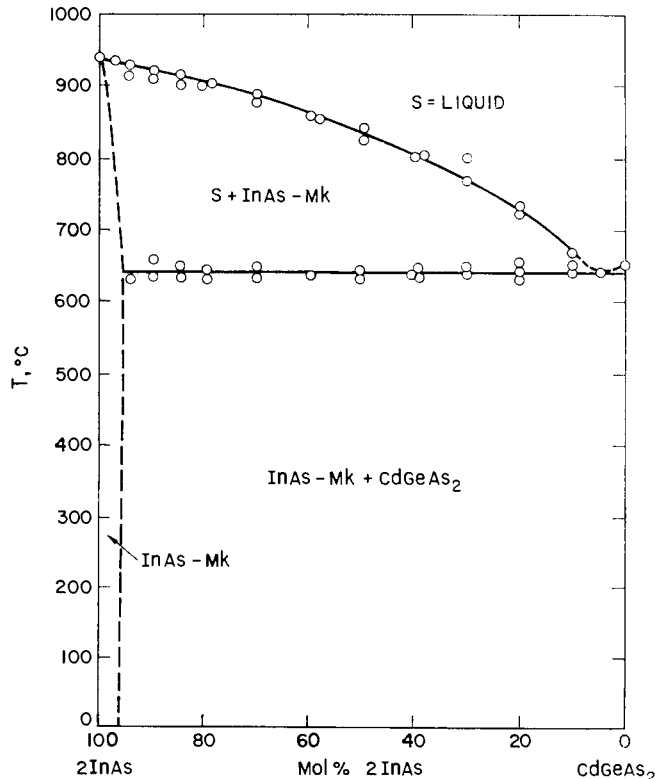


FIG. 2.47. The CdGeAs₂-InAs system. (After Borchers and Maier, 1963b).

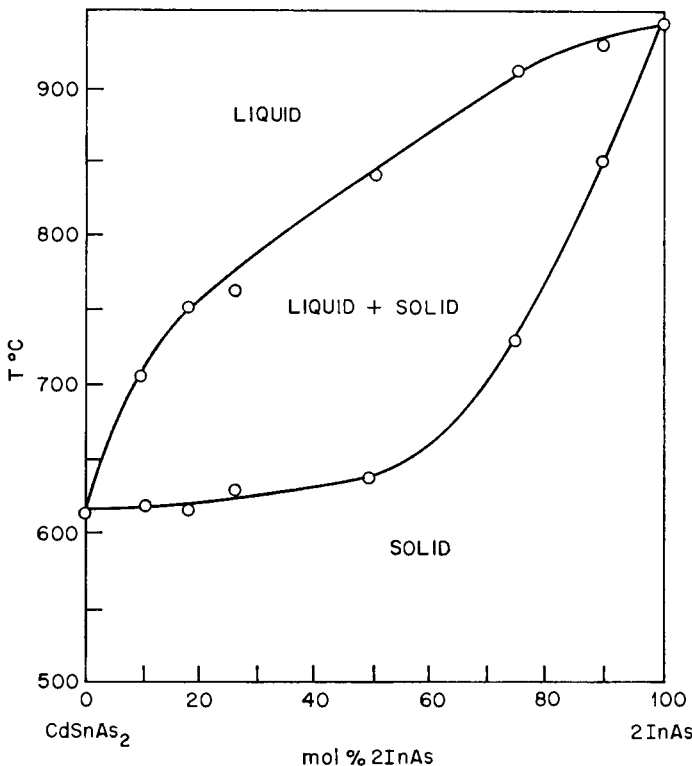


FIG. 2.48. A portion of the CdSnAs_2 -InAs system (as given by Borshchevskii *et al.*, 1967). Range of stability of the chalcopyrite phase not shown.

CdGeAs_2 in InAs exhibits little mutual solid solubility (Fig. 2.47) while CdSnAs_2 -InAs forms a complete series of zincblende solid solutions at elevated temperatures (Fig. 2.48). Room temperature X-ray studies by Goryunova and Prochukhan (1960) showed that at the composition 50 mol % CdSnAs_2 -50 mol % 2 InAs, the zincblende phase began to form with further increase in InAs.

2.11 Crystal Growth, General Considerations

The choice of a growth technique for a particular material will depend on many factors: the chemical reactivity of the compound and constituent elements, the vapor pressures of the constituent elements and dissociation pressure of the compound at the growth temperature, melting point of the compound and whether the compound melts (or freezes) congruently or incongruently, the extent over which the composition can deviate from stoichiometry and still be single phase, and the presence or absence of phase transformations.

An intuitive feeling for chemical reactivity and level of dissociation, based on past experience, is usually utilized in making a first choice. For example, one normally expects sulfides and phosphides to exhibit high dissociation pressures, unless proven otherwise in a particular case. Qualitative information concerning melting points and congruency can sometimes be obtained after the first several attempts at the growth of a particular phase, but it is extremely helpful (and necessary) to have quantitative in-

TERNARY CHALCOPYRITE SEMICONDUCTORS

formation regarding phase equilibria for a particular system for final choice of crystal growth technique and understanding the results of crystal growth. However, such information is almost always obtained *after* a particular interesting compound has been discovered because the motivation for such studies derive from the fact that the compound has been shown to be of technological or scientific importance.

Because of the tendency for thermal decomposition and of the large affinity of the constituents for oxygen, the chalcopyrites are generally prepared in closed systems.[†] The synthesis and subsequent crystal growth can be divided into four principal techniques. (1) Direct synthesis from stoichiometric amounts of the constituent elements, by gradual heating of the mixture, subsequent melting, followed by gradual cooling through the freezing point. This technique yields the largest crystals and is preferred if the dissociation pressure is relatively low or controllable. (2) Direct synthesis involving binary compounds of the constituent elements. This results in lower pressures within the ampoule during the early portion of the synthesis stage and minimizes the chances of explosions. (3) Vapor transport of the constituent elements. This process is known as chemical vapor deposition (CVD), and makes use of a small amount of a volatile element, such as I₂, to form volatile compounds of the constituent elements to promote transport and vapor phase mixing for subsequent condensation of single crystals of the desired compound. Atoms of the transport agent may be present as an impurity in the crystals. (4) Solution or flux growth, i.e. precipitation of the desired compound from a saturated solvent.

In general, the procedure for the growth of chalcopyrite crystals via the melt consists of sealing the component elements in evacuated quartz tubes and heating slowly to the desired temperature. The vapor pressures of P and S are large so that slow heating rates are employed to minimize pressure buildup and excessive heating which may result from strongly exothermic reactions. Since Se, Te, and As exhibit lower vapor pressures, heating can be relatively more rapid. The dissociation pressures of phases formed during heating are lower than the vapor pressures of S and P, for example, so that when the reaction is complete or nearly complete at the lower temperatures, heating rates can usually be increased. Of course, one can make up the initial charge by use of binary compounds of the component elements. For successful crystal growth in the subsequent cooling, the choice of proper cooling rate and establishment of optimum temperature gradient at the interface are of importance. Slow cooling rates of the order of 5–20°/day and temperature gradients of the order of 0.4°/cm are generally required to produce void- and crack-free single crystals.

It is usually good to use a crucible insert for Bridgeman growth or a boat for horizontal growth which does not react with the melt. These can be made of BN, vitreous carbon, graphite, or a quartz container coated with carbon via pyrolysis of benzene or CH₄. Examples of vitreous carbon boats and crucibles used by Buehler and his associates for the growth of phosphides are shown in Fig. 2.49. It has been found by many workers that problems of adherence of crystals or ingots to the walls of crucibles and

[†] In principle, open-tube chemical vapor deposition techniques can be applied for growing chalcopyrite crystals, but are not likely to produce large single crystals. For epitaxial crystal growth, however, open-tube techniques offer many advantages in controlling growth rates and impurity levels. Though open-tube chemical vapour deposition has become one of the most potent methods for epitaxial semiconductor crystal growth, this technique has been neglected to date for chalcopyrite crystal growth work.

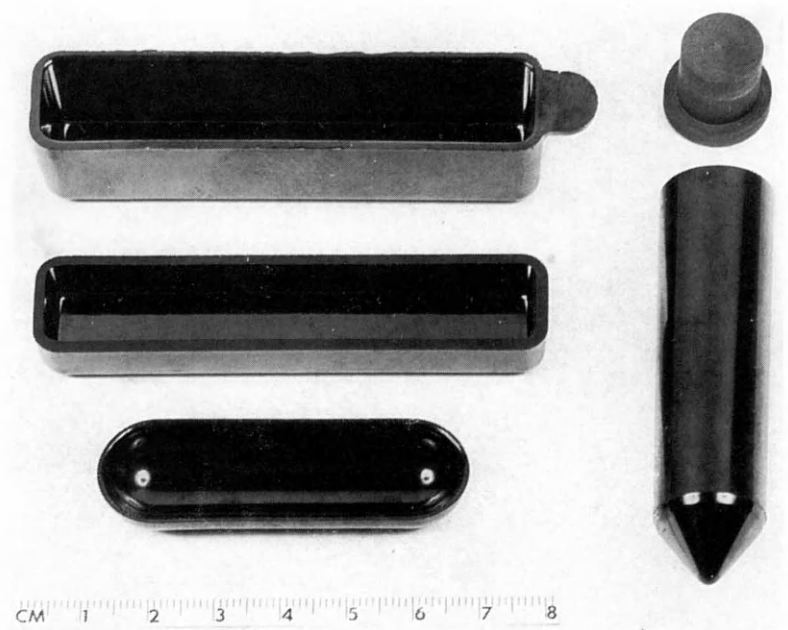


FIG. 2.49. Vitreous carbon boats and crucible used to grow single crystals of phosphides.

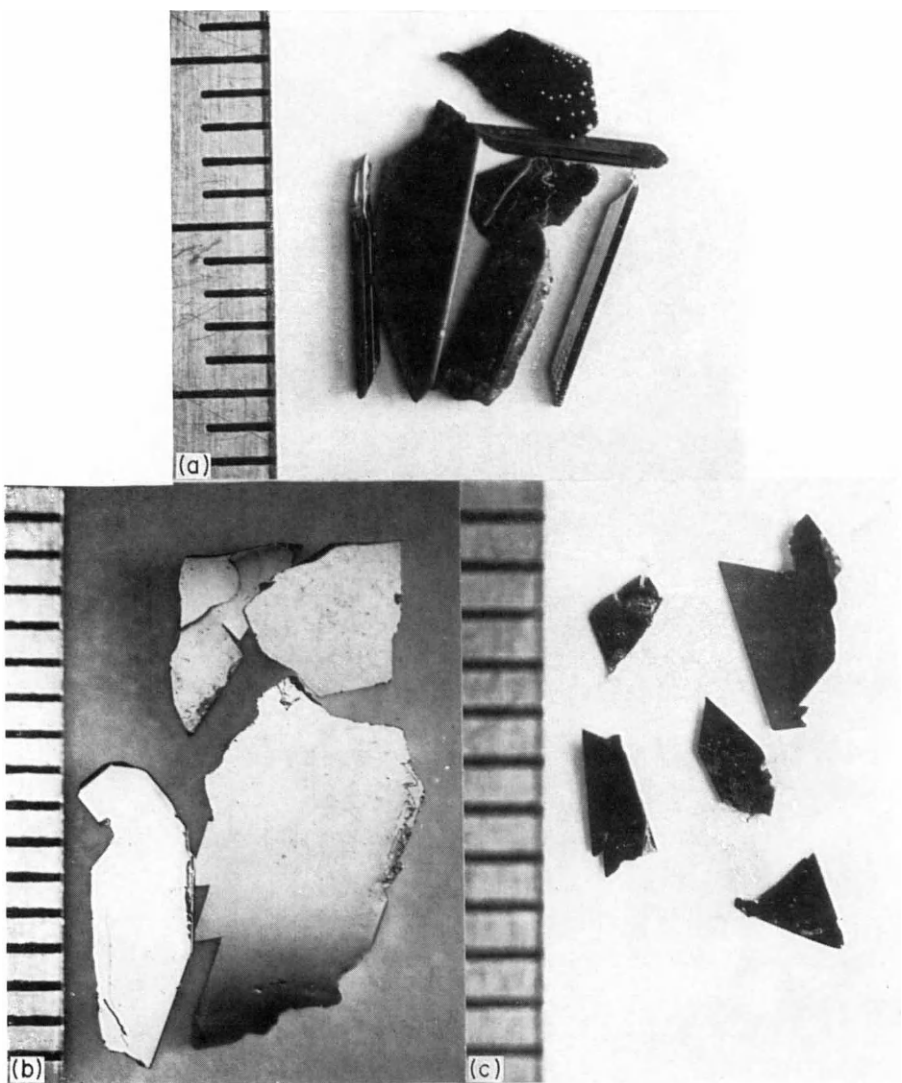


FIG. 2.50. Crystals of (a) $\text{CuGaS}_{1.5}\text{Se}_{0.5}$, (b) CuGaSSe , and (c) $\text{CuGaS}_{0.5}\text{Se}_{1.5}$ grown by CVD (Robbins and Lambrecht, 1972). Scale is in millimeters.

THE CHALCOPYRITE STRUCTURE AND CRYSTAL GROWTH

boats can be minimized or eliminated by use of carbon coatings or carbon crucibles. The use of crucible or boat inserts to contain the charge within the sealed ampoule, rather than a sealed quartz ampoule coated internally with carbon, also has the added advantage of preventing cracking of the ampoule due to thermal expansion of the melt on solidification (if expansion rather than contraction occurs) or due to contraction on cooling to room temperature if adherence to the ampoule walls should occur.

CVD and solution growth techniques are usually used if a compound exhibits a very high dissociation pressure at the melting point or forms incongruently or undergoes solid-state phase transitions. These techniques generally yield small crystals because the normal procedure, particularly early in an investigation, is to allow nucleation to occur in a random fashion. Slow growth rates have to be employed, particularly for compounds forming via peritectic reactions involving the flux material, and the morphology of the resulting crystals is often platelet or needle-like. Since the growth habit in growth from dilute solutions is primarily dictated by the interplay of nucleation and diffusion, one has very little control over crystal morphology and orientation. Nucleation phenomena can be influenced by inhibitor additions, but the desired perfection and purity usually forbids such measures. In CVD and solution growth, lower temperatures are utilized, and it has been argued that these techniques yield more stoichiometric and perfect crystals. This is not necessarily true, and will become apparent in our later discussions. The reader is referred to several books and reviews concerning crystal growth for expanded discussions on this subject (e.g. Schäfer, 1964, and Nitsche, 1967, for CVD; and Gilman, 1963, and Laudise, 1970, for expanded discussions of other crystal growth techniques).

Solid-state transitions are, in general, an impediment to the growth of large homogeneous single crystals, particularly if the crystal structures of the two phases are quite different and ordering involves long diffusion distances. Large volume changes accompanying the transitions can also lead to cracking. Even if the ordering can occur quite easily, defects, which may have a pronounced effect on electrical and optical properties, are probably present to some degree due to incomplete ordering, and, in the case of point defects, contribute to a minimization of the free energy of the ordered phase.

2.11.1 Growth of I-III-VI₂ Crystals

The techniques used for crystal growth of the I-III-VI₂ compounds are summarized in Table 2.10. Austin *et al.* (1956) appear to be the first group to make a concerted attempt to grow large crack-free single crystals of several of these compounds. They prepared 50–100 g ingots of AgInS₂, AgInSe₂, CuInSe₂, AgInTe₂, and CuInTe₂ in evacuated quartz ampoules, and their attempts to grow large crystals by directional solidification, zone melting, or pulling techniques were unsuccessful. All the ingots were polycrystalline and contained numerous cracks. The difficulty was attributed to the differential thermal expansion (DTE) between the *a*- and *c*-directions. The DTE for CuInSe₂ was given as $3 \times 10^{-6}/^{\circ}\text{C}$. However, AgInTe₂ ingots showed less cracking, yet exhibits a much larger DTE ($9 \times 10^{-6}/^{\circ}\text{C}$).†

Over fifty ingots of CuInSe₂ were prepared by Austin *et al.*, and the best *n*-type samples, although containing twins, had carrier concentrations of less than $10^{16}/\text{cm}^3$.

† The density of CuGaTe₂, CuGaSe₂, CuInTe₂, and CuInSe₂ decreases on melting (Glazov *et al.*, 1970.) The variation of density with temperature for these compounds is also given by these workers.

TERNARY CHALCOPYRITE SEMICONDUCTORS

Zone melting or directional solidification resulted in slight changes in lattice constants along the length of the ingot. Additions of Cu and Se did the same, but the infrared transmission of the samples differing in lattice constant was similar. It was not possible to compensate for the loss of a volatile component in CuInSe_2 as the vapor appeared to be of complex composition.

Lerner (1966) prepared 60–80 g ingots of CuGaSe_2 and AgInSe_2 containing five to ten large crystals by zone leveling techniques. Stoichiometric quantities of the elements were sealed into evacuated quartz ampoules previously coated with carbon by pyrolysis of benzene or CH_4 . The cylindrical ampoules, 25 cm × 12 mm i.d. had a point at the end. The initial reaction was carried out in a vertical furnace, and heating was done slowly to avoid explosions. After melting was complete, the ampoule was lowered out of the furnace at a rate of ~7 cm/hr to prevent cracking of the ampoule. The ampoules were then given about twenty zone-leveling passes each way in a vertical zone-melting apparatus. The zoning rate was about 5 cm/hr, except for the last pass, which was done at a rate of ~0.5 mm/hr. The molten zone was about 2 cm long while the total ingot length was ~20 cm.

Cound *et al.* (1970) prepared AgGaS_2 crystals from stoichiometric melts contained in sealed quartz ampoules by the Stockbarger method.† His best crystals were transparent and pale yellow in color.

Kasper (1972) prepared ingots of AgGaS_2 , CuGaS_2 , and CuInS_2 containing crystals several millimeters in size by slow directional solidification. AgGaS_2 melts were cooled from ~1020°C at a rate of ~1°/hr. In many cases, the SiO_2 boats were cracked because of thermal contraction of the ingots on cooling. When the starting composition was exactly AgGaS_2 , the portion of the ingot that crystallized first was light yellow in color which blended into a green part, which crystallized last. When the initial melt stoichiometry was $\text{Ag}_{0.97}\text{Ga}_{1.01}\text{S}_2$, completely yellow material was obtained. Oxygen contaminated melts yielded green material.

Kasper found that the results obtained from stoichiometric CuGaS_2 melts depended on (1) the maximum temperature to which the melt was raised, (2) time at this temperature, and (3) cooling rate. Melts of CuGaS_2 , which freezes incongruently, yielded ingots in which the first to crystallize had a composition near $\text{Cu}_{0.88}\text{Ga}_{1.04}\text{S}_2$ and contained light orange crystals. Darker, more stoichiometric crystals appeared later along the ingot. The darker crystals are copper rich. When the melt temperature was above 1160°C, the first material to crystallize was yellow. Below 1160°C, all crystals were orange and darker. Reproducible results, i.e. in terms of crystallite size and color, were obtained when the melt was held at 1150°C for one day and then slowly cooled at a rate of 1–1.5°/hr. CuInS_2 melts were cooled at a rate of 1°C/hr.

Kasper (1972) prepared ingots of CuAlS_2 and CuAlSe_2 by slowly cooling stoichiometric melts contained in graphite boats sealed into evacuated quartz ampoules. Heating was done slowly to above the melting points, estimated to be ~1300°C for CuAlS_2 and ~1200°C for CuAlSe_2 . The ampoules were cooled directionally at a rate of 3°/hr from 1280°C and 1200°C for CuAlS_2 and CuAlSe_2 respectively, and crystals several millimeters in size were present in the ingots. The CuAlS_2 crystals were white and seemed to be stable in air, while the CuAlSe_2 crystals were yellow and decomposed slowly due to moisture.

† In the Stockbarger method, the crucible remains stationary and the furnace travels, while in the Bridgman technique, the crucible is moved through the temperature gradient.

THE CHALCOPYRITE STRUCTURE AND CRYSTAL GROWTH

TABLE 2.10. *Summary of crystal growth techniques for I-III-VI₂ compounds*

Compound	Technique†	Compound	Technique
CuAlS ₂	CVD ^a	AgAlS ₂	CVD ^g
CuAlSe ₂	CVD ^a	AgAlSe ₂	CVD ^g
CuAlTe ₂	CVD ^g	AgAlTe ₂	CVD ^g
CuGaS ₂	M ^d , CVD ^g , LM(In) ^h	AgGaS ₂	M ^{c,d} , CVD ^g
CuGaSe ₂	M ^{b,f}	AgGaSe ₂	M ^f
CuGaTe ₂	M ^f	AgGaTe ₂	M ^f
CuInS ₂	M ^d	AgInS ₂	M ^e
CuInSe ₂	M ^{e,f}	AgInSe ₂	M ^{b,e,f}
CuInTe ₂	M ^{e,f}	AgInTe ₂	M ^{e,f}

† M = directly from stoichiometric melts, including Bridgman, zone melting, and horizontal directional solidification techniques; CVD = chemical vapor deposition with I₂ or Cl₂ as transport agent; LM() = from low melting liquid metals.

^a Honeyman (1969).

^b Lerner (1966); ingots contained 5–10 large single crystals.

^c Cound *et al.* (1970).

^d Kasper (1972).

^e Austin *et al.* (1956); ingots polycrystalline.

^f Zhuze *et al.* (1958).

^g Honeyman and Wilkinson (1971); see Table 2.11.

^h Yamamoto and Miyauchi (1972). CuGa_{1-x}In_xS₂ crystals also grown from In solutions.

TABLE 2.11. *CVD growth parameters and crystal yield for several I-III-VI₂ compounds (After Honeyman and Wilkinson, 1971)*

Compound	Ampoule dimensions		Temperature (°C)	Transport time	Crystals obtained
	Diameter (mm)	Length (cm)			
CuGaS ₂	18	20	800–700 850–750	3 days	High-yield yellow-green crystals, stable in atmosphere
CuAlTe ₂	18	20	780–650	5 months	Very low yield, red hexagonal platelets
AgGaS ₂	18	20	840–740	2 weeks	Moderate yield, straw yellow, transparent crystals
AgAlS ₂	15	14	800–600	3 weeks	Colorless crystals, very unstable in air
AgAlSe ₂	18	20	750–630	3 months	Low yield, yellow-black crystals
AgAlTe ₂	18	20	830–630	2 weeks	No crystals

Honeyman (1969) prepared small crystals of CuAlS₂ and CuAlSe₂ by CVD using I₂ as the carrier element. Prereacted material prepared at 1000°C over a period of several days was ground to powder, then placed into 15 cm × 15 mm quartz tubes with enough I₂ to give a concentration of 5 mg/cm³ of tube volume, evacuated and sealed. The tube was then placed in a horizontal, double-wound furnace with a temperature gradient

TERNARY CHALCOPYRITE SEMICONDUCTORS

along it so that the ends of the tube were maintained at different temperatures (800°C at powder-end and 700°C at the other). This temperature gradient was maintained for a period of several days, during which crystals were found along the cooler end of the tube. Honeyman's CuAlS₂ crystals were dark green or black depending on their thickness, and analyzed Cu:Al:S to be 1:1:1.9. The morphology of the crystals were needle-like (2 cm long and several millimeters wide) and plate-like (several millimeters wide and about 100 µm thick). Some of the larger needles were hollow. The selenide crystals were yellow-orange and exhibited needle and plate-like morphologies and dimensions similar to the sulfides.

Honeyman and Wilkinson (1971) reported the results of CVD growth of several other I-III-VI₂ compounds, and their crystal growth parameters and results are listed in Table 2.11. The charges for the CVD runs were prepared from prereacted compounds. Iodine was the transport agent; the amount added was such to give a concentration of 5 mg/cm³ of ampoule volume. The Al-bearing compounds were initially formed in an Al₂O₃ crucible before transferring to a quartz ampoule. Note from the table that the Ag compounds required longer times for growth, and this was attributed to the low vapor pressure of silver iodide, approximately 30 times less than that for copper iodide at the same temperature. The formation of tellurium tetraiodide was proposed to explain the difficulty in growing the tellurides.

It is only recently that the growth of I-III-VI₂ compounds from low-melting metallic solvents has been reported, in contrast to the use of this technique for the growth of single crystals of several II-IV-V₂ compounds (next section). The use of low-melting metals as solvents is also practicable for the preparation of single crystal epitaxial layers. Yamamoto and Miyachi (1972) reported the growth of small, single crystals of CuGaS₂ and CuGa_{1-x}In_xS₂ single crystals from In solutions. To grow CuGaS₂, they sealed mixtures of the component elements which would yield solutions of 10 mol% CuGaS₂ and 90 mol% In into evacuated quartz ampoules 50 mm long and 20 mm i.d. The ampoules were then held at 1150°C for ~6 hr, followed by cooling at rates of 4–300°C/hr. Excess In was removed in hot HCl. Single crystals of CuGaS₂, yellow-orange in color, exhibiting plate (up to 5 mm² faces {101} and 0.1 mm thick) and needle (up to 10 mm long) morphologies, were obtained. Surprisingly, the amount of In incorporated into the crystals was less than 1%.

For reproducible preparation of CuGa_{1-x}In_xS₂ single crystals, the procedure was the same, except the Cu:Ga:S ratio for the 10 mol% solution was 1:1 – y:2. x was not quite equal to y in the final crystals. With increasing In content, the color of the crystals changed from the yellow-orange of CuGaS₂ through red for the intermediates to black for CuInS₂. Yamamoto and Miyachi suggested that these results indicate that CuGaS₂ is thermodynamically more stable than CuInS₂.

Single crystals of solid solutions in the CuGa(S_{1-x}Se_x)₂ and (AgInS₂)_{1-x}(ZnS)_x systems have been prepared by CVD and in the (CuGaSe₂)_{1-x}(ZnSe)_x system by directional solidification in boats or by the Bridgman technique (Robbins and Lambrecht, 1973; Lambrecht, 1974).

For melt growth in the (CuGaSe₂)_{1-x}(ZnSe)_x system, the stoichiometric charges were contained in vitreous carbon boats or crucibles and enough excess Se added to maintain a pressure of approximately 4 atm at 1200°C. The resulting ingots were polycrystalline, but crystallites as large as 1 × 0.5 × 0.5 cm³ were present.

For CVD growth in the CuGaS_{2-x}Se_x system, 5 g of prereacted polycrystalline material with enough I₂ to give 5 mg/cm³ of tube volume was used. The sealed ampoule

was maintained in a temperature gradient of $2.6^{\circ}/\text{cm}$ ($1000\text{--}950^{\circ}\text{C}$) for 2 weeks. Examples of several crystals in this system grown by this procedure are shown in Fig. 2.50. The morphology of the crystals was generally plate-like with the *c*-axis in the plane of the major face. Since crystals grew randomly throughout the tube rather than being confined to the cold end, large lateral thermal gradients appear not to be necessary. The smaller transverse gradient of the furnace used for this work appeared to be the most critical, and one experiment for CuGaSSe, indeed, showed this to be the case. CuInSSe crystals were grown in a gradient of $2.6^{\circ}/\text{cm}$, and exhibited plate-like and needle morphologies, while crystals of $(\text{AgInS}_2)_{1-x}(\text{ZnS})_x$ were grown in a gradient of $1.96^{\circ}/\text{cm}$ ($1000\text{--}950^{\circ}\text{C}$) for 2 weeks. In all of the above cases, the composition of the crystals appeared to be approximately that of the starting material.

2.11.2 Growth of Single Crystals of II-IV-V₂ Compounds

The crystal growth techniques employed for these compounds are summarized in Table 2.12. Since several different techniques have been employed for a given compound and more work of this nature has been done on these materials compared to the I-III-VI₂ compounds, the crystal growth discussions in this section will be confined to particular compounds rather than discussing growth within the context of a particular method. In addition, the work of all of the authors cited in Table 2.12 will not be discussed; only the work for which significant information pertaining to their techniques for a given material will be elaborated on.

2.11.2.1 *MgSiP₂* and *MgGeP₂*

Trykozko and Goryunova (1968) prepared small crystals from Sn solution by placing stoichiometric amounts of Mg, Si, and P with sufficient Sn to produce a solution of 5 mol% MgSiP₂ into graphite or Al₂O₃ crucibles, sealing in an evacuated thick-walled quartz ampoule which had been previously coated with graphite by pyrolysis of acetone (Mg reacts with SiO₂), heating the assembly to and holding at 1100°C for 3 hr, and cooling at a rate of $50^{\circ}/\text{hr}$. Direct synthesis was also carried out at 1100°C for 4 hr. For this latter process, a coarse-grained orange powder was obtained together with unreacted magnesium phosphide and Si. The MgSiP₂ crystals grown from Sn were usually in the form of hollow needles $\sim 8 \text{ mm}$ long (needle axis, [111]), but plate-like crystals $2.5 \times 2 \times 0.3 \text{ mm}^3$ also formed.

The Sn-solution technique of Springthorpe and Harrison (1969) is somewhat similar to the above. Stoichiometric quantities of the elements and sufficient Sn to form a 10 mole % solution are placed in a high purity carbon crucible and then sealed in an evacuated silica tube. The ampoule is then heated in a vertical furnace at a rate of $60^{\circ}/\text{hr}$ to $\sim 1150^{\circ}\text{C}$, followed by slow cooling at $6^{\circ}/\text{hr}$ to $\sim 400^{\circ}\text{C}$ followed by air quenching. Hot concentrated HCl is used to extract the crystals, which are orange-yellow, hexagonal prisms, typically $2 \times 0.5 \times 0.5 \text{ mm}^3$ with the prism axis in the [111] tetragonal direction.

For MgGeP₂, which only exhibits the zincblende structure, Springthorpe and Pamplin (1968) (see Table 2.13) employed Sn as the solvent. The size and morphology of the crystals were not discussed. Their procedure for growing MgGeP₂ and the other II-IV-V₂ compounds shown in Table 2.13 from Sn solution consisted of placing the stoichiometric amounts of the constituent elements and sufficient Sn to form a 10–20 mol% solution into a thick-walled silica ampoule, evacuating, and sealing off. The ampoule is then heated at $50\text{--}100^{\circ}\text{C}/\text{hr}$ in a rocking furnace to within about 100°C of the normal

TERNARY CHALCOPYRITE SEMICONDUCTORS

TABLE 2.12. *Summary of crystal growth techniques employed for II-IV-V₂ compounds*

Compound	Technique
MgSiP ₂	LM(Sn) ^{a,b}
MgGeP ₂	LM(Sn) ^w
ZnSiP ₂	M ^l , LM(Sn) ^{v,w,gg} , LM(Zn) ^q , LM(In) ^x , LM(Bi) ^x , LM(Sb) ^y , CVD ^{n,o,r,w,x,ee,ff}
ZnSiAs ₂	M ^w , LM(Sn) ^{v,w} , CVD ^{w,hh}
ZnGeP ₂	M ^{i,j,k,l,o,s} , CVD ^{j,w} , LM(Bi) ^{bb}
ZnGeAs ₂	M ^{dd}
ZnSnP ₂	LM(Sn) ^{c,d,e,f,g,h,w}
ZnSnAs ₂	M ^{u,cc,dd} , LM(Sn) ^x
ZnSnSb ₂	LM(Sn) ^t
CdSiP ₂	LM(Sn) ^{k,v,w,y} , CVD ^{n,o,w,y,z} , LM(In) ^x , LM(Bi) ^x , LM(Sb) ^x
CdSiAs ₂	LM(CdAs) ^p , LM(Sn) ^v
CdGeP ₂	M ^{i,m} , LM(Sn) ^w
CdGeAs ₂	M ^{dd}
CdSnP ₂	LM(Sn) ^{o,v,w}
CdSnAs ₂	M ^{u,aa,dd}

† M = directly from the melt, including Bridgman, zone melting, and horizontal directional solidification techniques; CVD = chemical vapor deposition with I₂ or Cl₂ as transport agent; LM()=from solution, i.e. from low melting liquid metals.

^a Trykozko and Goryunova (1968).

^b Springthorpe and Harrison (1969); attempts to prepare MgSiAs₂ and MgGaAs₂ by this technique failed.

^c Loshakova *et al.* (1966).

^d Berkovskii *et al.* (1968); cooling rate $\sim 5^\circ/\text{hr}$.

^e Goryunova *et al.* (1969).

^f Borshchevskii *et al.* (1968); 5 mol% ZnSnP₂ in Sn, 4 \times 6 \times 0.5 mm³ crystals.

^g Rubenstein and Ure (1968).

^h Springthorpe and Pamplin (1968); Mughal *et al.* (1969), peritectic (930°C).

ⁱ Masumoto *et al.* (1966).

^j Ray *et al.* (1969).

^k Isomura and Masumoto (1972).

^l Buehler *et al.* (1973).

^m Buehler and Wernick (1972); Wiley *et al.* (1973).

ⁿ Valov and Ushakova (1968); Valov (1969).

^o Buehler and Wernick (1971); Buehler *et al.* (1971).

^p Averkieva *et al.* (1969, 1970a, b). Composition of liquid phase influences the hole concentration and hole mobility. Purest single crystals exhibit hole concentrations of 10¹⁵–10¹⁶/cm³ at room temperature (Averkieva *et al.*, 1971).

^q Alekperova *et al.* (1969a, b).

^r Alekperova *et al.* (1969a, b); flourine system.

^s Ivanova *et al.* (1970), 3–5 mm diam., 20–27 mm long crystals.

^t Goryunova *et al.* (1968a, b).

^u Gasson *et al.* (1962).

^v Vaipolin *et al.* (1965a, b).

^w Springthorpe and Pamplin (1968); see also Table 2.13.

^x Borshchevskii *et al.* (1967).

^y Bychkov *et al.* (1966). Crystals grown from Sn solutions were $\sim 2 \times 1.5 \times 0.1$ mm³ and used as feed material for CVD. Thin needles up to 10 mm long and plates 4 \times 1.5 \times 0.05 mm³ produced by CVD. All crystals were n-type.

^z Valov and Plechko (1968a, b). SiCl₄ used as source of transport agent, Cl₂. Largest crystals 13 \times 3.5 \times 1 mm³.

THE CHALCOPYRITE STRUCTURE AND CRYSTAL GROWTH

^{aa} Leroux-Hugon (1966). By zone melting; *n*-type crystals.

^{bb} Bertoti and Somogyi (1971), Somogyi and Bertoti (1972). Crystals were high resistivity *p*-type and hole mobility determined to be 18 cm²/V-s.

^{cc} Masumoto and Isomura (1965). Bridgman method, lowering rate 3 mm/hr.

^{dd} Kwan and Woolley (1970). Graphite crucible inserts for ZnSnAs₂ and ZnGeAs₂. Cooling rate 10°C/hr. Coarse-grain polycrystalline ingots.

^{ee} Tietjen and Amick (1966).

^{ff} Akopyan and Zlakin (1966).

^{gg} Bertoti (1970).

^{hh} Shay *et al.* (1971).

melting point of the compound. After rocking at the maximum temperature for ~6 hr, the ampoule may be slowly cooled (2.5–10°C/hr) until very little II–IV–V₂ compound remains in solution in the tin. This temperature is ~750°C for ZnSiP₂ (which is discussed in more detail below) as indicated by their solubility data shown in Fig. 2.51. The molten Sn can be decanted for reuse and residual Sn on the grown crystals easily removed with hot, concentrated HCl, in which most of the compounds shown in Table 2.13 are insoluble.

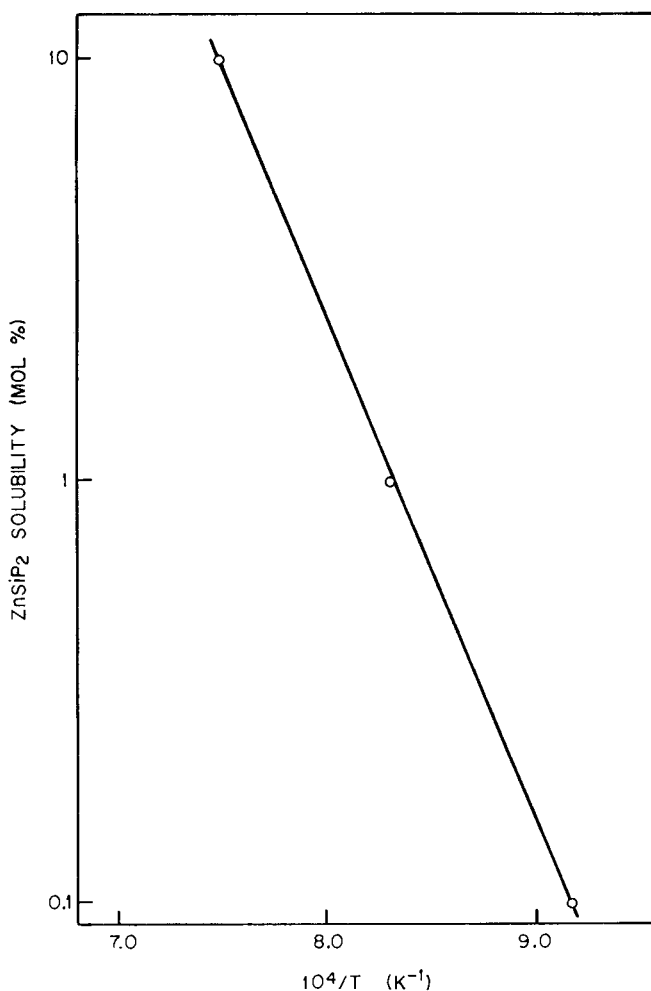


FIG. 2.51. Solubility of ZnSiP₂ in liquid Sn as a function of temperature.
(After Springthorpe and Pamplin, 1968.)

TERNARY CHALCOPYRITE SEMICONDUCTORS

TABLE 2.13. *Summary of crystal growth results of Springthorpe and Pamplin (1968)*

Compound	Method of growth	Structure†	Lattice Parameters‡		Remarks
			$a \pm 0.001 \text{ \AA}$	$c \pm 0.002 \text{ \AA}$	
MgGeP ₂	LM(Sn)	z†	5.652		
ZnSiP ₂	LM(Sn), CVD	c	5.400	10.440	5–10 mm long, 1–10 mm ³ in volume. Well developed faces, long dimension [111]. By CVD, $\sim 5 \times 1 \times 0.5 \text{ mm}^3$
ZnSiAs ₂	M, LM(Sn), CVD	c	5.610	10.884	(CVD $\sim 5 \times 1 \times 0.5 \text{ mm}^3$, mixed crystals with ZnSiP ₂ also grown)
ZnGeP ₂	LM(Sn)	c	5.491	10.800	
ZnSnP ₂	LM(Sn)	z	5.652		Crystals flat plates ($4 \times 4 \times 0.5 \text{ mm}^3$). [111] perpendicular to plane of plate
CdSiP ₂	LM(Sn), CVD	c	5.684	10.442	5–10 mm long, 1–10 mm ³ in volume. Habit same as ZnSiP ₂ . CVD, $\sim 5 \times 1 \times 0.5 \text{ mm}^3$
CdSiAs ₂	LM(Sn)	c	5.883	10.880	
CdGeP ₂	LM(Sn)	c	5.768	10.823	
CdSnP ₂	LM(Sn)	c	5.901	11.512	

† c = chalcopyrite; z = zincblende.

‡ The lattice parameters should be compared with those listed in Table 2.2, particularly for ZnGeP₂, CdSiP₂, CdGeP₂, and ZnSiAs₂, to note the incorporation of substantial amounts of Sn in solid solution.

2.11.2.2 *ZnSiP₂ and CdSiP₂*

Because of the high dissociation pressures exhibited by these compounds, growth from liquid Sn and CVD has been used exclusively. The procedure for growth of ZnSiP₂ from Sn solution used by Springthorpe and Pamplin is described in the previous section. Bertoti (1970) used 6 mol% ZnSiP₂–Sn solutions (Zn, Si, and P added as elements) and these solutions cooled from 1200°C at a rate of 4.5°C/hr. The crystals exhibited needle-like or prismatic habit ($8 \times 2 \times 1 \text{ mm}^3$). As observed by others, the longitudinal axis of the crystals coincided with the [1̄11] of the tetragonal cell with faces parallel to this direction having the following indices: (112), 1̄1̄2, (101), (10̄1), (011), and (01̄1). Small facets of (001) or (100) orientation were also found. Buchler and Wernick (1971) used prereacted ZnSiP₂ and CdSiP₂ powder to form 8 mol% Sn solutions.

Larger crystals of these compounds have been prepared by CVD. Si is the least volatile of the elements in these phosphides and is the element that needs to be transported to the crystal growth temperature or lower temperature. The nature or form of the source materials has been either one of the following: (1) the component elements, (2) a Group II–Group V binary compound with Si, and (3) powder of the pre-reacted

THE CHALCOPYRITE STRUCTURE AND CRYSTAL GROWTH

compound. The rate of heating to the crystal growth temperature is adjusted accordingly to avoid explosions. I_2 , Cl_2 , and $ZnCl_2$ or $CdCl_2$ (as a source of Cl_2) are the transport agents employed, i.e. to form $SiCl_4$.

Buehler and Wernick (1971) grew crystals of $ZnSiP_2$ and $CdSiP_2$ from prereacted powder using small amounts of $ZnCl_2$ ($CdCl_2$) (generally 0.006–0.010 g/cm³ of ampoule volume which for the ampoules used, amounted to 0.3% of the total weight of the charge) in thick-walled quartz ampoules. Large rates of transport to the cold end of the ampoule were obtained, but because of uncontrolled nucleation, a large number of small crystals formed; the largest measured $1 \times 1 \times 0.5$ mm³. When powders of the elements were used as starting material, a much slower heating rate, 5½ days to reach 1000°C, had to be employed to permit time for the Group II–Group V phase to form at the lower temperatures so as to reduce the pressure in the ampoule and thus avoid explosions. As heating progressed the ternary compound formed almost *in situ* at the silicon particle sites. During the heating period, as well as at the final temperature, a gradient of 6°/cm was maintained. $ZnSiP_2$ and $CdSiP_2$ crystals, randomly nucleated at the cold end, were small, the largest being $1 \times 0.5 \times 0.2$ mm³.

Springthorpe and Pamplin (Table 2.13) used solution grown material as the source and ~30–50 mg of I_2 per cm³ of tube volume (1 cm diam. sealed quartz tubes) for $ZnSiAs_2$, $ZnSiP_2$, and $CdSiP_2$. A source temperature of ~950°C and temperature differential of ~25°C were employed. Approximately 30–50% of the source material was transported during a 7–10 day period and crystals as large as ~ $5 \times 1 \times 0.5$ mm³ obtained. Crystals of solid solutions in the $ZnSiAs_2$ – $ZnSiP_2$ system were obtained by this technique also, but the source material was sintered mixtures of the ternaries of appropriate composition (see their lattice constant data in Fig. 2.41).

A variation of the above techniques was employed by Buehler and Wernick (1971) and consisted of using ZnP_2 or CdP_2 as the source of Zn (Cd) and P and a single crystal bar of Si, well in excess of the stoichiometric amount, as the source of Si. A schematic drawing of the loaded ampoule within the furnace is shown in Fig. 2.52. The binary phosphide was located in the “cold” end of the thick-walled quartz tube so that during the heating period the vapor pressures of Zn(Cd) and phosphorus over the silicon bar could be controlled. In addition, the use of ZnP_2 and CdP_2 allowed reaching the growth temperatures (950–1000°C) in a rather short period of time (approximately 8 hr) without deleterious results. The 5–6° furnace tilt was found to be essential to promote longitudinal convection. A radial gradient of about 2°/cm promoted circulation of the Si bearing halide vapor from bottom to top within the ampoule and growth occurred normal to the Si rod even though the longitudinal gradient was about 6°/cm. After a 10-day growth period, crystals began to appear at the cold end because of the steeper gradient, resulting in a decrease in the number and size of the crystals on the Si bar. Eventually all of the compound was transported to the cold end. The use of a Si single crystal rod results in a smaller number of nucleation sites for crystal growth, compared to powdered silicon, and limited the rate of reaction with the halogen by presenting a minimum surface area to the transport agent. A photograph of a typical yield of their $ZnSiP_2$ crystals is shown in Fig. 2.53. The cross-section of the rod at the start was rectangular, and it is easily seen how this cross-section has changed as a result of transport. Crystals of $ZnSiP_2$ and $CdSiP_2$ grown by this technique are of the order $5 \times 2 \times 1$ mm³ after 10 days. The long dimension of the crystals is the growth direction and usually corresponded to the $\langle 111 \rangle$ direction, while the well-developed surfaces were $(\bar{1}12)$ and (110) (all indices referred to the chalcopyrite cell).

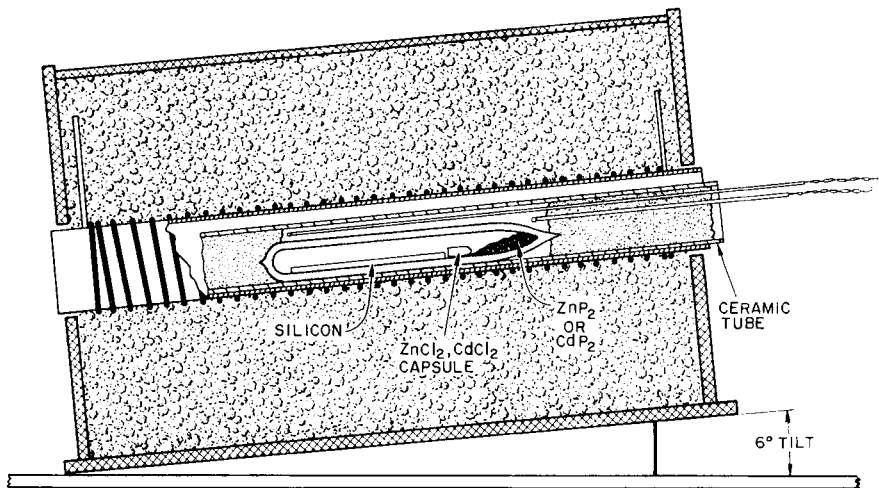


FIG. 2.52. Pictorial representation of loaded ampoule for growth of ZnSiP_2 and CdSiP_2 crystals by the technique of Buehler and Wernick (1971).

2.11.2.3 ZnGeP_2 and CdGeP_2

Examination of Table 2.12 shows that single crystals and polycrystalline ingots of these compounds have been mostly prepared by directional solidification from stoichiometric melts. This is because they exhibit much smaller dissociation pressures at their melting points compared to ZnSiP_2 and CdSiP_2 (Section 2.4). Growth from liquid Sn, Bi, and Bi-Pb eutectic solutions yields small crystals saturated with the solvent element.

ZnGeP_2 is an important infrared nonlinear optical material (Sections 6.2, 6.3, and 6.4), and relatively large, crack-free crystals are required for this application. Buehler *et al.* (1973) have grown large, crack-free single crystals, without seeding, by directional solidification in boats in very shallow temperature gradients. The volume change, which is unknown, associated with the solid-state transition, is no impediment to the growth of crack-free crystals. Earlier papers discussing the preparation of ZnGeP_2 reported that the ingots contained numerous cracks and entrapped bubbles (see, for example, Buehler and Wernick, 1971; Masumoto *et al.*, 1966; Isomura and Masumoto, 1972; Mughal *et al.*, 1969; Ray *et al.*, 1969).

The technique of Buehler *et al.* consists of placing stoichiometric amounts of the elements, sufficient to produce 7–10 g ingots, and excess P as P_4 or in the form of ZnP_2 to provide material for the vapor phase so as to maintain a melt as near the desired composition as possible, into a vitreous carbon boat, and sealing into an evacuated quartz ampoule. The ampoule is then slowly heated in a resistance-wound furnace at an average rate of $125^\circ/\text{day}$ to above the liquidus. It is positioned in the furnace in such a way that, on cooling, the natural gradient moves unidirectionally through the melt. Crack- and bubble-free single crystals were reproducibly grown in temperature gradients below $0.4^\circ/\text{cm}$, while the furnace is cooled at rates approaching $25^\circ/\text{day}$. The temperature gradient for a given run could be changed by placing the ampoule in a different position in the furnace. When the temperature gradients at the liquid-solid interface were in excess of $0.4^\circ/\text{cm}$, usually large-grain polycrystalline ingots containing numerous cracks and bubbles were produced. When the temperature of the ingot is below the solid-state transition, the furnace could be cooled at rates approaching $25^\circ/\text{day}$.



FIG. 2.53. Typical ZnSiP₂ crystals grown by vapor transport using a Si rod as the source of Si. Magnification 2.8× (after Buehler and Wernick, 1971).

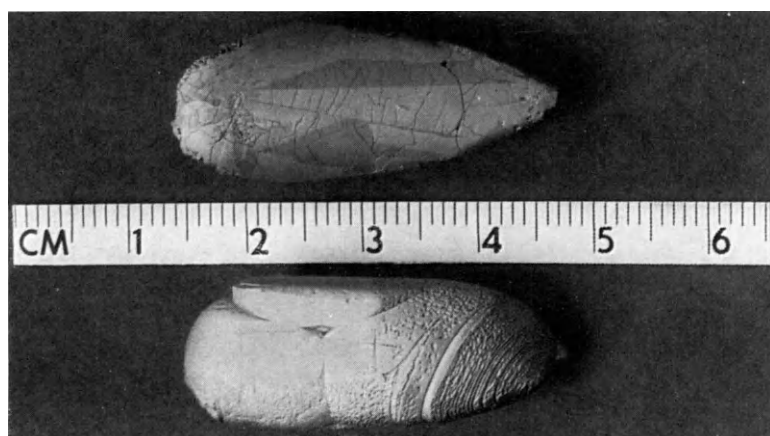


FIG. 2.54. Photograph of a self-seeded crack-free single crystal of ZnGeP₂ (bottom) and large-grain polycrystalline ingot containing numerous cracks (top) (after Buehler *et al.*, 1973).

THE CHALCOPYRITE STRUCTURE AND CRYSTAL GROWTH

A photograph of two ZnGeP_2 ingots synthesized and solidified in the same furnace at a furnace cooling rate of $8^\circ/\text{day}$ through the melting point and solid-state transition is shown in Fig. 2.54. The one grown in a $0.24^\circ/\text{cm}$ gradient is a single crystal (lower portion of photograph) while the other, grown in a $2.4^\circ/\text{cm}$ gradient, is polycrystalline and severely cracked. Both ingots were solidified from stoichiometric melts which also initially contained sufficient excess P to give 3.5 atm of P_4 at the melting point. The total vapor pressure for stoichiometric ZnGeP_2 at the melting point is 3.5 atm and is an extremely strong function of temperature near the melting point (Buehler and Wernick, 1971; and unpublished work).

Since ZnGeP_2 is an important nonlinear optical material, optical absorption measurements were employed for characterizing the crystals of Buehler *et al.* The role of excess ZnP_2 in the starting melt was investigated in this manner. For example, the optical absorption spectrum of a ZnGeP_2 crystal grown from a $51.25 \text{ mol\% ZnP}_2$ - 48.72 mol\% Ge melt under near isothermal conditions ($0.24^\circ/\text{cm}$), is shown in Fig. 2.55. Note the extra absorption of a few cm^{-1} which exists between the band edge and 2μ . The spectrum of a ZnGeP_2 crystal grown from a melt whose initial composition was 53 mol\% ZnP_2 - 47 mol\% Ge is shown in Fig. 2.56. Note the rise in the extra absorption. The spectrum for a crystal grown from a melt whose initial composition was 55 mol\% ZnP_2 - 45 mol\% Ge is shown in Fig. 2.57. The optical quality of this crystal is quite poor; the level of absorption in the transparency region increases drastically. This data tends to rule out the possibility that the extra absorption at the band edge is due to excess Ge. The shape of the excess absorption strongly suggests that it arises from photoionization of a deep donor.

The optical absorption spectrum of a ZnGeP_2 crystal grown from a liquid Bi-Pb eutectic solution is shown in Fig. 2.58. Even though the growth temperature is low in comparison to the melt grown crystals, the optical absorption in the transparency region is poor and presumably arises from the incorporation of Bi and/or Pb in solid solution.

Large crack-free ingots of CdGeP_2 , containing three to ten large crystals (Fig. 2.59), have also been prepared by directional freezing in pyrolytic graphite or vitreous carbon boats sealed into evacuated quartz ampoules (Buehler and Wernick, 1972). The polycrystalline nature of these ingots is understandable because no seeding was done. Even so, the crystallite size was much larger than can be obtained by CVD or solution growth. The charges consisted of stoichiometric amounts of Cd, Ge, and P with or without excess P. When excess P was used, the amount was such as to yield a P pressure as P_4 of $5\text{--}10 \text{ atm}$ at 850°C . The growth procedure was similar to that employed for ZnGeP_2 , and a typical run consisted of heating the assembly to 500°C over a period of 24 hr, then heating to 850°C at a rate of $\sim 100^\circ/\text{day}$, and cooling to room temperature by decreasing the furnace temperature at a rate of $\sim 20^\circ/\text{day}$. The furnace gradient established at one end of the assembly at 850°C was about $4^\circ/\text{cm}$, and it is estimated that this gave a linear growth rate of $2.5\text{--}7.5 \text{ cm/day}$.

2.11.2.4 ZnSnP_2 and CdSnP_2

Single crystals of these compounds have been prepared from dilute solutions of Zn or Cd and P in liquid Sn, as summarized in Table 2.12. They form peritectically (Borschhevskii *et al.*, 1968; Mughal *et al.*, 1969; see also Fig. 2.40). For ZnSnP_2 , slow cooling yielded crystals with the chalcopyrite structure, while fast cooling yielded crystals with the disordered zincblende structure (Loshakova *et al.*, 1966; Berkovskii

TERNARY CHALCOPYRITE SEMICONDUCTORS

FIG. 2.56. Optical absorption spectrum of a ZnGeP₂ crystal grown in a gradient of 0.24°/cm from a melt whose initial composition was 53 mol% ZnP₂ and 47 mol% Ge. (After Buehler *et al.*, 1973.)

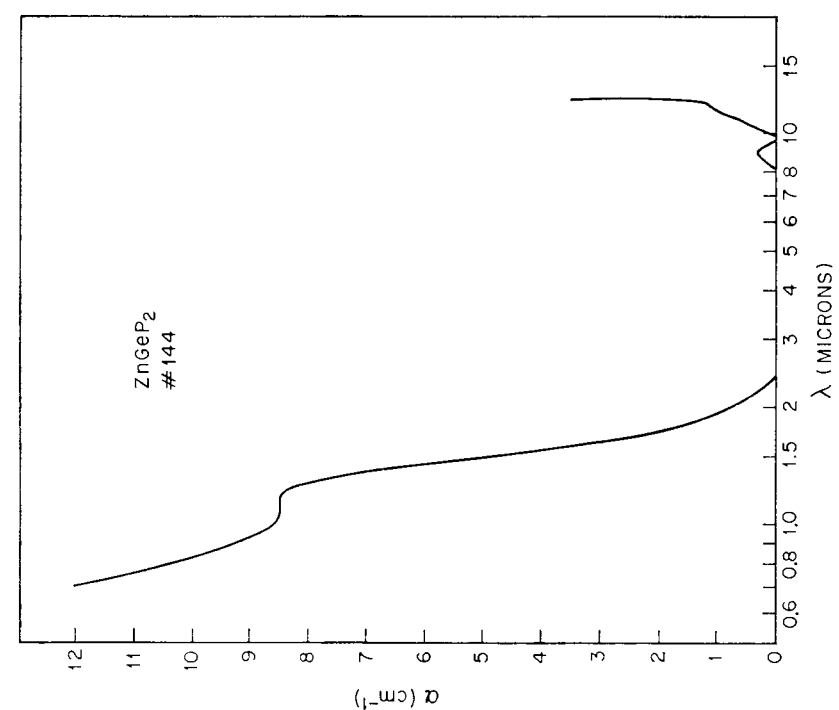


FIG. 2.55. Optical absorption spectrum of a ZnGeP₂ crystal grown from a 51.25 mol% Zn₁₂-48.72 mol% Ge melt under near isothermal conditions (0.24°/cm). (After Buehler *et al.*, 1973.)

THE CHALCOPYRITE STRUCTURE AND CRYSTAL GROWTH

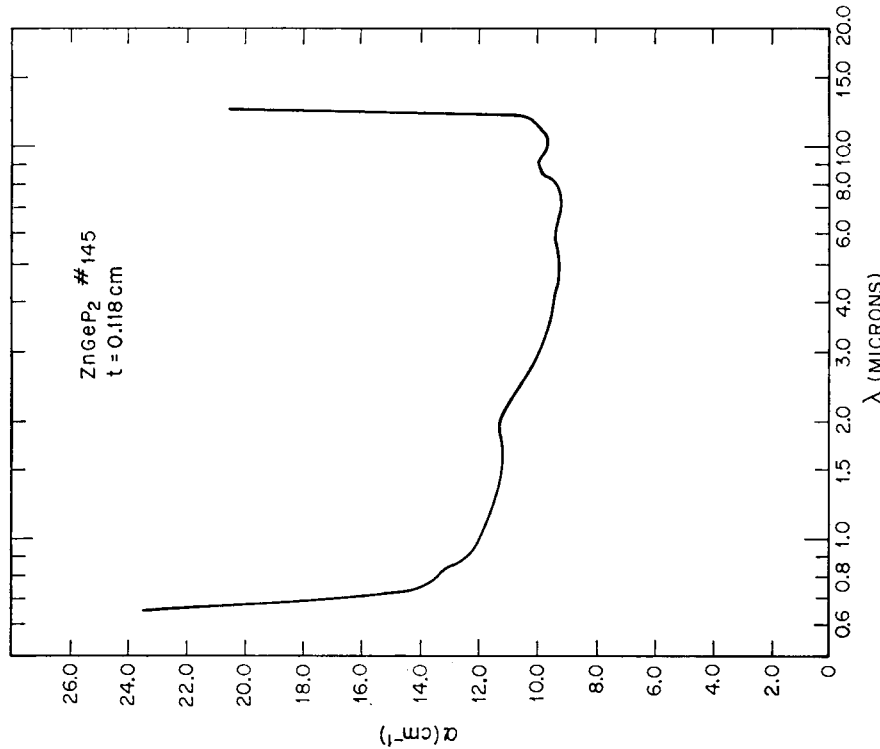


FIG. 2.57. Optical absorption spectrum of a ZnGeP_2 crystal grown in a gradient of 0.24°/cm from a melt whose initial composition was 55 mol % ZnP_2 and 45 mol % Ge. (After Buehler *et al.*, 1973.)

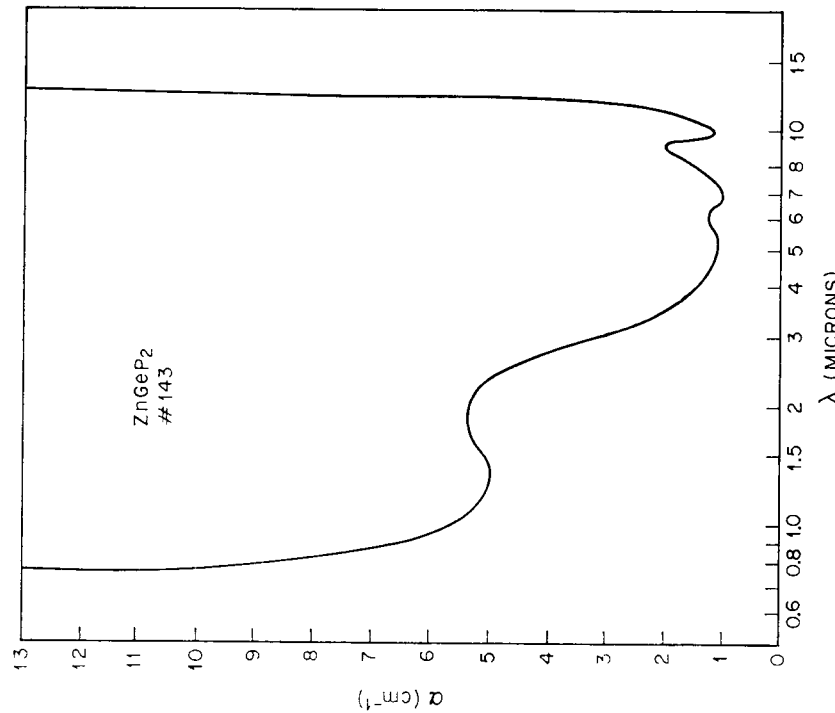


FIG. 2.58. Optical absorption spectrum of a ZnGeP_2 crystal grown from a liquid Bi-Pb solution. (After Buehler *et al.*, 1973.)

TERNARY CHALCOPYRITE SEMICONDUCTORS

et al., 1968; Goryunova *et al.*, 1969; Borshchevskii *et al.*, 1968). Rubenstein and Ure (1968) prepared tetragonal $ZnSnP_2$ crystals ($4 \times 4 \times 0.3 \text{ mm}^3$ average dimensions) by placing ZnP_2 , either red or black, with Sn, in concentrations varying between 2 and 6 mole %, into quartz tubes evacuated to 10^{-6} torr. The ampoule is placed upright in a furnace which is then heated to 800–900°C. The solution is held in a gradient of 10–30°C for a 10 cm column of solution. The lower temperature was at the bottom of the ampoule. After being held at temperature for several days, the temperature is lowered at $\sim 10^\circ/\text{hr}$ until 600°C is reached, whereupon the solution is cooled fairly rapidly to room temperature. The crystals are extracted by dissolving excess Sn in Hg at 100°C and residual Hg removed by vacuum heating of the crystals (Rubenstein, 1966).

As indicated above, the rate of cooling will determine which of the two forms of $ZnSnP_2$ crystallize. Berkovskii *et al.* (1968) found that chalcopyrite crystals were obtained at a cooling rate $\sim 5^\circ/\text{hr}$, and with increasing cooling rates the degree of disorder increased. For example, crystals obtained on cooling at a rate of $50^\circ\text{C}/\text{hr}$ were partially disordered. Their crystals were *p*-type with $\varrho \cong 10 \Omega\text{-cm}$ at 300 K and a net carrier density of $(4\text{--}9) \times 10^{16} \text{ cm}^{-3}$.

Details for the growth of $CdSnP_2$ from liquid Sn have been given by Buehler *et al.* (1971). Analogous to $ZnSnP_2$, $CdSnP_2$ forms peritectically (Fig. 2.40) and solution growth is used. Crystals of average dimensions $10 \times 3 \times 0.5 \text{ mm}^3$ can be grown from dilute solutions in the 90–99 mol % Sn composition range. A typical crystal growth run consists of adding CdP_2 powder with Sn into graphite or vitreous carbon boats; sealing the boat within an evacuated quartz ampoule; heating to 850°C and holding at this temperature for 24 hr; then cooling at a rate of $11^\circ/\text{day}$. Only $CdSnP_2$ crystallizes from liquid Sn in the temperature range 850–600°C. Below 600°C Sn_4P_3 precipitation may occur for cooling rates in excess of $80^\circ\text{C}/\text{day}$ until the melting point of Sn is reached. Excess Sn is removed by dissolution in Hg at 200°C for 10 min and residual Hg by subsequent dissolution in dilute nitric acid and vacuum heating. The thin, soft crystals of Sn_4P_3 , if present, are easily removed mechanically. A photograph of a typical yield of $CdSnP_2$ crystals for a $0.45^\circ/\text{hr}$ cooling rate is shown in Fig. 2.60.

The $CdSnP_2$ crystals grown by the above technique tend to be skeletal with {112}, {110}, and {111} faces predominant. They are *n*-type with resistivities typically $0.1 \Omega\text{-cm}$ with detectable impurities below 10^{17} cm^{-3} . Doping can be accomplished by adding the dopant to the original charge. Silver-doped crystals are *n*-type with $\varrho \cong 1 \Omega\text{-cm}$, while Cu-doping will produce *p*-type crystals with resistivities typically $100 \Omega\text{-cm}$.

2.11.2.5 Arsenides

As discussed in Section 2.4, the dissociation pressures of the arsenides at their melting points are much smaller in comparison to the phosphides, and this simplifies the crystal growth procedures from the standpoint of time required to reach temperature and minimization of the fear of explosions. Nevertheless, the dissociation pressures are high enough so that As-pressure control must be employed in the final analysis to produce stoichiometric crystals.

The techniques employed for the growth of these materials are summarized in Tables 2.12 and 2.13, and the container materials are, in general, similar to those employed for the phosphides. The melting points are lower and sealed systems are used.

If the equilibrium relations for the Zn–Sn–As system are correct (Fig. 2.35), the growth of large stoichiometric crystals of $ZnSnAs_2$ will be impossible. $CdSiAs_2$ forms peritectically and single crystals have been grown by the Russian workers from Cd–As

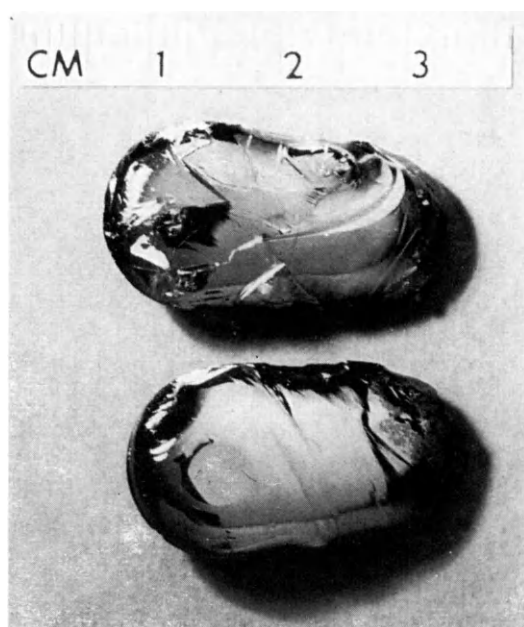


FIG. 2.59. Two directionally solidified ingots of CdGeP₂, each containing three or four large crystals (after Buehler and Wernick, 1972).



FIG. 2.60. Typical crystals of CdSnP_2 grown from liquid Sn 5× (after Buehler and Wernick, 1971).

THE CHALCOPYRITE STRUCTURE AND CRYSTAL GROWTH

solutions. Their technique is described below. CdGeAs₂ is a potentially important nonlinear optical material for the infrared (see Section 6.2), and some discussion regarding its growth is also presented below.

ZnSiAs₂, CdSiAs₂, and CdGeAs₂

The CVD experiments for the growth of ZnSiAs₂ crystals ($\sim 5 \times 1 \times 0.5$ mm³) carried out by Springthorpe and Pamplin (1968) were done in 1 cm sealed silica tubes using solution-grown material as the source with a source temperature of $\sim 950^\circ\text{C}$ and temperature differential of $\sim 25^\circ\text{C}$. For effective transport to take place, they used larger amounts of I₂ than usually necessary: $\sim 30\text{--}50$ mg I₂/cm³ of tube volume. Approximately 30–50% of the source material was transported during a 7–10 day period. Shay *et al.* (1971) prepared ZnSiAs₂ crystals by CVD using stoichiometric amounts of the elements as source material and SnCl₂ ($\sim 0.3\%$ by weight of the total charge) as a source of Cl₂ for transport. The crystals were irregular in shape, but with facets as large as 3×6 mm and *p*-type with resistivities $\sim 10 \Omega\cdot\text{cm}$.

Since CdSiAs₂ forms peritectically, most of the crystal growth of single crystals and preparation of polycrystalline ingots (grains several millimeters in size) has been from Cd–As solutions (Averkieva *et al.*, 1969, 1970 a). Crystallization is done in quartz ampoules having a tapered bottom and located in a temperature gradient. Pieces of Si–As alloy are the solute or feed material which floats on top of the liquid Cd–As alloy and are located in the region of higher temperatures. Crystallization occurs in the conical section of the ampoule located at the lowest temperature. Crystals grown by this technique are *p*-type, and the composition of the solvent has a slight influence on the free hole density and energy gap as shown in Table 2.14.

TABLE 2.14. *Carrier concentrations and energy gaps of CdSiAs₂ crystals grown from Cd–As solutions. (After Averkieva *et al.*, 1970 a)*

Composition of solvent	Carrier density (cm ⁻³)	ΔE_g (eV) (300 K)	ΔE_g (eV) (83 K)
CdAs	2.5×10^{16}	1.51	1.57
CdAs ₂	5×10^{15}	1.52	1.58
CdAs _{1.5}	1.0×10^{15}	1.51	1.57
Cd ₃ As ₂	6.0×10^{16}	1.51	1.57
CdAs + 1 atm % In	—	1.41	1.49

The crystals of CdGeAs₂ used to date for optical studies have been obtained from polycrystalline ingots containing numerous cracks. Buehler (1972) studied the growth of CdGeAs₂ by directional solidification under near isothermal conditions, similar to that employed for ZnGeP₂ and CdGeP₂. In contrast to ZnGeP₂ and CdGeP₂, the ingots were polycrystalline, contained cracks, and metallographic examinations revealed the presence of a second phase. His results suggest that either CdGeAs₂ forms peritectically (see Fig. 2.39) or supercooling effects are important even under extremely slow growth conditions (CdGeAs₂ can be prepared in the glassy state; see Section 2.12).

2.11.2.6 *Antimonides and Bismuthides*

ZnSnSb₂ appears to be the only known II–IV–V₂ antimonide. It has been suggested that it forms peritectically, and cubic and tetragonal crystals were grown from Sn

TERNARY CHALCOPYRITE SEMICONDUCTORS

solution, depending on the cooling rate (Goryunova *et al.*, 1968a, b; Vaipolin *et al.*, 1971). The liquidus for a portion of the Sn-ZnSnSb₂ join is shown in Fig. 2.37.

Growth of single crystals of the zincblende form has been described by Goryunova *et al.* (1968a, b). Solutions of 10–35 mol % ZnSnSb₂ in Sn were cooled at rates of 3–100°/hr. Two methods were employed to completely remove the excess Sn. The first is solution of Sn in Hg at room temperature. The second is the conversion of Sn to the brittle gray form at low temperatures, resulting in decrepitation to “dust” so that the crystals can be mechanically separated.

No ternary II-IV-V₂ bismuthides are known to exist under ordinary conditions. Hand-waving arguments have been proposed regarding the lack of existence of bismuthides and many antimonides, and they are based on the fact that the bonding in these ternary compositions would be or tend to be quite metallic, rather than directionally covalent, in character. The lack of any diamond like III-V's based on V = Bi should be noted in this regard.

2.11.3 Growth of Epitaxial Layers

Techniques for the preparation of single crystal homo- and heteroepitaxial films to form *p-n* junctions for optoelectronic devices are fairly well established for several semiconductors and semiconductor systems, such as Si, Ga_{1-x}Al_xAs, GaAs_{1-x}P_x, and GaP. *p-n* junctions can be prepared by (1) diffusion, (2) vapor-phase growth, and (3) liquid-phase epitaxy from solution. Ion implantation is another method now receiving attention. Liquid-phase epitaxy has been used principally to grow *p-n* junctions in GaAs and Ga_{1-x}Al_xAs on highly doped *n*- and *p*-layers for injection lasers.

The term homojunction refers to a *p-n* junction in which both materials are identical except for conductivity type. For those cases in which the conductivity type of a given phase cannot be changed by doping, for example by diffusion, a single crystal film (or substrate) of another phase of opposite conductivity type can be employed, and the *p-n* junction so formed is referred to as a heterojunction and the process referred to as heteroepitaxy.

The ability to form suitable *p-n* junctions by any of the above processes will depend on many factors. One is the chemical stability of the substrate and/or film material at the reaction temperature. How well the substrate surface is prepared, the nature of the surface immediately prior to deposition and defect content of the substrate are important because the imperfection density at the junction and thus the presence of unwanted localized energy states in the energy gap is an important factor in determining optoelectronic properties. These unwanted localized energy states may arise from dislocations, lattice vacancies, inclusions, nonstoichiometry, and strain that is often introduced during or after crystal growth.

This is particularly important for the case of heterojunctions, where the lattice constants of the two substances generally do not match entirely. This introduces a lattice misfit strain which, at elevated temperature, exceeds the elastic limit and is relaxed by creating a network of misfit dislocations in the interfacial region. The density of interfacial dislocations can be minimized by choosing a substrate orientation or surface orientation and film material having lattice constants which differ very slightly. Close matching of thermal expansivities will also minimize the production of dislocations, cracking, and the presence of elastic strain on cooling from the growth temperature. The inability to achieve these important considerations may prevent the exploitation of various properties of a semiconductor via the formation of *p-n* junctions.

THE CHALCOPYRITE STRUCTURE AND CRYSTAL GROWTH

TABLE 2.15. Summary of heteroepitaxy studies with chalcopyrite compounds

System†	Reference	Junction plane	Remarks
CdS/CuGaS ₂	a	(112) of CuGaS ₂	n-type CdS on p-type CuGaS ₂ by molecular beam
Ge/ZnSiP ₂	b	Natural crystal faces of II-IV-V ₂ compound [(112), (101), (001)]	I ₂ transport of Ge. ZnSiP ₂ substrate grown from Sn solution
Ge/ZnGeP ₂	b	Natural crystal faces [(112), (101), (001)]	I ₂ transport of Ge. ZnGeP ₂ substrate from Sn solution
Ge/ZnSiAs ₂	b	Natural crystal faces [(112), (100)]	I ₂ transport of Ge. ZnSiAs ₂ substrate grown by I ₂ transport
Si/ZnSiP ₂	c	Natural crystal faces [(112), (101)]	H ₂ reduction of SiHCl ₃
Si-ZnSiP ₂ solution /Si solid	d	(111) of Si	Liquid phase epitaxy from solutions of Sn, In, Al, Zn, Ag, and Au by temperature gradient zone melting. Layer is Si-rich
ZnSiP ₂ /Si	g	(111) (110)	From solutions of 4 mol % ZnSiP ₂ in Sn, Pb, or 80% Sn-20% Pb
ZnSiP ₂ /GaP	g		From solutions of 4 mol % ZnSiP ₂ in Sn, Pb, or 80% Sn-20% Pb
ZnSiP ₂ /Si	g	(111)	Chemical transport in closed fluorine system. Layers polycrystalline
Cu ₂ S/CdSnP ₂	e		Polycrystalline p-type Cu ₂ S film by vacuum evaporation. Undoped and Cu-doped n-type CdSnP ₂
CdSn(As _x P _{2-x})/Si	g		Same technique as for CdSnAs ₂ /Si
CdSnP ₂ /CdGeP ₂	g		From Sn solution by traveling solvent method. Unoriented CdGeP ₂ crystals
CdGe _x Sn _{1-x} P ₂ /CdGeP ₂	g		Same as above
CdGe _{0.3} Sn _{0.7} P ₂ /Si	g		Same as above
CdGe _x Sn _{1-x} P ₂ /Ge	g		From Sn solution in closed system. Substrate immersed into liquid
Ge/CdSiP ₂	g		From Sn solution in closed system
Ge/CdSnP ₂	g		From Sn solution in closed system
CdSnP ₂ /InP	f	(100) of InP	Liquid phase epitaxy from Sn solutions
ZnSnAs ₂ /Ge	g		From Sn solution in closed system. Substrate immersed into liquid. Layer was solid solution of ZnSn _x Ge _{1-x} As ₂
CdSnAs ₂ /Si	g		Si, p-type. CdSnAs ₂ n-type. From CdSnAs ₂ melts in closed system. Usually polycrystalline layers 1-5 mm thick

† The notation A/B means A is deposited on B, the substrate. ^a Wagner *et al.* (1973).

^b Springthorpe *et al.* (1969). ^c Bertoti (1970). ^d Popov and Pamplin (1972).

^e Goryunova *et al.* (1971a, b, c). ^f Shay *et al.* (1973a, b). ^g Valov *et al.* (1973).

TERNARY CHALCOPYRITE SEMICONDUCTORS

TABLE 2.16. Lattice parameters for Si, Ge, and several II-VI and III-V Compounds†

Material	a (Å) (cubic)	(Wurtzite form)	
		a (Å)	c (Å)
Si	5.4307		
Ge	5.6576		
AlP	5.467		
GaP	5.4504		
InP	5.8687		
InAs	6.0584		
GaAs	5.6533		
AlAs	5.660		
ZnS	5.42	3.8225	6.2610
CdS	5.832	4.160	6.756
ZnSe	5.656	3.996	6.626
CdSe	6.06	4.299	7.010
ZnTe	6.085		
CdTe	6.477		

† Compiled from W. B. Pearson, *Handbook of Lattice Spacings and Structures of Metals*, Vol. 2, Pergamon Press, 1967.

Several I-III-VI₂ and II-IV-V₂ compounds (e.g. CuGaS₂ and CdSnP₂) can be doped *n*- and *p*-type, and, in principle, homojunction preparation is possible (Chapter 7). However, much of the junction work to date has been via heteroepitaxy, and only this aspect will be discussed here. A summary of the heteroepitaxy studies involving chalcopyrite compounds is given in Table 2.15. The preparation and optoelectronic properties of CdS/CuGaS₂ and CdSnP₂/InP are the only two cases which have been studied in some detail to date. The optoelectronic results are discussed in Chapter 5. The lattice constants of several binary semiconductors are given in Table 2.16 and can be compared with the structural information given in Tables 2.1 and 2.2.

CdS and ZnS cannot be made usefully *p*-type, and Wagner *et al.* (1973) prepared heterodiodes of CdS/CuGaS₂ by molecular beam epitaxy of *n*-type CdS on *p*-type CuGaS₂. The lattice mismatch between CuGaS₂ and CdS is much greater than between CuGaS₂ and ZnS, but the former system was chosen because the room temperature energy gaps are nearly the same and the conductivity of CdS is more easily controlled. Their procedure consisted of cutting platelets having (112) surfaces† from melt-grown crystals, mechanically polishing, etching in warm 1:1 HCl + HNO₃, annealing at 850°C in saturated sulfur vapor, and quenching to produce a room temperature *p*-type resistivity of ~1 Ω-cm (Tell *et al.*, 1971, 1972). The substrates are then cleaned in CS₂, re-etched if desired, and CdS films ~5 μm thick grown in vacuum at various substrate temperatures in a molecular beam apparatus providing Cd and S sources. CdS films grown on mechanically polished CuGaS₂ substrates were hexagonal

† The (112) plane in the tetragonal cell is equivalent to the (111) plane in the cubic zincblende structure.

THE CHALCOPYRITE STRUCTURE AND CRYSTAL GROWTH

and single crystals with [0001] approximately normal to the substrate surface. On chemically etched multifaceted substrates, the CdS films were epitaxial but polycrystalline.

n-type CdS films with room temperature resistivities of $\sim 1 \Omega\text{-cm}$ were obtained with substrate temperatures about 200°C . It should be noted, however, that *p*-type CuGaS₂ crystals heated in vacuum to temperatures above 100°C develop a highly resistive surface layer accompanied by a simultaneous increase in bulk resistivity. However, the quality of the CdS epitaxy improves as the substrate temperature is increased from 75° to 210°C . A substrate temperature of $\sim 130^\circ\text{C}$ resulted in CdS films and diodes of reasonable electrical properties to permit light emission in d.c. operation (see Section 5.5 for details, including methods of making electrical contacts).

As pointed out in Section 2.11.2.4, CdSnP₂ crystals grown from Sn solution without intentional doping are *n*-type with resistivities typically $\sim 0.01 \Omega\text{-cm}$. Low resistivity *p*-type conduction has not been observed, although high resistivity ($>100 \Omega\text{-cm}$) *p*-type crystals have been obtained by Cu-doping. *n*-type CdSnP₂ on *p*-type InP heterodiodes have been prepared by liquid phase epitaxy from Sn solution (Shay *et al.*, 1973a, b; Bachmann *et al.*, 1973). The *a*-axis lattice constant of CdSnP₂ (5.900 \AA) is close to $a = 5.8788 \text{ \AA}$ of InP, and epitaxial growth of CdSnP₂ on (100) InP substrates should therefore produce a lattice mismatch of about 0.5%.

Zn- and Cd-doped *p*-type InP crystals were used. The experimental arrangement for growing epitaxial layers of CdSnP₂ is shown on Fig. 2.61. A solution of 90% Sn, 1.5% Cd, and 8.5% P (see CdP₂-Sn phase diagram, Fig. 2.40) was contained in a vitreous carbon crucible *C* closed off by a plug *P* which held the InP substrate *S* in a dovetail slit. The carbon baffle *B* eliminates line-of-sight contact between melt and substrate prior to tipping, and is essential for maintaining a clean and intact substrate surface. The carbon crucible was sealed off in an evacuated quartz ampoule and placed in a tipping furnace *F* (Fig. 2.61a). For a typical run, the furnace temperature was raised to 525°C

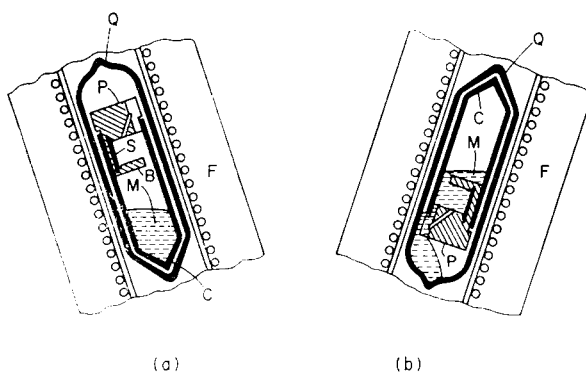


FIG. 2.61. Schematic LPE arrangement used by Shay *et al.* (1973a) to grow CdSnP₂ layers on InP. Furnace positions (a) prior to and (b) after tipping, respectively. *F* is the furnace, *Q* the quartz ampoule, *C* the vitreous carbon crucible, *P* the carbon plug with InP substrate and baffle *B*, and *M* the Sn solution.

TERNARY CHALCOPYRITE SEMICONDUCTORS

and held there for $\frac{1}{4}$ hr to homogenize the melt. Precaution was taken that the substrate crystal and the solution were almost at the same temperature in this stage.

After homogenization, the furnace was cooled rapidly to 510°C and tipped (Fig. 2.61 b) to bring the solution into contact with the substrate. Epitaxial growth was then induced by cooling at a rate of $\sim 15^\circ\text{C}/\text{hr}$. A drainage path in the carbon plug allows the melt to slowly flow out of C, thereby feeding the growth area at the seed surface continuously with fresh solution which helps establish uniform growth conditions. Several per cent of In was found in the CdSnP₂ layers, and the solubility of InP in Sn containing no Cd and P is shown in Fig. 2.62. The substrate was separated from the adherent Sn solution by extraction with Hg (Buehler *et al.*, 1971). Residual contamination with Sn was removed by etching in a HF/HNO₃ solution followed by chemical polishing in a bromine/methanol solution. The reader is referred to Section 5.4 for details of making contacts and optoelectronic studies.

Springthorpe *et al.* (1969) deposited epitaxial layers of Ge by both open tube and closed tube I₂ vapor transport onto crystals of ZnSiP₂, ZnGeP₂, and ZnSiAs₂ (see Table 2.13). For the open-tube work, a furnace having three independently controlled heating zones was used. The I₂ source was maintained at $\sim 60^\circ\text{C}$, the Ge source zone at $\sim 550^\circ\text{C}$, and the Ge deposition zone at $\sim 350^\circ\text{C}$. Purified H₂ at 25 ml/min was the

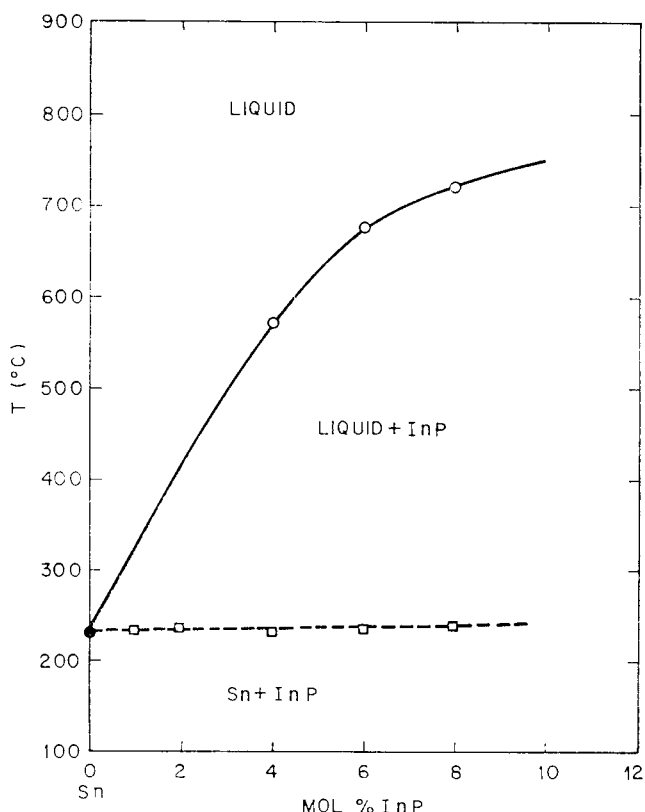


FIG. 2.62. The solubility of InP in Sn as determined by DTA. (After Buehler and Wernick, 1972.)

THE CHALCOPYRITE STRUCTURE AND CRYSTAL GROWTH

carrier gas. Deposition was done on the natural crystal faces at rates of $\sim 20 \mu\text{m}/\text{hr}$. Epitaxial deposits were obtained on all exposed substrate faces when the substrates were placed in the region of maximum temperature gradient between the Ge source and deposition zones.

Heavily faceted triangular deposits were obtained on the (112) faces of ZnSiP_2 . Heavily faceted deposits were also obtained on the (100) surfaces of ZnGeP_2 and they exhibited a square pyramidal topography. Preliminary studies of the electrical properties of $n-n$ Ge/ ZnSiP_2 diodes supported their observations of abrupt junctions. Attempts to deposit GaAs and Si on ZnSiP_2 at temperatures in the range 600–850°C were unsuccessful because of decomposition of ZnSiP_2 .

On the other hand, Bertoti (1970) reported successful deposition of Si on natural faces of ZnSiP_2 crystals by the hydrogen reduction of SiHCl_3 . The growth temperature of the layers was 1050–1150°C and the growth rate was 0.5–0.8 $\mu\text{m}/\text{min}$. It is unlikely that deposition occurred at these temperatures because of the high dissociation pressure of ZnSiP_2 (see Section 2.4). Further support for this possibility is the fact that: (1) ZnSiP_2 begins to decompose at $\sim 400^\circ\text{C}$, (2) Curtis and Wild (1970) found that ZnSiP_2 cannot be formed in an open-tube system (total pressure one atmosphere) above 850°C, and (3) Buehler and Wernick (1971) show that, consistent with the Curtis and Wild result, ΔG° , the standard free energy change for the decomposition of ZnSiP_2 is zero at $\sim 930^\circ\text{C}$ (negative above). Thus it appears that the Si deposit was due to the decomposition of ZnSiP_2 . The nature of the Si/ ZnSiP_2 interfaces also suggest that decomposition, rather than deposition occurred. It is, of course, a method of obtaining epitaxial Si. The $n-n$ heterojunctions so produced were rectifying.

Curtis and Wild (1970) grew polycrystalline layers of ZnSiP_2 on single crystals of GaP, Si, ZnSiP_2 , and CdSiP_2 substrates in an open-flow system by mixing SiCl_4 , PH_3 , and Zn vapor in H_2 . As indicated above, they noted that ZnSiP_2 could not be prepared at temperatures above 850°C at 1 atm and, as discussed in Section 2.4, reactant vapor pressures of greater than 1 atm are required for the synthesis of ZnSiP_2 at high temperatures.

Since ZnSiP_2 substrates decompose above $\sim 400^\circ\text{C}$, Popov and Pamplin (1972) made use of this fact to deposit Si-rich solid solutions of Si and ZnSiP_2 (5% ZnSiP_2) onto Si by temperature gradient zone melting. In their techniques, Zn and P vapor from a ZnSiP_2 source goes into solution in a low melting alloy drop on the face of a (111) Si substrate, which then is moved along the Si surface by the temperature gradient. The metals used for creating the molten alloy on the surface of Si were Sn, In, Au, Al, Zn, and Ag, and of these, the best solvents were found to be Au and Ag. Of course, the Si- ZnSiP_2 alloy deposit will be saturated with the solvent element.

2.12 Glass Formation in Chalcopyrite Systems

Chalcopyrite glass formation in the II-IV-V₂ systems has been studied extensively, notably by the Russians (CdGeP_2 : Vaipolin *et al.*, 1965a, b; Goryunova *et al.*, 1968a, b; Grigorovici *et al.*, 1968; CdGeAs_2 : Borshchevskii *et al.*, 1967; Abraham *et al.*, 1968; Boltovets *et al.*, 1971; $\text{CdGe(As}_x\text{P}_{1-x})_2$: Borisova *et al.*, 1969; $\text{CdGe}_x\text{Sn}_{1-x}\text{As}_2$, Aksenov *et al.*, 1970a; CdSiAs_2 : Aksenov *et al.*, 1970b; CdGeAs_2 – CdAs , CdGeP_2 – CdP_2 : Goryunova *et al.*, 1971a, b). Insofar as crystal growth of the II-IV-V₂ compounds are concerned, glass formation is not an impediment to successful growth of

TERNARY CHALCOPYRITE SEMICONDUCTORS

CdGeP₂ crystals because the cooling rates from the liquid state required for glass formation are quite high. A cooling rate in excess of 50°C/s is required for CdGeAs₂ (Boltovets *et al.*, 1971), but the growth of large single crystals of this material is difficult (see Section 2.11.2.4). In the case of CdGeP₂ and CdSiAs₂, the optical energy gaps of the crystalline and amorphous forms are sufficiently different that infrared transmission studies are a means for detecting the presence of a glass phase (see Section 7.4). An X-ray study of amorphous CdGeP₂ (Grigorovici *et al.*, 1968) suggested that the short-range ordering of the crystalline phase is essentially preserved in the glassy state.

2.13 Effect of High Pressure and Temperature on Ternary Compounds

The effect of high pressure on the elements crystallizing in the diamond cubic arrangement and several 3–5 and 2–6 compounds having the cubic zincblende or hexagonal wurtzite structure have been extensively investigated in recent years [see the review article by Klement and Jayaraman (1966)]. Pressure-induced phase transformations to denser structures, which in many cases exhibit metallic conductivity, seem to be the rule for these materials.

A limited amount of high-pressure studies have been performed on ternary diamond-like semiconductors. For example, CdSnAs₂, CdGeAs₂, ZnSnAs₂, ZnGeAs₂, and CuFeS₂ have been studied as a function of temperature and pressure up to 40 kbars (Storm *et al.*, 1968). CdSnAs₂ was shown to decompose at elevated temperatures and above 5 kbars to SnAs (cubic NaCl structure), Cd₃As₂, and As. Similarly, CdGeAs₂ exhibited decomposition when quenched from 8 kbar and 700°C. At room temperature, CdSnAs₂ and CdGeAs₂ did not decompose or change structure up to 40 kbars. Cubic ZnSnAs₂ decomposed, whereas ZnGeAs₂ transformed to the cubic ZnS structure. CuFeS₂ decomposes at a pressure of ~2 kbars at elevated temperatures, but does not decompose at room temperature up to 40 kbars. CdSnAs₂ was reported to transform to a disordered cubic NaCl structure and CdGeAs₂ to a disordered tetragonal cell, $a = 4.632 \text{ \AA}$ and $c = 5.307 \text{ \AA}$ (Katzman *et al.*, 1969a, b).

AgInTe₂, CuInTe₂, AgInSe₂, CuInSe₂, and AgInS₂ transform at high pressures to denser phases, which exhibit NaCl or NaCl-like structures, whereas CuInS₂ transforms to a zincblende-type phase (Range *et al.*, 1969).

2.14 Mechanical Behavior of Chalcopyrite Compounds

No quantitative information is available on the mechanical behavior of these compounds which, in general, are brittle at room temperature. Hardness tests, which result in local plastic as well as elastic deformation, are qualitative indicators of cohesive strength. The hardnesses of several chalcopyrite compounds have been determined, and they are shown in Table 2.17. Melting points, as is well known, are also qualitative indicators of cohesion, and these are given in Tables 2.6 and 2.7.

It has been shown that the relative magnitude of the elastic properties of groups of materials exhibiting a specific type of bonding, i.e. covalent, ionic, or metallic, correlate with hardness. For example, the microhardness of covalent, ionic, and metallic crystals have been correlated with several elastic moduli by Chin (1973) and Gilman (1969), and their results are shown in Fig. 2.63. It can be seen that covalently bonded crystals are considerably harder than metals and ionic crystals. Thus, for a given value of the

THE CHALCOPYRITE STRUCTURE AND CRYSTAL GROWTH

TABLE 2.17. Hardness of chalcopyrite crystals

Compound	Microhardness (kg/mm ²)	Compound	Microhardness (kg/mm ²)		
CuAlS ₂	—	AgInSe ₂	230 ± 20 ^b	228 ± 10 ^c	
CuAlSe ₂	—	AgInTe ₂	190 ± 20 ^b		
CuAlTe ₂	—	MgSiP ₂		—	
CuGaS ₂	—	MgGeP ₂		—	
CuGaSe ₂	430 ± 20 ^b 441 ± 5 ^c	ZnSiP ₂	1100 ± 100 ^a		
CuGaTe ₂	360 ± 20 ^b	ZnSiAs ₂	920 ± 20 ^a		
CuInS ₂	—	ZnGeP ₂	980 ± 80 ^a		
CuInSe ₂	260 ± 20 ^b	ZnGeAs ₂	680 ± 10 ^a		
CuInTe ₂	210 ± 20 ^b	ZnSnP ₂	650 ^a		
CuTlS ₂	—	ZnSnAs ₂	455 ± 10 ^a		
CuTlSe ₂	90 ± 20 ^b	ZnSnSb ₂		—	
AgAlS ₂	—	CdSiP ₂		—	
AgAlSe ₂	—	CdSiAs ₂		—	
AgAlTe ₂	—	CdGeP ₂	850 ± 70 ^a		
AgGaS ₂	—	CdGeAs ₂	471 ± 10 ^c	385 ± 5 ^d	380 ± 10 ^d
AgGaSe ₂	450 ± 20 ^b	CdSnP ₂		—	
AgGaTe ₂	180 ± 20 ^b	CdSnAs ₂	395 ± 5 ^a	350 ± 8 ^d	335 ± 3 ^d
AgInS ₂	—				

^a Borshchevskii *et al.* (1967) and references therein.^b Zhuze *et al.* (1958).^c Lerner (1966).^d Osmanov *et al.* (1968).

modulus, the sp^3 semiconductors exhibit the highest hardnesses, or, said in another way, materials having a large covalent component to the bonding will exhibit comparatively larger elastic moduli.

The reader, while examining the data in Table 2.17, should bear in mind that hardness can be an anisotropic property of a crystal. Also, one cannot at this time position these hardness values on Fig. 2.63, but some speculation is perhaps in order. As the atomic number increases, atoms are more polarizable, bonding becomes more "metallic" in character, and it is therefore not surprising to see the I-III-VI₂ compounds exhibiting lower hardnesses than the II-IV-V₂ compounds. Within a given group, the larger the molecular weight, the smaller the hardness. Perhaps Fig. 2.63 can be used to estimate the shear moduli of several of the chalcopyrite phases. For example, from a molecular weight point of view, 2 GaAs \cong ZnGeAs₂, their hardnesses are comparable, and maybe their shear moduli are comparable. Borshchevskii *et al.* (1967) has shown that there exists a qualitative relationship between the hardnesses of the II-IV-V₂ and III-V compounds. For example, the hardness of ZnGeP₂ (980) is nearly the same as 2 GaP (940). Similarly, ZnGeAs₂ (680) exhibits a hardness approximately the same as 2 GaAs (700), and ZnSnP₂ (650) is in between GaP (940) and InP (535).

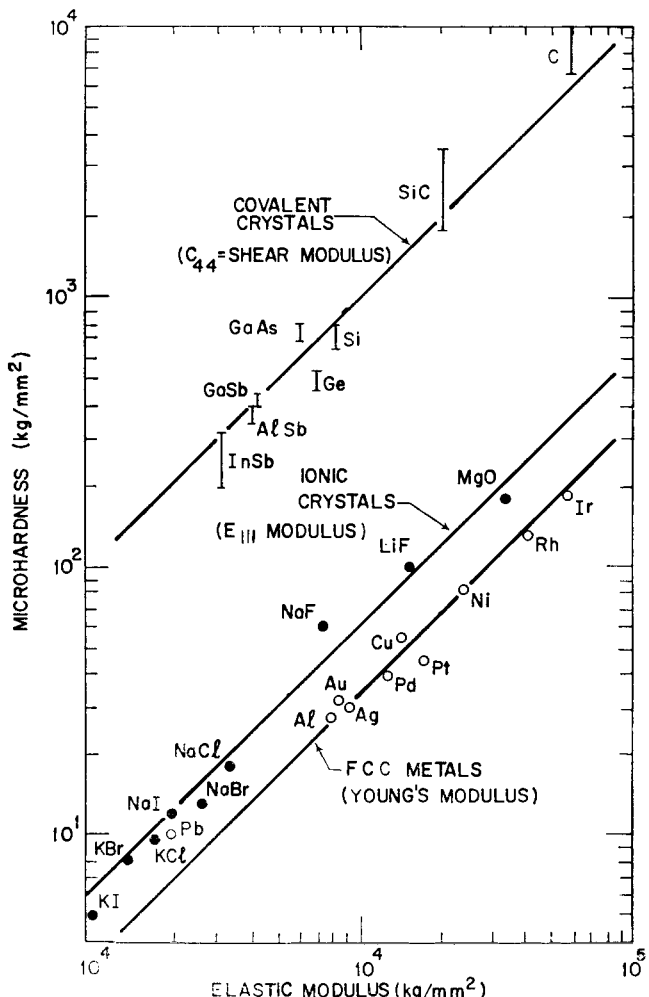


FIG. 2.63. Hardness versus elastic modulus for several FCC metals, essentially covalent crystals, and ionic materials. (After Gilman, 1969, and Chin, 1973.)

References

- ABRAHAMS, S. C., and BERNSTEIN, J. L. (1970) *J. Chem. Phys.* **52**, 11, 5607.
 ABRAHAMS, S. C., and BERNSTEIN, J. L. (1971) *J. Chem. Phys.* **55**, 2, 796.
 ABRAHAMS, S. C., and BERNSTEIN, J. L. (1973a) *J. Chem. Phys.* **59**, 5415
 ABRAHAMS, S. C., and BERNSTEIN, J. L. (1973b) *J. Chem. Phys.* (in press)
 ABRAHAM, A., VORLICEK, V., and ZAVETOVA, M. (1968) *Czech. J. Phys.* **B18**, 958.
 AKOPYAN, I. KH., and ZLALKIN, L. P. (1966) *Dokl. Akad. Nauk SSSR* **168**, 541.
 AKSENOV, V. V., PETROV, V. M., KHAREKHORIN, F. F., and YURSHKIN, B. I. (1970a) *Izv. Akad. Nauk SSSR, Neorgan. Mater.* **6** (4), 826.
 AKSENOV, V. V., PETROV, V. M., and KHAREKHORIN, F. F. (1970b) *Izv. Akad. Nauk SSSR, Neorgan. Mater.* **6** (10), 1881.
 ALEKPEROVA, E. E., VALOV, Y. A., VALOVA, E. A., and USHAKOVA, T. N. (1969a) *Izv. Akad. Nauk SSSR, Inorg. Mater.* **5** N2.

THE CHALCOPYRITE STRUCTURE AND CRYSTAL GROWTH

- ALEKPEROVA, E. E., VALOV, Y. A., GORYUNOVA, N. A., RYVKIN, S. M., and SHPENKOV, G. P. (1969 b) *Phys. Status Solidi* **32**, 49.
- APPLE, E. F. (1958) *J. Electrochem. Soc.* **105**, 251.
- AUSTIN, I. G., GOODMAN, C. H. L., and PENGELLY, A. E. (1956) *J. Electrochem. Soc.* **103**, 609.
- AVERKIEVA, G. K., GORYUNOVA, N. A., PROCHUKAN, V. D., RUD, Y. V., and SERGINOV, M. (1969) *Phys. Status Solidi* **34**, K5.
- AVERKIEVA, G. K., GORYUNOVA, N. A., PROCHUKAN, V. D., and SERGINOV, M. (1970 a) *Akad. Nauk SSSR, Doklady tekh. Fiz.* **191** (4), 811.
- AVERKIEVA, G. K., KARYMSHAKOV, R. K., PROCHUKAN, V. D., and SERGINOV, M. (1970 b) *Fizika tekh. Pol.* **4** (3), 591.
- AVERKIEVA, G. K., GORYUNOVA, N. A., PROCHUKAN, V. D., RUD, Y. V., and SERGINOV, M. (1971) *Phys. Status Solidi* **5**, 571.
- BACHMANN, K. J., BUEHLER, E., and SHAY, J. L. (1973) To be published
- BELOVA, I. K., KOSHKIN, V. M., and PALATNIK, L. S. (1967) *Izv. Akad. Nauk SSSR, Neorgan. Mater.* **3**, 4, 617.
- BERGER, L. I., and PROCHUKAN, V. D. (1969) *Ternary Diamond-like Semiconductors*, Consultants Bureau, New York.
- BERKOVSKII, F. M., GARBUZOV, D. Z., GORYUNOVA, N. A., LOSHAKOVA, G. V., RYVKIN, S. M., and SHPENKOV, G. P. (1968) *Soviet Phys. Semi.* **2** (5), 618.
- BERTOTI, I. (1970) *J. Mater. Sci.* **5**, 1073.
- BERTOTI, I., and SOMOGYI, K. (1971) *Phys. Status Solidi*, **6**, 439.
- BOLTOVETS, N. S., BORSHCHEVSKII, A. S., and OSMANOV, E. O. (1971) *Mater. Sci. Eng.* **7**, 56.
- BORISOVA, Z. U., GORYUNOVA, N. A., KOZLOVA, N. I., OSMANOV, E. O., and RUD, Y. V. (1969) *Soviet Phys. Semi.* **2** (10), 1292.
- BORCHERS, H., and MAIER, R. G. (1963 a) *Metallurg* **8** (17), 775.
- BORCHERS, H., and MAIER, R. G. (1963 b) *Metallurg* **10** (17), 1006.
- BORSHCHEVSKII, A. S., and ROENKOV, N. D. (1969) *Russ. J. Inorg. Chem.* **14** (8), 1183.
- BORSHCHEVSKII, A. S., and ROENKOV, N. D. (1971) *Elektronnaya Tekhnika (Materialy)* **1**, 55.
- BORSHCHEVSKII, A. S., GORYUNOVA, N. A., KESAMANLY, F. P., and NASLEDOV, D. N., (1967) *Phys. Status Solidi* **21**, 9 (this is an excellent review of the status of these compounds up to ~1967).
- BORSHCHEVSKII, A. S., VAIPOLIN, A. A., GORYUNOVA, N. A., and LOSHAKOVA, G. V. (1968) *Izv. Akad. Nauk SSSR, Neorgan. Mater.* **4** (6), 878.
- BOYD, G. D., KASPER, H., McFEE, J. H., and STORZ, F. G. (1972) *IEEE J. Quantum Electr. QE* **8**, 900.
- BRANDT, G., RAUBEN, A., and SCHNEIDER, J. (1973) *J. Phys. Chem. Solids* **34**, 443.
- BUEHLER, E. (1972) Private communication.
- BUEHLER, E., and WERNICK, J. H. (1971) *J. Crystal Growth* **8**, 324.
- BUEHLER, E., and WERNICK, J. H. (1972) NBS Special Publication No. 364, *Solid State Chemistry, Proceedings of the 5th Materials Research Conference, July 1972*, p. 591.
- BUEHLER, E., WERNICK, J. H., and SHAY, J. L. (1971) *Mater. Res. Bull.* **6**, 303.
- BUEHLER, E., WERNICK, J. H., and STORM, A. R. (1972) Unpublished.
- BUEHLER, E., WERNICK, J. H., and WILEY, J. D. (1973) *J. Electr. Mat.* **2**, 445.
- BYCHKOV, A. G., PLECHKO, R. L., VALOV, Y. A., and GORYUNOVA, N. A. (1966) *Izv. Akad. Nauk SSSR, Neorgan. Mater.* **2**, 2078.
- CERVENKA, L., and KASPER, J. (1970) *Czech. J. Phys. B* **20**, 101.
- CHIN, G. Y. (1973) To be published.
- CONGIU, A., GARBATO, L., and MANCA, P. (1973) *Mater. Res. Bull.* **8**, 293.
- COULD, V. M., DAVIES, P. H., HULME, K. F., and ROBERTSON, D. (1970) *J. Phys. C* **3**, L83.
- CURTIS, B. J., and WILD, P. (1970) *Mater. Res. Bull.* **5**, 69.
- ECKERLIN, P. (1961) *Fortschr. Miner.* **39**, 334.
- FISCHER, A. G. (1959) *J. Electrochem. Soc.* **106**, 839.
- FOLBERTH, O. G. (1959) *Z. Naturf.* **14a**, 94.
- FOLBERTH, O. G., and PFISTER, H. (1960) *Acta crystallogr.* **13**, 199.
- FOLBERTH, O. G., and PFISTER, H. (1961) *Acta crystallogr.* **14**, 325.
- FRUEH, A. J. (1950) *J. Am. Miner. Soc.* **35**, 283.
- GASSON, D. B., HOLMES, P. J., JENNINGS, I. C., MARATHE, B. R., and PARROTT, J. E. (1962) *J. Phys. Chem. Solids* **23**, 1291.
- GLAZOV, V. M., MAL'SAGOV, A. V., and KRESTOVNIKOV, A. N. (1970) *Izv. Akad. Nauk SSSR, Neorgan. Mater.* **6**, 143.
- GIESECKE, G., and PFISTER, H. (1961) *Acta crystallogr.* **14**, 1289.

TERNARY CHALCOPYRITE SEMICONDUCTORS

- GILMAN, J. J. (ed.) (1963) *The Art and Science of Growing Crystals*, Wiley, New York.
- GILMAN, J. J. (1969) *Aus. J. Phys.* **13**, 327.
- GOODMAN, C. L. H. (1958) *J. Phys. Chem. Solids* **6**, 305.
- GOODMAN, C. L. H., and DOUGLAS, R. W. (1954) *Physica* **20**, 1107.
- GORDY, W., and THOMAS, W. J. O. (1956) *J. Chem. Phys.* **24**, 439.
- GORYUNOVA, N. A. (1965) *The Chemistry of Diamond-like Semiconductors* (ed. J. C. Anderson), MIT Press, Cambridge, Mass., p. 142.
- GORYUNOVA, N. A., and PARTHÉ, E. (1967) *Mater. Sci. Eng.* **2**, 1.
- GORYUNOVA, N. A., and PROCHUKHAN, V. D. (1960) *Soviet Phys. Solid State* **2**, 161.
- GORYUNOVA, N. A., MAMAEV, S. M., and PROCHUKHAN, V. D. (1962) *Dokl. Akad. Nauk SSSR* **142**, 623.
- GORYUNOVA, N. A., SOKOLOVA, V. I., and BIN-SI, T. (1963a) *Dokl. Akad. Nauk SSSR* **152**, 363.
- GORYUNOVA, N. A., KESAMANLY, F. P., and OSMANOV, E. O. (1963b) *Soviet Phys. Solid State* **5**, 1484.
- GORYUNOVA, N. A., KESAMANLY, F. P., NASELDOV, S. N., and RUD, J. V. (1964) *Soviet Phys. Solid State* **6**, 89.
- GORYUNOVA, N. A., BARANOV, B. V., GRIGORYEVA, V. S., KRADINOVA, L. V., MAKSIMOVA, V. A., and PROCHUKHAN, V. D. (1968a) *Izv. Akad. Nauk SSSR, Neorgan. Mater.* **4**, 7, 1060.
- GORYUNOVA, N. A., RYVKIN, S. M., SHPENIKOV, G. P., TICHINA, I. I., and FEDOTOV, V. G. (1968b) *Phys. Status Solidi* **38**, 489.
- GORYUNOVA, N. A., BELLE, M. L., ZLATKIN, L. B., LOSHAKOVA, G. V., POPLAVNOI, A. S., and CHALDYSHEV, V. A. (1969) *Soviet Phys. Semi.* **2**, 9, 1126.
- GORYUNOVA, N. A., AVSKON, A. V., KARPOVICH, I. A., LEONOV, E. I., and ORLOV, V. M. (1971a) *Phys. Status Solidi* **2**, K117.
- GORYUNOVA, N. A., AVSKON, A. V., KARPOVICH, I. A., LENOV, E. I., and ORLOV, V. M. (1971b) *Proceedings of the International Conference in Physics and Chemistry of Semiconductor Heterojunctions and Layer Structures*, Budapest, p. 2.
- GORYUNOVA, N. A., KUZMENKO, G. S., and OSMANOV, E. O. (1971c) *Mater. Sci. Eng.* **7**, 54.
- GRIGOROVICI, R., MANAILA, R., and VAIPOLIN, A. A. (1968) *Acta crystallogr. B* **24**, 535.
- HAHN, H., FRANK, G., KLINGER, W., MEYER, A.-d., and STÖRGER, G. (1953) *Z. anorg. Chem.* **271**, 153.
- HONEYMAN, W. N. (1969) *J. Phys. Chem. Solids* **30**, 1935.
- HONEYMAN, W. N., and WILKINSON, K. H. (1971) *J. Phys. D: Appl. Phys.* **4**, 1182.
- ISOMURA, S., and MASUMOTO, K. (1972) *Phys. Status Solidi* (a) **13**, 223.
- IVANOVA, I. M., IVANOV, E. K., ZLATKIN, L. B., and PROCHUKHAN, V. D. (1970) *Soviet Phys. Semi.* **3**, 1587.
- KARYMSHAKOV, R. K., and RADUL, V. A. (1970) *Soviet Phys. Semi.* **4** (2), 333.
- KASPER, H. M. (1972) NBS Special Publication No. 364, *Solid State Chemistry, Proceedings of the 5th Materials Research Symposium*, July 1972, p. 671.
- KATZMAN, H., DONOHUE, T., LIBBY, W. F., LUO, H., and HUBER, J. (1969a) *J. Phys. Chem. Solids* **30**, 1609.
- KATZMAN, H., DONOHUE, T., LIBBY, W. F., and LUO, H. (1969b) *J. Phys. Chem. Solids* **30**, 2794.
- KLEMENT, W., Jr., and JAYARAMAN, A. (1966) In *Progress in Solid State Chemistry* (ed. H. Reiss), Pergamon Press, Oxford, pp. 289–376.
- KWAN, C. C. Y., and WOOLLEY, J. C. (1970) *Can. J. Phys.* **48**, 2085.
- LAMBRECHT, V. G. (1972) *Mater. Res. Bull.* **7**, 1411.
- LAMBRECHT, V. G. (1974) *J. Solid State Chem.* in press.
- LAUDISE, R. A. (1970) *The Growth of Single Crystals*, Prentice-Hall.
- LERNER, L. S. (1966) *J. Phys. Chem. Solids* **27**, 1.
- LEROUX-HUGON, P. (1963) *Compl.-Rend.* **256**, 118.
- LEROUX-HUGON, P. (1966) *J. Phys. Chem. Solids* **27**, 1205.
- LIND, M. D., and GRANT, R. W. (1973) *J. Chem. Phys.* **58** (1), 357.
- LOSHAKOVA, G. V., PLECHKOV, R. L., VAIPOLIN, A. A., PAVLOV, B. V., VALOV, Y. A., and GORYUNOVA, N. A. (1966) *Izv. Akad. Nauk SSSR, Neorgan. Mater.* **2**, 1966.
- MASON, D. R., and O'KANE, D. F. (1960) *Proceedings of the International Conference in Semiconductors and Physics, Prague*, p. 1026.
- MASUMOTO, K., and ISOMURA, S. (1965) *J. Phys. Chem. Solids* **26**, 163.
- MASUMOTO, K., ISOMURA, S., and GOTO, W. (1966) *J. Phys. Chem. Solids* **27**, 1939.
- MAUNAYE, M., and LANG, J. (1970) *Mater. Res. Bull.* **5**, 793.
- MUGHAL, S. A., PAYNE, A. J., and RAY, B. (1969) *J. Mater. Sci.* **4**, 895.
- NITSCHE, R. (1967) In *Crystal Growth* (ed. H. S. Peiser), Pergamon Press, Oxford, p. 215.
- OSMANOV, E. O., RUD, Y. V., and STRYALKOVSKII, M. E. (1968) *Phys. Status Solidi* **26**, 85.

THE CHALCOPYRITE STRUCTURE AND CRYSTAL GROWTH

- PALATNIK, L. S., and BELOVA, E. K. (1967) *Izv. Acad. Nauk SSSR, Neorgan. Mater.* **3**, 2194.
- PAMPLIN, B. R. (1960) *Nature* **188**, 136.
- PAMPLIN, B. R. (1964) *J. Phys. Chem. Solids* **25**, 675.
- PAMPLIN, B. R. (1970) *Proceedings of the International Conference on Heterojunctions, Budapest*, I-327.
- PAMPLIN, B. R., and SHAH, J. S. (1965) *Nature* **207**, 180.
- PAMPLIN, B. R., and SHAH, J. S. (1969) *J. Electrochem. Soc.* **116** (11), 1565.
- PANKRATZ, L. B., and KING, G. E. (1970) RI 7435, US Bureau of Mines.
- PARTHÉ, E. (1963) *Z. Kristallogr.* **119**, 204.
- PARTHÉ, E. (1964) *Crystalchemistry of Tetrahedral Structures*, Gordon & Breach, New York.
- PARTHÉ, E. (1972) *Crystalchemistry of Tetrahedral Structures*, Gordon & Breach, New York.
- PARTHÉ, E., YVON, K., and DEITCH, R. H. (1969) *Acta crystallogr. B* **25**, 1164.
- PAULING, L. (1960) *The Nature of the Chemical Bond*, Cornell Univ. Press, Ithaca, New York.
- PFISTER, H. (1963) *Acta Crystallogr.* **16**, 153.
- PHILLIPS, J. C. (1970) *Rev. Mod. Phys.* **42** (3), 317.
- PHILLIPS, J. C. (1973) *Bonds and Bands in Semiconductors*, Academic Press, New York and London.
- POPOV, V. P., and PAMPLIN, B. R. (1972) *J. Cryst. Growth* **15**, 129.
- RABENAU, A., and ECKERLIN, P. (1959) *Naturwissenschaften* **46**, 106.
- RANGE, K.-J., ENGERT, G., and WEISS, A. (1969) *Solid State Commun.* **7**, 1749.
- RAY, B., PAYNE, A. J., and BURRELL, G. J. (1969) *Phys. Status Solidi* **35**, 197.
- ROBBINS, M., and LAMBRECHT, V. G., Jr. (1973) *J. Solid State Chem.* **6**, 402.
- ROBBINS, M., and MIKSOVSKY, M. (1972) *J. Solid State Chem.* **5** (3), 462.
- ROBBINS, M., PHILLIPS, J. C., and LAMBRECHT, V. G., Jr. (1973) *J. Phys. Chem. Solids* **34**, 405.
- RODOT, H. (1960) *Proceedings of the International Conference on Semiconductor Physics, Prague*, p. 1010.
- ROSENBERG, A. J. and STRAUSS, A. J. (1960) *Bull. Am. Phys. Soc.* **5** (1), 83.
- RUBENSTEIN, M. (1966) *J. Electrochem. Soc.* **113**, 623.
- RUBENSTEIN, M., and URE, R. W., Jr. (1968) *J. Phys. Chem. Solids* **29**, 551.
- SCHÄFER, H. (1964) *Chemical Transport Reactions* (translated by H. Frankfort), Academic Press, New York.
- SCHLEGEL, H., and SCHULLER, A. (1952) *Z. Metallk.* **43**, 421.
- SHAY, J. L., BUEHLER, E., and WERNICK, J. H. (1971) *Phys. Rev. B* **3**, 2004.
- SHAY, J. L., BACHMANN, K. J., BUEHLER, E., and WERNICK, J. H. (1973a) *Appl. Phys. Lett.* **23**, 226.
- SHAY, J. L., TELL, B., KASPER, H., and SCHIAVONE L. M. (1973b) *Phys. Rev. B* **7**, 4485.
- SOMOGYI, K., and BERTOTI, I. (1972) *Jap. J. Appl. Phys.* **11**, 103.
- SPRINGTHORPE, A. J., and HARRISON, J. G. (1969) *Nature* **222**, 977.
- SPRINGTHORPE, A. J., and PAMPLIN, B. R. (1968) *J. Cryst. Growth* **3**, 313.
- SPRINGTHORPE, A. J., HARVEY, R. J., and PAMPLIN, B. R. (1969) *J. Cryst. Growth* **6**, 13.
- STORM, A. R., JAYARAMAN, A., and WERNICK, J. H. (1968) *J. Phys. Chem. Solids* **29**, 623.
- STRUNZ, H., GEIER, G. H., and SEELINGER, E. (1968) *Neues Jb. Miner. Mk.* **11-12**, 241.
- TELL, B., SHAY, J. L., and KASPER, H. M. (1971) *Phys. Rev. B* **4**, 2463.
- TELL, B., SHAY, J. L., and KASPER, H. M. (1972) *J. Appl. Phys.* **43**, 2469.
- TIETJEN, J. J., and AMICK, J. A. (1966) *J. Electrochem. Soc.* **113**, 724.
- TRYKOZKO, R., and GORYUNOVA, N. A. (1968) *Izv. Akad. Nauk SSSR, Neorgan. Mater.* **4** (12), 2101.
- VAIPOLIN, A. A., GASHIMZADE, F. M., GORYUNOVA, N. A., KESAMANLY, F. P., NASLEDOV, D. N., OSMANOV, E. O., and RUD, J. V. (1964a) *Izv. Akad. Nauk SSSR, Fiz.* **28**, 1085.
- VAIPOLIN, A. A., GORYUNOVA, N. A., OSMANOV, E. O., RUD, J. V., and TRETIAKOV, D. N. (1964b) *Dokl. Akad. Nauk SSSR*, **154**, 116 (*Proc. Acad. Sci. USSR, Chem. Sect.* **154**, 146).
- VAIPOLIN, A. A., GORYUNOVA, N. A., OSMANOV, E. O., and RUD, J. V. (1965a) *Dokl. Akad. Nauk SSSR* **160**, 633.
- VAIPOLIN, A. A., OSMANOV, E. O., and TRETIAKOV, D. N. (1965b) Report of the XX International Congress on Theoretical and Applied Chemistry, Yupak, Moscow (proceedings never published).
- VAIPOLIN, A. A., OSMANOV, E. O., and Tretiakov, D. N. (1967) *Izv. Akad. Nauk SSSR, Neorgan. Mater.* **2**, 1876.
- VAIPOLIN, A. A., GORYUNOVA, N. A., KLESHCHINSKI, L. I., LOSHAKOVA, G. V., and OSMANOV, E. O. (1968) *Phys. Status Solidi* **29**, 435.
- VAIPOLIN, A. A., KRADINOVA, L. V., and PROCHUKHAN, V. D. (1971) *Soviet Phys.-Cryst.* **15** (4), 703.
- VALOV, Y. A. (1969) *Izv. Akad. Nauk SSSR, Neorgan. Mater.* **5**, 2115.
- VALOV, Y. A., and PLECHKO, R. L. (1968a) *Izv. Akad. Nauk SSSR, Neorgan. Mater.* **4**, 701.

TERNARY CHALCOPYRITE SEMICONDUCTORS

- VALOV, Y. A. and PLECHKO, R. L. (1968b) *Izv. Akad. Nauk SSSR, Neorgan. Mater.* **4**, 993.
VALOV, Y. A. and USHAKOVA, T. N. (1968) *Izv. Akad. Nauk SSSR, Neorgan. Mater.* **4** (7), 1054.
VALOV, Y. A., GORYUNOVA, N. A., LEONOV, E. I., and ORLOV, V. M. (1973) *Acta Phys. hung.* **33**, 1.
VAN VECHTEN, J. A., and PHILLIPS, J. C. (1970) *Phys. Rev.* **2B**, 2160.
VOITSEKHOVSKY, A. V. (1964) *Ukr. fiz. Zh.* **9**, 796.
WAGNER, S., SHAY, J. L., TELL, B., and KASPER, H. M. (1973) *Appl. Phys. Lett.* **22**, 351.
WILEY, J. D., BUEHLER, E., SHEY, J. L., and WERNICK, J. H. (1973) *J. Electronic Materials* **2**, 601.
WOOLLEY, J. C., and WILLIAMS, E. W. (1966) *J. Electrochem. Soc.* **113**, (9), 899.
YAMAMOTO, N., and MIYAUCHI, T. (1972) *Jap. J. Appl. Phys.* **11**, 1383.
ZHUZE, V. P., SERGEEVA, V. M., and SHTRUM, E. L. (1958) *Soviet Phys. Tech. Phys.* **3** (10), 1925.

CHAPTER 3

ELECTRONIC STRUCTURE OF II-IV-V₂ COMPOUNDS

3.1 Theoretical Concepts

We have emphasized in Chapter 2 that II-IV-V₂ chalcopyrite semiconductors are the simplest structural analogs of III-V zincblende compounds. It is natural, therefore, to expect that the energy band structure of a ternary compound is related to that of its binary analog, and we shall take such an approach in the present discussion. From the chalcopyrite primitive cell in Fig. 2.1 (p. 6) it is apparent that, although the atomic site positions are virtually the same as for the zincblende structure, there are three inequivalent noncubic aspects of this structure: (1) a compression of the crystal lattice along the z-axis ($c < 2a$), (2) a distortion of the anion sites away from the $(\frac{1}{4}, \frac{1}{4}, \frac{1}{4})$ and symmetrically related positions, and (3) a doubling of the unit cell in the z-direction resulting from an ordering of the two cations. This approach has proven useful since it turns out that the direct energy gaps in II-IV-V₂ compounds are very close (± 0.3 eV) to the energy gaps in the respective binary analogs. Furthermore, it also happens that the lifting of the degeneracy of the direct energy gaps is dominated by the noncubic potential associated with the built-in lattice compression. Hence the concept of a binary-ternary analogy of electronic properties has meaning. Analysis of the band structure at energies above the direct energy gap is not so simple, however, and requires inclusion of all three of the noncubic potentials listed above.

Pursuing this analogy further, the simplest approximation to the energy band structure of a ternary compound is obtained by imbedding the band structures of the zincblende binary analog into the chalcopyrite Brillouin zone. A comparison of the Brillouin zones is shown in Fig. 3.1. Since the volume of the unit cell of the chalcopyrite lattice is 4 times greater than that of zincblende, the Brillouin zone is 4 times smaller. Consequently, there is a 4-to-1 mapping of energy levels in the zincblende Brillouin zone into that of chalcopyrite. Some typical examples of the correspondence between the high-symmetry points in the respective Brillouin zones are the following (Chaldyshev and Pokrovskii, 1960, 1963; Karavaev and Poplavnoi, 1966; Karavaev *et al.*, 1968):

$$\begin{aligned} I(0, 0, 0), X(0, 0, 2\pi/a), W(0, 2\pi/a, \pi/a), W(2\pi/a, 0, \pi/a) &\rightarrow I(0, 0, 0), \\ L(\pi/a, -\pi/a, -\pi/a), \Sigma(\pi/a, \pi/a, 0) &\rightarrow N(\pi/a, \pi/a, 0), \\ X(0, 2\pi/a, 0), X(2\pi/a, 0, 0), \Delta(0, 0, \pi/a) &\rightarrow T(0, 0, \pi/a). \end{aligned} \tag{3.1}$$

Qualitatively, the band structures fall into two distinct classes corresponding to ternary compounds for which the binary analogs have direct or indirect bandgaps respectively. Examples of theoretical calculations for ZnGeAs₂ (the analog of GaAs) and ZnGeP₂ (the analog of GaP) are shown in Figs. 3.2 and 3.3 (Shileika, 1973). For these cal-

TERNARY CHALCOPYRITE SEMICONDUCTORS

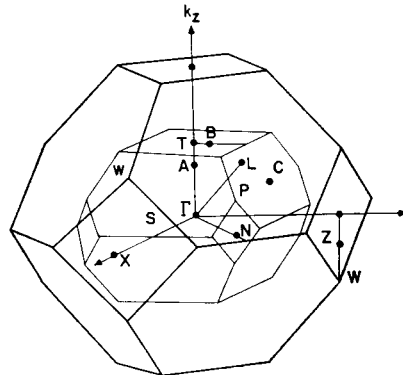


FIG. 3.1. Comparison of the Brillouin zones of the zincblende and chalcopyrite lattices.

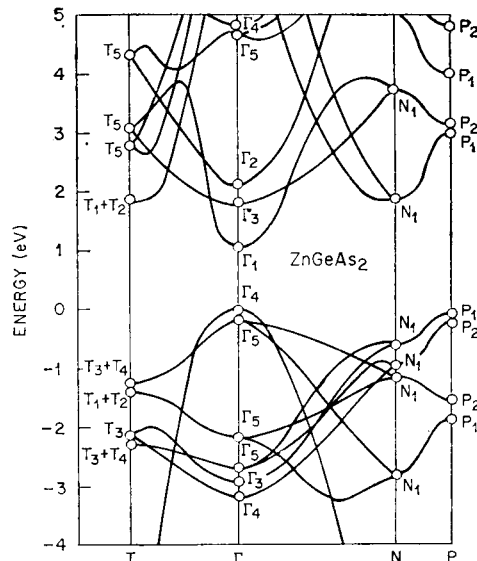


FIG. 3.2. Approximation to the band structure of ZnGeAs_2 obtained by imbedding the band structure of GaAs into the chalcopyrite Brillouin zone. (Shileika, 1973.)

culations, the effects of spin-orbit interaction have been omitted. The energy levels were calculated at high symmetry points Γ , T , N , and P of the chalcopyrite Brillouin zone, and lines were drawn between calculated energy levels taking into account the compatibility relations. As expected for the ternary analog of GaAs, ZnGeAs_2 has a direct energy gap at the center of the Brillouin zone Γ . The lowest conduction band Γ_1 corresponds to the Γ_1 conduction band of GaAs and is approximately isotropic. Our symmetry notation follows that of Koster *et al.* (1963). The triple degeneracy of the valence band in GaAs (Γ_{15}) is lifted in ZnGeAs_2 such that a nondegenerate level Γ_4

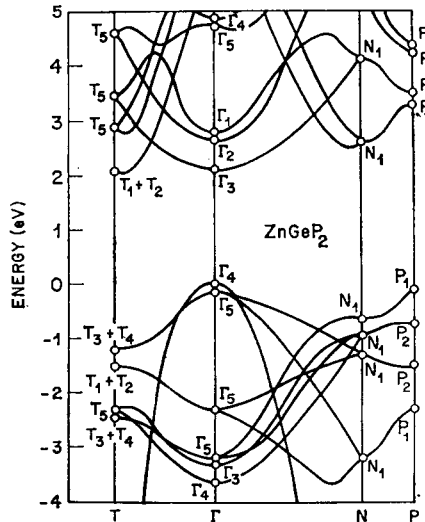


FIG. 3.3. Approximation to the band structure of ZnGeP_2 obtained by imbedding the band structure of GaP into the chalcopyrite Brillouin zone. (Shileika, 1973.)

lies above a doubly degenerate level Γ_5 . The higher conduction band minima Γ_3 and $T_1 + T_2$, Γ_2 and T_5 , and N_1 are derived from the minima X_1 , X_3 , and L_1 in zincblende respectively. According to theoretical calculations (and intuition) CdSnAs_2 , CdGeAs_2 , ZnSnAs_2 , ZnGeAs_2 , CdSnP_2 , CdSiAs_2 , ZnSnP_2 , and CdGeP_2 have such a conduction band structure.

The energy band structure of ZnGeP_2 is especially interesting since the binary analog GaP has an indirect energy gap, $\Gamma_{15} \rightarrow X_1$. The three equivalent X points in GaP map into two inequivalent points in ZnGeP_2 , Γ , and T [eq. (3.1)]. The conduction band minimum Γ_3 has been mapped from the X point $(0, 0, 2\pi/a)$ in zincblende. Its effective masses are highly anisotropic, $m_{||}(\Gamma_3) > m_{\perp}(\Gamma_3)$, where the subscript denotes the orientation of the energy surface relative to the z-axis. The minimum $T_1 + T_2$ has been mapped from the two X points in zincblende $(2\pi/a, 0, 0)$ and $(0, 2\pi/a, 0)$, and the opposite anisotropy of the effective masses occurs $m_{||}(T_1 + T_2) < m_{\perp}(T_1 + T_2)$. It is not obvious off-hand whether the conduction band at Γ or at T will lie at lower energy. If the energy level Γ_3 is the lowest conduction band, we have the interesting situation that the ternary compound has a direct energy gap whereas the binary analog has an indirect energy gap. We have designated these new direct energy gaps as "pseudo-direct", since they will manifest characteristics of direct energy gaps to the extent that the pseudopotentials of the two cations in the ternary compound are different. If the pseudopotentials of the two different cations are essentially the same, the optical and electronic properties of the ternary compound near the lowest energy gap will be indistinguishable from those of an indirect bandgap even though the lowest gap is direct in principle. The compounds ZnSiAs_2 , ZnGeP_2 , ZnSiP_2 , and CdSiP_2 are expected to have energy band structures similar to that of ZnGeP_2 .

3.2 Lowest Direct Energy Gaps

3.2.1 Experimental Results

The structure of the lowest direct energy gaps in the II–IV–V₂ compounds has been most clearly elucidated experimentally by electroreflectance measurements. In Fig. 3.4 we compare the electrolyte electroreflectance spectra of CdSnP₂ to that of InP, its binary analog. The electroreflectance experimental techniques are thoroughly described by Cardona (1969). The CdSnP₂ spectra were measured respectively for light polarized parallel and perpendicular to the optic axis, and show three peaks labeled *A*, *B*, and *C* close in energy to the spin-orbit split E₀ and E₀ + Δ₀ peaks in InP. The E₀ and E₀ + Δ₀ transitions in InP result from spin-orbit splitting of transitions from the *p*-like Γ₁₅ valence band to the *s*-like Γ₁ conduction band. We conclude, therefore, that the *A*, *B*, and *C* transitions in CdSnP₂ are derived from the lowest direct bandgap of InP and result from transitions to the conduction band from three closely spaced valence bands. The triple degeneracy of the *p*-like valence bands is completely removed in a chalcopyrite crystal due to the simultaneous effects of the noncubic crystalline field and spin-orbit interaction.

The model relating the lowest direct energy gaps in CdSnP₂ and InP is shown in Fig. 3.5. In passing from zincblende to chalcopyrite, the Γ₁₅ valence band splits into a nondegenerate level Γ₄ lying above a doubly degenerate Γ₅. Transitions from the Γ₄ valence band to the Γ₁ conduction band are allowed only for E ∥ z, and Γ₅ → Γ₁ transitions are allowed only for E ⊥ z. With the inclusion of spin-orbit interaction, the Γ₅ valence band splits into Γ₇ and Γ₆ levels, and the polarization selection rules are somewhat relaxed. The ordering of the Γ₆ and Γ₇ levels in Fig. 3.5 was originally chosen to be compatible with the symmetries of spin-orbit split levels in the absence of a crystal-field splitting. The resulting ordering agrees with experiment since the *B* peak is only observed for E ⊥ z (Fig. 3.4) as expected for a Γ₆ → Γ₆ transition. The electroreflectance spectra of many compounds have been obtained on (112) facets which tend to be highly developed during growth. A typical spectrum is shown in Fig. 3.6 for CdSiAs₂, a ternary analog of GaAs. For this orientation E ∥ z is only nominal, and at most two-thirds of the intensity is along the optic axis. Hence the *B* peak appears for E ∥ z with an apparent strength one-third of that for E ⊥ z even though Γ₆ → Γ₆ transitions are not allowed for E ∥ z. Similar electroreflectance spectra for ZnGeAs₂ and CdGeAs₂ are shown in Fig. 3.7.

Hopfield (1960) has discussed a model for the splitting of *p*-like levels in a nearly cubic crystal, including both the effects of a noncubic crystalline field and spin-orbit interaction. Within this so-called, quasicubic model, the energies of the Γ₇ levels relative to the Γ₆ level in the valence band of a chalcopyrite crystal are given by

$$E_{1,2} = -\frac{1}{2}(\Delta_{so} + \Delta_{cf}) \pm \frac{1}{2} \left[(\Delta_{so} + \Delta_{cf})^2 - \frac{8}{3}\Delta_{so}\Delta_{cf} \right]^{1/2} \quad (3.2)$$

Here Δ_{so} is the spin-orbit splitting of the valence bands in a cubic field, and Δ_{cf} is the crystal-field splitting of the valence bands in the absence of spin-orbit interaction. The diagonalization of the Hamiltonian matrix giving the eigenvalues in eq. (3.2) also yields wavefunctions from which polarization intensity ratios can be determined. The ratio of

ELECTRONIC STRUCTURE OF II-IV-V₂ COMPOUNDS

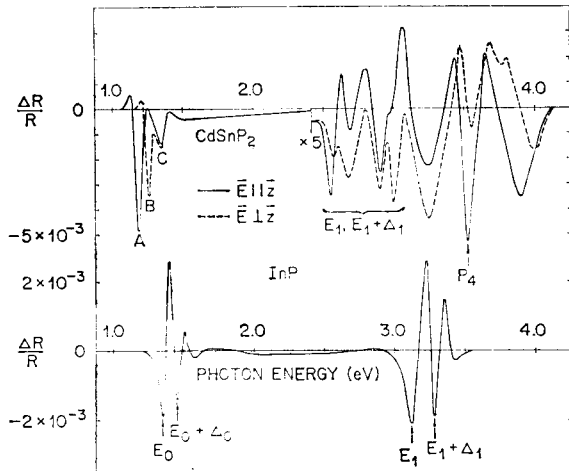


FIG. 3.4. Comparison of the room-temperature electrolyte electro-reflectance spectrum of a (112) platelet of CdSnP₂ and that of its binary analog InP. (Shay *et al.*, 1970 b.)

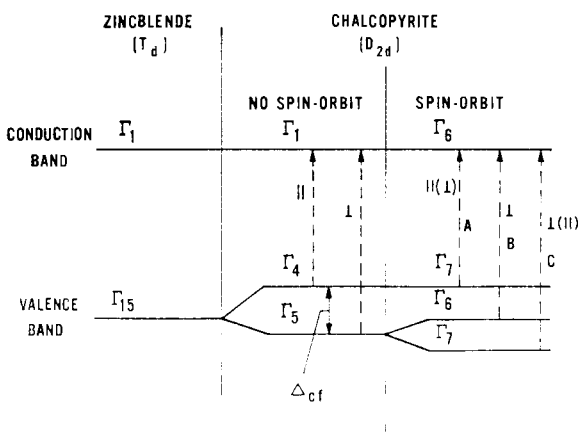


FIG. 3.5. Band structure and selection rules for the transitions in a chalcopyrite crystal derived from the $\Gamma_{15} \rightarrow \Gamma_1$ energy gap in a zinc-blende crystal. (Shay *et al.*, 1970 a.)

TERNARY CHALCOPYRITE SEMICONDUCTORS

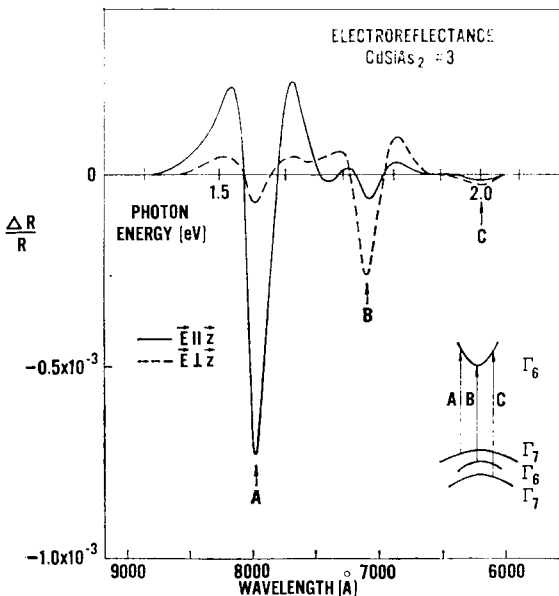


FIG. 3.6. Room-temperature electrolyte electroreflectance spectrum of a (112) platelet of CdSiAs_2 near the direct energy gap. (Shay and Buehler, 1971 b.)

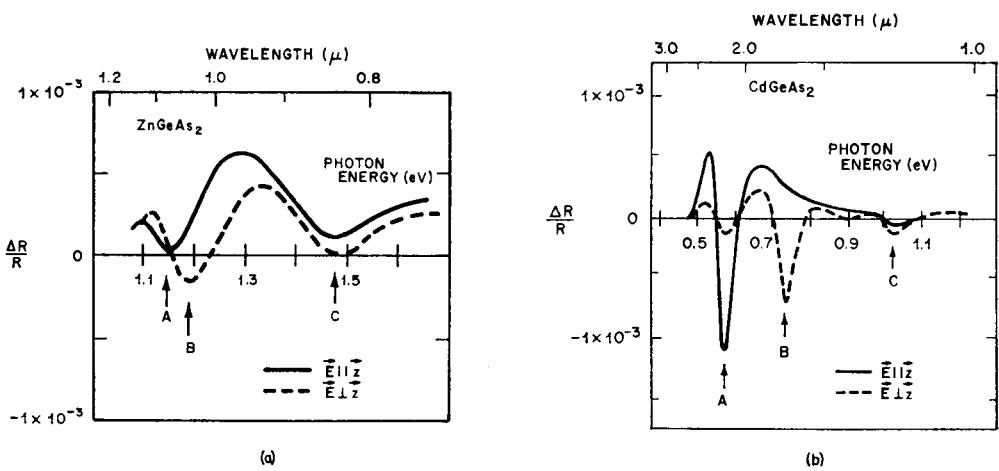


FIG. 3.7. Electroreflectance spectrum of (a) ZnGeAs_2 and (b) CdGeAs_2 . (Shileika, 1973.)

the strengths of transitions from a given Γ_7 valence band to the Γ_6 conduction band for light polarized, respectively, parallel or perpendicular to the optic axis is given by

$$I_{\parallel}/I_{\perp} = (2 + 3 E/\Delta_{so})^2, \quad (3.3)$$

where E is given by eq. (3.2). Equation (3.2) has been used to deduce the valence band parameters of many II-IV-V₂ crystals from electroreflectance measurements and the results are summarized in Table 3.1. By convention, a positive spin-orbit (or crystal

TABLE 3.1. A , B , and C energy gaps, and values of crystal-field (Δ_{cf}) and spin-orbit (Δ_{so}) parameters of the valence bands of II-IV-V₂ chalcopyrite crystals at room temperature

Compound	$2 - \frac{c}{a}$	Energy gaps (eV)			- Δ_{cf} (eV)		Δ_{so} (eV)		References
		A	B	C	Expt.	Theory ^a	Expt.	Theory ^b	
ZnSiP ₂	0.067	2.96	3.06	—	0.27	—	0.07	c	
ZnSiAs ₂	0.057	2.12	2.22	2.47	0.13	0.20	0.28	0.29	d
ZnGeP ₂	0.040	2.34	2.40	2.48	0.08	0.05	0.09	0.11	c
ZnGeAs ₂	0.034	1.15	1.19	1.48	0.06	0.18	0.31	0.34	e
ZnSnP ₂	0	1.66	1.66	1.75	0	0.08	0.09	0.16	f
ZnSnAs ₂	0	0.73	0.73	1.07	0	0.04	0.34	0.42	g
CdSiP ₂	0.163	2.45	2.75	—	0.56	—	0.09	e, h	
CdSiAs ₂	0.151	1.55	1.74	1.99	0.24	0.29	0.29	0.33	i
CdGeP ₂	0.123	1.72	1.90	1.99	0.20	0.14	0.11	0.13	j
CdGeAs ₂	0.112	0.57	0.73	1.02	0.21	0.25	0.33	0.37	e
CdSnP ₂	0.048	1.17	1.25	1.33	0.10	0.14	0.10	0.18	k
CdSnAs ₂	0.044	0.26	0.30	0.77	0.06	—	0.48	0.44	l

^a Poplavnoi *et al.* (1969); Goryunova *et al.* (1970a).

^b Hubner and Unger (1972).

^c Shay *et al.* (1973).

^d Shay *et al.* (1971a).

^e Shileika (1973).

^f Krivaite *et al.* (1972).

^g Kwan and Woolley (1971a).

^h Thermoreflectance at 120 K.

ⁱ Shay and Buehler (1971b).

^j Shay *et al.* (1971b).

^k Kavaliauskas *et al.* (1971a); Shay *et al.* (1970a, b).

^l Values of A and B from absorption data of Sikkharulidze and Ukhanov (1968); C from Karavaev *et al.* (1972).

field) parameter lifts the triple degeneracy of p -levels (Γ_{15}) such that the doubly degenerate level is higher in energy than the nondegenerate level. Equations (3.2) and (3.3) differ slightly from others given elsewhere due to our choice of energy scale in which the positive energy direction is the same for valence and conduction band levels.

3.2.2. Quasicubic Model

Although we have seen in Section 3.1 that there are three inequivalent noncubic aspects of the chalcopyrite structure, it has been found that the crystal-field splitting Δ_{cf} of the valence bands in II-IV-V₂ crystals is dominated by the noncubic potential

TERNARY CHALCOPYRITE SEMICONDUCTORS

associated with the built-in lattice compression of as much as several per cent along the z -axis. For example, where InP compressed along the (001) axis sufficiently to achieve the distortion inherent in CdSnP₂, the crystal-field splitting of the valence band maximum would be given by

$$\Delta_{cf} = \frac{3}{2} b(2 - c/a), \quad (3.4)$$

where b is the deformation potential for InP. Using the experimental deformation potential for InP (Gavini and Cardona, 1970) and the lattice constants of CdSnP₂ from Chapter 2, eq. (3.4) predicts $\Delta_{cf} = -0.12$ eV for CdSnP₂, as compared with the observed value of -0.10 eV.

We have plotted in Fig. 3.8 the experimental crystal-field parameters Δ_{cf} for several II-IV-V₂ compounds as a function of their respective lattice distortions. The straight line drawn through the data is consistent with eq. (3.4) for $b = -1.2$. Experimental deformation potentials for III-V compounds cluster about -1.5 , although different measurement techniques result in values differing by as much as a factor of 2 (Gavini and Cardona, 1970; Yu *et al.*, 1971). The noticeable correlation between Δ_{cf} and $2 - c/a$ in Fig. 3.8, as well as the agreement between the average deformation potential $b = -1.2$ deduced from Fig. 3.8 and the experimental values for III-V compounds, is convincing evidence that the built-in uniaxial compression is the dominant noncubic potential insofar as the uppermost valence bands are concerned.

Although ZnSnAs₂ crystallizes in the chalcopyrite structure, it has no compressive

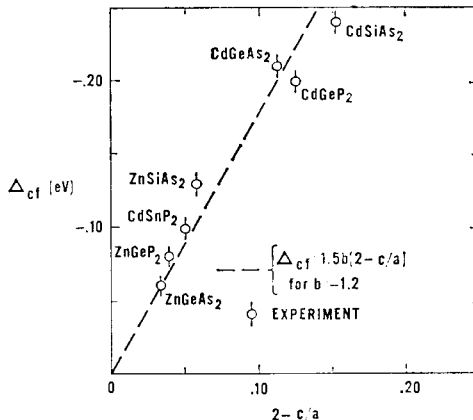


FIG. 3.8. Plot of experimental crystal field parameters Δ_{cf} versus the respective compressive lattice distortions, $2 - c/a$. The dashed curve corresponds to a uniaxial deformation potential $b = -1.2$.

distortion, i.e. $c/a = 2.00$. The absence of any splitting of the A, B doublet in the electroreflectance spectrum in Fig. 3.9 is consistent with the conclusion just given that Δ_{cf} is dominated by $2 - c/a$ in II-IV-V₂ compounds.

The spin-orbit parameters observed in II-IV-V₂ compounds are in all cases close to the spin-orbit splittings observed in the binary analogs. For example, $\Delta_{so}(ZnGeP_2) = 0.09$ eV is to be compared with $\Delta_{so}(GaP) = 0.10$ eV; and $\Delta_{so}(ZnGeAs_2) = 0.31$ eV is to be compared with $\Delta_{so}(GaAs) = 0.34$ eV. In summary, then, the "quasicubic" model suggests that the uppermost valence bands of a ternary compound are basically the same as those which would be observed in the binary analog were the binary analog strained to achieve the lattice distortion present in the ternary compound.

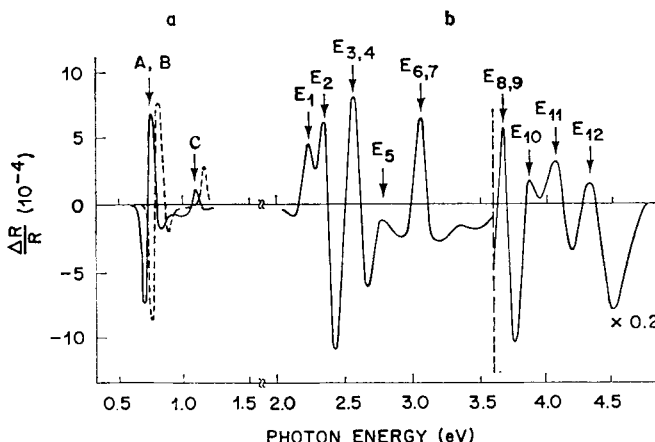


FIG. 3.9. Electroreflectance spectrum of ZnSnAs₂ (chalcopyrite structure) at 295 K (solid curve) and at 77 K (dashed curve): (a) dry-sandwich method; (b) electrolyte method. (Krivaite *et al.*, 1971.)

The results of theoretical calculations of A_{ef} and A_{so} are also included in Table 3.1. It can be seen that these more sophisticated calculations do not achieve a better representation of the observed band structure than does the quasicubic model.

It is apparent in Fig. 3.4 that the lowest energy transition (peak *A*) is polarized $\mathbf{E} \parallel \mathbf{z}$, opposite to the polarization dependence observed in the tetrahedrally coordinated wurtzite semiconductors such as CdS. This behavior was recognized early (Shay *et al.*, 1970a), and led to the proposal that the crystal-field splitting of the valence bands of II-IV-V₂ compounds was negative, i.e. opposite in sign to that observed in wurtzite II-VI compounds. It was later shown (Rowe and Shay, 1971; Shay, 1972a, b) that this negative crystal-field splitting is a natural consequence of the very large built-in compressive distortion of the lattice constants of these ternary compounds as just discussed. On the other hand, the lattice constants of the wurtzite crystals such as CdS are very nearly ideal, and the (smaller) crystal-field splitting of the valence bands is dominated by phenomena other than lattice compression.

It has been found that eq. (3.3) provides a quantitative explanation of the polarization properties observed in II-IV-V₂ compounds. For example, using the valence band parameters in Table 3.1, eq. (3.3) predicts that $I_{\parallel}/I_{\perp} \sim 20$ and 8.5 for the *A* peak in CdSnP₂ and ZnSiAs₂ respectively. These values are in good agreement with the data in Figs. 3.4 and 3.14.

3.2.3 Band Structure Near $\mathbf{k} = 0$

Kildal (1972) has generalized the Kane (1957) theory of energy band structure near $\mathbf{k} = 0$ to the ternary chalcopyrite compounds by including in the Hamiltonian a \mathbf{k} -independent crystal-potential anisotropy adjusted to reproduce the experimentally observed valence band splittings at $\mathbf{k} = 0$. At $\mathbf{k} = 0$ the energies are E_c , E_1 , 0, and E_2 , where E_c is the energy of the conduction band relative to the Γ_6 valence band, and E_1 and E_2 are given by eq. (3.2). E_1 is therefore the energy of the highest lying valence band, and the bandgap energy is $E_g = E_c - E_1$. To second order in \mathbf{k} the energies of

TERNARY CHALCOPYRITE SEMICONDUCTORS

the conduction and valence bands are given by

$$\begin{aligned}
 E_c &= E_g + E_1 + \frac{\hbar^2 k^2}{2m} + \frac{(k_z P)^2(E_g + E_1 + 2\Delta_{so}/3)}{E_g(E_g + E_1 - E_2)} \\
 &\quad + \frac{(k_x^2 + k_y^2)P^2}{E_g + E_1} \left[1 - \frac{(\Delta_{so}/3)(E_g + E_1 + \Delta_{cf})}{E_g(E_g + E_1 - E_2)} \right] \\
 E_{v_1} &= E_1 + \frac{\hbar^2 k^2}{2m} - \frac{(k_z P)^2(E_1 + 2\Delta_{so}/3)}{E_g(E_1 - E_2)} + \frac{(k_x^2 + k_y^2)P^2(E_1 + \Delta_{cf})\Delta_{so}}{3E_1E_g(E_1 - E_2)} \\
 E_{v_2} &= \frac{\hbar^2 k^2}{2m} - \frac{1}{2} \frac{(k_x^2 + k_y^2)P^2}{E_g + E_1}, \\
 E_{v_3} &= E_2 + \frac{\hbar^2 k^2}{2m} + \frac{(k_z P)^2(E_2 + 2\Delta_{so}/3)}{(E_1 - E_2)(E_g + E_1 - E_2)} \\
 &\quad - \frac{(k_x^2 + k_y^2)P^2(E_2 + \Delta_{cf})\Delta_{so}}{3E_2(E_g + E_1 - E_2)(E_1 - E_2)}
 \end{aligned} \tag{3.5}$$

These equations give the energy splittings and the effective masses of the four bands excluding the effects of higher lying bands. The matrix element P is nearly constant for all III-V compounds that can be described by Kane's theory. Within 20% Ehrenreich (1961) finds

$$P^2 = \frac{\hbar^2}{2m} \times (20 \text{ eV}). \tag{3.6}$$

Close to $\mathbf{k} = 0$ the energy bands are of the form

$$E = E_0 \pm \frac{\hbar^2}{2} \left(\frac{k_x^2 + k_y^2}{m_T} + \frac{k_z^2}{m_L} \right) \tag{3.7}$$

where the plus and minus signs refer to the conduction and valence bands respectively. In eq. (3.7) m_T and m_L define the transverse and the longitudinal effective masses. We can use them to define a density of states effective mass m_d ,

$$m_d^3 = m_L m_T^2, \tag{3.8}$$

and a conductivity effective mass m_σ ,

$$\frac{1}{m_\sigma} = \frac{1}{3} \left(\frac{1}{m_L} + \frac{2}{m_T} \right) \tag{3.9}$$

In Table 3.2 we list the effective masses calculated for several II-IV-V₂ crystals using Kildal's theory, the valence band parameters in Table 3.1, and assuming that the value of P^2 given in eq. (3.6) for III-V compounds can be used for the ternaries. For the sake of numerical consistency, the values of E_1 and E_2 used in eq. (3.5) were calculated from eq. (3.2) for given Δ_{so} and Δ_{cf} . The effective masses for CdGeAs₂ differ slightly from Kildal's (1972) due to our use of experimental values for the valence band splittings from Table 3.1. Some of the larger masses in Table 3.2 are probably inaccurate since they can only be determined accurately by considering the effects of higher bands

since they receive very little contribution from the conduction band interaction. There is no contribution to the m_L value for valence band v_2 within this model. Figure 3.10a shows the expected band structure of CdGeAs₂ near $\mathbf{k} = 0$. The highest valence band (v_1) has a smaller longitudinal but a larger transverse effective mass than does the v_2 band.

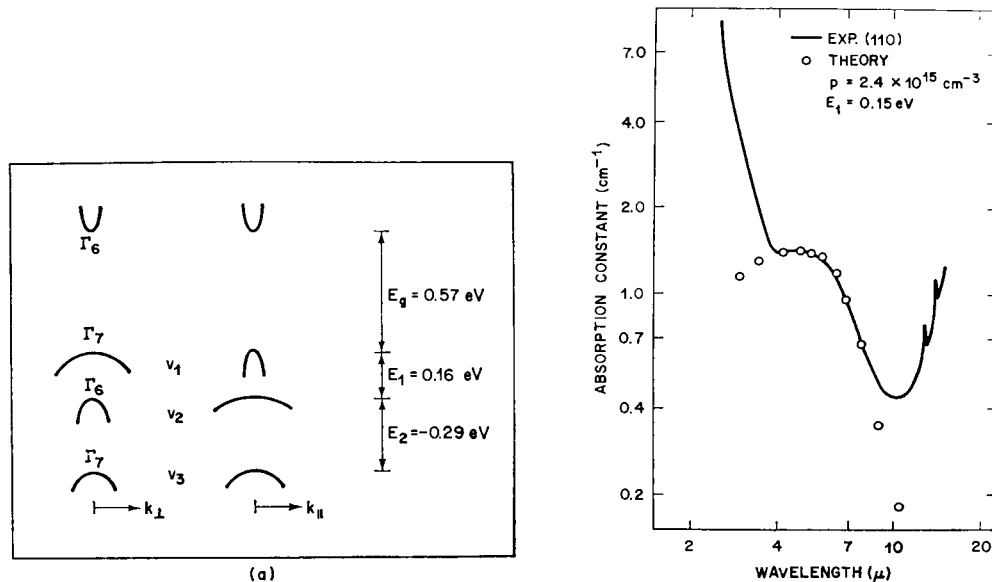


FIG. 3.10. (a) Band structure of CdGeAs₂ near $\mathbf{k} = 0$. (b) Absorption coefficient in *p*-CdGeAs₂. (After Kildal, 1972; Mamedov and Osmanov, 1971.)

Experimental values of the effective masses are available for a few compounds and are summarized in Chapter 7. Infrared plasma reflection and thermoelectric power measurements result in an effective electron mass in CdGeAs₂ ~ 0.03 times the free electron mass. This value is in remarkably good agreement with the calculated mass of $0.036 m_0$ in Table 3.2. The hole effective mass in CdGeAs₂ was found to be $0.3 m_0$ from thermoelectric power measurements. This value agrees surprisingly well with the calculated density of states effective mass of $0.25 m_0$ in Table 3.2. From measurements of the plasma reflection spectrum of CdSnAs₂ using polarized light, Karymshakov *et al.* (1970) determined a conduction-band mass anisotropy $m_L/m_T \sim 0.8$ for a free electron concentration of $5 \times 10^{18} \text{ cm}^{-3}$. Although the nonparabolicity of the conduction band at this carrier concentration (see Fig. 7.16, p. 187) precludes a direct comparison with the values in Table 3.2 calculated at $\mathbf{k} = 0$, the sense of the observed anisotropy agrees with the theoretical prediction. From all of these results it can be concluded that Kildal's generalization of the Kane model gives an adequate description of the band structure near $\mathbf{k} = 0$ in CdGeAs₂ and CdSnAs₂, and should also work well for the other chalcopyrites.

Kildal (1972) has calculated the spectral dependence of the intervalence band absorption in chalcopyrite crystals using the theoretical band structure just described. In Fig. 3.10b we show Kildal's fit of the theory to the absorption coefficient measured in *p*-CdGeAs₂. From this comparison he deduced an intervalence band splitting E_1

TERNARY CHALCOPYRITE SEMICONDUCTORS

TABLE 3.2. *Calculated effective masses for the conduction and valence bands (units of the free electron mass)*

CdSnAs ₂					CdSnP ₂			
	<i>m_T</i>	<i>m_L</i>	<i>m_d</i>	<i>m_σ</i>	<i>m_T</i>	<i>m_L</i>	<i>m_d</i>	<i>m_σ</i>
<i>c</i>	0.018	0.016	0.017	0.017	0.060	0.056	0.059	0.059
<i>v₁</i>	0.10	0.018	0.057	0.041	(−4.6)	0.069	1.14	0.20
<i>v₂</i>	0.031	—			0.14	—		
<i>v₃</i>	0.12	0.16	0.13	0.13	0.17	2.6	0.43	0.25
CdGeAs ₂					CdGeP ₂			
	<i>m_T</i>	<i>m_L</i>	<i>m_d</i>	<i>m_σ</i>	<i>m_T</i>	<i>m_L</i>	<i>m_d</i>	<i>m_σ</i>
<i>c</i>	0.039	0.030	0.036	0.035	0.088	0.080	0.085	0.085
<i>v₁</i>	0.67	0.034	0.25	0.094	(−1.3)	0.099	0.56	0.26
<i>v₂</i>	0.079	—			0.23	—		
<i>v₃</i>	0.13	0.56	0.22	0.18	0.26	(−1.7)	0.49	0.36
CdSiAs ₂					ZnSiAs ₂			
	<i>m_T</i>	<i>m_L</i>	<i>m_d</i>	<i>m_σ</i>	<i>m_T</i>	<i>m_L</i>	<i>m_d</i>	<i>m_σ</i>
<i>c</i>	0.084	0.074	0.080	0.080	0.103	0.098	0.10	0.10
<i>v₁</i>	(−3.6)	0.096	1.07	0.27	(−6.1)	0.15	1.76	0.42
<i>v₂</i>	0.21	—			0.28	—		
<i>v₃</i>	0.29	7.8	0.86	0.42	0.43	2.29	0.75	0.59
ZnGeAs ₂					ZnGeP ₂			
	<i>m_T</i>	<i>m_L</i>	<i>m_d</i>	<i>m_σ</i>	<i>m_T</i>	<i>m_L</i>	<i>m_d</i>	<i>m_σ</i>
<i>c</i>	0.060	0.058	0.059	0.059	0.108	0.105	0.11	0.11
<i>v₁</i>	0.82	0.084	0.38	0.21	(−1.8)	0.15	0.79	0.39
<i>v₂</i>	0.14	—			0.32	—		
<i>v₃</i>	0.25	0.41	0.29	0.29	0.38	(−6.2)	0.97	0.56

=0.15 eV, remarkably close to the value of 0.16 eV determined from (later) electro-reflectance measurements (Table 3.1). This good agreement confirms the assignment of the shoulder near 5 μm in Fig. 3.10b to intervalence band transitions.

3.3 Pseudodirect Energy Gaps

The restructuring of the Brillouin zone for chalcopyrite crystals relative to that for zincblende crystals results in the interesting possibility that a ternary compound (ZnGeP₂) can have a direct energy gap whereas its binary analog (GaP) has an indirect energy gap. These direct energy gaps have been designated “pseudodirect” (see Section 3.1), and the model for these energy gaps is shown in Fig. 3.11. Due to the 4 to 1 mapping of energy levels in the zincblende Brillouin zone into the (smaller) chalcopyrite Brillouin

zone, one of the X conduction band levels of GaP appears at Γ in ZnGeP₂ and has the symmetry Γ_3 . In the absence of spin-orbit interaction, $\Gamma_4 \rightarrow \Gamma_3$ transitions are forbidden altogether, and $\Gamma_5 \rightarrow \Gamma_3$ transitions are only allowed for $\mathbf{E} \perp \mathbf{z}$. Including spin-orbit interaction, the double degeneracy of the Γ_5 valence band is lifted, and $\Gamma_4 \rightarrow \Gamma_3$ transitions (now $\Gamma_7 \rightarrow \Gamma_7$) become weakly allowed. It is important to notice that the valence bands in Fig. 3.11 are the same as the valence bands in Fig. 3.5. Hence electroreflectance peaks due to pseudodirect A' , B' , and C' transitions should manifest the same splittings as the direct A , B , and C peaks. This feature is crucial to the identification of pseudodirect transitions in experimental spectra.

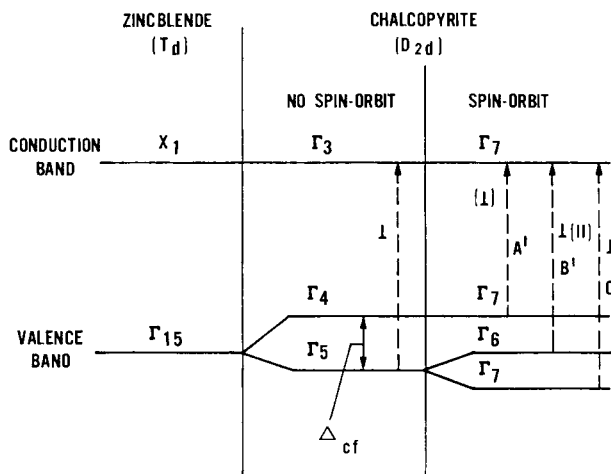


FIG. 3.11. Band structure and selection rules for pseudodirect transitions in a chalcopyrite crystal derived from the $\Gamma_{15} \rightarrow X_1$ indirect transitions in a zincblende crystal.

Although experimental studies of pseudodirect energy gaps are scanty by comparison with studies of the direct energy gaps, recent electroreflectance and wavelength-modulated absorption studies have located these energy gaps in ZnGeP₂ and ZnSiAs₂. These studies have confirmed the existence of pseudodirect energy gaps and hence have verified the essential validity of this concept. The wavelength-modulated absorption spectrum of ZnGeP₂ (Fig. 3.12a) shows three peaks A' , B' , and C' at 2.08, 2.145, and 2.21 eV at 77 K. The energies of these peaks at 300 K are 1.99, 2.055, and 2.12 eV. The energy separations between the A' , B' , and C' peaks are approximately equal to those between A , B , and C in the electroreflectance spectrum (Fig. 3.13). Hence A' , B' , and C' are attributed to pseudodirect transitions derived from the indirect transition $\Gamma_{15} \rightarrow X_1$ in zincblende crystals. The polarization dependences of the A' , B' , and C' peaks agree qualitatively with the predictions of Fig. 3.11. The A' peak is very weak since this $\Gamma_7 \rightarrow \Gamma_7$ transition becomes allowed only when spin-orbit interaction is included. The energy separation between the A and A' peaks shows that at 300 K the Γ_1 conduction band in ZnGeP₂ is located 0.40 eV above the lowest conduction band Γ_3 (Fig. 3.3).

The wavelength-modulated absorption spectrum of ZnSiAs₂ (Fig. 3.12b) shows two peaks A' and B' at 1.80 and 1.90 eV at 77 K. The energies of these peaks are 1.74 and 1.83 eV at 300 K. Since the energy separation of the A' and B' peaks is the same as

TERNARY CHALCOPYRITE SEMICONDUCTORS

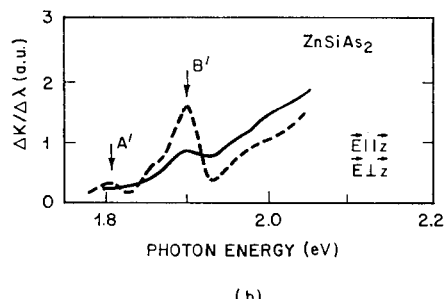
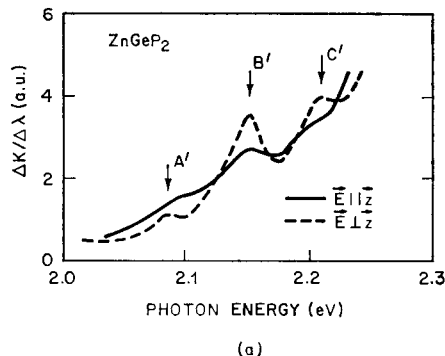


FIG. 3.12. Wavelength-modulated absorption spectra of ZnGeP_2 (a) and ZnSiAs_2 (b). The A' , B' , and C' structures are attributed to the pseudodirect transitions depicted in Fig. 3.11. (Shileika, 1973.)

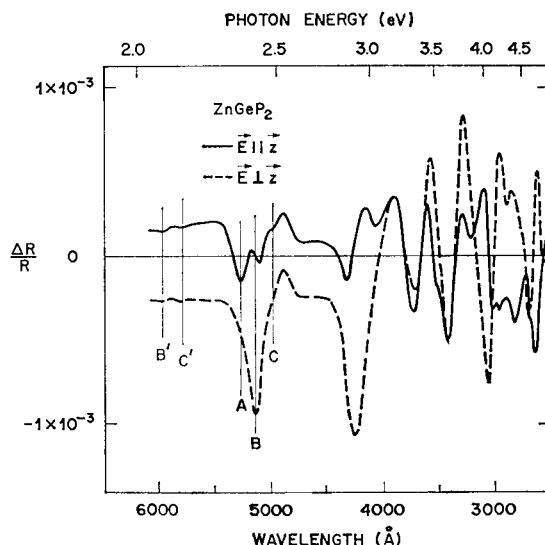


FIG. 3.13. Electrolyte-electroreflectance spectrum of ZnGeP_2 . The orientation was approximately (112). (Shay *et al.*, 1973.)

between the *A* and *B* peaks in the electroreflectance spectrum (Fig. 3.14), the *A'* and *B'* peaks are attributed to pseudodirect transitions to the Γ_3 conduction band minimum derived from the X_1 minimum in zinblende crystals. The *C'* peak expected near 2.15 eV was not observed in the wavelength-modulated spectrum (Fig. 3.12b), since it is obscured by a much stronger *A* transition at 2.18 eV (77 K). From these data it is found that the Γ_3 conduction band lies 0.38 eV below the Γ_1 conduction band in ZnSiAs₂.

In the modulation spectra of these pseudodirect II-IV-V₂ compounds, structure due to pseudodirect optical transitions to the next *X* conduction band (X_3) have not been well pronounced. Very weak structure perhaps due to these transitions has been reported in the thermorelectance and wavelength modulated absorption spectra of ZnGeP₂ near 2.3 eV (Shileika 1973).

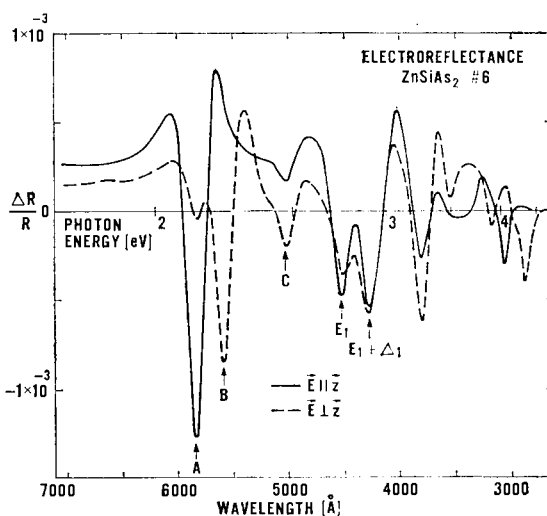


FIG. 3.14. Electrolyte-electroreflectance spectrum of an (001) platelet of ZnSiAs₂. (Shay *et al.*, 1971a.)

In Fig. 3.15 we show the electroreflectance spectrum of ZnSiP₂, a crystal which is also expected to have a pseudodirect energy gap. However, no resolved structure is observed in the energy region of the expected pseudodirect energy gaps (~2.2 eV). Indeed, the polarization properties of the spectra near the direct energy gaps are themselves anomalous. The peaks labeled *A* and *B* in Fig. 3.15 are the first strong peaks in the spectra, and generally have been attributed to the fundamental direct gap in other II-IV-V₂ compounds. However, the *A* peak in Fig. 3.15 is polarized $E \perp z$ and *B* is polarized $E \parallel z$. This behavior is opposite to that for all other II-IV-V₂ compounds investigated to date. On the face of it, the polarization properties indicate that Δ_{cf} is positive in ZnSiP₂, and therefore is dominated by one of the noncubic potentials listed earlier other than the lattice compressive. On the other hand, the *A* and *B* peaks in Fig. 3.15 may not be due to transitions to the Γ_1 conduction band as they are in other compounds. The conduction band structure of ZnSiP₂ would then be different from either of the models in Fig. 3.2 or 3.3.

TERNARY CHALCOPYRITE SEMICONDUCTORS

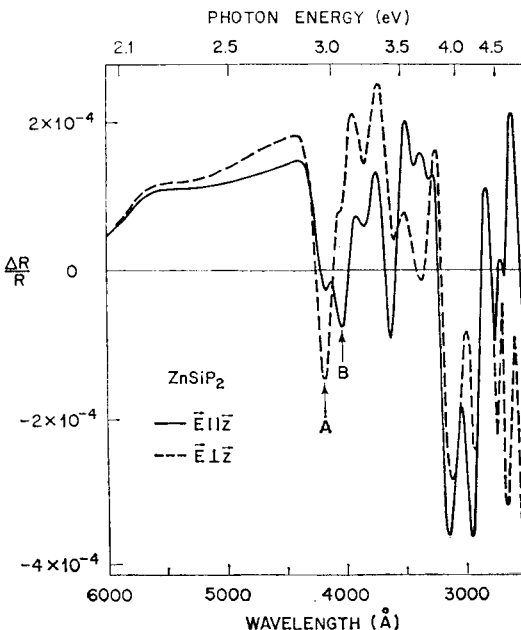


FIG. 3.15. Electrolyte-electroreflectance spectrum of a (112) platelet of ZnSiP₂. (Shay *et al.*, 1973.)

This crystal-field anomaly reported for ZnSiP₂ is especially disturbing in comparison with ZnSiAs₂ (Fig. 3.14) for which the normal ordering of the valence bands was observed. One would intuitively expect that any "chemical" effects associated with the difference between the cation species Zn and Si would be independent of the anion in the ternary compound.

This dilemma could be resolved if the lowest conduction band level in ZnSiP₂ were derived from Γ_{15} rather than Γ_1 . The lowest direct energy gap would then be derived from $\Gamma_{15} \rightarrow \Gamma_{15}$ transitions in III-V compounds rather than $\Gamma_{15} \rightarrow \Gamma_1$ as observed for all other II-IV-V₂ compounds. If the conduction band crystal-field splitting were such that Γ_5 was below Γ_4 , then A would be assigned to $\Gamma_5 \rightarrow \Gamma_5$ (\perp), B to $\Gamma_5 \rightarrow \Gamma_5$ (\parallel), and the weaker structure near 3.2 eV would be assigned to $\Gamma_5 \rightarrow \Gamma_4$ (\perp) transitions. This suggestion seems tenuous, however, since the $\Gamma_{15} \rightarrow \Gamma_{15}$ energy gaps in GaP and AlP (the binary analogs) are 4.8 and 4.6 eV respectively, i.e. ~ 1.7 eV above the energy of the A and B transitions in Fig. 3.15.

Although pseudodirect transitions have not been identified in the electroreflectance spectrum of ZnSiP₂, two unidentified bands have been observed in the low-temperature absorption spectrum. As shown in Fig. 3.16, the steep absorption edge at 77 K lies at lower energy for $E \perp z$ than for $E \parallel z$ and two bands are observed at 2.23 and 2.27 eV respectively. Similar results were obtained at 4.2 K. Although Belle *et al.* (1965) did not provide absolute values for the data in Fig. 3.16, comparison of the 300 K data with other measurements indicates that the amplitudes of the absorption bands are ~ 200 cm⁻¹. Since photoluminescence measurements to be described in Chapter 5 evidence an energy gap near 2.05 eV at 2 K, the bands at 2.23 and 2.27 eV seem to lie at energies above the lowest band gap. Perhaps these bands result from B' and C' pseudodirect transitions.

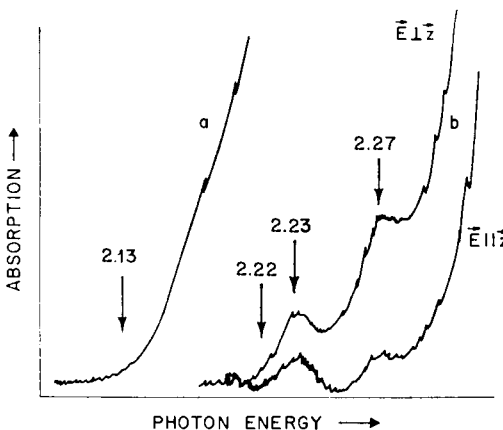


FIG. 3.16. Absorption edge of ZnSiP₂ at (a) 300 K, and (b) 77 K. (Belle *et al.*, 1965.)

Bendorius *et al.* (1972a) have performed a very nice experiment which shows clearly the essentially different natures of the lowest conduction band minima in direct and pseudodirect crystals. Since pseudodirect transitions are expected to be relatively weak, the slope of the absorption edge of the pseudodirect gap crystals is expected to be less sharp than that of the direct gap crystals. Furthermore, it is well known that the hydrostatic pressure dependence of the $\Gamma_{15} \rightarrow \Gamma_1$ and $\Gamma_{15} \rightarrow X_1$ energy gaps in III-V semiconductors have opposite signs and considerably different magnitudes (Zallen and Paul, 1967). Thus there is good reason to predict two strongly distinct values of dE_g/dP for II-IV-V₂ compounds due to the two kinds of lowest conduction band minima. For direct gap crystals with the lowest conduction band minimum Γ_1 , one expects a large positive pressure coefficient as for the $\Gamma_{15} \rightarrow \Gamma_1$ energy gap in III-V semiconductors. For the pseudodirect II-IV-V₂ crystals the values of dE_g/dP should be small and negative, since the absorption edge results from optical transitions to the lowest conduction band, either Γ_3 or $T_1 + T_2$, both originating from X_1 in zincblende.

The absorption spectra of two typical direct and pseudodirect II-IV-V₂ crystals are shown in Fig. 3.17. It can be seen that the fundamental absorption edge of CdSiAs₂ is sharp and shifts rapidly to higher energies when the hydrostatic pressure increases, whereas the absorption edge of CdSiP₂ is smooth, and shifts slowly to lower energies with increasing pressure. Similar results on other II-IV-V₂ crystals are shown in Fig. 3.18 and 3.19. The slopes of fundamental absorption edge (characterized by the parameter $S = \Delta \ln K / \Delta \hbar\omega$), lowest energy gaps, and their pressure coefficients are summarized in Table 3.3. As expected, the ternary compounds fall naturally into two groups according to the values of the slope of fundamental absorption edge and pressure coefficients of the energy gap. Thus it is concluded that CdGeAs₂, ZnSnAs₂, ZnGeAs₂, CdSnP₂, CdSiAs₂, ZnSnP₂, and CdGeP₂ have Γ_1 as the lowest conduction band minimum, and ZnSiAs₂, ZnGeP₂, ZnSiP₂, and CdSiP₂ have Γ_3 or $T_1 + T_2$ as the lowest conduction band minimum.

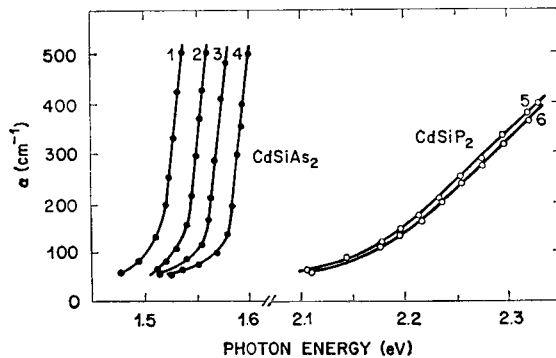


FIG. 3.17. The absorption edge of CdSiAs_2 (curves 1–4) and CdSiP_2 (curves 5–6) at various hydrostatic pressures in kg cm^{-2} : (1) 1; (2) 2280; (3) 4360; (4) 6480; (5) 6300; (6) 1. (Bendorius *et al.*, 1972a.)

TABLE 3.3. *The slopes of fundamental absorption edge ($S = \Delta \ln K/\Delta \hbar\omega$), approximate energy gaps (E_g).† and their pressure coefficients (dE_g/dP)*

Compound	S (eV^{-1})	E_g (eV)	dE_g/dP ($10^{-6} \text{ eV kg}^{-1} \text{ cm}^2$)
CdGeAs_2	20	0.5	9.3
ZnSnAs_2	49	0.67	8.2
ZnGeAs_2	34	1.05	9.7
CdSnP_2	33	1.14	7.3
CdSiAs_2	64	1.52	10.0
ZnSnP_2	41	1.62	7.5
CdGeP_2	28	1.67	9.7
ZnSiAs_2	6	1.7	1.6
ZnGeP_2	8	2.0	1.2
ZnSiP_2	7	2.1	-0.5
CdSiP_2	9	2.2	-0.7

† The values of the energy gap E_g were determined by the linear extrapolation of the steep part of the absorption curves (α plotted versus $\hbar\omega$) to $\alpha = 0$.

3.4 Optical Anisotropy of II–IV–V₂ Compounds

3.4.1 CdSnP_2

The room temperature transmission spectra of CdSnP_2 are shown in Fig. 3.20 for light polarized, respectively, parallel and perpendicular to the optic axis. As discussed earlier, for a (112) platelet $E \parallel z$ is only nominal. As the photon energy is increased from 1.10 eV, the transmission for $E \parallel z$ is rapidly extinguished as a result of the onset of direct transitions associated with the A energy gap at 1.17 eV (Table 3.1). The transmission spectrum for $E \perp z$ has a similar shape but is shifted to higher energy

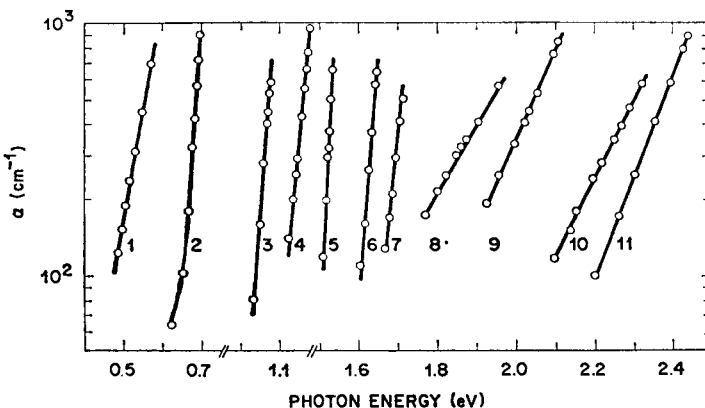


FIG. 3.18. Photon-energy dependence of the absorption coefficients for several II-IV-V₂ semiconductors: (1) CdGeAs₂; (2) ZnSnAs₂; (3) ZnGeAs₂; (4) CdSnP₂; (5) CdSiAs₂; (6) ZnSnP₂; (7) CdGeP₂; (8) ZnSiAs₂; (9) ZnGeP₂; (10) ZnSiP₂; (11) CdSiP₂. (Bendorius *et al.*, 1972a.)

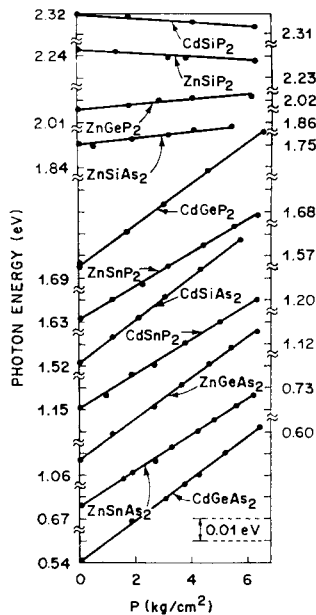


FIG. 3.19. Hydrostatic pressure dependences of the absorption edges (at $\alpha = 300 \text{ cm}^{-1}$) of II-IV-V₂ compounds. (Bendorius *et al.*, 1972a.)

by ~ 0.03 eV. Although it is tempting to attribute this shift to the separation in energy of two energy levels, we will show that the dichroism manifest in Fig. 3.20 is in fact entirely due to a single electronic transition having a highly anisotropic oscillator strength.

It is known from electroreflectance studies in CdSnP₂ that the *B* transition is allowed only for $E \perp z$ and has approximately the same strength as does the *A* transition for $E \parallel z$, and that the *A* and *B* energy gaps are split by 0.08 eV. Therefore, we can estimate

TERNARY CHALCOPYRITE SEMICONDUCTORS

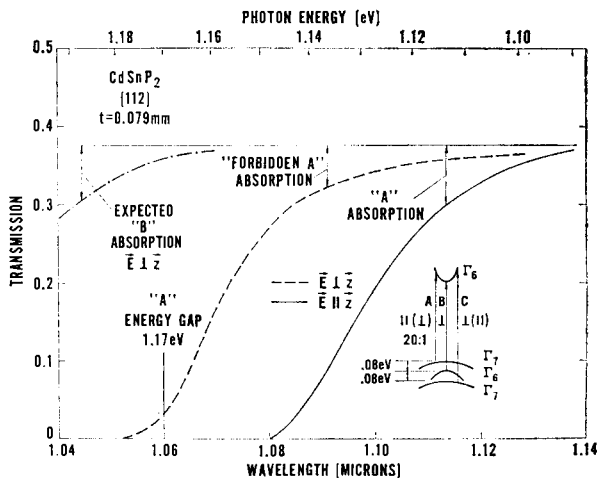


FIG. 3.20. Room temperature transmission of a (112) platelet of CdSnP_2 .
(Shay and Buehler, 1971a.)

the transmission spectrum for $E \perp z$ due to the B transition alone by shifting the experimental curve for $E \parallel z$ 0.08 eV to higher energy as shown in Fig. 3.20. It is apparent that the absorption associated with the B transition is *not* producing the absorption measured for $E \perp z$. We shall now show quantitatively that the dichroism in Fig. 3.20 results entirely from the A transition.

The absorption coefficients determined in the usual way from the transmission curves in Fig. 3.20 are shown in Fig. 3.21 for the ordinary and extraordinary rays. Electroreflectance measurements as well as the quasicubic model [eq. (3.3)] have shown that the oscillator strength for the A transition in CdSnP_2 is 19.4 times larger for $E \parallel z$ than for $E \perp z$. Therefore we can show that the dichroism in Fig. 3.20 results from the A transition by showing that the relevant absorption coefficients are in the ratio 19.4 to 1. To account for the (112) geometry one must multiply the experimental values for α^e by 1.5 to obtain the absorption coefficient which would obtain for the extraordinary ray for propagation normal to the optic axis. The resulting derived quantities are shown as the closed squares in Fig. 3.21 and form a smooth curve with $18\alpha^\circ$ which are shown as closed circles. The observed ratio of 18 is consistent with electroreflectance data which cannot accurately measure large polarization ratios. Since the two derived quantities in Fig. 3.21 form a smooth curve as a function of photon energy, we conclude that essentially all of the dichroism in Fig. 3.20 results from the anisotropy of the A -transition oscillator strength. An important ramification of this work is that a measurement of the shift of the absorption edge for polarizations parallel and perpendicular to the optic axis is *not* a measurement of the valence band splitting as has sometimes been assumed.

Since the absorption coefficient of the ordinary ray α° has the same shape as α^e , the spectrum of α° simulates that of α^e for a crystal 18 times thinner. This technique should considerably reduce the difficulty of observing exciton absorption in ternary crystals since one can work with much thicker crystals and undesirable strain effects will be greatly reduced.

We have suppressed from the transmission spectra in Fig. 3.20 deep interference fringes resulting from the almost perfectly parallel faces of the naturally grown platelet.

ELECTRONIC STRUCTURE OF II-IV-V₂ COMPOUNDS

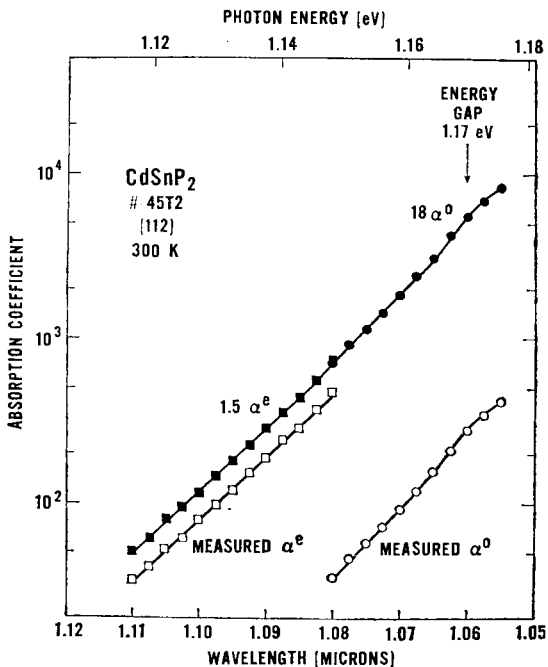


FIG. 3.21. Absorption coefficients derived from the transmission curves in Fig. 3.20 (open points). The solid points are derived from the experimental data in a manner described in the text. Since the solid points form a smooth curve, the dichroism manifest in Fig. 3.20 results from the anisotropy of the oscillator strength of the single electron transition $\Gamma_7 \rightarrow \Gamma_6$ (A in Fig. 3.4). (Shay and Buehler, 1971a.)

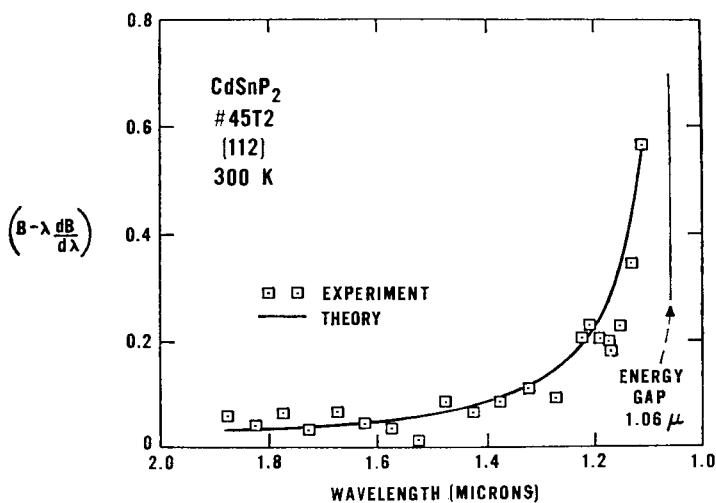


FIG. 3.22. Dispersion of the "effective birefringence" near the direct energy gap of CdSnP₂. (Shay and Buehler, 1971a.)

TERNARY CHALCOPYRITE SEMICONDUCTORS

From the separation in wavelength of these fringes we have measured $n - \lambda dn/d\lambda$ for both the ordinary and extraordinary rays. We refer to this quantity as an effective index of refraction since it reduces to the index n whenever dispersion ($dn/d\lambda$) becomes negligible. The difference between these effective indices, the effective birefringence, is shown in Fig. 3.22. This quantity is positive in the near infrared, and increases rapidly for wavelengths approaching the energy gap at $1.06 \mu\text{m}$. The data contrast to the birefringence in II-VI wurtzite compounds which becomes negative at wavelengths approaching the energy gap.

It is easy to see qualitatively that the contributions of the fundamental edge to the birefringence should be positive and increase at wavelengths close to the band gap. Since α^e is much greater than α^o for photon energies just below the lowest energy gap, a Kramers-Kronig transformation would show that n^e exceeds n^o , a positive birefringence. We have verified this qualitative argument by numerically calculating the birefringence which results from the built-in uniaxial distortion of the CdSnP_2 unit cell. We represent the birefringence near the energy gap as the sum of two terms

$$B(\lambda) = B_0 + B_1(\lambda), \quad (3.10)$$

where $B_1(\lambda)$ is the contribution of the fundamental band gap and B_0 is a wavelength-independent term resulting from higher-lying band gaps and other contributions to the birefringence. The quantity B_1 has been evaluated from the equations for the stress-induced birefringence of binary crystals (Higginbotham *et al.*, 1969; Yu *et al.*, 1971) using effective masses, etc., appropriate to InP (the binary analog of CdSnP_2), but using the lattice constants appropriate to CdSnP_2 . The solid curve in Fig. 3.22 provides a good fit to the data using $B_0 = -0.04$ and arbitrarily increasing B_1 by 50%. A similar enhancement was found necessary to fit piezobirefringence data for GaAs and probably represents the uncertainty in our present theoretical understanding of stress-induced birefringence in binary crystals. From the good agreement in Fig. 3.22, we conclude that the dispersion of the birefringence near the fundamental gap in CdSnP_2 results principally from the built-in compression of the chalcopyrite unit cell.

3.4.2 CdGeP_2

In Fig. 3.23 we present the absorption coefficient of CdGeP_2 near the direct energy gap. Whereas the polarization ratio for the A transition is expected to be 45 [eq. (3.3)], the absorption coefficient for $\mathbf{E} \parallel \mathbf{z}$ is only about 5 times larger than for $\mathbf{E} \perp \mathbf{z}$ at energies below the A energy gap at 1.72 eV. The smaller polarization ratio has been attributed to a polarization-independent contribution to the absorption coefficient (due to impurities) which masks the contribution from the A energy gap for $\mathbf{E} \perp \mathbf{z}$.

It is reasonable to attribute the rapid increase in α_{\perp} for photon energies greater than 1.7 eV to the onset of direct transitions associated with the A energy gap. The theoretical lineshape for such a transition, ignoring for the moment the Coulomb attraction of the electron and hole, is of the form

$$\alpha = \alpha_0(h\nu - E_g)^{1/2}, \quad (3.11)$$

where E_g is the energy gap. The theoretical curve in Fig. 3.23 provides a good fit to the data for $E_g = 1.711 \text{ eV}$ and $\alpha_0 = 2400 \text{ cm}^{-1}/\text{eV}^{1/2}$.

There is reason for questioning the physical significance of the good agreement between theory and experiment indicated in Fig. 3.23, since the energy gap determined

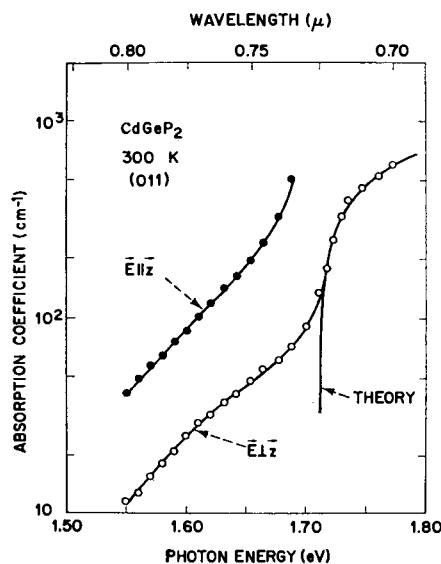


FIG. 3.23. Absorption coefficient of CdGeP₂ at 300 K. (Shay *et al.*, 1971 b.)

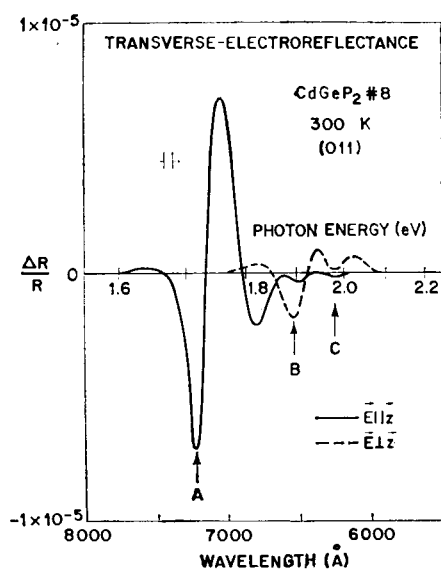


FIG. 3.24. Transverse electroreflectance spectrum of CdGeP₂. (Shay *et al.*, 1971 b.)

TERNARY CHALCOPYRITE SEMICONDUCTORS

from the fit to eq. (3.10) is less than the energy of the *A* peak at 1.72 eV in the electroreflectance data (Fig. 3.24). Furthermore, it is well known from studies of binary zinc-blende crystals (e.g. GaAs) that the Coulomb attraction of electrons and holes modifies the shape of the absorption edge even at room temperature. Consequently, the true energy gap probably lies slightly above the value for E_g determined by the best fit of eq. (3.11) to experiment.

The contribution of excitons to the absorption edge of CdGeP₂ is more clearly seen at low temperatures, as shown in Fig. 3.25. The lowest bound state lies between 1.81 and 1.82 eV at the knee in the data, but is considerably broadened by residual impurities. In the absence of any broadening, the absorption edge would consist of a hydrogenic series of discrete lines at energies R/n^2 below the energy gap (for integer values of n), and a continuous absorption above the energy gap of the form $[1 - \exp(-2\pi z)]^{-1}$,

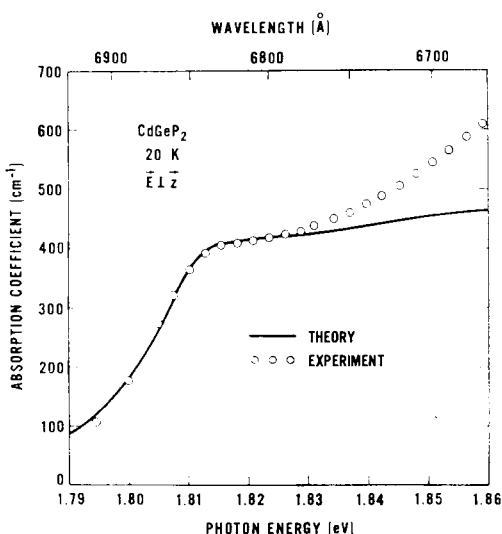


FIG. 3.25. Absorption coefficient of CdGeP₂ at 20 K for $\mathbf{E} \perp \mathbf{z}$. (Shay *et al.*, 1971 b.)

where $z^2 = R/(E - E_g)$. R is the exciton rydberg and E_g is the energy gap. Sell and Lawaetz (1971) have recently shown that the most reliable method for determining R from broadened experimental data, such as we have in Fig. 3.25, is to fit the data near the exciton peak (or knee) to a composite theoretical curve, including discrete and continuum excitons, broadened by a Lorentzian function $\Gamma\pi^{-1}(E^2 + \Gamma^2)^{-1}$, where 2Γ is the full width at half maximum. The solid curve in Fig. 3.25 is an attempt to fit the data below 1.83 eV with such a broadened composite theoretical model. At 20 K, we obtain $E_g = 1.819$ eV, $R = 7.7$ meV, and $\Gamma = 1.4R = 10.8$ meV.

At photon energies above 1.83 eV, the data in Fig. 3.25 becomes progressively larger than the theoretical values describing the exciton absorption at the lowest energy gap. Sell and Lawaetz (1971) have shown that in GaP a similar discrepancy results from two effects: (a) the nonparabolicity of the valence bands, and (b) the onset of broadened exciton absorption at the next energy gap. Both effects should also be important in CdGeP₂, but quantitative estimates of these effects are not presently possible.

Quite apart from the determination of the exciton rydberg, the good fit between theory and experiment in Fig. 3.25 is significant because it is independent evidence that the dichroism of the absorption edge in II-IV-V₂ semiconductors results from the anisotropy of the A transition alone. Although transitions at the A energy gap are predominantly polarized $\mathbf{E} \parallel \mathbf{z}$ by a factor of ~ 45 to 1 [eq. (3.3)], the absorption for $\mathbf{E} \perp \mathbf{z}$ is also dominated by the A transition, as is attested to by the appearance of an exciton below the A energy gap in Fig. 3.25.

Goryunova *et al.* (1970b) have recently reported measurements of the birefringence of several II-IV-V₂ compounds including CdGeP₂. The birefringence which they report for CdGeP₂ is actually a lower limit to the true effective birefringence of CdGeP₂. Nonetheless, eq. (3.10) has been used to explain their results. The solid curve in Fig. 3.26 provides a good fit to the data using $B_0 = -0.005$ and arbitrarily increasing B_1 by 60%. From the good agreement we conclude that the dispersion of the birefringence near the fundamental gap in CdGeP₂ results principally from the built-in compression of the chalcopyrite unit cell.

Although we have shown that this built-in uniaxial compression dominates the ordering and splittings of the valence bands as well as the dispersion of the birefringence near the direct energy gap in II-IV-V₂ crystals, it does not dominate the asymptotic values of the birefringence at long wavelengths. Uniaxial compression of a large band-gap zincblende crystal such as GaP produces a *negative* birefringence at long wavelengths because of a dominance of higher-lying energy gaps. CdGeP₂ and all other II-IV-V₂ compounds investigated to date are *positive* birefringent (Chapter 6). Clearly one of the other noncubic aspects of the chalcopyrite structure outlined earlier (Section 3.1) is dominating the long-wavelength birefringence, but a quantitative theory for this phenomenon is not yet available.

3.5 Higher Lying Energy Gaps

Whereas the near ultraviolet optical spectra of III-V compounds are dominated by the spin-orbit-split doublets E_1 and $E_1 + A_1$, associated with electronic transitions in the A direction of the Brillouin zone, the optical spectra of II-IV-V₂ crystals are considerably richer in structure, showing six or more distinct electronic transitions (Fig. 3.4). The discovery of this multiplicity of structure (Shay *et al.*, 1970b, c) has led to considerable controversy regarding its proper interpretation. Attention has been focused mainly on the lowest four ultraviolet transitions which lie at approximately the same photon energy as the E_1 and $E_1 + A_1$ doublet in the binary analog.

Kavaliauskas *et al.* (1971a) have proposed that these four transitions in CdSnP₂ are centered about the N point of the chalcopyrite Brillouin zone. Due to the ordering of the cations, the chalcopyrite Brillouin zone has one quarter of the volume of the zincblende Brillouin zone, and there is a 4 to 1 mapping of energy levels from a zincblende crystal to its chalcopyrite ternary analog. Although five-sixths of the A direction is preserved in chalcopyrite, the L point $1/2, 1/2, 1/2$ of zincblende maps to the N point of chalcopyrite. Kavaliauskas *et al.* (1971a) have further proposed that the two doublets in CdSnP₂ involve N_1 valence bands derived from InP valence bands mapped to the N point from two *different* L points.

Kwan and Woolley (1971b) have assigned the second and third peaks in ZnSiAs₂ to the region of the chalcopyrite Brillouin zone corresponding to the A direction in zincblende. The first peak was attributed to some other, unidentified region of the Brillouin

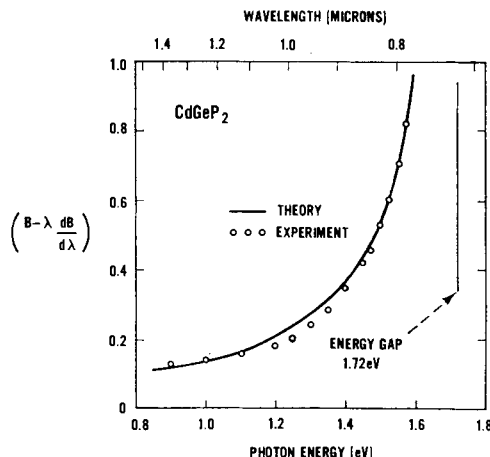


FIG. 3.26. Dispersion of the effective birefringence near the direct energy gap of CdGeP₂ at 300 K. (Shay *et al.*, 1971 b.)

zone, and a fourth peak was not observed. Stokowski (1972) has suggested that the two lower energy transitions correspond to the E_1 and $E_1 + \Delta_1$ transitions, but the two higher energy transitions are centered on the N point, and originate on degenerate valence bands derived from the two L points mapped to a single N point.

We originally suggested that in both CdSnP₂ and ZnSiAs₂, the two lower energy transitions were derived from E_1 and $E_1 + \Delta_1$ in the respective binary analog, but that the higher-energy transitions originated in other regions of the Brillouin zone. Later observation that the higher energy doublet in both CdSiAs₂ and CdGeAs₂ was strongly polarized $\mathbf{E} \perp z$ led us to suggest that it originated at the N point in the chalcopyrite Brillouin zone. We have recently proposed a new assignment for these four transitions in chalcopyrite crystals which consolidates earlier interpretations (Shay, 1972 a, b).

In Fig. 3.27 we compare the reflectance and electroreflectance spectra of CdSiAs₂ and GaAs in the 2–4 eV region of photon energy. As already explained, the spin-orbit-split doublet E_1 and $E_1 + \Delta_1$ in GaAs results from transitions along the Λ direction of the zincblende Brillouin zone. The great strength of this structure in the reflectance indicates that energy levels throughout an enormous region of the Brillouin zone are contributing. Experimentally derived estimates for various zincblende crystals are that 30–80% of the Γ - L distance is contributing to this structure. We notice in Fig. 3.27 that the reflectance spectrum of CdSiAs₂, although polarization dependent and split into two peaks separated ~ 0.5 eV, is essentially the same as that observed in GaAs, and that the four transitions in the CdSiAs₂ electroreflectance spectra occur in the same energy region as the strong structure in the reflectance spectrum. This, we believe, is the key to the proper identification of the E_1 quartet observed in all II–IV–V₂ crystals. The great strength of the reflectance structure indicates that in CdSiAs₂ as well, energy levels throughout a large region of the Brillouin zone are contributing, and that all four transitions originate in the region of the chalcopyrite Brillouin zone corresponding to the Λ direction in zincblende.

The appearance of four transitions in CdSiAs₂ corresponding to only two transitions in GaAs is precisely the behavior expected for the energy bands in the Λ direction under the simultaneous influences of spin-orbit interaction and the noncubic crystalline field.

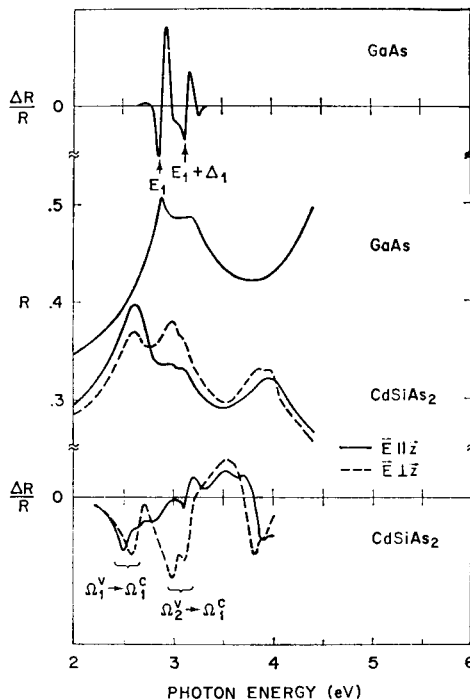


FIG. 3.27. Comparison of the reflectance and electroreflectance of CdSiAs₂ with that of GaAs its binary analog. (Shay, 1972a.)

The compatibility table of Sandroch and Treusch (1964) shows that in the absence of spin-orbit interaction, the valence band Λ_3 is split by the chalcopyrite field into Ω_1 and Ω_2 bands. The Λ_1 conduction band becomes Ω_1 . The $\Omega_2^v \rightarrow \Omega_1^c$ transition is only allowed for radiation polarized normal to the optic axis, whereas $\Omega_1^v \rightarrow \Omega_1^c$ is allowed for both polarizations. Including spin, the Ω_1 and Ω_2 valence band as well as the Ω_1 conduction band split into $\Omega_4 + \Omega_3$ doublets. Since the conduction band spin-orbit splitting should be negligible, we expect that there should be two doublets in CdSiAs₂ corresponding to the E_1 doublet in GaAs. The lower energy doublet should have mixed polarization properties but the higher energy doublet should be polarized primarily $E \perp z$.

These predictions are in good agreement with the data in Fig. 3.27 as well as data for other II-IV-V₂ compounds (Figs. 3.28–3.30). The higher energy structure is strongly polarized $E \perp z$ as expected for $\Omega_2^v \rightarrow \Omega_1^c$ transitions. In Table 3.4 we summarize the energies of the four peaks observed in several II-IV-V₂ compounds. We suggest that in each of these compounds, the E_1 , E_2 , E_3 , and E_4 transitions are derived from the E_1 doublet of the respective binary analog, and all originate in basically the same region of the Brillouin zone, namely the portion of the Λ direction in zincblende preserved in the chalcopyrite Brillouin zone.

It can be seen from Fig. 3.31 that for CdSnAs₂, at least twelve peaks E_1-E_{12} , with intensities dependent upon the polarization of light, have been observed in the energy region corresponding to the E_1 , E'_1 , and E_2 structures of its closest analog InAs. These data present a formidable challenge for theorists engaged in calculating optical properties of semiconductors.

TERNARY CHALCOPYRITE SEMICONDUCTORS

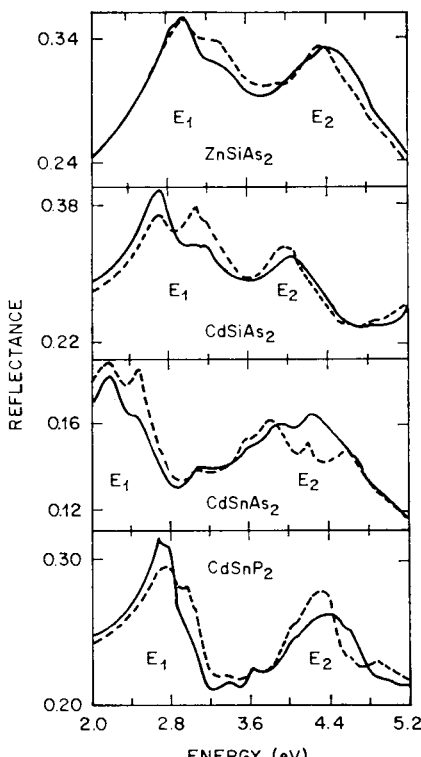


FIG. 3.28. Reflectance spectra at 2 K for light polarized $E \perp z$ (dashed curve) and $E \parallel [111]$ (solid curve). (Stokowski, 1972.)

TABLE 3.4 Energies of the characteristic electroreflectance peaks E_{1-4} of II-IV-V₂ crystals (in eV)

Compound	T (K)	E_1	E_2	E_3	E_4	References
ZnSiP ₂	120	3.35	3.51	3.8	4.0	a
ZnSiAs ₂	300	2.74	2.90	3.25	3.50	b
ZnGeP ₂	120	3.02	3.14	3.22	3.48	a
ZnGeAs ₂	300	2.26	2.42	2.72		a
ZnSnP ₂	300	2.80	2.96	3.11		c
ZnSnAs ₂	77	2.34	2.46	2.63	2.67	d, e
CdSiP ₂	300	3.3		3.7		a
CdSiAs ₂	300	2.50	2.57	2.99	3.10	f
CdGeP ₂	300	2.6				g
CdGeAs ₂	300	2.0	2.09	2.44	2.58	f
CdSnP ₂	300	2.56	2.69	2.90	3.00	h
CdSnAs ₂	77	2.13	2.25	2.51	2.60	d, i

^a Shileika (1973).

^b Shay *et al.* (1971a).

^c Krivaite *et al.* (1972).

^d Kavaliauskas *et al.* (1971 b).

^e Krivaite *et al.* (1971).

^f Shay and Buehler (1971 b).

^g Zlatkin *et al.* (1971).

^h Shay *et al.* (1970b).

ⁱ Bendorius *et al.* (1972b).

ELECTRONIC STRUCTURE OF II-IV-V₂ COMPOUNDS

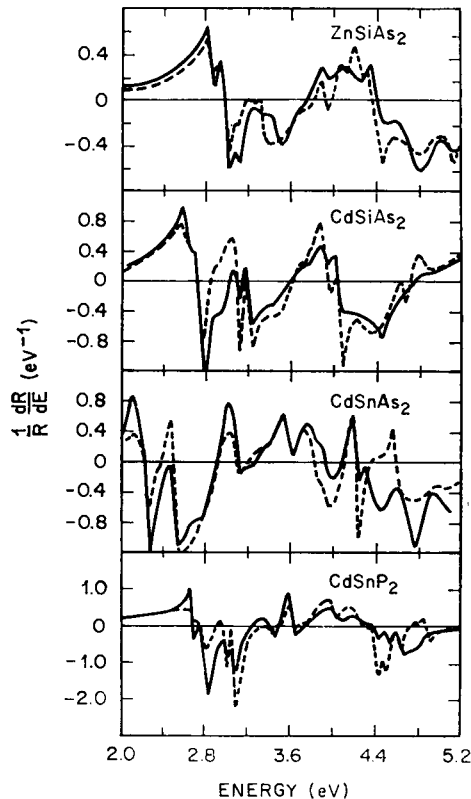


FIG. 3.29. Logarithmic derivative of the reflectance of 2 K for light polarized $E \perp z$ (dashed curve) and $E \parallel [111]$ (solid curve). (Stokowski, 1972.)

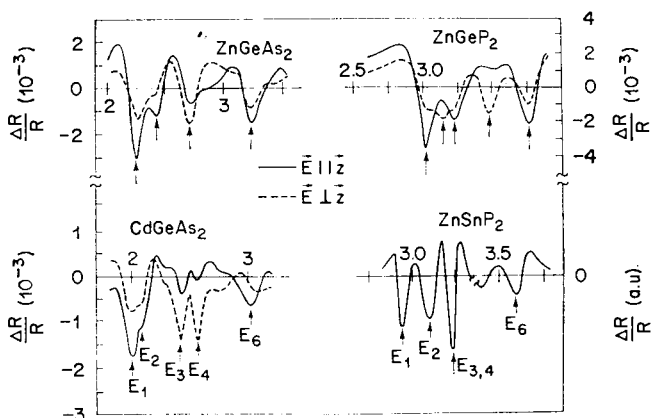


FIG. 3.30. Electroreflectance spectra of CdGeAs_2 , ZnGeAs_2 and ZnSnP_2 , and the thermorelectance spectrum of ZnGeP_2 . (Shay and Buehler, 1971 b; Shileika, 1973; Krivaite *et al.*, 1972.)

TERNARY CHALCOPYRITE SEMICONDUCTORS

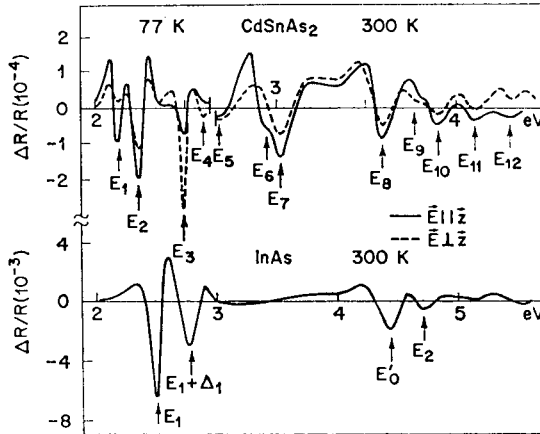


FIG. 3.31. Comparison of the electroreflectance of CdSnAs_2 with that of its binary analog InAs. (Bendorius *et al.*, 1972 b.)

References

- BELLE, M. L., VALOV, YU. A., GORYUNOVA, N. A., ZLATKIN, L. B., IMENKOV, A. N., KOSLOV, M. M., and TSARENKOV, B. V. (1965) *Dokl. Akad. Nauk SSSR* **163**, 606 [Soviet Phys. Doklady **10**, 641 (1966)].
- BENDORIUS, R., PROCHUKHAN, V. D., and SHILEIKA, A. (1972a) *Phys. Status Solidi* (b) **53**, 745.
- BENDORIUS, R. A., KRIVAITA, G. Z., SHILEIKA, A. YU., KARAVAEV, G. F., and CHALDYSHEV, V. A. (1972b) In *Proceedings of the 11th International Conference on Physics of Semiconductors, Warsaw*. CARDONA, M. (1969) In *Solid State Physics*, Suppl. 11, Academic Press.
- CHALDYSHEV, V. A., and POKROVSKII, V. N. (1960) *Izv. vyssh. ucheb. zaved. Fiz.* **3** (2), 173.
- CHALDYSHEV, V. A., and POKROVSKII, V. N. (1963) *Izv. vyssh. ucheb. zaved. Fiz.* **6** (5), 103.
- EHRENREICH, H. (1961) *J. Appl. Phys.* **32**, 2155.
- GAVINI, A., and CARDONA, M. (1970) *Phys. Rev. B* **1**, 672.
- GORYUNOVA, N. A., BELLE, M. L., ZLATKIN, L. B., LOSHAKOVA, G. V., POPLAVNOI, A. S., and CHALDYSHEV, V. A. (1968) *Fizika tekhn. Pol.* **2**, 1344 [Soviet Phys. Semiconductors **2**, 1126 (1969)].
- GORYUNOVA, N. A., POPLAVNOI, A. S., POLYGALOV, YU. I., and CHALDYSHEV, V. A. (1970a) *Phys. Status Solidi* **39**, 9.
- GORYUNOVA, N. A., ZLATKIN, L. B., and IVANOV, E. K. (1970b) *J. Phys. Chem. Solids* **31**, 2557.
- HIGGINBOTHAM, C. W., CARDONA, M., and POLLAK, F. H. (1969) *Phys. Rev.* **184**, 821.
- HOPFIELD, J. J. (1960) *J. Phys. Chem. Solids* **15**, 97.
- HUBNER, K., and Unger, K. (1972) *Phys. Status Solidi* (b) **50**, K105.
- KANE, E. O. (1957) *J. Phys. Chem. Solids* **1**, 249.
- KARAVAEV, G. F., and POPLAVNOI, A. S. (1966) *Fizika tverd. Tela* **8**, 2143 [Soviet Phys. Solid State **8**, 1704 (1967)].
- KARAVAEV, G. F., POPLAVNOI, A. S., and CHALDYSHEV, V. A. (1968) *Fizika tekhn. Pol.* **2**, 113 [Soviet Phys. Semiconductors **2**, 93 (1968)].
- KARAVAEV, G. F., KRIVAITA, G. Z., POLYGALOV, YU. I., CHALDYSHEV, V. A., and SHILEIKA, A. YU. (1972) *Fizika tekhn. Pol.* **6**, 2211 [Soviet Phys. Semiconductors **6**, 1863 (1973)].
- KARYMSHAKOV, R. K., UKHANOV, YU. I., and SHMARTSEV, YU. V. (1970) *Fizika tekhn. Pol.* **4**, 1988 [Soviet Phys. Semiconductors **4**, 1702 (1971)].
- KAVALIAUSKAS, J., KARAVAEV, G. F., LEONOV, E. I., ORLOV, V. M., CHALDYSHEV, V. A., and SHILEIKA, A. (1971a) *Phys. Status Solidi* (b) **45**, 443.
- KAVALIAUSKAS, J., VUL, S. P., and SHILEIKA, A. YU. (1971b) *Fizika tekhn. Pol.* **5**, 2209 [Soviet Phys. Semiconductors **5**, 1925 (1972)].
- KILDAL, H. (1972) Ph. D. thesis, Stanford University, Technical Report AFML-TR-72-277, Wright-Patterson Air Force Base, Ohio.

ELECTRONIC STRUCTURE OF II-IV-V₂ COMPOUNDS

- KOSTER, G. F., DIMMOCK, J. O., WHEELER, R. C., and STATZ, H. (1963) *Properties of the Thirty-two Point Groups*, MIT, Cambridge.
- KRIVAITE, G. Z., KORNEEV, E. F., and SHILEIKA, A. Yu. (1971) *Fizika tekhn. Pol.* **13**, 2242 [*Soviet Phys. Semiconductors* **5**, 1961 (1972)].
- KRIVAITE, G. Z., KRADINOVA, L. V., and SHILEIKA, A. Yu. (1972) *Fizika tekhn. Pol.* **6**, 2306 [*Soviet Phys. Semiconductors* **6**, 1945 (1973)].
- KWAN, C. C. Y., and WOOLLEY, J. C. (1971a) *Phys. Status Solidi (b)* **44**, K93.
- KWAN, C. C. Y., and WOOLLEY, J. C. (1971b) *Appl. Phys. Lett.* **18**, 520.
- MAMEDOV, B. K., and OSMANOV, E. O. (1971) *Fizika tekhn. Pol.* **5**, 1268 [*Soviet Phys. Semiconductors* **5**, 1120 (1972)].
- POPLAVNOI, A. S., POLYGALOV, YU. I., and CHALDYSHEV, V. A. (1969) *Izv. vyssh. ucheb. Zaved. Fiz.* **12** (11), 58; **13** (6), 95 (1970); **13** (7), 17 (1970) [*Soviet Phys. J.* **12**, 1415 (1972); **13**, 766 (1973); **13**, 849 (1973)].
- ROWE, J. E., and SHAY, J. L. (1971) *Phys. Rev. B* **3**, 451.
- SANDROCH, V. R., and TREUSCH, J. (1964) *Z. Naturf.* **19a**, 844.
- SELL, D. D., and LAWAETZ, P. (1971) *Phys. Rev. Lett.* **26**, 311.
- SHAY, J. L. (1972a) *Phys. Rev. Lett.* **29**, 1008.
- SHAY, J. L. (1972b) *Proceedings of the 11th International Conference on the Physics of Semiconductors, Warsaw*, p. 787.
- SHAY, J. L., and BUEHLER, E. (1971a) *Phys. Rev. Lett.* **26**, 506.
- SHAY, J. L., and BUEHLER, E. (1971b) *Phys. Rev. B*, **3**, 2598.
- SHAY, J. L., BUEHLER, E., and WERNICK, J. H. (1970a) *Phys. Rev. Lett.* **24**, 1301.
- SHAY, J. L., BUEHLER, E., and WERNICK, J. H. (1970b) *Phys. Rev. B*, **2**, 4104.
- SHAY, J. L., BUEHLER, E., and WERNICK, J. H. (1970c) *Proceedings of the 10th International Conference on the Physics of Semiconductors, Boston*, p. 589.
- SHAY, J. L., BUEHLER, E., and WERNICK, J. H. (1971a) *Phys. Rev. B*, **3**, 2004.
- SHAY, J. L., BUEHLER, E., and WERNICK, J. H. (1971b) *Phys. Rev. B*, **4**, 2479.
- SHAY, J. L., TELL, B., BUEHLER, E., and WERNICK, J. H. (1973) *Phys. Rev. Lett.* **30**, 983.
- SHILEIKA, A. (1973) *Surface Sci.* **37**, (730).
- SIKHARULIDZE, G. A., and UKHANOV, Yu. I. (1968). *Phys. Status Solidi* **26**, K33.
- STOKOWSKI, S. E. (1972) *Phys. Rev. B*, **6**, 1294.
- YU, P. Y., CARDONA, M., and POLLAK, F. H. (1971) *Phys. Rev. B*, **3**, 340.
- ZALLEN, R., and PAUL, W. (1967) *Phys. Rev.* **155**, 703.
- ZLATKIN, L. B., IVANOV, E. K., KARAVAEV, G. F., and CHALDYSHEV, V. A. (1971) *Fiz. tekhn. Pol.* **5**, 2058 [*Soviet Phys. Semiconductors* **5**, 1794 (1972)].

CHAPTER 4

ELECTRONIC STRUCTURE OF I-III-VI₂ SEMICONDUCTORS

4.1 Introduction

In this chapter we review studies of the energy band structure of I-III-VI₂ semiconductors, the simplest ternary analogs of II-VI zincblende compounds. Whereas we have shown in Chapter 3 that the structure of the valence band maximum in a II-IV-V₂ chalcopyrite compound is simply related to the energy bands in its III-V analog, the uppermost valence bands of a I-III-VI₂ compound are profoundly influenced by the proximity of noble metal *d*-levels in the valence band. Two manifestations of the hybridization of anion *p*-levels and noble metal *d*-levels have been observed (Shay *et al.*, 1972; Shay and Kasper, 1972; Shay and Tell, 1973). The direct energy gaps observed in the I-III-VI₂ compounds are low relative to the energy gaps in the II-VI analogs by amounts up to 1.6 eV, and the spin-orbit splittings of the uppermost valence bands are reduced relative to binary compounds, due to a partial cancellation of the positive spin-orbit parameters for *p*-levels and the negative spin-orbit parameters for *d*-levels. Quantitative estimates of the *d*-like character range from 16% to 45% over this series of compounds. The essential validity of the concept of *p-d* hybridization in these compounds is supported by an observed correlation between the downshift of the energy gap relative to the binary analog and the percent *d*-like character.

The presence of the noble metal *d*-levels in the valence band has been confirmed directly by the observation of electroreflectance structure due to transitions from the *d*-levels themselves to the lowest conduction band minimum. The fivefold degeneracy is completely lifted by spin-orbit interaction and the tetragonal crystal field. Our understanding of the ordering and splittings of these *d*-levels is not as advanced as for the uppermost valence bands. This is probably one of the most fruitful areas for future research in these compounds.

4.2 Experimental Results

4.2.1 Valence Band Structure

In Fig. 4.1 we show the 77 K electroreflectance spectrum of AgInSe₂ (Shay *et al.*, 1973). The lowest energy gap at 1.24 eV is ~0.6 eV less than that of CdSe, the binary analog. As suggested by the inset, we attribute the *A*, *B*, and *C* structures in Fig. 4.1 to transitions to a single conduction band from three closely spaced valence bands derived from the *p*-like Γ_{15} level in zincblende compounds. The threefold degeneracy is completely lifted by the combined influences of spin-orbit interaction and the noncubic crystalline field. This degeneracy is also completely lifted in CdSe which takes the

ELECTRONIC STRUCTURE OF I-III-VI₂ SEMICONDUCTORS

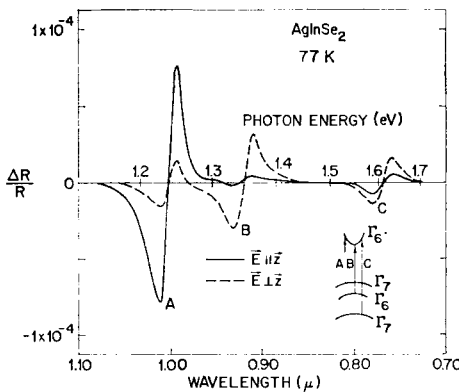


FIG. 4.1. Electroreflectance spectrum of AgInSe₂. The orientation was approximately (100). (Shay *et al.*, 1973.)

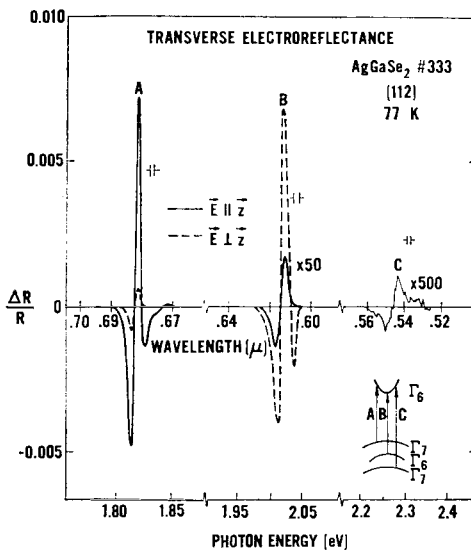


FIG. 4.2. Electroreflectance spectrum of AgGaSe₂. (Tell *et al.*, 1972.)

wurtzite structure. The crystal-field parameter Δ_{cf} for AgInSe₂ is ~ 4 times larger than for CdSe, and of opposite sign. Whereas Δ_{cf} is dominated by the built-in lattice compression in AgInSe₂, in wurtzite CdSe it is dominated by a different phenomenon, the rotation of next-nearest-neighbours by 60° relative to the site positions in the zincblende structure.

In Fig. 4.2 we show the electroreflectance spectrum of AgGaSe₂, the binary analog of which is Zn_{0.5}Cd_{0.5}Se. The energy gap of AgGaSe₂ is 0.5 eV less than that of the hypothetical binary analog. It is apparent in Fig. 4.2 that transitions from three closely spaced valence bands are observed in this compound as well, and the polarization properties are similar to those shown in Fig. 4.1. Due to the (112) orientation however, at most two-thirds of the intensity is parallel to the optic axis, so $E \parallel z$ is only nominal. This accounts for the appearance of the B peak for $E \parallel z$ (solid curve) even though

TERNARY CHALCOPYRITE SEMICONDUCTORS

$\Gamma_6 \rightarrow \Gamma_6$ transitions are only allowed for $E \perp z$. The *A*, *B*, and *C* structures in Fig. 4.2 result from electric field modulation of exciton reflection spectra, one exciton associated with each direct band gap. The energy of the lowest energy exciton observed in Fig. 4.2 agrees with the value 1.815 eV determined from reflection measurements to be discussed in Section 4.4.

The electroreflectance spectrum of CuInSe₂ measured at 77 K is shown in Fig. 4.3. Since the built-in compressive distortion of this compound is small (actually slightly elongated), the crystal field parameter should be small and the electroreflectance spectrum should be polarization-independent. As expected, two polarization independent structures are observed and labeled *A*, *B* and *C* respectively in Fig. 4.3. Using the theory of Aspnes and Rowe (1971) for electroreflectance line shapes, the energy gap of CuInSe₂

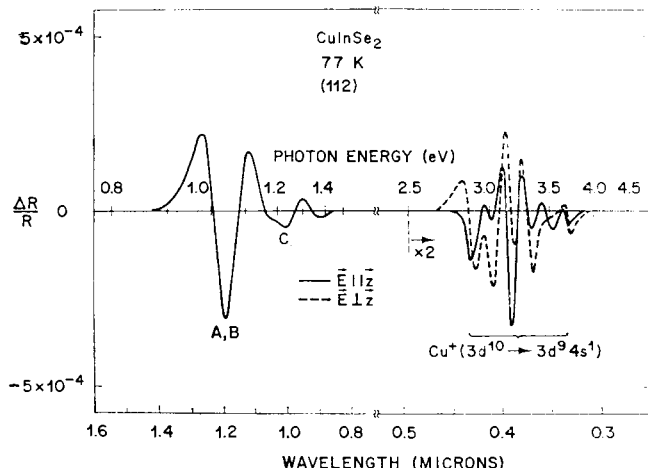


FIG. 4.3. Electroreflectance spectrum of CuInSe₂. (Shay *et al.*, 1973.)

deduced from the data in Fig. 4.3 is 1.013 eV at 77 K, which is ~ 1.3 eV less than the energy gap in the binary analog Zn_{0.5}Cd_{0.5}Se. Due to the lack of any polarization dependence to these structures, their separation of 0.23 eV is attributed to the spin-orbit parameter. This splitting is much less than the corresponding spin-orbit splitting of CdSe (0.42 eV) or ZnSe (0.43 eV), which comprise the binary analog. Similar results are obtained for CuGaSe₂ from the data in Fig. 4.4. The lowest band gap (1.68 eV) is ~ 1 eV below that of ZnSe the binary analog, and the spin-orbit parameter of 0.23 eV [deduced from the data using eq. (3.2)] is considerably less than the spin-orbit splitting measured in ZnSe (0.43 eV). These two anomalies, the downshift of the energy gaps relative to the binary analogs, and the reduced spin-orbit splittings, have been observed to various degrees in all I-III-VI₂ compounds investigated. Both effects results from the presence of noble metal *d*-levels in the valence band in a manner that we will describe later.

Despite the nearly cubic lattice constants of CuInSe₂ and the polarization independence of the *A*, *B*, and *C* structures, a strongly polarization dependent spectrum is observed in the 3–4 eV region (Fig. 4.3). This structure has been attributed to transitions to the lowest conduction band from valence band states derived from Cu 3*d*-levels, and has been labeled Cu⁺ ($3d^{10} \rightarrow 3d^9 4s^1$) to emphasize that significant portions of the

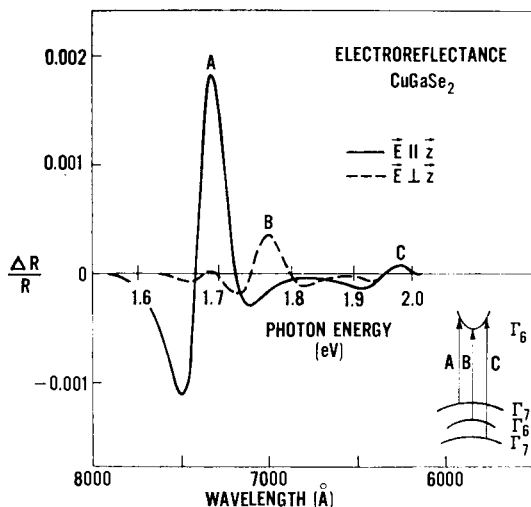


FIG. 4.4. Electrolyte electroreflectance spectrum of CuGaSe₂. (Shay *et al.*, 1972.)

wave function in both the initial and final states are centered on the Cu⁺ ions. It is thought that the polarization properties of this structure result from the large tetragonal distortion of the selenium atoms (almost) tetrahedrally located about the copper sites. Although it is difficult to unambiguously exclude the possibility that this structure is derived from the E_1 transitions in II-VI compounds, the superficial features of these data in CuInSe₂ are quite different from those of the ultraviolet structure observed in II-IV-V₂ crystals and related to E_1 transitions in III-V compounds (Section 3.5).

In another sample of CuInSe₂, the A , B , and C structures were considerably sharper than shown in Fig. 4.3. As can be seen in Fig. 4.5, the C structure is well resolved from the A , B doublet, and, in addition, the splitting of the doublet is resolved. From these data a spin-orbit parameter of 0.233 eV is determined. Note that the structure at the lowest energy gap (A in Fig. 4.5) is predominantly polarized $E \perp z$. This behavior has never before been observed in a chalcopyrite compound, but is the expected result for a crystal with a built-in dilation ($c > 2a$) rather than compression as is the usual situation. The measured splitting of the A and B peaks is 3.8 meV.

Whereas three valence bands have been observed in every selenide investigated, three valence bands have never been observed in the electroreflectance spectrum of any sulfide. Electroreflectance spectra for the series CuInS₂, CuGaS₂, and CuAlS₂ are shown in Fig. 4.6. For both CuGaS₂ and CuAlS₂, transitions from two valence bands are observed, one of which is observed only for $E \perp z$ and the other observed only for $E \parallel z$. For CuInS₂, only one, polarization-independent, spectrum is observed at 300 K. However, in low-temperature reflectance experiments (Section 4.4) the bandgap of CuInS₂ is found to be a polarization-independent doublet split by 10 meV. Similarly, the low-temperature reflectance of CuGaS₂ has resolved the higher energy transition into a doublet split by ~14 meV (Fig. 4.7). Consequently, it appears that the phenomenon reducing this spin-orbit splitting in the selenides, reduces the (smaller) spin-orbit splitting of sulfides to a value close to zero.

In Figs. 4.8 and 4.9 we present the electroreflectance spectra of CuInS₂ and CuGaS₂ over a wider spectral range. The polarization dependent structures in the 3-4 eV region are attributed to transitions from the Cu d -levels as already discussed for CuInSe₂.

TERNARY CHALCOPYRITE SEMICONDUCTORS

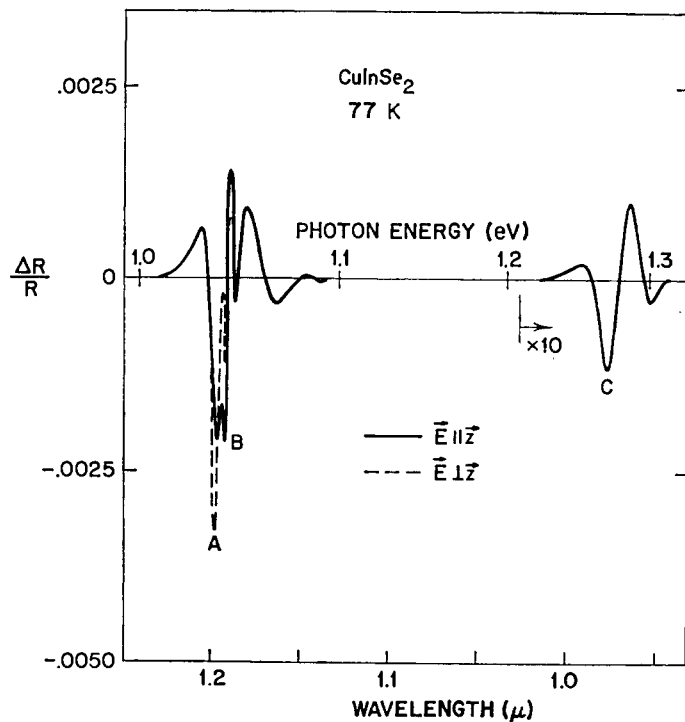


FIG. 4.5. Electroreflectance spectrum of a selected sample of CuInSe₂ for which the *A*, *B* splitting is resolved (Shay *et al.*, 1973.)

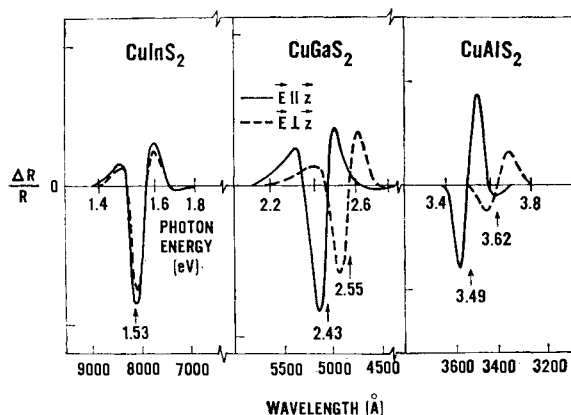


FIG. 4.6. Electrolyte electroreflectance spectra of CuInS₂, CuGaS₂, and CuAlS₂ near their respective direct energy gaps. (Shay *et al.*, 1972.)

ELECTRONIC STRUCTURE OF I-III-VI₂ SEMICONDUCTORS

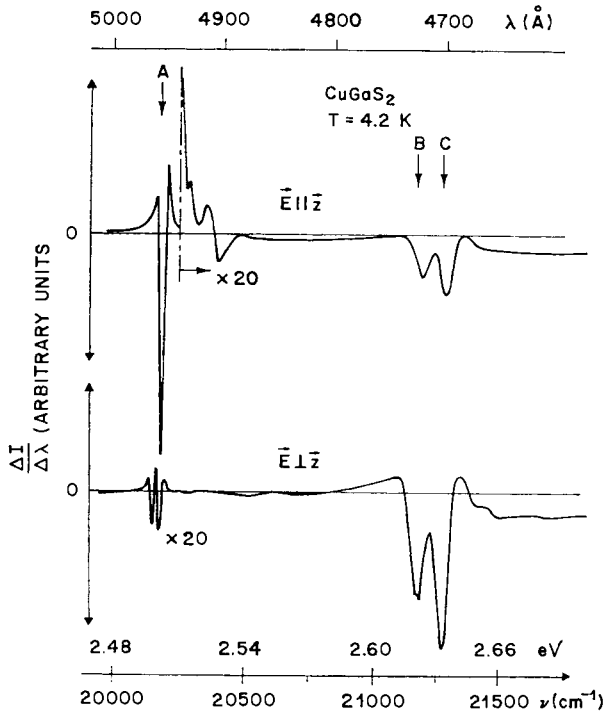


FIG. 4.7. Wavelength modulated reflectance spectra of CuGaS_2 at 4.2 K.
(Ringeissen *et al.*, 1972; Regolini *et al.*, 1973.)

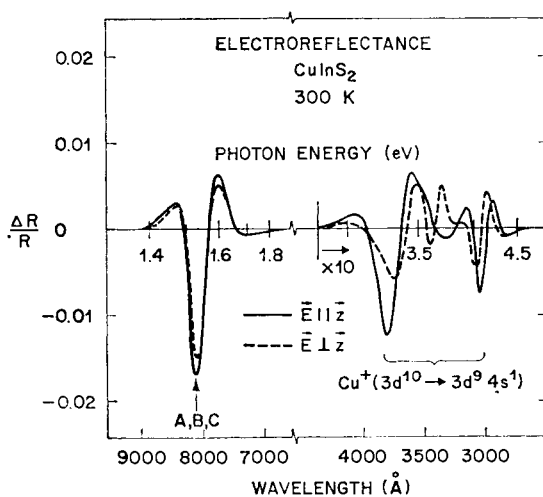


FIG. 4.8. Electrolyte electroreflectance spectrum of CuInS_2 . (Tell *et al.*, 1971.)

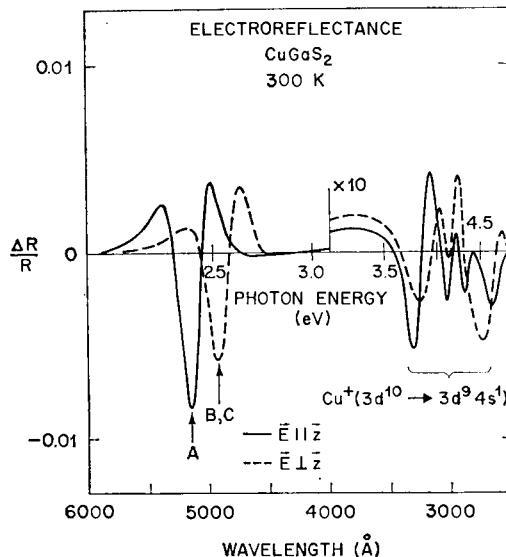


FIG. 4.9. Electrolyte electroreflectance spectrum of CuGaS_2 . (Tell *et al.*, 1971.)

4.2.2 Temperature Dependence of the Direct Energy Gap

In Fig. 4.10 we show the temperature dependences of the energy gaps of the chalcopyrite compounds CuInSe_2 and AgInSe_2 as well as those of CdSe and ZnSe , which comprise the binary analogs. It is apparent that the temperature dependences for the ternaries are anomalously low, especially for AgInSe_2 , for which no variation is observed within experimental error (± 5 meV). This effect cannot be explained by a decrease with temperature of the crystal field splitting, since Δ_{cf} decreases only by 22 meV between 77 and 300 K, which would tend to increase the energy gap by only ~ 14 meV.

Theoretical calculations of the temperature dependence of the energy gap in GaAs have shown that $\sim 10\%$ of the observed variation results from the lattice dilation with increasing temperature and $\sim 90\%$ results from electronic effects (Walter *et al.*, 1970). Hence the observations in AgInSe_2 could be explained by a lattice contraction with increasing temperature at a rate ~ 10 times larger than the dilation observed in GaAs. Although the temperature dependences of the lattice constants of AgInSe_2 has not been measured, it is considered extremely unlikely that such a peculiar dependence would occur.

The energy gap of CdSe , the binary analog of AgInSe_2 , decreases by ~ 80 meV as the temperature increases from 77 to 300 K, yet we find no variation of the energy gap in AgInSe_2 . Since the physical and electrical properties of AgInSe_2 and CdSe are otherwise very similar, this observation is clearly at odds with the usual explanation that the temperature dependence of the energy gap in a semiconductor is dominated by self-energies associated with phonon scattering (Long, 1968).

4.3 *p-d* Hybridization

The energy gaps observed in nine I-III-VI₂ compounds are listed in Table 4.1 together with the crystal-field and spin-orbit parameters derived from the data using

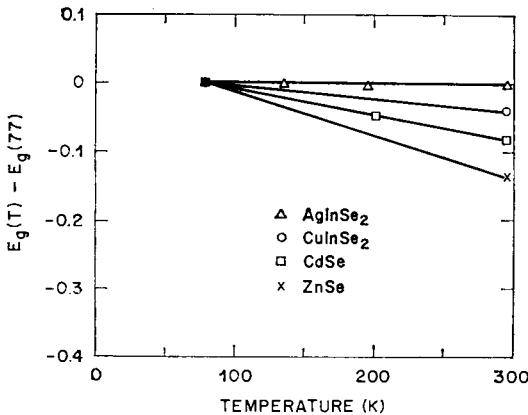


FIG. 4.10. Comparison of the temperature dependences of the energy gaps of AgInSe_2 and CuInSe_2 with those of CdSe and ZnSe which form the binary analogs. (Shay *et al.*, 1973.)

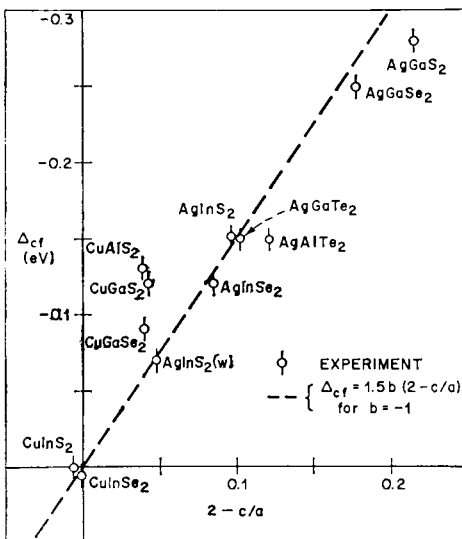


FIG. 4.11. Plot of the experimental crystal field parameters versus the respective compressive lattice distortions. The dashed curve corresponds to a uniaxial deformation potential of -1.0 .

eq. (3.2). The energy gaps have been determined from the electroreflectance data using the theory of Aspnes and Rowe (1971). In some cases the energy gaps differ slightly from previously reported values due to this refinement. We also include in Table 4.1 the theoretical results of Poplavnoi and Polygalov (1971) and the spin-orbit parameters observed in the binary analogs.

In Fig. 4.11 we have plotted the observed crystal-field parameters for several compounds as a function of their respective built-in lattice compressions. As discussed in

TERNARY CHALCOPYRITE SEMICONDUCTORS

 TABLE 4.1. Room temperature valence band parameters of I-III-VI₂ crystals (in eV)

	References	Energy gaps			-Δ _{cf}		Binary analog	Δ _{so}		Estimated % d-like
		A	B	C	Theory ^a	Expt.		Theory ^a	Expt.	
CuAlS ₂	b	3.49	3.62	3.62	—	0.13	0.07	—	0	35
CuGaS ₂	c	2.43	2.55	2.55	0.12	0.12	0.07	0.13	0	35
CuGaSe ₂	b	1.68	1.75	1.96	0.03	0.09	0.43	0.44	0.23	36
CuInS ₂	c	1.53	1.53	1.53	0.05	<0.005	0.07	0.17	-0.02	45
CuInSe ₂ †	d	1.04	1.04	1.27	0.04	-0.006	0.43	0.48	0.23	34
AgGaS ₂ †	e	2.73	3.01	3.01	—	0.28	0.07	—	0	20
AgGaSe ₂ †	e	1.83	2.03	2.29	—	0.25	0.42	—	0.31	16
AgInS ₂	f	1.87	2.02	2.02	—	0.15	0.07	—	0	20
AgInSe ₂	d	1.24	1.33	1.60	—	0.12	0.42	—	0.30	17

† 77 K.

^a Poplavnoi and Polygalov (1971).

^b Shay *et al.* (1972).

^c Tell *et al.* (1971).

^d Shay *et al.* (1973).

^e Tell *et al.* (1972).

^f Shay *et al.* 1974).

Section 3.2, uniaxial compression of a binary zincblende compound produces a negative Δ_{cf} given by

$$\Delta_{cf} = \frac{3}{2} b(2 - c/a), \quad (4.1)$$

where b is the (negative) deformation potential. It is apparent from Fig. 4.11 that the experimental values are negative as expected, and that eq. (4.1) can be fitted to the data if $b \approx -1.0$. This value is comparable to typical deformation potentials in zincblende II-VI compounds (Langer *et al.*, 1970). From this result we conclude that the sign and magnitude of Δ_{cf} in I-III-VI₂ compounds is dominated by the built-in lattice compression.

It is apparent from Table 4.1 that the observed spin-orbit parameters are considerably smaller than either the theoretical values or the splittings observed in the binary analogs. We pointed out earlier that the energy gaps observed in these ternary compounds are low relative to the energy gaps in the binary analogs by amounts up to 1.6 eV. It has been suggested that both of these effects result from the presence of noble metal d -levels in the valence bands in a manner sketched qualitatively in Fig. 4.12. The fivefold degenerate d -levels split into a threefold Γ_{15} and a twofold Γ_{12} in a tetrahedral field; p -levels transform as Γ_{15} . Allowing for spin splits the p -like Γ_{15} into a doublet Γ_8 above a singlet Γ_7 , whereas the d -like Γ_{15} splits into a doublet Γ_8 below a singlet Γ_7 . These results follow simply from a diagonalization of the $L \cdot S$ matrices. Interaction between the Γ_{15} levels in Fig. 4.12 will have two effects. The uppermost Γ_{15} will be raised to higher energy, i.e. the bandgap will be reduced, and the spin-orbit splitting of the uppermost valence bands will be reduced since the negative Δ_{so} of the d -levels

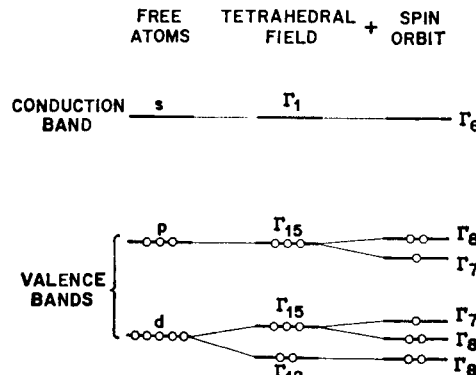


FIG. 4.12. Sketch of the expected behavior of *d*-levels in a tetrahedral field.

partially cancels the positive Δ_{so} of *p*-levels. A quantitative estimate of the amount of hybridization has been obtained (Shay *et al.*, 1972) using

$$\Delta_{so} = \alpha \Delta_p + (1 - \alpha) \Delta_d, \quad (4.2)$$

where Δ_{so} is the spin-orbit parameter observed in the ternary compound, Δ_p is the spin-orbit splitting observed in the (*p*-like) binary analog, Δ_d is the negative spin-orbit splitting of the *d*-levels themselves, and α is the fractional *p*-like character of the uppermost valence bands. Equation (4.2) has been used to deduce the hybridizations ($1 - \alpha$) from the observed Δ_{so} . For the present purpose we set $\Delta_{so} = 0$ for those sulfides for which no spin-orbit splitting was observed. The hybridizations estimated in this way are listed in Table 4.1, and vary from 16% to 45% *d*-like character over the series of compounds.

In Fig. 4.13 we have plotted for each compound, the downshift of the energy gap relative to its binary analog, and the fractional *d*-like character of the uppermost valence bands. We find that there is a noticeable correlation between these quantities, and that a straight line drawn through the data extrapolates to the known downshift and hybridization of the well understood zincblende compound CuCl (Cardona, 1963; Song, 1967a, b). We interpret this simple relationship as quantitative proof for the validity of *p-d* hybridization in I-III-VI₂ compounds.

The large hybridizations listed in Table 4.1 suggest that the *d*-bands are not far below the *p*-levels. The electroreflectance structures in the 3–4 eV regions of Figs. 4.3, 4.8, and 4.9 have been attributed to transitions from the Cu *d*-levels themselves to the lowest conduction band minimum. The arguments leading to this conclusion are as follows. The onsets of these structures are close to the separation of 3*d* and 4*s* levels on the Cu-atom (2.8 eV). Indeed, similar arguments were put forth to explain the anomalously low values for the energy gaps in copper halides. Furthermore, as already mentioned, the large hybridizations shown in Table 4.1 imply that the 3*d* levels are nearby. Also, despite the nearly cubic lattice constants ($2 - c/a \sim 0$), the structures in the 3–4 eV region of Figs. 4.3, 4.8, and 4.9 are strongly polarization dependent. These polarization properties may result from the large tetragonal distortion of the anions (almost) tetrahedrally located about the copper sites. Lastly, the general features of this structure are considerably different from those of the ultraviolet spectra of II-IV-V₂ compounds

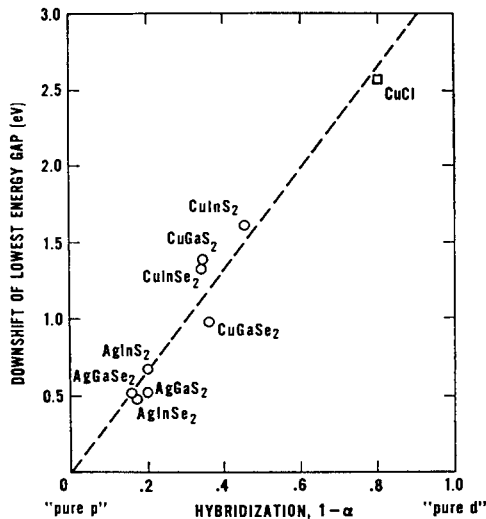


FIG. 4.13. Plot of the downshift of the energy gap of a I-III-VI₂ compound relative to its binary analog, as a function of the *d*-like character of the uppermost valence bands determined from the observed spin-orbit splittings. (Shay and Kasper, 1972.)

which result from transitions related to the Λ transitions in zincblende compounds (Section 3.5).

From the data in Fig. 4.3 one can estimate directly the ordering and symmetries of the five levels derived from the Cu *d*-band in CuInSe₂. It is easy to show that the five-fold degenerate *d*-levels lead to three Γ_7 states and two Γ_6 states at $\mathbf{k} = 0$ in the point group D_{2d} . Since transitions from Γ_6 levels to the Γ_6 conduction band are forbidden for $E \parallel z$, we determine directly from Fig. 4.3 that the second and fourth bands (observed only for $E \perp z$) have Γ_6 symmetry. Hence the valence bands derived from Cu 3*d*-levels have the ordering $\Gamma_7, \Gamma_6, \Gamma_7, \Gamma_6$, and Γ_7 in CuInSe₂.

Since the only available energy band calculation ignores Cu *d*-levels, it is not surprising that it fails to explain the structure of the uppermost valence bands. In Table 4.1, we compare the theoretical crystal-field (A_{cf}) and spin-orbit (A_{so}) parameters with the experimental results and find that the agreement is totally unsatisfactory. The observed spin-orbit parameters are in all cases less than theoretical values due to the admixture of *d* wavefunctions into the *p*-like valence band states. The observed crystal-field parameters (A_{cf}) are in most cases considerably more negative than the theoretical values, which suggests that the uniaxial deformation potential of *d*-bands may be larger than for *p*-bands. The most notable failure of the energy band calculation ignoring *d*-bands is the prediction that CuInS₂ and CuInSe₂ have indirect energy gaps ~ 0.3 eV below the direct gaps. Extensive measurements of the photoluminescence spectra to be presented in Chapter 5 show clearly that both of these compounds as well as all other sulfides and selenides of Cu and Ag with In, Ga, or Al, have direct energy gaps. It has been suggested, therefore, that the proximity of Cu *d*-levels dominates the energy band structure of I-III-VI₂ compounds containing Cu, and must be included in a realistic energy band calculation.

4.4. Exciton Optical Properties

Exciton states dominate the low-temperature optical properties of many I-III-VI₂ compounds, as they do for the II-VI analogs. The near normal reflection spectrum of CuGaS₂ is shown in Fig. 4.14 near the lowest energy exciton, which is active only for E || z. The solid curve in Fig. 4.14 is a theoretical fit to the reflectivity using two uncoupled, damped classical oscillators representing the exciton ground state and the first excited state. The contribution of each to the complex dielectric function is given by

$$\epsilon = \frac{4\pi\beta E_o^2}{(E_o^2 - E^2) - iE\Gamma}, \quad (4.3)$$

where E_o is the oscillator energy in eV, Γ in the damping constant in eV, and $4\pi\beta$ is a dimensionless quantity proportional to the oscillator strength. The reflectivity R is given by

$$R = \frac{(n - 1)^2 + k^2}{(n + 1)^2 + k^2}, \quad (4.4)$$

where n and k are the refractive index and extinction coefficient, respectively, obtained from the real (ϵ') and imaginary (ϵ'') parts of the dielectric function

$$\epsilon = \epsilon' + ie'' = (n + ik)^2. \quad (4.5)$$

The parameters used for the solid curve in Fig. 4.14 are included in Table 4.2.

In the hydrogenic approximation, the exciton Rydberg is equal to four-thirds of the separation between the ground and first-excited states. For CuGaS₂ (Fig. 4.14) this amounts to 29 meV. For comparison, the exciton Rydbergs in the binary analogs CdS and ZnS are 29 and 40 meV respectively (Segall and Marple, 1967). The oscillator strength of the ground state exciton in CuGaS₂ is $4\pi\beta = 0.015$, which is slightly larger than the equivalent for CdS (~ 0.012).

The absorption spectrum of CuGaS₂ measured at 2 K for E ⊥ z is shown in Fig. 4.15. For comparison, the peak absorption at the A($n = 1$) exciton expected for E || z is estimated to be $\sim 1.5 \times 10^6$ cm⁻¹ using the oscillator strength determined by the fit to the reflectivity in Fig. 4.14. Therefore the A exciton is ~ 2500 stronger for E || z than for E ⊥ z. If we naively assume the applicability of eq. (3.3) we calculate from this polarization ratio, a spin-orbit parameter Δ_{so} of ~ 5.1 meV which is to be compared with the observed value of 21 meV from the data in Fig. 4.7. Consequently, the strength of the absorption peak A($n = 1$) in Fig. 4.15 is weaker than would be expected on the basis of the observed spin-orbit splitting. Of course, the very hybridization of p- and d-levels which reduces Δ_{so} to such a small value renders eq. (3.3) invalid, since it was derived using p-like wave functions alone. The points in Fig. 4.15 represent a theoretical fit to the absorption spectra using the parameters in Table 4.2 for the A($n = 1$) exciton, and $4\pi\beta = 0.015$ and $\Gamma = 4$ meV for the B and C excitons at ~ 2.64 eV. From the A and B,C energy gaps listed in Table 4.2, we deduce a crystal-field parameter Δ_{cf} of 126 meV for CuGaS₂ at 2 K, which is to be compared with the room temperature value of 120 ± 5 meV (Table 4.1). Since we have seen earlier (Fig. 4.11) that Δ_{cf} is dominated by the lattice distortion, this slight decrease of Δ_{cf} with increasing temperature probably results from a reduction in the lattice distortion ($2 - c/a$). This cannot be substantiated at present since all available lattice constants have been measured at

TERNARY CHALCOPYRITE SEMICONDUCTORS

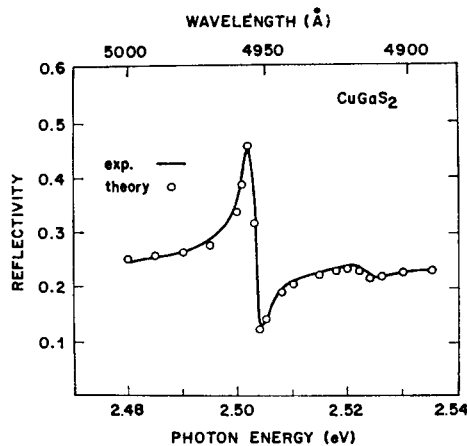


FIG. 4.14. Exciton reflectance spectrum of a (112) platelet of CuGaS₂, at 2 K for $E \parallel z$. The solid curve is a classical oscillator fit using the parameters in Table 4.2. (Tell and Kasper, 1973.)

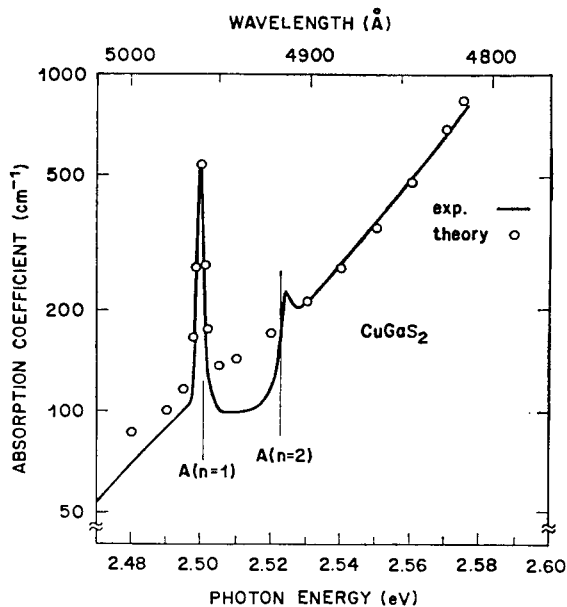


FIG. 4.15. Absorption coefficient of CuGaS₂ at 2 K for $E \perp z$. The vertical lines indicate the excitons observed in the reflectivity (Fig. 4.14). The solid curve is a classical oscillator fit using the parameters in Table 4.2. (Tell and Kasper, 1973.)

TABLE 4.2. Exciton parameters at 2K

Crystal	A exciton						B exciton				References	
	$n = 1$			$n = 2$			$n = 1$					
	E_{\star} (eV)	Γ (meV)	$4\pi\beta$	E_{\star} (eV)	Γ (meV)	$4\pi\beta$	E_{\star} (eV)	Γ (meV)	$4\pi\beta$	E_g (eV)		
CuGaS ₂	2.501	1.5	0.01	2.523	3	0.00125	29	2.530	2.627	~2.656	a, b	
CuInS ₂	1.536	1.3	0.01					1.554	3.0	0.02	c	
AgGaS ₂	2.698	1.2	0.015	2.719			28	2.726	2.98		d	
AgGaSe ₂	1.815			1.826			15	1.830	~2.02		d	
AgInS ₂ [†]	2.025								2.092		e	
AgInSe ₂	1.245										f	

[†] Wurtzite structure, all else chalcopyrite.^a Tell *et al.* (1971), Regolini *et al.* (1973), Ringeissen *et al.* (1972).^b Tell and Kasper (1973).^c Shay *et al.* (1972).^d Tell *et al.* (1972).^e Shay *et al.* (1974).^f Shay *et al.* (1973).

TERNARY CHALCOPYRITE SEMICONDUCTORS

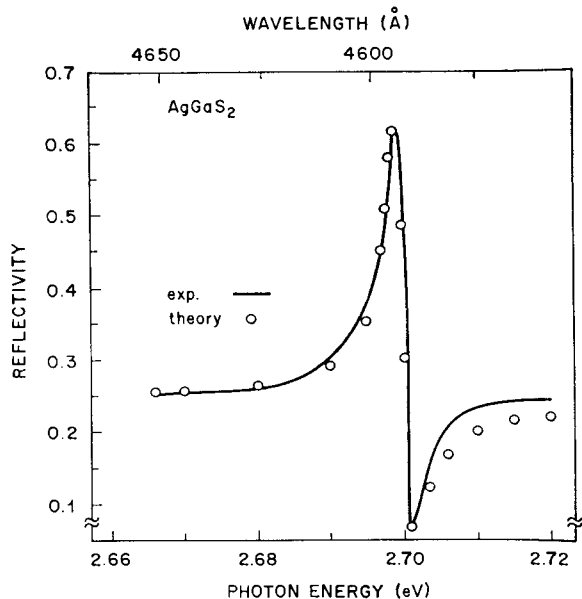


FIG. 4.16. Exciton reflectance spectrum of a (112) platelet of AgGaS_2 at 2 K for $\mathbf{E} \parallel \mathbf{z}$. (Tell *et al.*, 1972.)

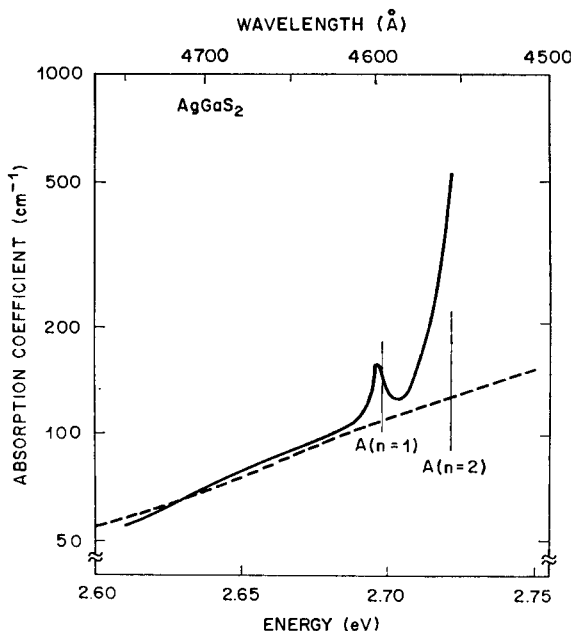


FIG. 4.17. Absorption coefficient of AgGaS_2 at 2 K for $\mathbf{E} \perp \mathbf{z}$. (Tell *et al.*, 1972.) The vertical lines indicate the energies of the $A(n=1)$ and $A(n=2)$ excitons in the reflectance spectrum. (Tell and Kasper, 1971.)

ELECTRONIC STRUCTURE OF I-III-VI₂ SEMICONDUCTORS

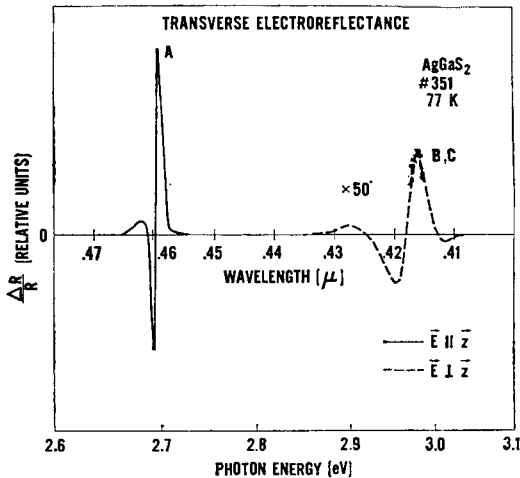


FIG. 4.18. Transverse electroreflectance spectra of a (112) platelet of AgGaS₂ at 77 K. (Tell *et al.*, 1972.)

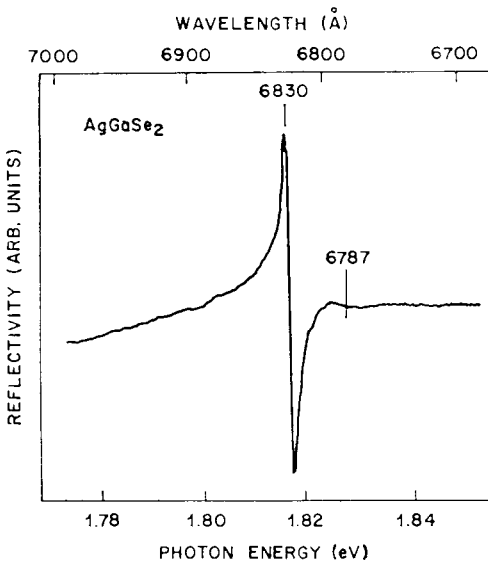


FIG. 4.19. Exciton reflectance spectrum of AgGaSe₂ at 2 K. (Tell and Kasper, 1971.)

300 K. A similar decrease in Δ_{ef} has been observed in AgInSe₂ (Shay *et al.*, 1973) in which Δ_{ef} decreased from 143 to 121 meV between 77 and 300 K.

The exciton reflectance spectrum of AgGaS₂ is shown in Fig. 4.16 together with a single oscillator fit. The absorption spectrum measured for $E \perp z$ is shown in Fig. 4.17. The dashed curve is an estimated background absorption resulting from the heavily broadened *B* and *C* excitons at 2.98 eV. Correcting for the different linewidths as observed in absorption and reflection, and for the (112) orientation of the platelets, the polarization ratio of the *A*($n = 1$) exciton is found to be $\sim 10^4$. From the observed

TERNARY CHALCOPYRITE SEMICONDUCTORS

polarization ratio, one estimates a spin-orbit parameter A_{so} of ~ 5.8 meV. The broadening of the electroreflectance spectrum (Fig. 4.18) precludes observation of such a small splitting of the B,C doublet. Since the hybridization of the valence bands in AgGaS_2 is much less than in CuGaS_2 (Table 4.1), eq. (3.3) might provide a realistic estimate of A_{so} .

A single reflectivity anomaly is also observed in AgGaSe_2 at 2 K for light polarized $\mathbf{E} \parallel z$ (Fig. 4.19). The weak structure near 1.826 eV is attributed to the $n = 2$ excited state. Since the polarization ratio at the A exciton is estimated to be ~ 15 based on room temperature electroreflectance measurements, it is not surprising that the 2 K absorption coefficient for $\mathbf{E} \perp z$ is too large to permit observation of the line spectrum.

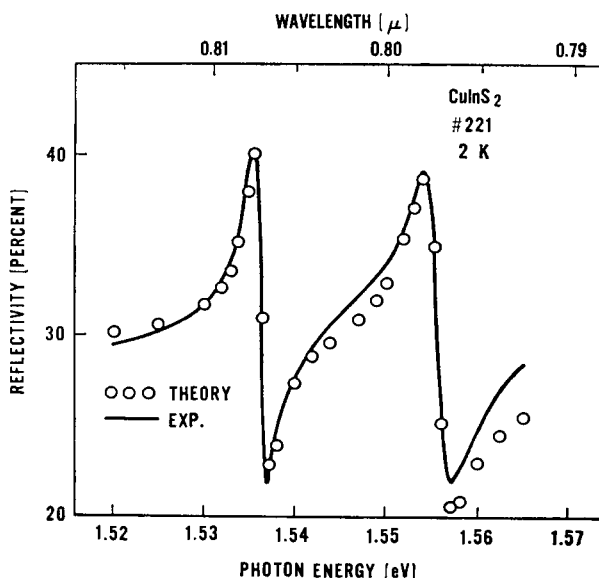


FIG. 4.20. Exciton reflectance spectrum of a (112) platelet of CuInS_2 at 2 K. (Tell *et al.*, 1971.)

The absence of any polarization dependence to the low-temperature reflectivity spectrum of CuInS_2 (Fig. 4.20) indicates that the splitting of the energy levels is spin-orbit in nature. For virtually all tetrahedrally coordinated crystals, spin-orbit interaction splits the valence bands such that the lowest energy transition is doubly degenerate followed by a nondegenerate transition at slightly higher energy. For CuInS_2 just the opposite is observed. The damped-oscillator fit to the data in Fig. 4.20 yields an oscillator strength for the higher energy transition which is twice as strong as that for the lower-energy transition. This result indicates a negative spin-orbit splitting such as previously observed in only two compounds, CuCl (Cardona, 1963) and ZnO (Thomas, 1960).

Recent measurements of the modulated-reflectance spectra of $\text{CuGa}_x\text{In}_{1-x}\text{S}_2$ alloys confirm this conclusion (Tell *et al.*, 1974). As shown in Fig. 4.21 the addition of slight amounts of Ga to CuInS_2 shifts the direct energy gap (A) to higher energies, lifts the degeneracy of the B,C transitions, and produces an observable polarization dependence

ELECTRONIC STRUCTURE OF I-III-VI₂ SEMICONDUCTORS

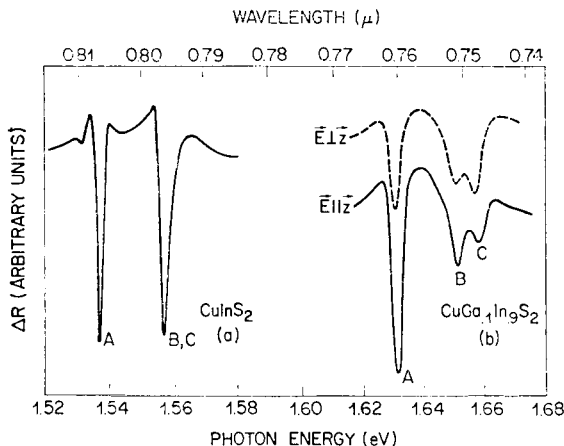


FIG. 4.21. Wavelength modulated reflectance spectra at 2 K of (a) CuInS₂ and (b) CuGa_{0.1}In_{0.9}S₂. The CuInS₂ sample was a (112) platelet and the alloy was a (102) platelet, so $E \parallel z$ is only nominal, where z is the optic axis (Tell *et al.*, 1974).

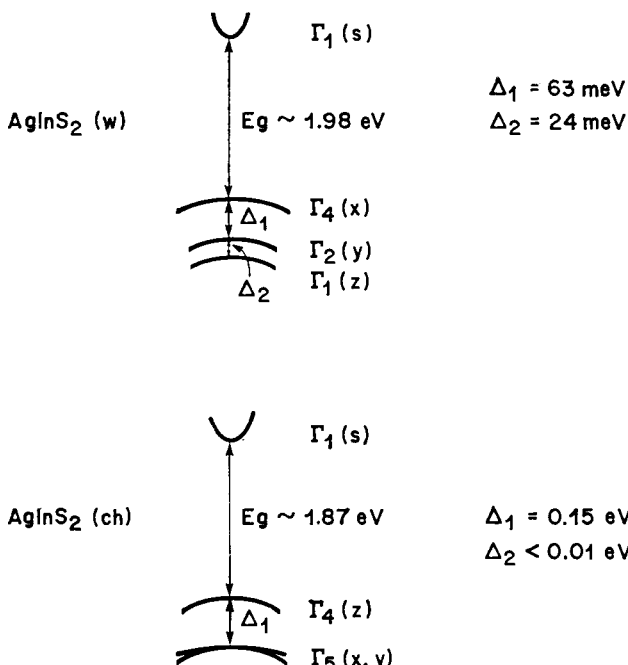


FIG. 4.22. Energy band structures of orthorhombic (w) and chalcopyrite (ch) AgInS₂ as deduced from room temperature electroreflectance measurements (Shay *et al.*, 1974).

TERNARY CHALCOPYRITE SEMICONDUCTORS

in the spectrum. The crystal field splitting derived from these data is linear in x varying from zero in CuInS₂ to ~ 131 meV in CuGaS₂. From these results it is concluded that (1) the spin-orbit splitting is negative in CuInS₂, (2) the crystal-field splitting dominates the valence band structure in CuGaS₂, and (3) the vanishing crystal-field splitting in CuInS₂ results from an accidental cancellation of competing phenomena.

The symmetries and splittings of the uppermost valence bands in orthorhombic and chalcopyrite AgInS₂ have recently been determined from electroreflectance measurements on oriented crystals using polarized radiation (Fig. 4.22). The principal features of the valence-band structures in both phases are dominated by the deviations of the lattice constants from ideal wurtzite and chalcopyrite, respectively. On the other hand, the small splitting of the lowest two valence bands in orthorhombic AgInS₂ is attributed to the "wurtzite-like" potential.

The temperature dependence of the lowest energy excitons in these I-III-VI₂ compounds is quite surprising. Whereas the free exciton shifts 1.5 meV to lower energy in CuGaS₂ as the temperature is raised from 2 to 77 K, the free exciton shifts 1.3, 5.4, and 2.7 meV to higher energy in CuInS₂, AgGaS₂ and AgGaSe₂ respectively. The physical origin of these shifts is as yet unidentified.

References

- ASPNES, D., and ROWE, J. E. (1971) *Phys. Rev. Lett.* **27**, 188.
CARDONA, M. (1963) *Phys. Rev.* **129**, 69.
LANGER, O. W., EUWEMA, R. N., ERA, K., and KODA, T. (1970) *Phys. Rev. B*, **2**, 4005.
LONG, D. (1968) *Energy Bands in Semiconductors*, Interscience pp. 50ff.
POPLAVNOI, A. S., and POLYGALOV, YU. I. (1971) *Izv. Akad. Nauk SSSR, Neorgan. Mater.* **7**, 1706, 1711 [*Inorgan. Mater. (USSR)* **7**, 1527, 1531 (1971)].
REGOLINI, J. L., LEWONCZAK, S., RINGEISSEN, J., NIKITINE, S., and SCHWAB, C. (1973) *Phys. Status Solidi (b)* **55**, 193.
RINGEISSEN, J., REGOLINI, J. L., and LEWONCZAK, S. (1972) *Proceedings of the 1st International Conference on Modulation Spectroscopy, Tucson, Arizona*.
SEGALL, B., and MARPLE, D. T. F. (1967) In *Physics and Chemistry of II-VI Compounds* (ed. M. Aven and J. S. Prener), North-Holland, p. 319.
SHAY, J. L., and KASPER, H. M. (1972) *Phys. Rev. Lett.* **29**, 1162.
SHAY, J. L., and TELL, B. (1973) *Surface Science* **37**, 748.
SHAY, J. L., TELL, B., KASPER, H. M., and SCHIAVONE, L. M. (1972) *Phys. Rev. B*, **5**, 5003.
SHAY, J. L., TELL, B., KASPER, H. M., and SCHIAVONE, L. M. (1973) *Phys. Rev. B*, **7**, 4485.
SHAY, J. L., TELL, B., KASPER, H. M., SCHIAVONE, L. M. and THIEL, F. (1974) *Phys. Rev. B*, (to be published).
SONG, K. S. (1967a) *J. Phys. (Paris)* **28**, 195.
SONG, K. S. (1967b) *J. Phys. Chem. Solids* **28**, 2002.
TELL, B., and KASPER, H. M. (1971) *Phys. Rev. B*, **4**, 4455.
TELL, B., and KASPER, H. M. (1973) *Phys. Rev. B*, **7**, 740.
TELL, B., SHAY, J. L., and KASPER, H. M. (1971) *Phys. Rev. B*, **4**, 2463.
TELL, B., SHAY, J. L., and KASPER, H. M. (1972) *Phys. Rev. B*, **6**, 3008.
TELL, B., SHAY, J. L., and KASPER, H. M. (1974) (to be published).
THOMAS, D. G. (1960) *J. Phys. Chem. Solids* **15**, 86.
WALTER, J. P., ZUCCA, R. R. L., COHEN, M. L., and SHEN, Y. R. (1970) *Phys. Rev. Lett.* **24**, 102.

CHAPTER 5

LUMINESCENCE

SINCE many of the II-IV-V₂ compounds and all of the I-III-VI₂ compounds discussed in Chapters 3 and 4 have direct energy gaps, radiative recombination in these crystals can be rather efficient. The energy gaps in the various compounds span the range from the infrared ($\sim 5 \mu$), to the ultraviolet ($\sim 0.35 \mu$). In this chapter we review studies of the (1) spontaneous luminescence, (2) stimulated emission and laser action, and (3) light-emitting diodes employing ternary chalcopyrite compounds.

5.1 Luminescence Spectra of II-IV-V₂ Compounds

5.1.1 CdSnP₂

The photoluminescence of undoped crystals of CdSnP₂ at 1.7 K reveals the presence of sharp (~ 0.3 meV FWHM) bound exciton lines a few meV below the energy gap at 1.240 eV (Fig. 5.1). These lines are only found at selected regions on a given crystal. For uniform excitation the dominant luminescence is a broad featureless band (~ 30 meV FWHM) located 83 meV below the energy gap. The addition of Ag to the Sn:CdP₂ solution during growth results in an efficient emission which is exceptionally homogeneous over a given crystal (Fig. 5.2). At low excitation levels there are three bands at 1.004, 1.028, and 1.072 μ ; a weaker band is sometimes observed at 1.124 μ . For comparison the energy gap is located at 1.000 μ (1.240 eV). As the excitation level is increased, the 1.004 μ line grows linearly in the excitation intensity, but the three bands at longer wavelength rapidly saturate. For example, at an excitation intensity of 1 kW/cm² the 1.004 μ line is ~ 100 times more intense than the bands at longer wavelength. At the impurity concentrations present in these crystals ($\sim 10^{18}$ cm⁻³), donor levels merge into the continuum, and for the free-carrier concentrations present ($\sim 10^{17}$ cm⁻³), excitons do not exist since they are screened out by the free electrons. Therefore the 1.004 μ line which lies ~ 5 meV below the energy gap in a pure crystal is attributed to "band-to-band" recombination, and the three bands at longer wavelengths are attributed to Ag impurity complexes.

The photoluminescence spectrum of a crystal of CdSnP₂ doped with Cu is also shown in Fig. 5.2 and compared with the emission measured for an Ag-doped crystal under identical conditions. The photoluminescence from the Cu-doped crystals consists of a broad band 0.13 eV below the bandgap, and several diffuse bands closer to the bandgap. The band-to-band recombination is at least 100 times weaker than in Ag-doped crystals. Since the CdSnP₂:Cu crystals are weakly *p*-type, the broad band may result from a conduction band to acceptor-level transition for a Cu acceptor energy of 0.13 eV.

At the high excitation-levels available with a pulsed N₂ laser, a new emission band

TERNARY CHALCOPYRITE SEMICONDUCTORS

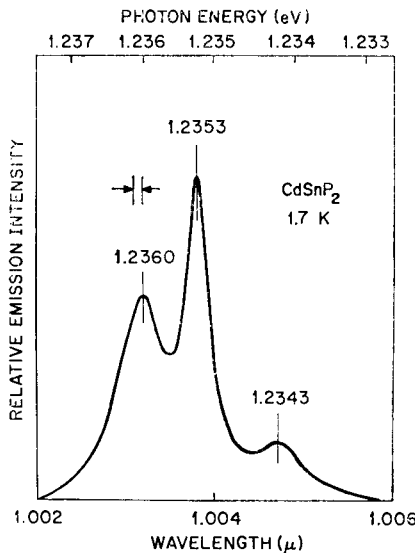


FIG. 5.1. Photoluminescence spectrum of undoped CdSnP_2 . (Shay *et al.*, 1970a.)

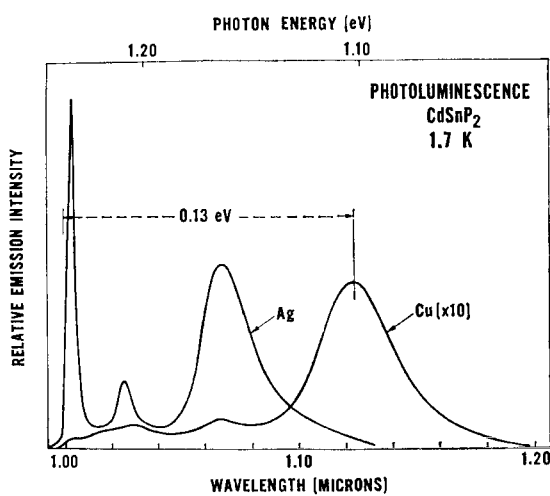


FIG. 5.2. Photoluminescence spectrum of CdSnP_2 doped with Cu or Ag. (Shay *et al.*, 1972.)

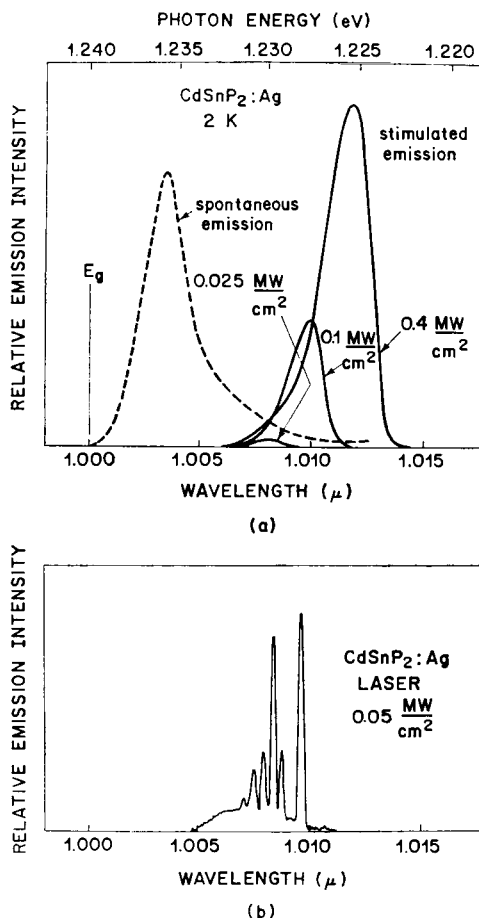


FIG. 5.3. (a) Comparison of the spontaneous-emission spectrum and the stimulated spectra observed for three values of the N_2 laser intensity. (b) Laser emission spectra of $\text{CdSnP}_2:\text{Ag}$ measured slightly above threshold of $\sim 50 \text{ kW/cm}^2$. (Shay *et al.*, 1972.)

appears $\sim 10 \text{ meV}$ below the band-to-band recombination in Ag-doped crystals as shown in Fig. 5.3a. The intensity of the new band increases superlinearly in the excitation intensity and shifts to longer wavelengths with unusual saturation characteristics similar to those previously observed in InP and GaAs. These features suggest that the new band results from stimulated (superradiant) emission. Indeed, in crystals suitably prepared to form Fabry-Perot cavities, narrow-line laser emission is observed as shown in Fig. 5.3b. The question immediately arises as to whether the spontaneous and stimulated (or laser) emission result from the same mechanism, i.e. band-to-band recombination, since the displacement to lower energy by $\sim 10 \text{ meV}$ could indicate a different recombination mechanism. As shown in Fig. 5.4, in an applied magnetic field the spontaneous- and stimulated-emission spectra shift to higher energies at precisely the same rate, implying that they result from the same recombination mechanism, namely band-to-band transitions. The shift in a magnetic field should therefore follow the shift of the bandgap, $\frac{1}{2} \hbar \omega_c$, but it is clear from Fig. 5.4 that the measured

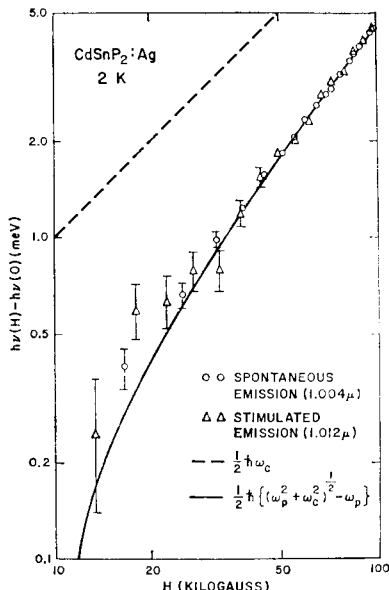


FIG. 5.4. Shift of the spontaneous and stimulated emission peaks in Fig. 5.3a as a function of magnetic field. (Shay *et al.*, 1971a).

shift is considerably less. It has been suggested that the resolution of this discrepancy requires proper account of electron-plasmon coupling (Shay *et al.*, 1971a).

As the temperature is increased, the laser emission shown in Fig. 5.3b shifts to longer wavelength following the shift of the bandgap ($\sim 2.5 \times 10^{-4}$ eV/K at high temperatures). Whereas the optically pumped CdSnP_2 lasers at $1.015\ \mu$ at 80 K, it has been reported that electron-beam-pumped CdSnP_2 lasers at $1.011\ \mu$ at 80 K (Berkovskii *et al.*, 1968a). The difference of $\sim 40\ \text{\AA}$ in the emission wavelength for electron-beam-pumped and optically pumped CdSnP_2 lasers has not been explained, although it may result from the lower diffraction losses associated with the deeper penetration depth of the electron beam.

5.1.2 CdSiAs_2

The photoluminescence spectrum of a crystal of CdSiAs_2 grown by iodine transport is shown in Fig. 5.5. Since this crystal was *p*-type at 300 K, the 21 meV spacing between the doublets may represent the binding energy of the dominant acceptor. In such a case, the higher energy components of each doublet would involve transitions from the conduction band to the valence band (1.635 eV) and to the acceptor (1.614 eV). The lower energy components would involve transitions from a donor to the valence band (1.632 eV) and to the acceptor (1.611 eV). Further study is required to substantiate this model.

The cathodoluminescence spectrum of a CdSiAs_2 crystal grown from solution is shown in Fig. 5.6. At a low excitation intensity, the emission band at $\sim 0.79\ \mu$ was attributed to the electronic transitions from the conduction band to a shallow acceptor ~ 0.03 eV above the valence band maximum. When the pumping level was increased, the short-wavelength band near $0.77\ \mu$ increased quadratically and became predominant at a current density of $\sim 1\ \text{A/cm}^2$ (curve 1 in Fig. 5.7). The intensity of this radiation

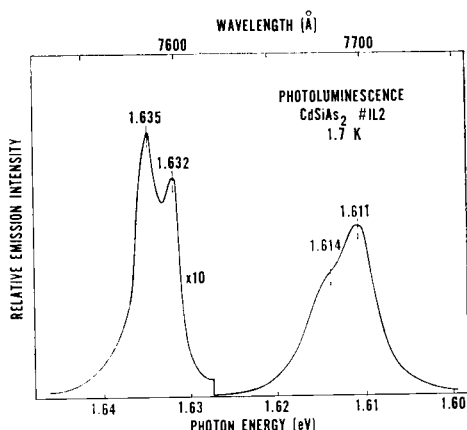


FIG. 5.5. Photoluminescence spectrum of a CdSiAs₂ crystal grown by iodine transport.

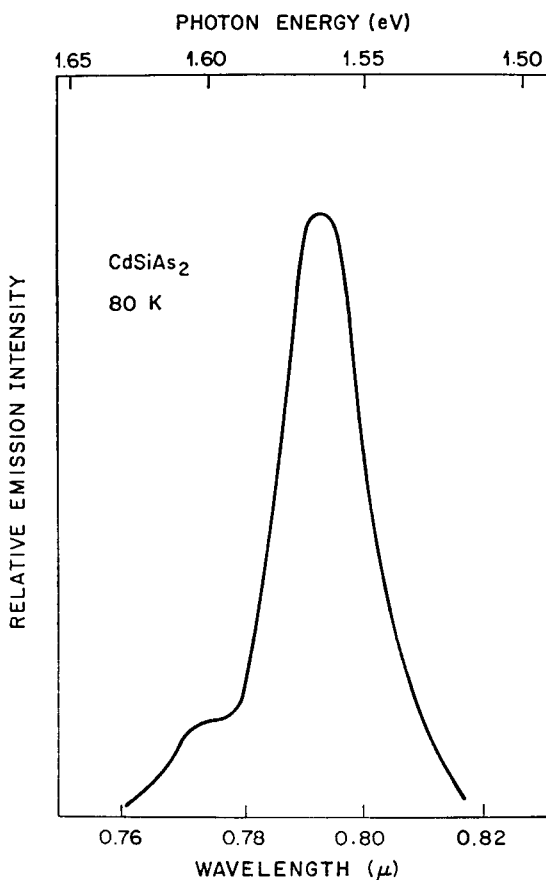


FIG. 5.6. Cathodoluminescence spectrum (at 80 K) of a CdSiAs₂ crystal grown from a (CdAs) solution. (Averkieva *et al.*, 1971).

increased suddenly by about two orders of magnitude at an excitation intensity of $\sim 3 \text{ A/cm}^2$ (60 kW/cm^2) and the width of the emission line decreased to 10 \AA (curve 2 in Fig. 5.7). These observations indicated that the threshold for coherent emission had been reached. Since the half width of the 0.77μ line was less than kT at subthreshold excitation, it was concluded that the stimulated radiation was due to radiative annihilation of excitons. This interpretation is probably not right, since it is currently believed that near bandgap laser action in covalent crystals (such as GaAs and CdSiAs₂) results from basically band-to-band transitions modified by the electron-hole gas due to the excitation (Johnston, 1972).

5.1.3 ZnSiP₂

A rather bright, red photoluminescence (Nahory *et al.*, 1970) and cathodoluminescence (Shay *et al.*, 1970b) has been observed in ZnSiP₂ crystals grown by iodine transport (Fig. 5.8). Time resolved spectral measurements have established that this red emission arises from the radiative recombination of a bound exciton with phonon sidebands, $L_1 = 6.5 \text{ meV}$, a local mode, and $\hbar\omega_{L0} = 22.7 \text{ meV}$, a bulk lattice mode. Zeeman studies of the splitting of the highest energy emission line reveal that the center responsible for the emission is an exciton bound to an ionized or iso electronic impurity (Shah and Buehler, 1971). From the failure of the emission and excitation spectra in Fig. 5.8 to overlap at a no-phonon line, Shah (1972) has concluded that the unidentified center cannot absorb or emit light without the help of a phonon of energy $\hbar\omega_0 = 9.3 \text{ meV}$. Consequently, ZnSiP₂ has an indirect or a weak pseudodirect energy gap. This result agrees with the electroreflectance measurements discussed in Section 3.3 which showed that the lowest direct energy gap in ZnSiP₂ with an appreciable oscillator strength lies at 2.96 eV at 300 K . The absorption edge near 2 eV and the luminescence in Fig. 5.8 therefore involve a lower lying conduction band minimum. Other emission lines unrelated to the spectrum in Fig. 5.8 have been observed in ZnSiP₂ and imply the existence of an energy gap near 2.05 eV at 2 K .

ZnSiP₂ crystals doped with various donors or acceptors display broad emission bands peaking at energies between 1.5 – 1.8 eV depending upon the impurity (Alekperova *et al.*, 1969). The absolute quantum yield in the brightest of these crystals has been estimated to be 0.05% at 80 K . *p*-type conductivity has never been reported for ZnSiP₂, so junction electroluminescence seems unlikely.

5.1.4 Other II–IV–V₂ Crystals

Luminescence spectra of other II–IV–V₂ crystals are rather scanty. Line narrowing as the excitation intensity was increased has been reported in CdGeAs₂ at 0.607 eV (Borshchhevskii *et al.*, 1968). The line narrowing was attributed to stimulated emission for electron-beam current densities above $\sim 1 \text{ A/cm}^2$ at a beam voltage of 25 kV . The photoluminescence spectrum of ZnSnP₂ depends upon the crystal structure (Berkovskii *et al.*, 1968b). Chalcopyrite crystals emit in a broad band centered at 1.52 eV . Sphalerite crystals emit in a band of comparable width centered at 1.26 eV . A near infrared (1.3 – 1.4 eV) photoluminescence has been observed in CdGeP₂ doped with In, Ga, or Te (Goryunova *et al.*, 1968; Wiley *et al.*, 1973). However, the lack of sufficient *p*- and *n*-type conductivity renders electroluminescence in this compound unlikely.

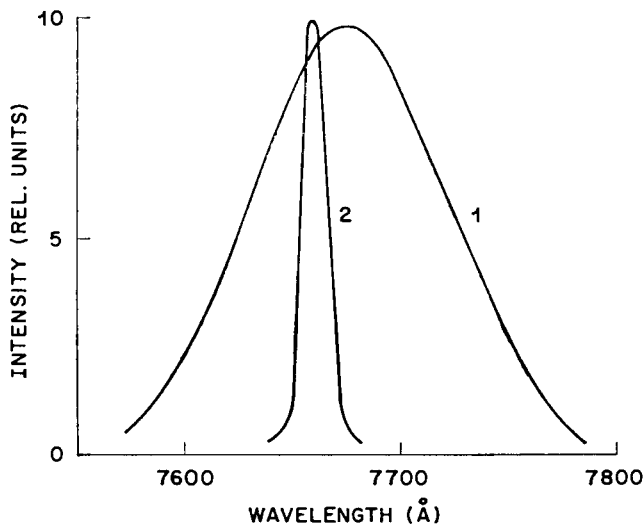


FIG. 5.7. Cathodoluminescence spectra (at 80 K) of the CdSiAs_2 crystal in Fig. 5.6 at high excitation levels: (1) 20 kW/cm^2 ; (2) 60 kW/cm^2 . (Averkieva *et al.*, 1971.)

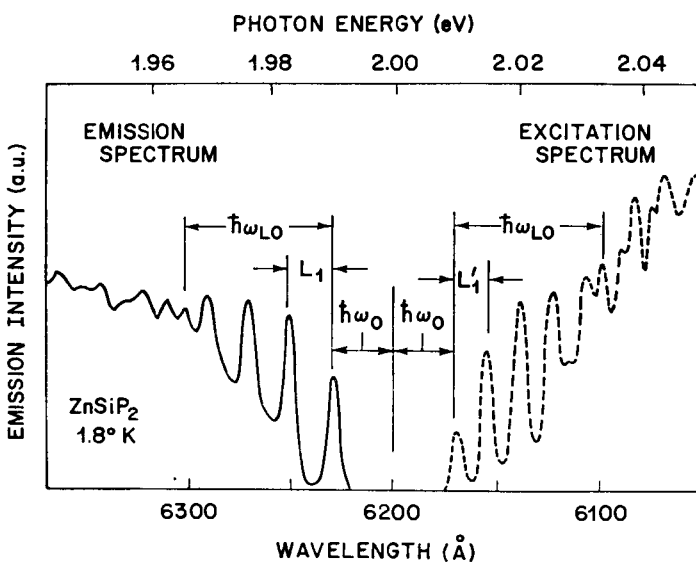


FIG. 5.8. Photoluminescence emission and excitation spectra of ZnSiP_2 . (Shah, 1972.)

5.2 Luminescence Spectra of I–III–VI₂ Compounds

5.2.1 AgInSe₂ and CuInSe₂

The 2 K photoluminescence and reflectivity spectra of AgInSe₂ are shown in Fig. 5.9. The weak anomaly observed in the reflectivity at 1.245 eV is attributed to the lowest energy exciton. The photoluminescence spectrum consists of a few lines near 1.240 eV and a broad band near 1.19 eV. The shoulder near 1.245 eV is believed to result from decay of free excitons, whereas the other lines and the band at 1.19 eV are attributed to impurities. In Fig. 5.10 we show the photoluminescence spectra of CuInSe₂ measured at 2 and 77 K. The observation of photoluminescence at the energy of the lowest direct energy gaps indicates that for both compounds there are no lower-lying indirect energy gaps. Since CuInSe₂ can be prepared both *p*- and *n*-type (Chapter 7), junction electroluminescence in the vicinity of 1.2 μ should be possible. Since AgInSe₂ has only been prepared usefully conducting *n*-type, *p*–*n* junction light-emitting diodes in this compound are not possible.

Very recently, Migliorato *et al.* (1974) have prepared *p*–*n* junctions in CuInSe₂ by short anneals of *n*-type crystals in Se vapor. The 77 K electroluminescent spectrum peaked at 1.34 μ which is \sim 0.11 eV below the energy gap. The internal quantum efficiency of the electroluminescence was \sim 10% at 77 K.

5.2.2 CuInS₂ and CuGaS₂

In Figs. 5.11 and 5.12 we show the low-temperature photoluminescence spectra of CuInS₂ and CuGaS₂ respectively. The emission peaks at 8075 Å (CuInS₂) and 4953 Å (CuGaS₂) are attributed to radiative recombination of free excitons associated with the lowest direct energy gaps. This identification is based on the observation of exciton reflection anomalies at approximately the same wavelengths (Chapter 4). The luminescence spectra of these compounds are similar to those of the II–VI analogs in that many bound exciton lines are observed at energies just below the free exciton, and edge emission bands are observed beginning \sim 100 meV below the energy gap. In II–VI compounds these edge emission bands have been attributed to donor–acceptor recombination transitions. Although CuInS₂ can be prepared usefully conducting both *p*- and *n*-type (Chapter 7), light-emitting diodes in this compound may have no practical interest since the wavelength of the emission (Fig. 5.11) is close to that of commercial GaAs devices.

On the other hand, the luminescence of CuGaS₂ is of considerable interest since efficient electroluminescence has been observed in CuGaS₂:CdS heterodiodes (Section 5.5). It has also been found that an edge emission similar to that shown in Fig. 5.12 can be induced in CuGaS₂ crystals by annealing them at temperatures above 400°C in the presence of Zn, Cd, or Mg. Not all types (i.e. stoichiometries) of CuGaS₂ are amenable to this activation treatment, the details of which are not yet completely understood.

5.2.3 CuGaS₂:I

It has been discovered that CuGaS₂ crystals prepared by iodine transport can be made usefully conducting *p*-type, and that such crystals manifest a characteristic and

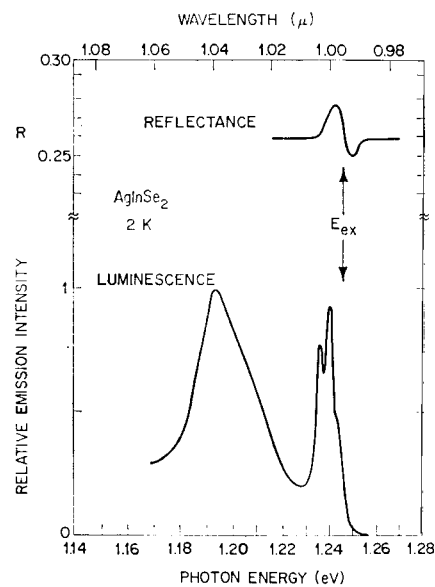


FIG. 5.9. Photoluminescence and reflection spectra of AgInSe_2 . (Shay *et al.*, 1973a.)

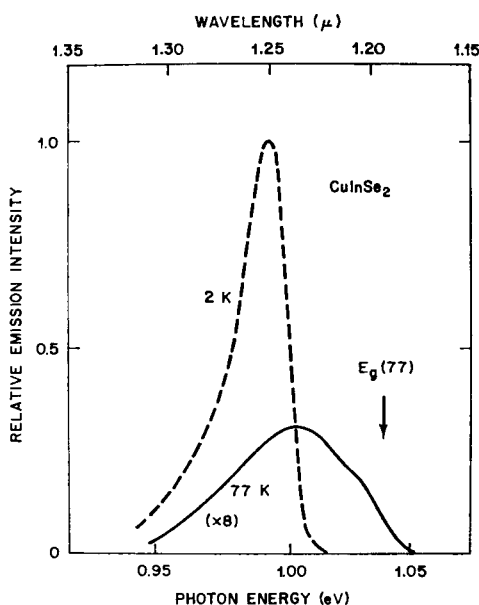


FIG. 5.10. Photoluminescence spectra of CuInSe_2 . (Shay *et al.*, 1973a.)

TERNARY CHALCOPYRITE SEMICONDUCTORS

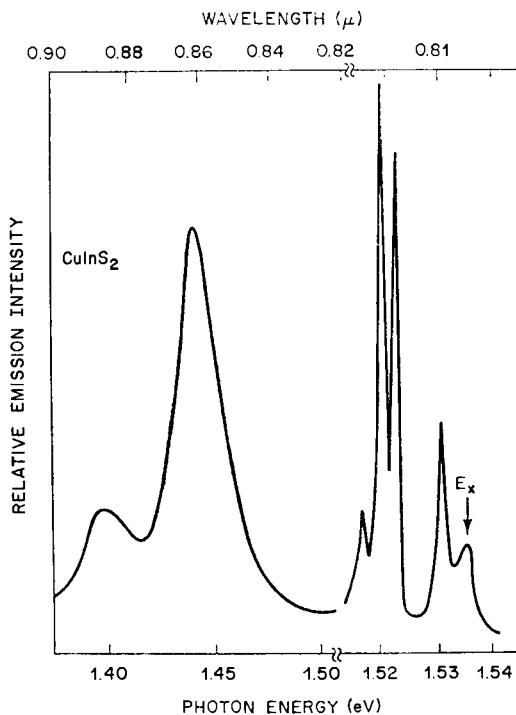


FIG. 5.11. Photoluminescence spectrum of CuInS_2 at 2 K. (Tell *et al.*, 1971.)

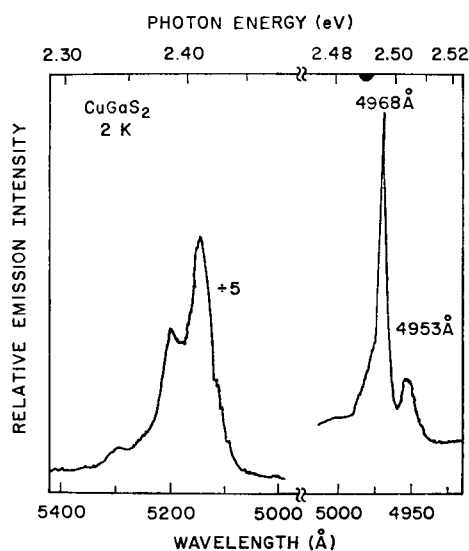


FIG. 5.12. Photoluminescence spectrum of CuGaS_2 . (Tell *et al.*, 1971.)

efficient green photoluminescence at low temperatures (Shay *et al.*, 1973b). Interest in iodine transport arises from the possibility of using this growth technique to epitaxially deposit *p*-type CuGaS₂ layers onto *n*-type II-VI compounds such as CdS and ZnS. This represents a potential method for fabricating heterostructure light emitting diodes between the *p*-type Cu I-III-VI₂ compounds and the *n*-type II-VI sulfides and selenides.

Figure 5.13 shows the photoluminescence spectra of a CuGaS₂ crystal grown by iodine transport. Virtually every crystal showed the same line spectrum with approximately the same intensity. Apparently the energies and relative amplitudes of the lines are characteristic of a recombination mechanism induced in CuGaS₂ by the presence of iodine. The spectrum consists of a series of equally spaced lines separated by 4.6 meV with the highest energy and dominant line at 2.402 eV (5163 Å). Although additional experiments will be required to positively identify the physical mechanism producing this emission, the regular spacing of the lines and the general shape of the spectrum suggests that it results from local-mode phonon sidebands of a bound exciton recombination.

It has been shown that annealing melt-grown CuGaS₂ at $\sim 700^{\circ}\text{C}$ in an environment of excess sulfur leads to useful *p*-type conductivity (Chapter 7), while samples intentionally doped with donors such as Cl and Cd become semi-insulating ($\rho > 10^6 \Omega\text{-cm}$). Since it is known that large quantities of the halogens are incorporated during vapor transport growth of II-VI sulfides and selenides, it might have been expected that such CuGaS₂ crystals would be insulating and remain high resistivity in spite of a sulfur anneal. Indeed, as grown, crystals were found to be insulating ($\rho > 10^6 \Omega\text{-cm}$). However, iodine transported CuGaS₂ crystals annealed under a saturation sulfur pressure at 700°C for 30 hr, become *p*-type with a resistivity typically $1 \Omega\text{-cm}$. Hence the extent of iodine incorporation does not diminish the potential for useful *p*-type conduction. The photoluminescence spectrum of an annealed crystal is also shown in Fig. 5.13 for the same experimental conditions as for the unannealed crystal. The line spectrum has given way to a much broader spectrum of about the same peak intensity, which is consequently much brighter. By measuring the emission with a calibrated silicon photodiode, it is estimated that the 2 K photoluminescence efficiency of annealed samples of CuGaS₂ is $\sim 10\%$.

5.2.4 AgGaS₂ and AgGaSe₂

AgGaS₂ and AgGaSe₂ are unique among the I-III-VI₂ compounds in that they have never been prepared usefully conducting, *n*- or *p*-type (Chapter 7). The photoluminescence spectra of these two compounds are shown in Figs. 5.14 and 5.15 for crystals grown from the melt. The spectrum measured for AgGaS₂ displays several sharp lines at energies slightly below the free exciton. There is a slight discrepancy (~ 2 meV) between the highest-energy emission line in Fig. 5.14 and the exciton energy determined by an oscillator fit to the reflectivity (Fig. 4.16). At 77 K, the emission in both crystals is dominated by emission bands at the same energies as the exciton reflection anomalies. The emission lines observed in Figs. 5.14 and 5.15 evidently indicate that there exist shallow donors or acceptors in these compounds although they have never been prepared usefully conducting. Perhaps these impurities are contained in some form of neutral complex and therefore are unable to contribute free carriers, or the crystals may self-compensate both *p*- and *n*-type conductivity.

Measurements of the cathodoluminescence of AgGaS₂ (Fig. 5.16) have found that

TERNARY CHALCOPYRITE SEMICONDUCTORS

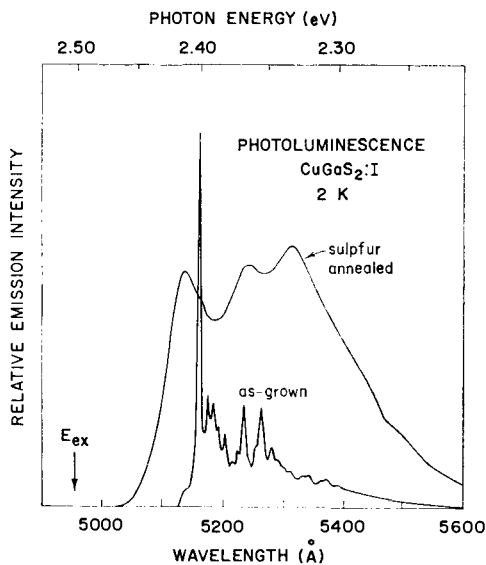


FIG. 5.13. Photoluminescence spectra of as-grown and sulfur-annealed crystals of CuGaS_2 grown by iodine transport. (Shay *et al.*, 1973b.)

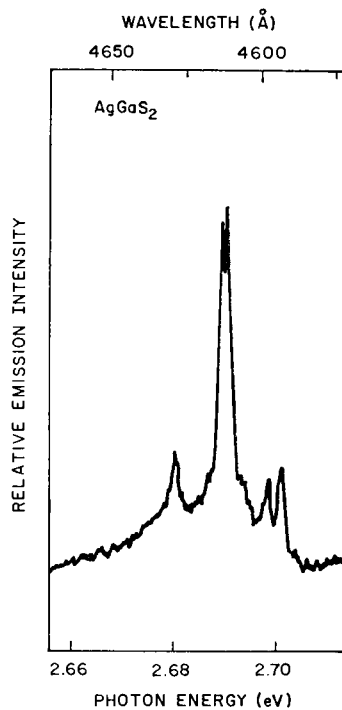


FIG. 5.14. Photoluminescence spectrum of AgGaS_2 . (Tell and Kasper, 1971.) The peak at 2.698 eV (4595 Å) indicates the energy of the free exciton as observed in the reflectance spectrum (Fig. 4.16, p. 124).

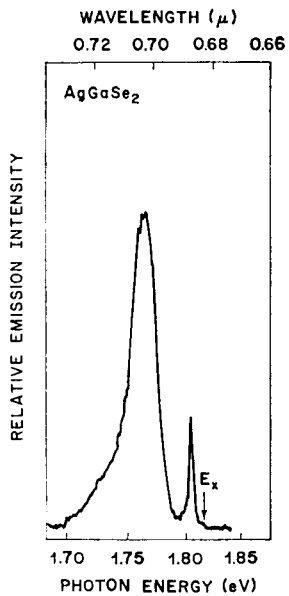


FIG. 5.15. Photoluminescence spectrum of AgGaSe_2 at 2 K. (Tell and Kasper, 1971.) The weak shoulder near 1.815 eV (6830 Å) is attributed to the free exciton.

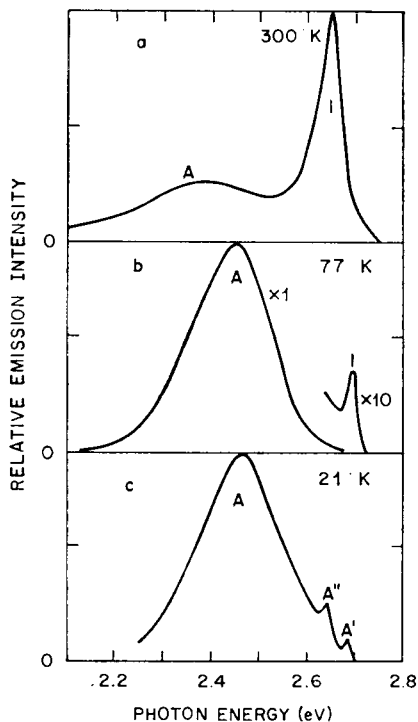


FIG. 5.16. Cathodoluminescence spectra of AgGaS_2 : (a) 300 K, (b) 77 K, and (c) 21 K. (Noblanc *et al.*, 1972.)

the dominant emission at low temperatures is a green “edge emission” near 2.45 eV, but that a blue, band-to-band (or exciton) emission near 2.65 eV dominates at room temperature (Noblanc *et al.*, 1972). The temperature dependence of the quantum efficiency of these bands has not been reported. The temperature dependence of the energy gap deduced from the shift of the band-to-band emission (I in Fig. 5.16) is $\sim 2 \times 10^{-4}$ eV/K.

5.3 Stimulated Emission Spectra of I-III-VI₂ Compounds

We now discuss the observation of optically pumped stimulated emission from four I-III-VI₂ compounds AgGaS₂, AgGaSe₂, CuGaS₂, and CuInS₂ spanning the visible spectrum from 4650 to 8200 Å. The presence of stimulated emission was inferred from the observation of a rapid increase in luminescence intensity for a small change in pump power above a critical level defined as threshold. The stimulated emission is noticeably collimated parallel to the excited surface. The onset of stimulated emission is accompanied by the appearance of a bright spot at the edge of the crystal, resulting from spontaneous emission which has been amplified in transversing the excited region. Attempts to observe Fabry-Perot cavity modes have thus far been frustrated by the difficulty in preparing suitable cavities from melt-grown crystals.

In Fig. 5.17, we show emission spectra for CuGaS₂ when excited by a pulsed N₂ laser (3371 Å) for various pump intensities. For relative pump intensities below 0.25, the amplitude of the luminescence varies linearly with pump power and resembles the spontaneous spectrum previously reported (Fig. 5.12). However, for pump intensities above ~ 0.25 , a new line appears near 5000 Å and increases superlinearly. For example, for a 70% increase in pump intensity (0.25 → 0.43), the emission at 5000 Å increases by a factor of 13. Such a superlinear variation of luminescence intensity with pump level, together with the collimated nature of the emission mentioned earlier, and the appearance of a bright green spot at the edge of the crystal are all characteristic of stimulated emission.

In Figs. 5.18–5.20 we show the stimulated emission spectra measured for AgGaS₂, AgGaSe₂, and CuInS₂ respectively. For all spectra, a relative pump intensity of 1 corresponds to an absolute intensity of about 3 MW/cm². In all the figures we have indicated the energies appropriate to the free exciton (E_{ex}), an LO phonon below the free exciton ($E_{ex} - \hbar\omega_{LO}$), and the expected location of an exciton-exciton scattering peak, one Rydberg below the free exciton ($E_{ex} - R$). The exciton Rydbergs have been taken from Table 4.2 (p. 123) or estimated from the binary analogs. The phonon energies have been estimated from known values for the binary analogs.

The stimulated emission observed in both CuGaS₂ at 5000 Å (Fig. 5.17) and AgGaS₂ at 4620 Å (Fig. 5.18) occurs at energies slightly above $E_{ex} - R$, where E_{ex} is the energy of the free exciton and R is the exciton Rydberg. It is therefore possible that the stimulated emission results from the exciton-exciton scattering mechanism identified by Benoit-a-la-Guillaume *et al.* (1969) and by Magde and Mahr (1970) in CdS and similar II-VI compounds. In this mechanism, one exciton is annihilated and another exciton is promoted to an excited state or to the continuum. Hence, the emitted photon is downshifted in energy by something less than one exciton Rydberg relative to the energy of a free exciton. Era and Langer (1971) have reported that this mechanism dominates the

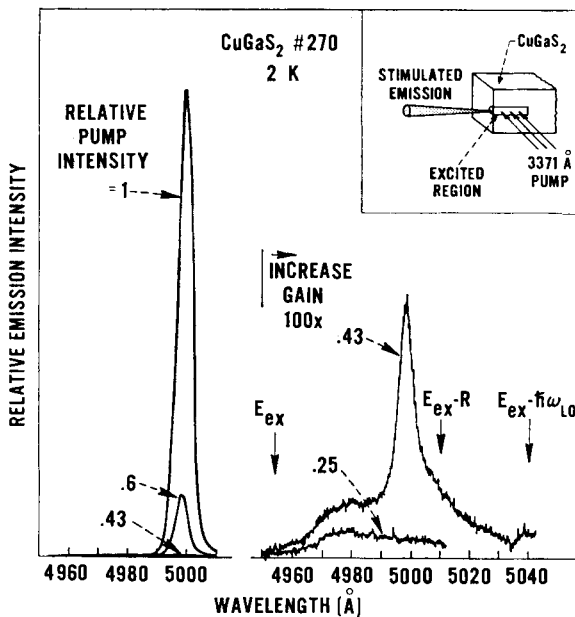


FIG. 5.17. Stimulated emission spectra of CuGaS₂. (Shay *et al.*, 1971 b.) A relative pump intensity of 1 corresponds to an absolute N₂ laser intensity of ~ 3 MW/cm².

stimulated emission observed at low pump intensities in pure as well as lightly doped CdS crystals. The stimulated emission observed in AgGaSe₂ at ~ 6980 Å (Fig. 5.19) and CuInS₂ at ~ 8175 Å (Fig. 5.20) does not correlate with $E_{ex} - R$ or $E_{ex} - \hbar\omega_{LO}$. Consequently, the stimulated emission in these latter crystals does not result from either the exciton-exciton scattering mechanism or the exciton-LO phonon process, but probably involves impurities or defects.

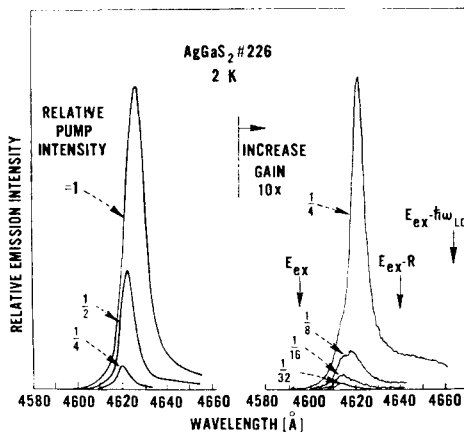


FIG. 5.18. Stimulated emission spectra of AgGaS₂. (Shay *et al.*, 1971 b.)

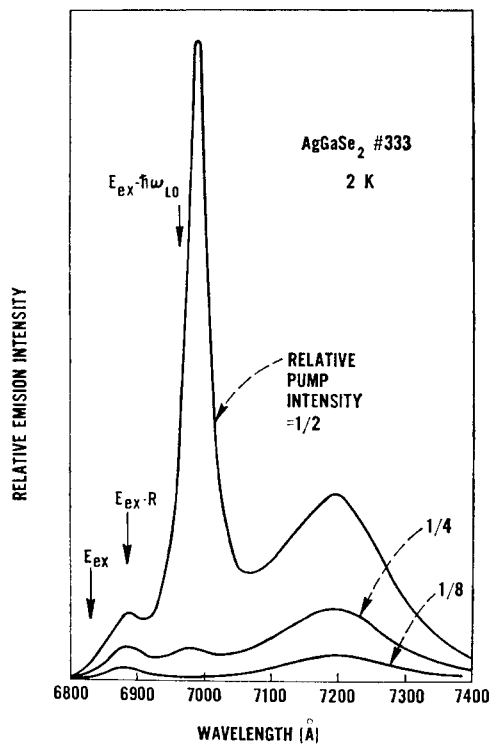


FIG. 5.19. Stimulated emission spectra of AgGaSe_2 . (Shay *et al.*, 1971 b.)

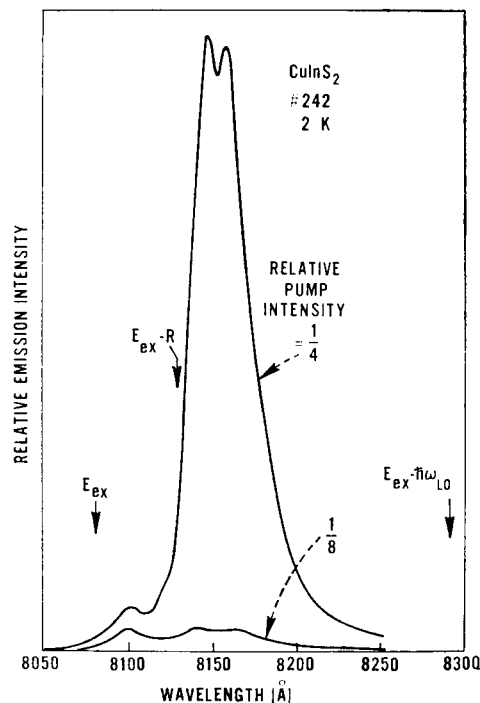


FIG. 5.20. Stimulated emission spectra of CuInS_2 . (Shay *et al.*, 1971 b.)

5.4 CdSnP₂-InP Heterodiodes

Heterodiodes have recently been prepared by liquid-phase epitaxial growth of *n*-type CdSnP₂ from Sn-solution onto *p*-type InP substrates (Shay *et al.*, 1973c). Such diodes may have practical applications as sources and detectors of infrared radiation, especially in communications systems employing glass fibers having very low loss near 1.05 μ . InP crystallizes in the zincblende structure with lattice constant $a = 5.8688 \text{ \AA}$, whereas CdSnP₂ takes the chalcopyrite structure with $c = 11.518$ and $a = 5.900 \text{ \AA}$. Thus epitaxial growth of CdSnP₂ on (100) substrates of InP should produce a lattice mismatch of only 0.5%. The details of the LPE growth are given in Chapter 2.

The room temperature current-voltage characteristic of a typical diode is shown in Fig. 5.21 for a layer grown on a lightly Zn-doped substrate ($p \sim 10^{16} \text{ cm}^{-3}$, $\mu \sim 150 \text{ cm}^2/\text{V}\cdot\text{s}$). A rectification ratio of $\sim 100,000$ is observed at 1 V at room temperature; at 77 K the reverse current was below 10^{-10} A for the voltages in Fig. 5.21. The slope of the I-V curve at the origin is $\sim 100 \text{ M}\Omega$ at room temperature. The voltage dependence of the capacitance is well behaved in that C^{-2} varies linearly with V . The slope corresponds to a one-sided junction with $N_a \sim 10^{16} \text{ cm}^{-3}$ at 77 and 300 K, in good agreement with the original doping of the InP substrate.

Under forward bias, an efficient electroluminescence has been observed from these heterodiodes, with a spectrum peaking near 1.4 μ . The temperature dependence of the external quantum efficiency of this emission (photons out/electrons transversing junction) is shown in Fig. 5.22. The computed internal quantum efficiency (also shown in Fig. 5.22) is ~ 25 times larger than the external quantum efficiency due to the small escape cone for light emitted from the InP-air interface. It was verified that the quantum efficiency is independent of the current in the range from 1 to 1000 mA. No electroluminescence was detected under reverse bias.

It is interesting that the electroluminescence spectrum peaks at 1.4 μ (0.89 eV) although the direct energy gaps of CdSnP₂ and InP are 1.17 and 1.34 eV respectively at room temperature. Although we have not determined from which side of the junction the emission originates, in either case, the emission is at least 0.3 eV below the energy gap. This shift might result from transitions involving impurity centers, or from a depression of the bandgap in the interfacial region below that of either compound (band tails). Indeed, chemical analysis reveals the presence of In in the CdSnP₂ layer at a level of several percent. Both the shift of the emission wavelength and the low value of the electron mobility probably result from this large In concentration. Since it would be desirable to have an electroluminescent diode emitting near 1.1 μ for use with glass fibers, future developments of these diodes are directed towards shifting the emission to shorter wavelengths, and improving the quantum efficiency. The present room temperature internal efficiency of 1% is very encouraging in view of the preliminary stage of this work.

The room temperature photovoltaic quantum efficiency (QE) of a typical diode is shown in Fig. 5.23 and compared with the QE of a commercial Si photodiode. The QE of the heterodiode reaches a maximum of 0.13 at a wavelength of 1.01 μ , which is to be compared with a value of 0.49 for the commercial Si detector. At longer wavelengths the decrease in the QE of the heterodiode is considerably less rapid than for the Si detector, so that the spectra cross at 1.09 μ . The quantum efficiency of the heterodiode exceeds 1% for all wavelengths between 0.96 and 1.3 μ .

TERNARY CHALCOPYRITE SEMICONDUCTORS

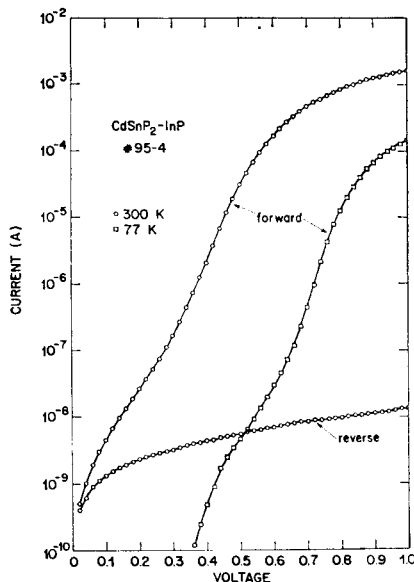


FIG. 5.21. Current-voltage characteristics for an InP-CdSnP₂ *p-n* heterodiode.

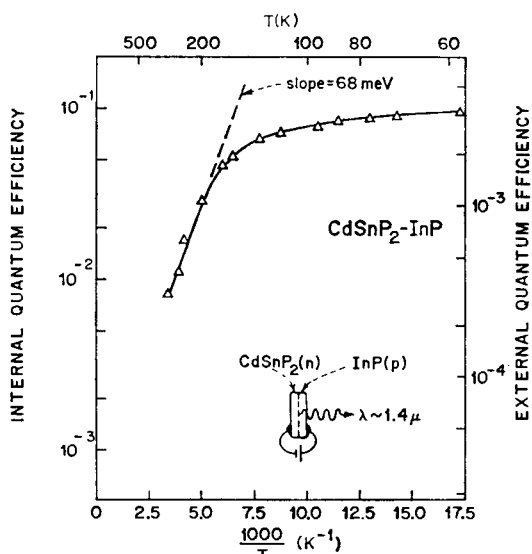


FIG. 5.22. Temperature dependence of the electroluminescence quantum efficiency of an InP-CdSnP₂ diode emitting near 1.4 μ . (Shay *et al.*, 1973c.)

The spectrum of the QE of the heterodiode in Fig. 5.23 displays the so-called "window" effect expected for heterodiodes, when the photovoltaic response is measured for light incident through the material with the larger bandgap, InP in this case. Hence the QE vanishes for $\lambda < 0.96 \mu$, due to the absorption in the InP window, and the long wavelength cutoff occurs when there is insufficient absorption by the CdSnP₂.

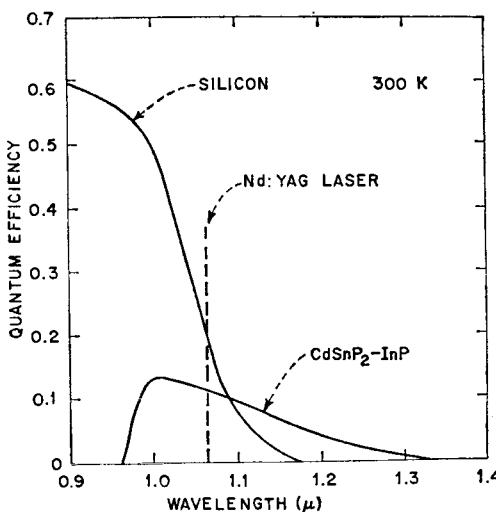


FIG. 5.23. Wavelength dependence of the photovoltaic quantum efficiency for the heterodiode of Fig. 5.22 and, for comparison, the quantum efficiency of a commercial Si detector. (Shay *et al.*, 1973.c.)

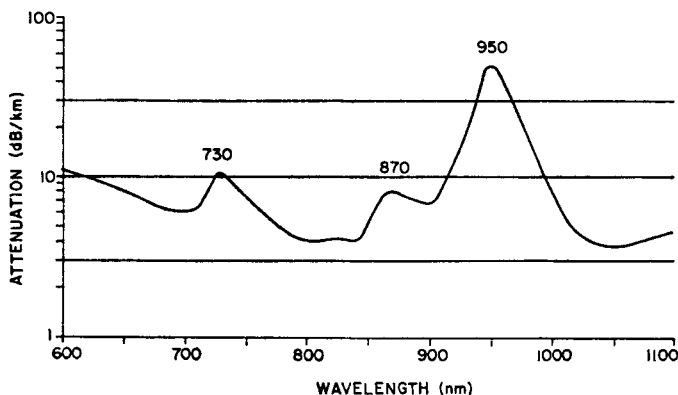


FIG. 5.24. Absorption spectrum of low loss glass fibers. (Keck *et al.*, 1973.)

Since recently reported glass fibers have exceptionally low loss (Fig. 5.24) for wavelengths near 1.05μ . (Keck *et al.*, 1973), one possible optical communication system would utilize a Nd:YAG laser source (1.06μ) and a Si photovoltaic detector. It can be seen in Fig. 5.23 that the quantum efficiency of the heterodiode (0.12) is only 40% less than that of the commercial Si detector (0.20) at this wavelength. Since reflection losses limit the maximum QE of the heterodiode to 0.7, future development may lead to a detector with a quantum efficiency 3.5 times larger than that of silicon at 1.06μ .

5.5 CdS–CuGaS₂ Electroluminescent Diodes

Although the II–VI compounds CdS and ZnS have direct bandgaps that are sufficiently wide to permit visible luminescence, *p*–*n* homojunction light-emitting diodes cannot be prepared from these materials because they cannot be prepared *p*-type. The recent discovery that the chalcopyrite compound CuGaS₂ has a direct bandgap in the green (5100 Å at 300 K) and can be made usefully *p*-type (but not *n*-type) immediately suggests the possibility of visible light-emitting heterodiodes between *p*-type CuGaS₂ and *n*-type CdS or ZnS. In such a device CuGaS₂ could serve both as an active electroluminescent material and as a hole injector. Although the lattice mismatch between CuGaS₂ and ZnS (1%) is considerably less than between CuGaS₂ and CdS (8%), the latter system was chosen for initial studies because the room temperature bandgaps of CuGaS₂ (2.43 eV) and CdS (2.45 eV) are nearly equal and because it is easier to obtain low-resistivity CdS than low-resistivity ZnS.

Diodes were prepared by growing epitaxial *n*-type CdS films on *p*-type CuGaS₂ substrates (Wagner *et al.*, 1973; Wagner, 1974). CdS films ~5 μm thick were grown epitaxially in vacuum on (112) CuGaS₂ surfaces with a coaxial isothermal double source (Fig. 5.25) similar to that described by Beecham (1970) at 400°C providing Cd and S vapor. With optimum growth parameters (substrate temperature $\geq 200^\circ\text{C}$), a room temperature resistivity of $\sim 1 \Omega\text{-cm}$ was obtained for the CdS films.

Conducting *p*-type CuGaS₂ crystals heated in vacuum to temperatures above 100°C develop a highly resistive surface layer and exhibit a simultaneous increase in bulk resistivity (Wagner *et al.*, 1973; Wagner, 1974). On the other hand, the quality of the CdS epitaxy improves as the substrate temperature is increased from 75 to 210°C. A substrate temperature of 130°C was therefore adopted as a compromise which resulted in epitaxial CdS films of reasonable quality and led to a diode forward resistance which was sufficiently low to permit light emission in d.c. operation. The d.c. current–voltage characteristic of a typical diode at 77 K presented in Fig. 5.26 demonstrates that the *p*–*n* junction is rectifying and is in series with a large non-ohmic resistance. This resistance may be due to an insulating layer formed in the CuGaS₂ by the temperature-controlled relaxation of the *p*-type conductivity or by compensation by Cd donors.

The electroluminescence spectrum for the diode of Fig. 5.26 in d.c. operation (200 μA, 25 V) at 77 K is shown in Fig. 5.27 together with the photoluminescence spectra (50 mW He–Cd laser excitation at 4416 Å) of the CdS layer and of a region of the CuGaS₂ surface which had been covered by the sample holder during film growth. It is clear from comparison of the spectra in Fig. 5.27 that the electroluminescence originates in the CuGaS₂. Visual examination also reveals that the electroluminescence emerges from the *p*–*n* junction region. At 77 K any other light emitted in the visible and near infrared is at least 100 times less intense than the green electroluminescence.

The electroluminescence efficiency at 77 K increases with d.c. diode current. For the highest currents sustainable without overheating, the efficiency–current relationship begins to saturate. In this saturation region an external quantum efficiency of 0.1% was observed at 77 K with a calibrated silicon photodetector. For extended operation at room temperature the diode current must be pulsed. The temperature dependence of the diode spectrum has been measured in pulsed operation (10 μs duration, 1 kHz repetition rate) up to 53°C. The pulsed spectra at 77 K and at room temperature are compared in Fig. 5.28. Between 77 K and room temperature the external quantum

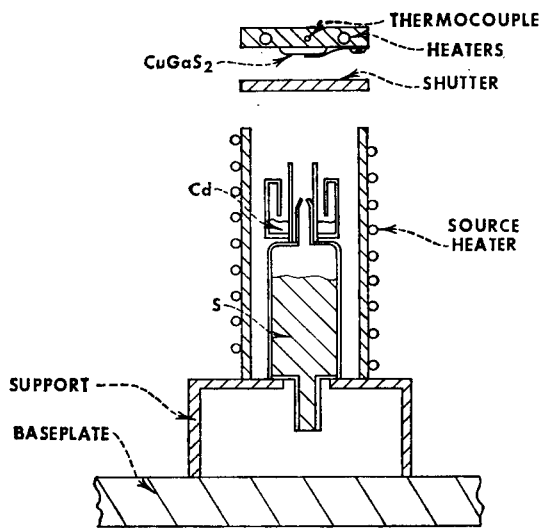


FIG. 5.25. Coaxial isothermal source for the deposition of CdS.
(Beecham, 1970.)

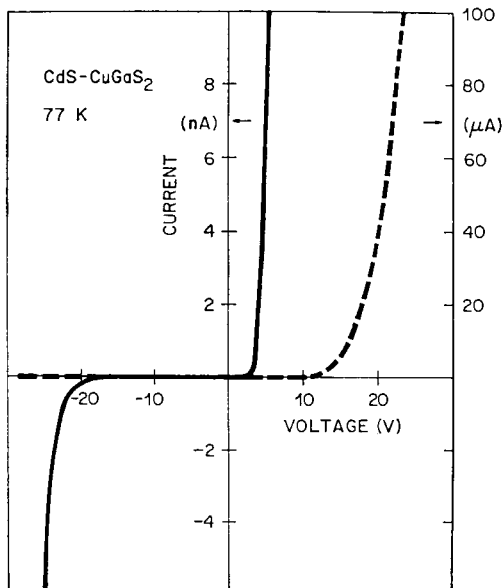


FIG. 5.26. d.c. current-voltage characteristic of a CdS-CuGaS₂ diode at 77 K. (Wagner *et al.*, 1973.) The current is plotted on two different scales to show the onset of forward current (at ~ 3 V) and the high current region. The junction area is $\sim 1 \text{ mm}^2$.

TERNARY CHALCOPYRITE SEMICONDUCTORS

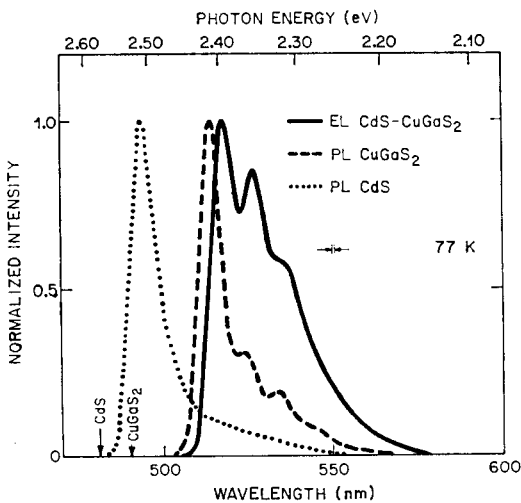


FIG. 5.27. Photoluminescence (PL) spectra of a CdS layer and of a bare CuGaS₂ substrate surface, and the d.c. electroluminescence (EL) spectrum of a CdS-CuGaS₂ diode, all at 77 K. The peak PL intensity of the CuGaS₂ is ~ 30 times that of the CdS. The positions of the fundamental band gaps are marked by arrows. (Wagner *et al.*, 1973.)

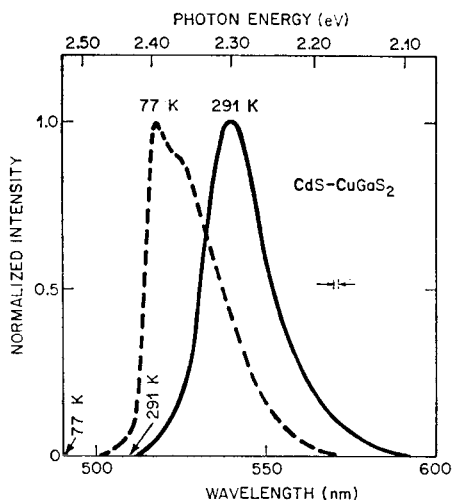


FIG. 5.28. Pulsed electroluminescence spectrum of a CdS-CuGaS₂ diode at 77 K and 291 K. The total intensity at 291 K is ~ 100 times less than at 77 K. The positions of the CuGaS₂ bandgap at 77 and 291 K are indicated by arrows. (Wagner *et al.*, 1973.)

efficiency drops by about a factor of 100, and the intensity peak shifts from 2.40 to 2.30 eV, corresponding closely to the shift in the fundamental bandgap of CuGaS₂.

The nature of the radiative recombination mechanism producing the electroluminescence just described is of considerable interest since a relatively high external quantum efficiency of 0.1% has been measured at 77 K despite the existence of a highly resistive layer at the CdS-CuGaS₂ interface and the expected high density of interfacial defects

due to the lattice mismatch. In other experiments it has been found that annealing CuGaS₂ at temperatures above 400°C in the presence of Cd, Zn, or Mg vapor in closed ampoules leads to efficient photoluminescence with a spectrum similar to the electroluminescence spectra for CuGaS₂ in Fig. 5.28. By analogy with II-VI compounds this "edge emission" probably results from donor-acceptor recombination involving an unidentified acceptor and Group II donors on Cu sites. Since the CuGaS₂ substrates were only weakly photoluminescent prior to the growth of the CdS film, it appears that the luminescence spectra of CuGaS₂ shown in Figs. 5.27 and 5.28 involve Cd atoms which have diffused a very short distance into the CuGaS₂ lattice even at 130°C.

An extrinsic acceptor which would stabilize the *p*-type conductivity of CuGaS₂ is needed. Such an acceptor would permit the growth of the CdS layers at higher temperatures to improve the metallurgical epitaxy without a concomitant increase in the resistivity of the CuGaS₂.

References

- ALEKPEROVA, E. E., VALOV, YU. A., GORYUNOVA, N. A., RYVKIN, S. M., and SHPENKOV, G. P. (1969) *Phys. Status Solidi* **32**, 49.
- AVERKIEVA, G. K., GORYUNOVA, N. A., PROCHUKHAN, V. D., RYVKIN, S. M., SERGINOV, M., and SHRETER, YU. G. (1971) *Fizika tekhn. Pol.* **5**, 174 [*Soviet Phys. Semiconductors* **5**, 151 (1971)].
- BEECHAM, D. (1970) *Rev. Sci. Instrum.* **41**, 1654.
- BENOIT-A-LA-GUILLAUME, C., DEBEVER, J. M., and SALVAN, F. (1969) *Phys. Rev.* **177**, 567.
- BERKOVSKII, F. M., GORYUNOVA, N. A., ORLOV, V. M., RYVKIN, S. M., SOKOLOVA, V. I., TSVETKOVA, E. V., and SHPENKOV, G. P. (1968a) *Fizika tekhn. Pol.* **2**, 1218 [*Soviet Phys. Semiconductors* **2**, 1027 (1969)].
- BERKOVSKII, F. M., GARBUZOV, D. Z., GORYUNOVA, N. A., LOSHAKOVA, G. V., RYVKIN, S. M., and SHPENKOV, G. P. (1968b) *Fizika tekhn. Pol.* **2**, 744 [*Soviet Phys. Semiconductors* **2**, 618 (1968)].
- BORSHCHEVSKII, A. S., VALOV, YU. A., GORYUNOVA, N. A., OSMANOV, E. O., RYVKIN, S. M., and SHPENKOV, G. P. (1968) *Fizika tekhn. Pol.* **2**, 1367 [*Soviet Phys. Semiconductors* **2**, 1145 (1968)].
- ERA, K. and LANGER, D. W. (1971) *J. Appl. Phys.* **42**, 1021.
- GORYUNOVA, N. A., RYVKIN, S. M., SHPENKOV, G. P., TYCHINA, I. I., and FEDOTOV, V. G. (1968) *Phys. Status Solidi* **28**, 489.
- JOHNSTON, W. D. (1972) *Phys. Rev. B*, **6**, 1455.
- KECK, D. B., MAURER, R. D., and SCHULTZ, P. C. (1973) *Appl. Phys. Lett.* **22**, 307.
Appl. Phys. Lett. **22**, 307.
- MAGDE, D., and MAHR, H. (1970) *Phys. Rev. Lett.* **24**, 890.
- MIGLIORATO, P., TELL, B., SHAY, J. L., and KASPER, H. M. (1974) *Appl. Phys. Lett.* **24**, 227.
- NAHORY, R. E., SHAH, J., LEITE, R. C. C., BUEHLER, E., and WERNICK, J. H. (1970) *Phys. Rev. B*, **1**, 4677.
- NOBLANC, J. P., LOUDETTE, J., DURAFFONG, G., and ROBERTSON, O. S. (1972) *Appl. Phys. Lett.* **20**, 257.
- SHAH, J. (1972) *Phys. Rev. B*, **6**, 4592.
- SHAH, J. and BUEHLER, E. (1971) *Phys. Rev. B*, **4**, 2827.
- SHAY, J. L., LEHENY, R. F., BUEHLER, E., and WERNICK, J. H. (1970a) *Appl. Phys. Lett.* **16**, 357.
- SHAY, J. L., LEHENY, R. F., BUEHLER, E., and WERNICK, J. H. (1970b) *J. Luminescence* **2**, 851.
- SHAY, J. L., JOHNSTON, W. D., BUEHLER, E., and WERNICK, J. H. (1971a) *Phys. Rev. Lett.* **27**, 711.
- SHAY, J. L., TELL, B., and KASPER, H. M. (1971b) *Appl. Phys. Lett.* **19**, 366.
- SHAY, J. L., SCHIAVONE, L. M., BUEHLER, E., and WERNICK, J. H. (1972) *J. Appl. Phys.* **43**, 2805.
- SHAY, J. L., TELL, B., KASPER, H. M., and SCHIAVONE, L. M. (1973a) *Phys. Rev. B*, **7**, 4485.
- SHAY, J. L., BRIDENBAUGH, P., TELL, B., and KASPER, H. M. (1973b) *J. Luminescence* **6**, 140.
- SHAY, J. L., BACHMANN, K., BUEHLER, E., and WERNICK, J. H. (1973c) *Appl. Phys. Lett.* **23**, 226.
- TELL, B., and KASPER, H. M. (1971) *Phys. Rev. B*, **4**, 4455.
- TELL, B., SHAY, J. L., and KASPER, H. M. (1971) *Phys. Rev. B*, **4**, 2463.
- WAGNER, S. W., SHAY, J. L., TELL, B., and KASPER, H. M. (1973) *Appl. Phys. Lett.* **22**, 351.
- WAGNER, S. W. (1974) *J. Appl. Phys.* **45**, 246.
- WILEY, J. D., BUEHLER, E., SHAY, J. L., and WERNICK, J. H. (1973) *J. Electronic Materials* **2**, 601.

CHAPTER 6

NONLINEAR OPTICAL APPLICATIONS

NONLINEAR optical phenomena are of practical interest for applications as sources of tunable radiation (parametric oscillators), as up converters of infrared radiation to a higher frequency (thereby permitting detection with a photomultiplier or photographic film), or difference frequency generation of far infrared radiation (perhaps for pollution detection). The nonlinear optical properties of ternary chalcopyrite crystals are of great current interest since these crystals are birefringent and therefore phase-matchable, and since they have large nonlinear optical coefficients as a result of their predominantly covalent bonding. In the present chapter we propose (1) to discuss some of the fundamental principles of nonlinear optical interactions, (2) to review the properties of the eleven chalcopyrite crystals studied to date, and (3) to review the highlights of the nonlinear optical devices which have been reported.

6.1 Nonlinear Optical Phenomena

6.1.1 General Principles

In contrast to linear optical phenomena for which a polarization wave is induced in a medium proportional to the electric field present, nonlinear optical phenomena involve that part of the polarization which is proportional to higher powers of the electric field. The second-order polarization $P_i(\omega_3)$ produced by the interaction of two applied electric fields $E_j(\omega_2)$ and $E_k(\omega_1)$ in a nonlinear optical medium is given by

$$P_i(\omega_3) = d_{ijk}(\omega_3, \omega_2, \omega_1) E_j(\omega_2) E_k(\omega_1), \quad (6.1)$$

where $d_{ijk}(\omega_3, \omega_2, \omega_1)$ is the second-order polarizability tensor and i, j , and k are indices indicating the component of the field in the respective crystallographic directions. In a given crystal class many of the tensor elements d_{ijk} are related by symmetry, and many are identically equal to zero. The nonzero elements have been worked out for all crystal systems and have been tabulated by Midwinter and Warner (1965). If the applied fields are plane waves of the form $e^{i(k_1 \cdot r - \omega_1 t)}$ and $e^{i(k_2 \cdot r - \omega_2 t)}$, then the induced polarization will be of the form $e^{i(k_3 \cdot r - \omega_3 t)}$, where $\mathbf{k}_3 = \mathbf{k}_1 + \mathbf{k}_2$ and $\omega_3 = \omega_1 + \omega_2$. The radiation at ω_3 resulting from this induced polarization will propagate away with a wave vector $|\mathbf{k}| = n\omega/c$ which, in general, will be unequal to $|\mathbf{k}_3|$ describing the spatial variation of the induced polarization. Clearly then the radiation resulting from polarization in one part of the crystal will be out of phase with, and therefore cancel, the radiation generated in another region of the crystal separated in space by the coherence length

$$l_c = \frac{\pi c}{(n_1 \omega_1 + n_2 \omega_2 - n_3 \omega_3)}. \quad (6.2)$$

If there were no dispersion, i.e. if the refractive index n were independent of frequency, then l_c would be infinite. In such a situation the radiation emanating from all parts of the medium would propagate in phase, and the signal reaching an observer is the maximum possible. In real crystals, the dispersion of the refractive index is sufficiently large that the coherence length is of order 0.05 mm. In such a case the net radiation emanating from most of the crystal is zero, and the net effective length of the radiating medium is at most l_c . The signal reaching the detector is therefore $\sim 10^{-4}$ of the maximum possible for a 0.5 cm long crystal.

Giordmaine (1962) and Maker *et al.* (1962) independently conceived of a scheme for matching the propagation constants of the source and radiation fields by utilizing the birefringence of anisotropic crystals. If the birefringence of the crystal is greater than the dispersion in the refractive index between fundamental and harmonic frequencies, then by suitable choice of the direction of propagation, the phase velocity of the harmonic can be matched with the phase velocity of the fundamental leading to long coherence lengths and large conversion efficiencies. For uniaxial crystals such as those taking the chalcopyrite structure (point group $\bar{4}2m$), there are two possible modes of propagation in a given crystallographic direction with different refractive indices for the two waves. By definition the ordinary wave propagates with the electric field normal to the optic axis and the extraordinary wave propagates with its electric field parallel to the projection of the optic axis in the plane normal to the direction of propagation. For positive uniaxial crystals the birefringence $B \equiv n^e - n^o$ is greater than zero; for negative uniaxial crystals $n^e - n^o$ is less than zero. Phase matching is achieved by using the birefringence to cancel the dispersion. One or two of the indices in eq. (6.2) are for ordinary waves, and the others are extraordinary waves. For certain combinations of frequencies, the denominator vanishes, the coherence length becomes infinite, and the maximum possible radiation is received from the crystal.

6.1.2 Phase Matching in $\bar{4}2m$ Crystals

We will now discuss the specific geometries for achieving phase-matched, three frequency interaction in ternary chalcopyrite crystals. For symmetry reasons there is one independent d_{ijk} and it is called d_{14} by convention. Two types of phase matching in birefringent crystals are possible: *type I*, in which ω_1 and ω_2 are of the same polarization (both *o*-rays or both *e*-rays), and *type II*, in which ω_1 and ω_2 are of orthogonal polarization (one is an *o*-ray, the other is an *e*-ray). The possible phase matching geometries for positive and negative uniaxial, $\bar{4}2m$ crystals are summarized in Table 6.1. We have assumed that the three waves are propagated with parallel wave normals, and that $\omega_3 > \omega_2 \geq \omega_1$. θ is the azimuthal angle of the propagation direction \mathbf{k} relative to the optic axis (\mathbf{z}). θ is the angle between the x -axis and the projection of \mathbf{k} in the x - y plane. Assuming that $dn/d\lambda \leq 0$ throughout the range from ω_1 to ω_3 , clearly the highest frequency ω_3 must have the lower index of n_3^o or n_3^e if the birefringence at ω_3 is to cancel the dispersion of the refractive index.

In birefringent media, the wave normal is different from the direction of energy propagation for normal incidence onto a crystal slab. Only the *o*-beam propagates in the same direction through the crystal, whereas the *e*-beam is deflected away from the slab normal. Hence at a certain distance into the crystal depending upon the diameter of the beam, the beams no longer overlap and hence no longer generate a third wave. This phenomenon of double refraction vanishes for propagation normal to the optic

TERNARY CHALCOPYRITE SEMICONDUCTORS

TABLE 6.1. *Phase-matching conditions for $\bar{4}2m$ crystals*

Positive uniaxial	Negative uniaxial
Type I	Type I
$\omega_1 = e$ ray, $\omega_2 = e$ ray, $\omega_3 = o$ ray	$\omega_1 = o$ ray, $\omega_2 = o$ ray, $\omega_3 = e$ ray
$P(\omega_3) = d_{14} \sin 2\theta \cos 2\Phi E(\omega_1) E(\omega_2)$	$P(\omega_3) = -d_{14} \sin \theta \sin 2\Phi E(\omega_1) E(\omega_2)$
$n_3^o = \frac{\omega_1}{\omega_3} n_1^o + \frac{\omega_2}{\omega_3} n_2^o$	$n_3^e = \frac{\omega_1}{\omega_3} n_1^e + \frac{\omega_2}{\omega_3} n_2^e$
Type II	Type II
$\omega_1 = o$ ray, $\omega_2 = e$ ray, $\omega_3 = o$ ray	$\omega_1 = e$ ray, $\omega_2 = o$ ray, $\omega_3 = e$ ray
$P(\omega_3) = -d_{14} \sin \theta \sin 2\Phi E(\omega_1) E(\omega_2)$	$P(\omega_3) = d_{14} \sin 2\theta \cos 2\Phi E(\omega_1) E(\omega_2)$
$n_3^o = \frac{\omega_1}{\omega_3} n_1^o + \frac{\omega_2}{\omega_3} n_2^o$	$n_3^e = \frac{\omega_1}{\omega_3} n_1^e + \frac{\omega_2}{\omega_3} n_2^e$

axis, i.e. $\theta = 90^\circ$. From Table 6.1 we conclude therefore that type II is the desired phase matching for positive uniaxial crystals, and type I is the desired phase matching for negative uniaxial crystals. Type II phase-matching requires more birefringence to phase match a given set of frequencies than type I. It is easy to show that the ratio of the required birefringence for type II and type I phase matching is

$$\left| \frac{B_2}{B_1} \right| = \frac{\omega_3}{\omega_2}, \quad (6.3)$$

which equals 2 for second harmonic generation SHG ($\omega_1 = \omega_2$, $\omega_3 = 2\omega_1$) and approaches 1 for $\omega_2 \rightarrow \omega_3$ and $\omega_1 \rightarrow 0$. It can be shown from the phase matching conditions in Table 6.1 that type II three-frequency phase-matching may be possible in materials even when SHG phase-matching is not, whereas if type I three-frequency phase-matching is possible, then SHG is also.

The refractive indices of the two waves which can propagate in a uniaxial crystal with a common wave normal at an angle θ to the optic axis are given by the following equation (Born and Wolf, 1964):

$$n^{\text{ord}} = n^o, n^{\text{ext}} = \frac{n^o n^e}{(n^{e^2} \sin^2 \theta + n^{o^2} \cos^2 \theta)^{1/2}}, \quad (6.4)$$

where n^o is the ordinary refractive index of the crystal and n^e is the extraordinary refractive index. If n^o and n^e are known at each of the frequencies ω_1 , ω_2 , and ω_3 , then the phase-matching angle θ may be calculated using eq. (6.4) and the appropriate equation in Table 6.1. This will produce a cone of possible phase-matched directions of semi-angle θ . It should be emphasized that phase-matching is not possible in all uniaxial crystals. Favorable optical properties are a large birefringence and a small dispersion.

The refractive indices of eleven ternary compounds have been measured by Boyd and coworkers using a prism technique to achieve resolutions of ± 0.0001 in the measured indices. These data are tabulated in the Appendix, and the birefringences are plotted as a function of wavelength in Fig. 6.1. From these data it has been concluded that three-frequency phase-matching is possible only in the crystals ZnSiAs_2 , CdGeAs_2 , ZnGeP_2 , AgGaS_2 , and AgGaSe_2 . The birefringences are inadequate in CdGeP_2 , CuGaS_2 ,

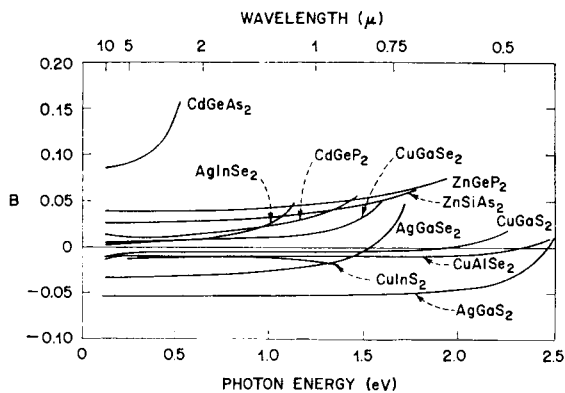


FIG. 6.1. Room temperature birefringences ($B \equiv n^e - n^o$) of several ternary compounds (for references see Table 6.2).

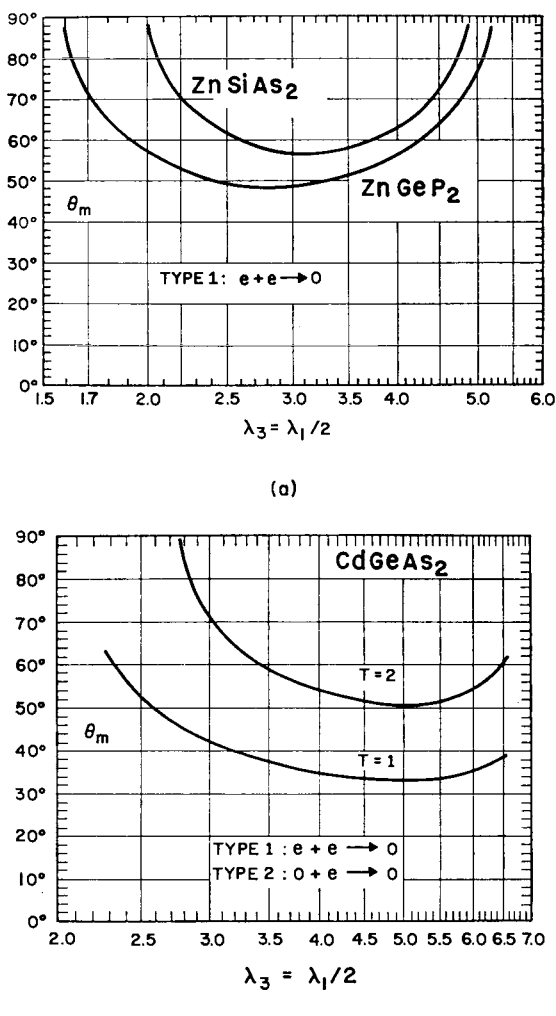


FIG. 6.2.

TERNARY CHALCOPYRITE SEMICONDUCTORS

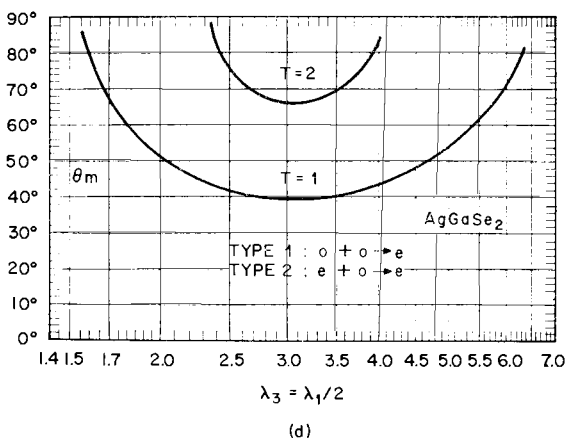
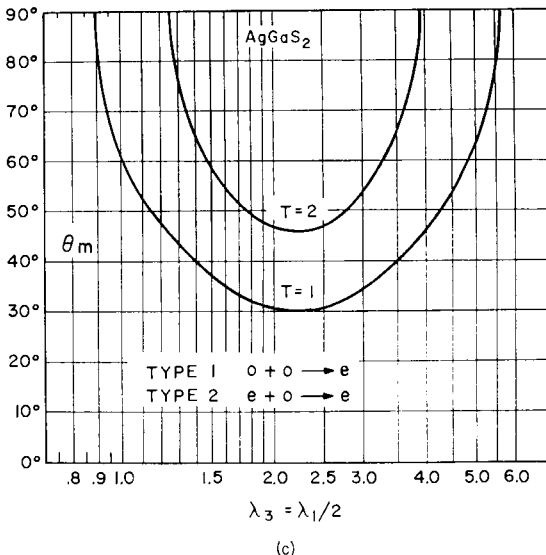


FIG. 6.2. Phase matching angle for second harmonic generation versus $\lambda_3 = \lambda_1/2$ in (a) ZnSiAs_2 and ZnGeP_2 , (b) CdGeAs_2 , (c) AgGaS_2 , and (d) AgGaSe_2 . (After Boyd *et al.*, 1971b, 1972a, b.)

CuInS_2 , CuAlSe_2 , CuGaSe_2 , and AgInSe_2 . The phase-matching angles θ required by eq. (6.4) and Table 6.1 for phase-matched SHG have been determined from the measured refractive index data and are shown in Fig. 6.2. Bear in mind that the nonlinear coefficient for type I SHG is reduced by the geometric factor $\sin^2 2\theta$ in positive uniaxial crystals such as ZnGeP_2 , ZnSiAs_2 , and CdGeAs_2 , and therefore goes to zero as θ approaches 90° . This factor significantly reduces the usefulness of ZnGeP_2 and ZnSiAs_2 for SHG. The birefringence of CdGeAs_2 is sufficiently large so that type II phase-matched SHG is possible. Similarly, in negative uniaxial crystals such as AgGaS_2 and AgGaSe_2 , the nonlinear coefficient for type II SHG goes to zero as $\sin^2 2\theta$ as θ approaches 90° . However, type I SHG is possible in both crystals (Fig. 6.2).

TABLE 6.2. *Nonlinear optical coefficients*

Crystal	$d_{14}/d_{14}(\text{GaAs})$	$\delta_{14}/\delta_{14}(\text{GaAs})$	References
CdGeAs ₂	2.62	1.58	a
CdGeP ₂	1.21	1.55	a
ZnGeP ₂	0.83	1.2	b
ZnSiAs ₂	0.81	0.96	a
CuInS ₂	0.079	0.46	c
CuGaS ₂	0.108	0.81	c
CuGaSe ₂	0.33	1.22	d
AgGaS ₂	0.134	1.37	c
AgGaSe ₂	0.368	1.86	d
AgInSe ₂	0.417	1.87	d

^a Boyd *et al.* (1972a).^b Boyd *et al.* (1971a).^c Boyd *et al.* (1971b).^d Boyd *et al.* (1972b).

Chemla *et al.* (1971) were the first to observe phase-matched SHG in a chalcopyrite crystal. They observed phase-matched doubling of a CO₂ laser at 10.6 μ for $\theta \sim 67.5^\circ$ in AgGaS₂, in good agreement with the predictions of Fig. 6.2. Surface damage occurred at 20 MW/cm² in a single pulse (15 ns) from a 1.06 μ Q-switched Nd:YAG laser.

The nonlinear coefficients have been measured by SHG using a Q-switched CO₂ laser at 10.6 μ as the pump. Wedge samples were used to measure d_{14} relative to d_{14} of GaAs, and the values measured for ten ternary crystals are summarized in Table 6.2. The nonlinearities can be placed on an absolute basis by using a recent determination of the optical nonlinear coefficient of GaAs by Levine and Bethea (1972), who conclude that

$$d_{14}(\text{GaAs}) = 215 \times 10^{-9} \text{ cm/statvolt} = 90.1 \times 10^{-12} \text{ m/V.}$$

As shown in Table 6.2, the nonlinear coefficients of the three selenides range from 33 to 42% of $d_{14}(\text{GaAs})$, as compared with those of the sulfides which range in value from 8 to 13% to $d_{14}(\text{GaAs})$. The nonlinearities of the II-IV-V₂ crystals are larger yet, varying from 81 to 262% of $d_{14}(\text{GaAs})$. The optical nonlinearity can also be expressed in terms of Miller's delta

$$\delta_{14} = d_{14}/\chi_1^2\chi_2, \quad (6.5)$$

where χ_1 and χ_2 are the linear susceptibilities at ω_1 and ω_2 respectively. The much larger d_{14} values of the selenides and the II-IV-V₂ compounds as compared to the sulfides can, in part, be accounted for by their larger linear susceptibilities, but even in terms of Miller's delta, the selenides and II-IV-V₂ compounds appear to be generally more nonlinear than the sulfides.

6.1.3 Physical Origin of Optical Properties

It is apparent in Fig. 6.1 that the birefringences of all crystals except CuInS₂ become more positive as the photon energy increases. We showed in Section 3.4 that this is the

TERNARY CHALCOPYRITE SEMICONDUCTORS

expected behavior as a result of the lifting of the degeneracy at the direct energy gap by the built-in lattice compression ($2 - c/a > 0$). Figures 3.22 and 3.26 (pp. 99 and 104) show that the dispersion of the birefringences in CdSnP_2 and CdGeP_2 can be explained quantitatively using the theory for piezobirefringence in binary crystals. Of more importance than the dispersion of the birefringence is its sign and magnitude at long wavelengths where the dispersion vanishes. It is of interest, therefore, to look for a correlation between birefringence and $2 - c/a$.

We show in Fig. 6.3 the birefringence at a wavelength of 5μ for the crystals in Fig. 6.1 plotted as a function of $2 - c/a$ for each crystal. Clearly no simple correlation exists especially for $2 - c/a < 0.10$. Three of the four crystals with large distortions ($2 - c/a > 0.10$) have large birefringences, but two are negative uniaxial (AgGaS_2 and AgGaSe_2) and one is positive uniaxial (CdGeAs_2). The fourth crystal has a very small birefringence (CdGeP_2). Upon closer inspection it happens that the birefringences of the first three crystals are consistent with a dominance by a large $2 - c/a$. The explanation for the apparent contradiction is as follows.

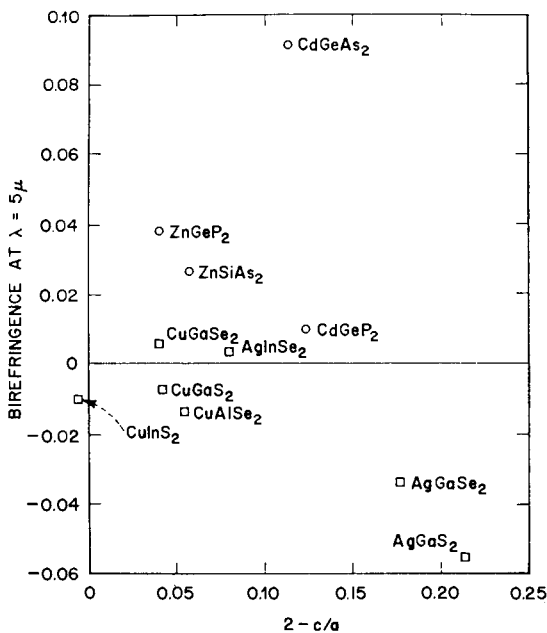


FIG. 6.3. Birefringence at a wavelength of 5μ versus $(2 - c/a)$ the compressional distortion for several ternary compounds. (For references see Table 6.2.)

Application of uniaxial stress to large bandgap binary compounds such as CdTe ($E_g = 1.7 \text{ eV}$) produces a negative B at long wavelengths (see Section 3.4). The positive B due to the polarization properties of the direct energy gap is overwhelmed by the negative B due to higher energy gaps. At photon energies approaching the direct energy gap B becomes positive due to the resonant enhancement of the effects of the direct gap. The strain-induced birefringence for such compounds has a zero crossing between the negative B at long λ and the positive B near the energy gap. These same features

are seen in the wavelength dependence of the birefringences of AgGaS_2 ($E_g = 2.73$ eV) and AgGaSe_2 ($E_g = 1.83$ eV) in Fig. 6.1. On the other hand, application of uniaxial stress to narrow bandgap binary crystals such as InSb ($E_g = 0.23$ eV) results in a birefringence that is positive at all wavelengths. The contribution to B due to the direct energy gap increases inversely as the value of the energy gap and dominates at all wavelengths in InSb . Hence the positive birefringence of CdGeAs_2 ($E_g = 0.57$ eV) results from the dominance of the contribution from the lowest direct energy gap in this crystal. The birefringence of CdGeP_2 ($E_g = 1.72$ eV) may simply be an intermediate case in which the contributions of the direct energy gap and those of higher energy gaps tend to cancel.

Levine (1973) has recently extended the Phillips–Van Vechten quantum dielectric theory of solids (Phillips, 1970) to calculate the nonlinear coefficients for a large variety of nonlinear optical materials. The bond charge calculation includes in a simple way three important contributions to the nonlinearity, i.e. the bond ionicity, the difference in the atomic radii of the atoms composing the bond, and the d -electron contributions. The results of Levine's calculation are summarized in Fig. 6.4 in which experimental and theoretical nonlinear coefficients and Miller's deltas are compared for many crystals. The agreement between theory and experiment is excellent as demonstrated by the small standard deviation of only 18%.

Levine (1973) has also discussed the relative nonlinearities in zincblende and chalcopyrite compounds. In spite of the fact that GaAs has a significantly smaller bandgap (1.43 eV), CdGeP_2 ($E_g = 1.72$ eV) has a somewhat larger nonlinear coefficient $d_{14}/d_{14}(\text{GaAs}) = 1.21$. This larger nonlinearity shows up even more clearly in the Miller's deltas since $\delta_{14}/\delta_{14}(\text{GaAs}) = 1.55$. Thus the II–IV– V_2 crystals can actually have larger nonlinearities than their corresponding III–V analogs. This is particularly important in view of the phase-matching possibilities in the ternary compounds. The reason for this is that the ionicity of the GeP band [which contributes most to $d_{14}(\text{CdGeP}_2)$] is significantly closer to the optimum value than is the ionicity of GaP . In view of the favorable nonlinear properties of II–IV– V_2 chalcopyrites, Levine concludes that it will be difficult to find materials with larger nonlinearities in the infrared spectral region.

Due to their large indices of refraction, the sulfides are especially good candidates for large nonlinear coefficients in the visible. Whereas the II–IV– V_2 chalcopyrites are found to be excellent infrared nonlinear materials, for somewhat similar reasons the more ionic larger bandgap I–III–VI₂ sulfides are also superior nonlinear crystals. However, Levine has suggested on theoretical grounds that the noble metals are not ideal due to deleterious effects associated with d -levels; the alkali metals would be better. For example, in spite of a partial cancellation in AgGaS_2 which reduces d_{14} by a factor of ~ 2 , its other favorable properties compensate sufficiently so that, in fact, its nonlinear susceptibility is comparable to that of $\text{Ba}_2\text{NaNb}_5\text{O}_{15}$ in the visible. However, if an alkali metal were used, e.g. LiGaS_2 , and if the structure remained the same (i.e. chalcopyrite), then one would expect a nonlinear coefficient significantly larger than that of $\text{Ba}_2\text{NaNb}_5\text{O}_{15}$. However, there are indications that LiGaS_2 is a wurtzite-like structure (similar to LiGaO_2). Since a geometrical factor for wurtzite is $\sqrt{3}$ times smaller than that for chalcopyrite, the net nonlinear coefficient of LiGaS_2 will probably be comparable to $\text{Ba}_2\text{NaNb}_5\text{O}_{15}$. Levine predicts that some new compounds which are likely candidates for visible nonlinearities larger than $\text{Ba}_2\text{NaNb}_5\text{O}_{15}$ are the defect chalcopyrites such as ZnGa_2S_4 and CdGa_2S_4 .

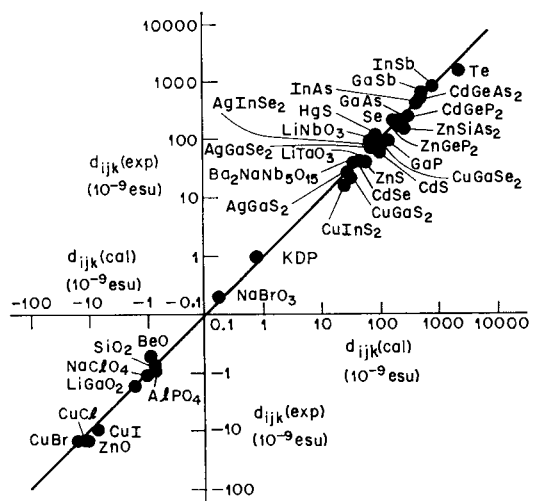
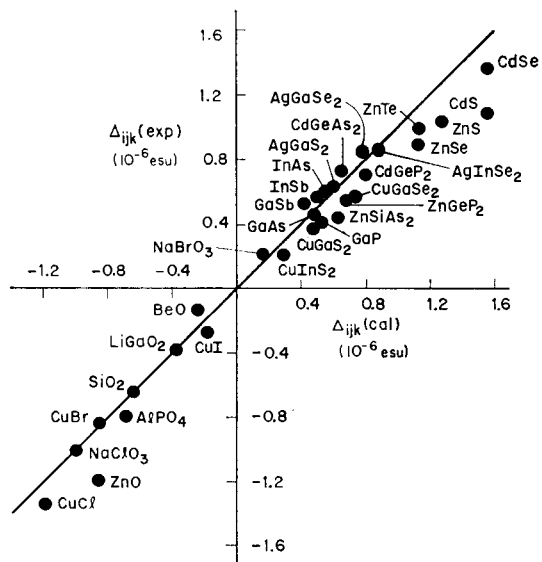


FIG. 6.4. Comparison of theoretical and experimental nonlinear optical coefficients (a) and Miller's delta (b). (Levine, 1973.)

6.2 The Optical Parametric Oscillator

We have shown in the last section that three-frequency phase-matching is achieved if

$$\left. \begin{array}{l} \omega_1 + \omega_2 = \omega_3, \\ n_1\omega_1 + n_2\omega_2 = n_3\omega_3, \end{array} \right\} \quad (6.6)$$

where the n_1 , n_2 , or n_3 are related to n^o and n^e by eq. (6.4). The possible solutions to eq. (6.6) are shown in Figs. 6.5–6.9 for selected angles of propagation θ relative to the optic axis. A vertical line corresponding to a chosen λ_3 intersects the solid curve for a chosen θ at two points λ_1 and λ_2 which satisfy the phase-matching conditions, eq. (6.6). For example, eq. (6.6) is satisfied in ZnGeP₂ (Fig. 6.5 b) for $\theta = 90^\circ$ if λ_2 and λ_3 are ordinary waves at 1.1 and 1.0 μ , respectively, and λ_1 is an extraordinary wave at 10 μ .

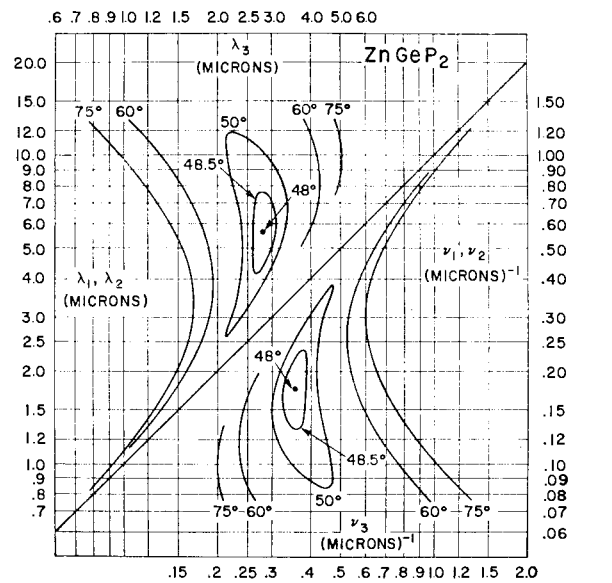
An optical parametric oscillator consists of a nonlinear medium situated within an optical cavity. The medium is excited by a laser beam at frequency ω_3 , and for excitation intensities above threshold, the device generates coherent radiation at the cavity resonant frequencies ω_1 and ω_2 if the phase-matching conditions of eq. (6.6) are satisfied. The cavity can be resonant at only ω_1 (singly resonant oscillator) or at both ω_1 and ω_2 (doubly resonant oscillator). The oscillation threshold for a doubly resonant parametric oscillator is lower than that for a singly resonant oscillator, in which only ω_2 is resonant, by a factor of $2/e_1$, where e_1 is the one way loss at ω_1 .

At present there are quite a few materials which are promising for infrared parametric oscillators. We will briefly discuss several of the available materials in terms of transmission range, nonlinear figure of merit and the possibilities for phase-matched parametric interactions using existing lasers as pumps. Since it is impossible to predict the ultimate optical quality which can be obtained, we will not use the presently measured minimum loss as a major criterion for comparison.

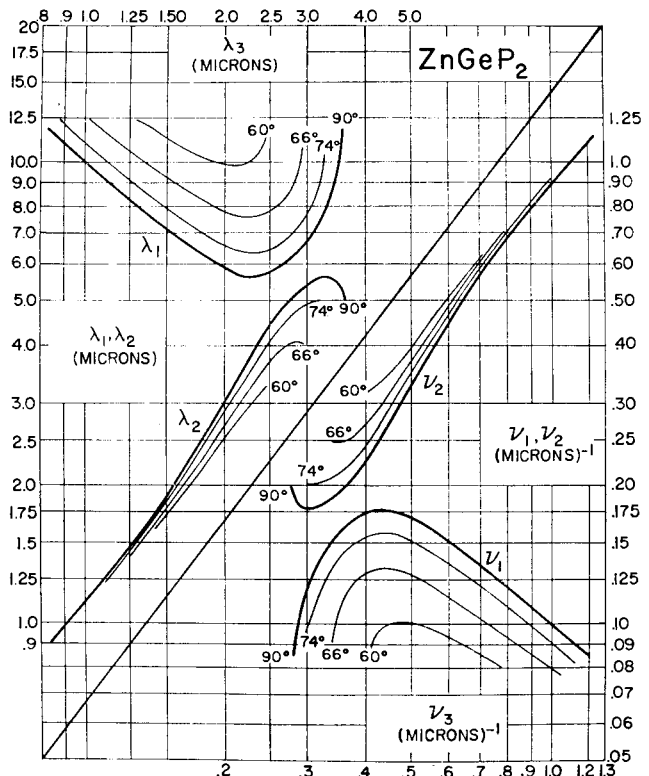
Following Boyd, Table 6.3 lists for seven crystals the nonlinear figures of merit d^2/n^3 , which are inversely proportional to the power thresholds for parametric oscillation. All of the materials in Table 6.3 have large figures of merit and, with the exception of LiNbO₃, are transparent to beyond 10 μ . LiNbO₃ is opaque beyond 5 μ , but is included for comparison because it is a very well-known nonlinear material which has been used commercially to construct a parametric oscillator with output wavelengths tunable to 3.5 μ . The figures of merit and regions of transparency are shown schematically in Fig. 6.10.

CdGeAs₂ ranks first in Table 6.3 with a figure of merit which is 6 times that of its nearest competitor, ZnGeP₂. CdGeAs₂ also has the smallest bandgap of this group (transparency range: 2.4–17 μ) and therefore stands somewhat apart from the other materials in that it cannot be used with the Nd:YAG laser and GaAs injection laser pumps which are considered below. As discussed by Byer *et al.* (1971), CdGeAs₂ is well suited for use with a CO laser pump (wavelength 5–6 μ). Their tuning curves indicate an output tuning range of 8–17 μ for a 5.3 μ pump. This material should also be useful for doubling of the CO laser and for parametric oscillators with a pump at shorter wavelengths. For example, for a pump wavelength λ_3 of 2.78 μ (HF laser), degenerate type II phase-matching occurs at an angle θ of 90°.

ZnGeP₂ has a transmission range which extends from 0.70 to 12 μ . Tuning curves for type I and type II phase-matching are given in Fig. 6.5. ZnGeP₂ could conveniently



(a)



(b)

FIG. 6.5. Three-frequency phase-matching in ZnGeP₂ versus the pump frequency ν_3 (or wavelength λ_3), i.e. $\nu_1 + \nu_2 = \nu_3$; (a) type 1: $e + e \rightarrow o$; (b) type 2: $o + e \rightarrow o$. (Boyd *et al.*, 1971a, 1972a.)

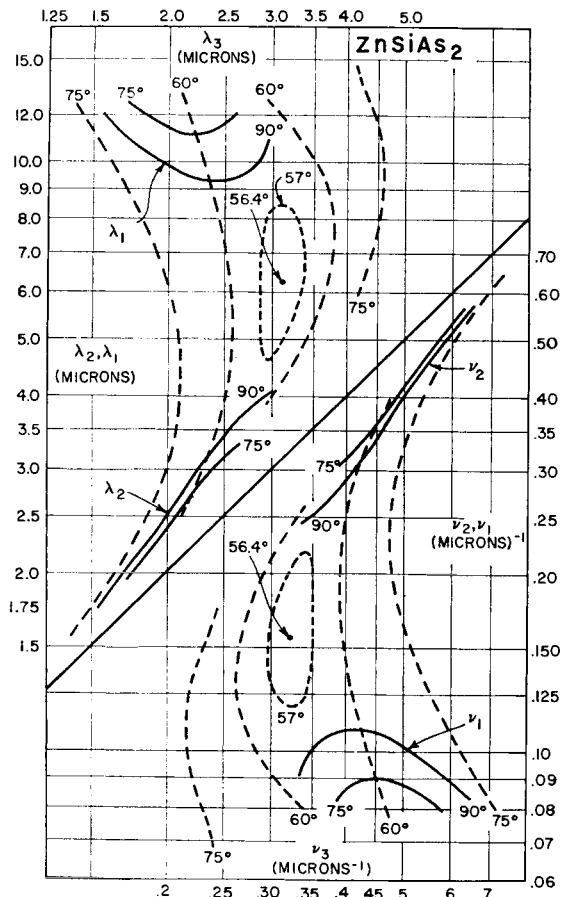


FIG. 6.6. Three-frequency phase-matching in ZnSiAs₂. Type 1 ($e + e \rightarrow o$) shown as dashed curves; type 2 ($o + e \rightarrow o$) shown as solid curves.
(Boyd *et al.*, 1972a.)

be used with the 1.833μ Nd: YAG laser which has been used to pump CdSe (see below). Figure 6.2 shows that degenerate type I phase-matching occurs at $\theta_m \cong 64^\circ$ in ZnGeP₂ for $\lambda_3 = 1.833 \mu$. Such an oscillator could easily be angle tuned by rotating the crystal toward smaller values of θ_m (the effective nonlinear coefficient for type I phase-matching is maximum for $\theta_m = 45^\circ$ in this positive birefringent material). Type II phase-matched operation at $\theta_m = 90^\circ$ is also possible in ZnGeP₂ using $\lambda_3 = 1.833 \mu$, as Fig. 6.5 shows. In this case operation is quite far from degenerate, but angle tuning of the output over a wavelength range of about $6\text{--}10 \mu$ is still possible. Another suitable pump for ZnGeP₂ is the 2.87μ line of the HF laser. With such a pump, tuning θ_m from 90° to 66° will tune λ_2 and λ_1 over the ranges $5.2\text{--}4.1 \mu$ and $6.4\text{--}9 \mu$ respectively.

AgGaSe₂ ranks third in Table 6.3 having a figure of merit which is one-third that of ZnGeP₂, 3 times that of CdSe, about 5 times that of AgGaS₂, and an order of magnitude larger than that of Ag₂AsS₃ (proustite). On the basis of this large figure of merit, AgGaSe₂ deserves serious consideration as a nonlinear material.

TERNARY CHALCOPYRITE SEMICONDUCTORS

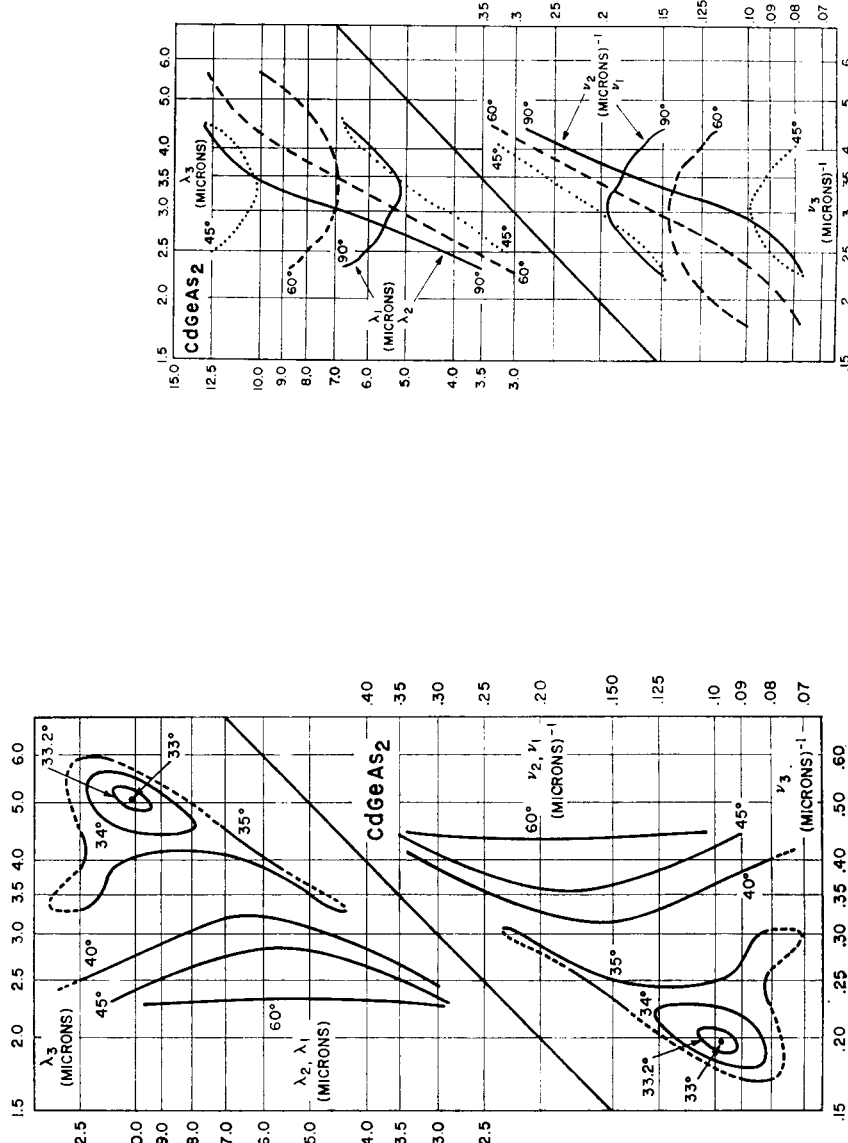
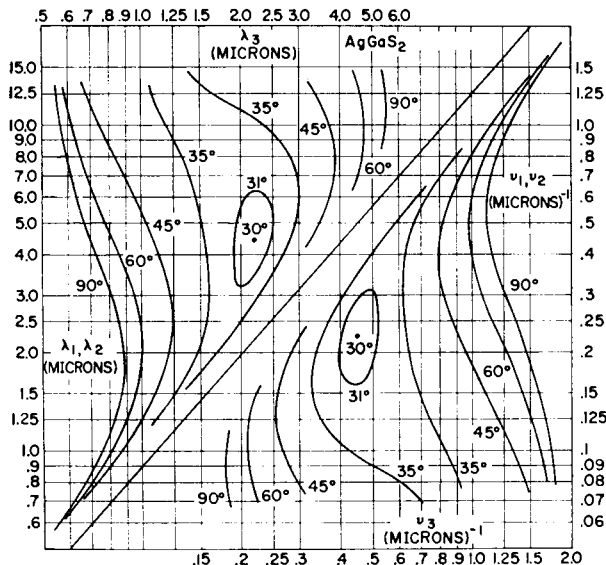
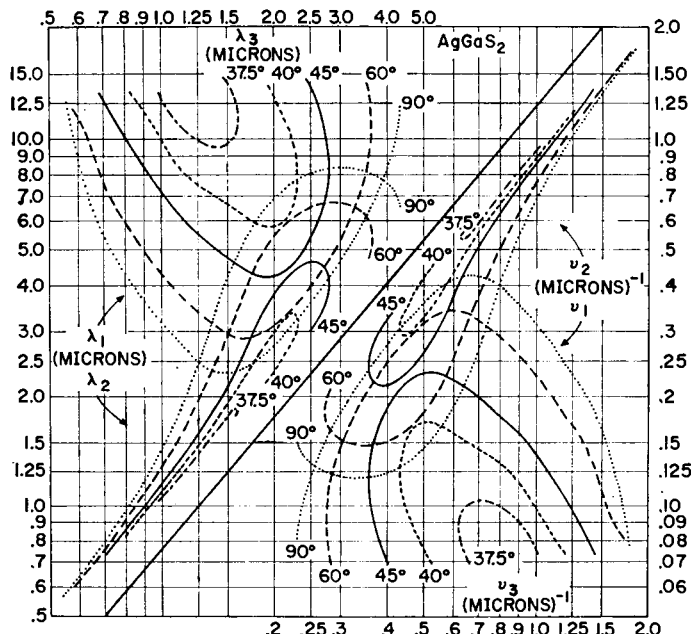


FIG. 6.7. Three-frequency phase-matching in CdGeAs₂. (a) Type 1:
 $e + e \rightarrow o$; (b) type 2: $o + e \rightarrow o$. (Boyd *et al.*, 1972a.)



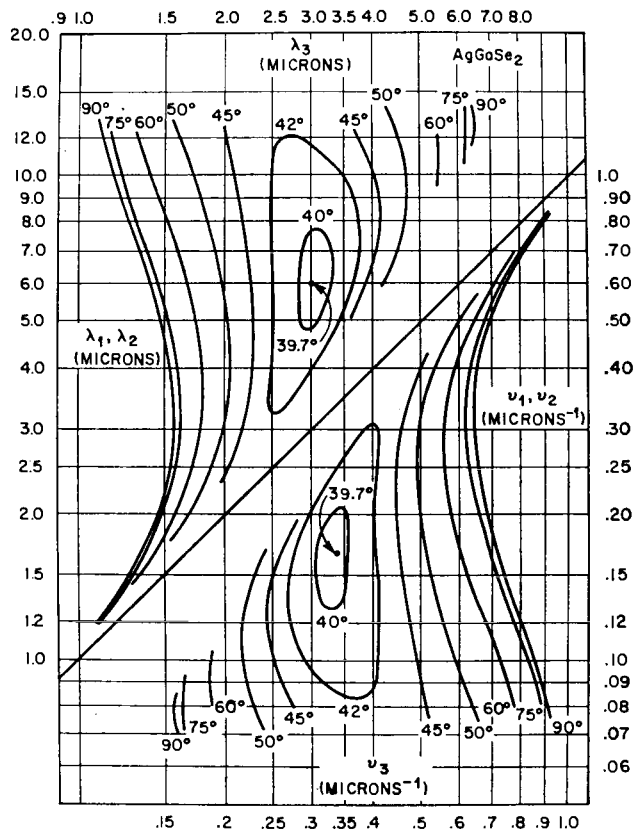
(a)



(b)

FIG. 6.8. Three-frequency phase-matching in AgGaS_2 . (a) Type 1: $\text{o} + \text{o} \rightarrow \text{e}$; (b) type 2: $\text{o} + \text{e} \rightarrow \text{e}$. (Boyd *et al.*, 1971 b.)

TERNARY CHALCOPYRITE SEMICONDUCTORS



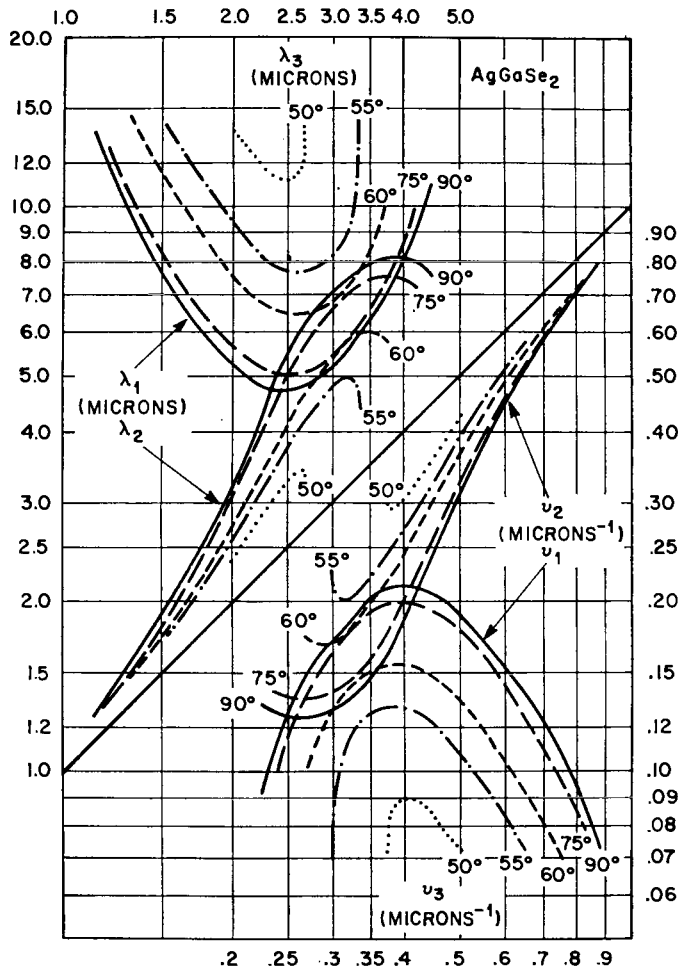
(a)

FIG. 6.9.

Herbst and Byer (1971) have shown that CdSe can be obtained with high optical quality and have published a tuning curve for an angle-tuned CdSe oscillator pumped with the $1.833\ \mu$ output of a Nd:YAG laser. Rotation of the crystal tunes the output wavelengths from 9.5 to $14\ \mu$ and in a narrow range near $2\ \mu$. A pump-tuned CdSe oscillator has outputs in the 2 - $4\ \mu$ and 8 - $12\ \mu$ ranges for pump wavelengths between 1.5 and $3\ \mu$. Phase-matched parametric mixing ($\theta_m = 77^\circ$) of a 1-watt CO₂ laser output at $10.6\ \mu$ with the $1.833\ \mu$ Nd:YAG pump produced a signal at $2.2\ \mu$ with 35% conversion efficiency.

A promising application for AgGaS₂ is the upconversion of $10.6\ \mu$ radiation to the visible by mixing with the xenon ion laser ($0.597\ \mu$). The phase-matching curves given in Fig. 6.8 also indicate that AgGaS₂ can conveniently be used as a parametric oscillator pumped by the GaAs injection laser ($0.9\ \mu$). The GaAs injection laser pump cannot be used with AgGaSe₂ because of its smaller bandgap.

Ag₃AsS₃ (proustite) is obtainable in large boules of good optical quality. Its birefringence is sufficient that three-frequency collinear phase matching is possible throughout its transparency range (0.6 - $13\ \mu$). Reliable operation of a doubly resonant Ag₃AsS₃ parametric oscillator has been achieved at a low repetition rate (2 pps) with a $1.06\ \mu$ pump and an output tuning range of 1.82 - $2.56\ \mu$. On the basis of this perform-



(b)

FIG. 6.9. Three-frequency phase-matching for AgGaSe_2 . (a) Type 1: $o + o \rightarrow e$; (b) type 2: $o + e \rightarrow e$.

ance it is predicted that proustite oscillators covering the range $1.2\text{--}9.5\mu$ are feasible. Double refraction cannot be avoided in proustite. For example, the degenerate type I phase-match angle is 29.5° for 1.06μ pump. Type II phase-matching at $\theta_m = 90^\circ$ is specifically ruled out by the combination of negative birefringence and $3m$ symmetry.

Table 6.4 summarizes the parametric oscillator examples given above and additional examples to be discussed below. One application which suggests itself is a AgGaSe_2 parametric oscillator pumped at 1.833μ (λ_3) as in the case of CdSe above. For type I phase-matching, degenerate operation ($\lambda_1 = \lambda_2 = 3.67\mu$) occurs at $\theta_m = 59^\circ$. At $\theta_m = 45^\circ$, λ_1 and λ_2 have diverged to 15 and 2.1μ respectively. Therefore the AgGaSe_2 oscillator output can be angle tuned to cover the $2\text{--}8\mu$ region not covered by the CdSe angle-tuned oscillator described above. However, the same output wavelength range can be obtained from an angle-tuned AgGaS_2 oscillator pumped with the 1.064μ line

TERNARY CHALCOPYRITE SEMICONDUCTORS

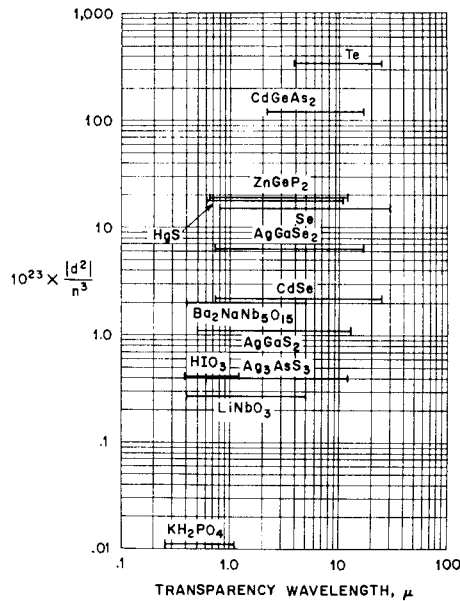


FIG. 6. 10. Comparison of the nonlinear figures of merit (d^2/n^3) and transparency regions for several crystals.

TABLE 6.3. Comparison of nonlinear figures of merit (after Boyd et al., 1972b)

Material	$d_{IJ} \times 10^{12}$ (m/volt)	$d_{eff} \times 10^{12}$ (m/volt)	n ($\lambda = 10.6 \mu$)	d_{eff}^2/n^3 ($\times 10^{23}$)	$\delta/\delta(\text{GaAs})$	Transmission range (λ in microns)
CdGeAs ₂	$d_{36} = 236$	236	3.58	121	1.58	2.4-17
ZnGeP ₂	$d_{36} = 75$	75	3.09	19	1.2	0.64-12
AgGaSe ₂	$d_{36} = 33$	33	2.57	6.4	1.9	0.73-17
CdSe	$d_{31} = 18$	18	2.45	2.2	0.86	0.75-25
AgGaS ₂	$d_{36} = 12$	12	2.32	1.1	1.4	0.49-12.5
Ag ₃ AsS ₃	$d_{31} = 8.4$ $d_{22} = 14$	9	2.7	0.40	0.44	0.6-13
LiNbO ₃	$d_{31} = 5$	5	2.09	0.27	1.34	0.4-5

of the Nd:YAG laser, which is probably a more convenient pump. In this case, degenerate operation ($\lambda_1 = \lambda_2 = 2.12 \mu$) occurs at $\theta_m \approx 56^\circ$, and by $\theta_m \sim 35^\circ$, λ_1 and λ_2 have diverged to approximately 10 and 1.2μ . Thus one might prefer the AgGaS₂ oscillator for this output wavelength range even though AgGaS₂ has a nonlinear figure of merit nearly 6 times smaller than that of AgGaSe₂. In addition, this factor of 6 is partially overcome by the higher pump frequency which reduces the AgGaS₂ oscillator threshold. d_{eff}^2/n^3 for both materials is reduced by $\sin^2 \theta_m$ for $\theta_m < 90^\circ$ over that listed in Table 6.3.

TABLE 6.4. *Parametric oscillator examples (after Boyd et al., 1972b)*

Material	Pump λ_3 (μ)	Phase-match Type	θ_m (deg.)	Tuning range λ_2, λ_1 (μ)
AgGaS ₂	1.06	1	56 → 35	1.2 ← 2.12 → 10
	0.89 → 0.80	1	90	1.07 ← 1.78 → 3.12
CdSe	1.833	2	90 → 65	2.1 ← 2.27, 9.5 → 20
	3.0 → 1.5	2	90	1.8 ← 4, 8 → 12
AgGaSe ₂	1.319	1	90 → 60	1.46 ← 1.6, 7.0 → 11.8
	1.833	1	59 → 45	2.1 ← 3.67 → 15
	1.55 → 1.06	1	90	1.14 ← 3.1 → 15
	5.3	1	58 → 60	8.5 ← 10.6 → 13
ZnGeP ₂	2.87	2	90 → 66	4.1 ← 5.2, 6.4 → 9.0
	1.833	1	64 → ~55	2.2 ← 3.67 → 12
CdGeAs ₂	5.3	2	55 → 50	7.5 ← 10.6 → 17
	2.8	2	90 → 45	3.6 ← 5.6 → 11
Ag ₃ AsS ₃	1.06	1	~30	1.2 ← 2.12 → 9.5

Since AgGaS₂ and AgGaSe₂ have smaller birefringences than does proustite, phase-matching is possible in these materials at $\theta_m = 90^\circ$, where there is no double refraction. It is possible to have $\theta_m = 90^\circ$ in a AgGaS₂ parametric oscillator pumped by a (Ga_xAl_{1-x})As injection laser that would give an output tuning range of 1.07–3.1 μ when pumped with various lasers available from 0.80 to 0.89 μ . In the case of AgGaSe₂, it is possible to phase-match at $\theta_m = 90^\circ$ using the 1.319 μ Nd: YAG laser line as pump and obtain outputs at 1.6 and 7.0 μ . Longer output wavelengths are obtainable for $\theta_m < 90^\circ$, but degenerate phase-matching is not possible with this pump in AgGaSe₂. The 1.319 μ Nd: YAG line is attractive, however, because it lases at room temperature, whereas the 1.833 μ Nd: YAG pump requires cooling of the laser rod.

Finally, we note that both AgGaSe₂ and AgGaS₂ can be used with the CO laser pump, but, as compared to CdGeAs₂, neither material is particularly well suited for this application. For example, consider an angle-tuned AgGaSe₂ parametric oscillator with pump wavelength $\lambda_3 = 5.3 \mu$. Phase-matching calculations show that the output wavelengths are tuned over the range 8.5–13 μ by changing θ only 2°. Such high sensitivity to angular orientation may be inconvenient.

Of the examples listed in Table 6.4 oscillators exist at present in CdSe and proustite but do not cover the full wavelength ranges available in these materials. CdSe is at present the best material for tuning beyond 10 μ . Perhaps the most promising competition for the potential tuning range of proustite are the angle-tuned AgGaS₂ oscillator with a 1.06 μ pump and the 1.833 μ -pumped ZnGeP₂ oscillator. The latter should ultimately have a significantly lower threshold than proustite.

6.3 Phase-matched Upconversion of 10.6 μ Radiation

Parametric upconversion has been suggested as a sensitive method for achieving fast room-temperature infrared detection (Milton, 1972). Previously, HgS, Ag₃AsS₃, and Ag₃SbS₃ have been phase-matched for upconversion of CO₂ laser radiation at angles θ

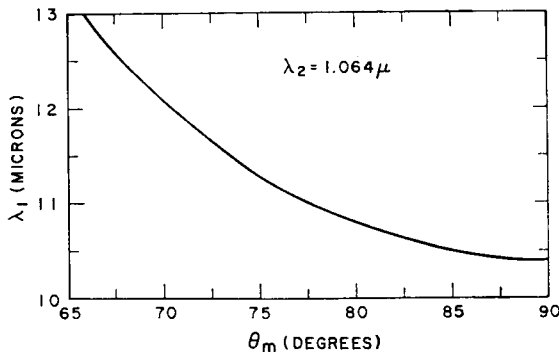


FIG. 6.11. Infrared wavelength λ_1 which is phase-matched upconverted by $\lambda_2 = 1.064 \mu$ versus phase-matching angle θ_m . (Boyd *et al.*, 1971c.)

of less than 30° to the optic axis. Ideally, θ must be 90° if the interaction length is not to be limited by double refraction. Boyd *et al.* (1971c) have recently reported phase-matched sum-mixing of 10.6μ (CO_2) and 1.064μ (Nd:YAG) radiation at near normal to the optic axis in ZnGeP_2 . The sum-mixing efficiency of ZnGeP_2 is 140 times superior to that of Ag_3AsS_3 (proustite) the next best material. The large angular aperture resulting from $\theta \sim 90^\circ$ indicates that ZnGeP_2 will be useful for image upconversion.

In Fig. 6.11 the infrared wavelength which is phase-matched with the 1.064μ Nd: YAG laser line is shown as a function of the angle of propagation θ relative to the optic axis. This curve has been calculated using the refractive index data tabulated in the Appendix. The CO_2 laser at 10.6μ is phase-matched at $\theta = 83.6^\circ$. Experimentally, Boyd *et al.* observed $\theta = 84.0^\circ$. This discrepancy can be accounted for by reducing the measured birefringence at 1.064μ by 0.001, which is within experimental error. In two other boules, phase-matching was observed at 84.1 and 89.2° . The latter can be accounted for by a decrease in the birefringence of 0.0006 at 1.064μ , close to the measured value of 0.001. These variations in phase-matching angles and birefringences may be due to stoichiometry variations, but this has not been proven.

Assuming optimum focusing, negligible absorption, and neglecting pump depletion, the optical mixing quantum efficiency for this upconversion of 10.6μ radiation in a crystal of length l cm with a pump power P_2 watts at 1.064μ is given by

$$\eta_{13} = (\omega_1 P_3 / \omega_3 P_1) = 0.014 l P_2. \quad (6.7)$$

If $P_2 = 1 \text{ W}$ and $l = 1 \text{ cm}$, the quantum efficiency is 0.014. Whenever $\theta < 90^\circ$, the effects of double refraction must be taken into account. For example, at $\theta = 84^\circ$, the double refractive angle is 0.17° , and the corresponding walkoff distance is 1.4 cm when the confocal parameter and crystal length are both 1 cm. Consequently, for upconversion of 10.6μ with the 1.064μ Nd: YAG laser, the effects of double refraction are not significant in ZnGeP_2 for crystals of 1 cm or less.

A comparison of ZnGeP_2 and Ag_3AsS_3 for sum-mixing of 10.6 and 1.064μ indicates that for $l = 1 \text{ cm}$ the upconversion quantum efficiency will be 140 times greater for ZnGeP_2 , neglecting loss. Since the sum frequency can be detected by S-1 image converters and photographic film, ZnGeP_2 may also be useful for image upconversion. The large angular aperture resulting from $\theta \sim 90^\circ$ is especially desirable for this application.

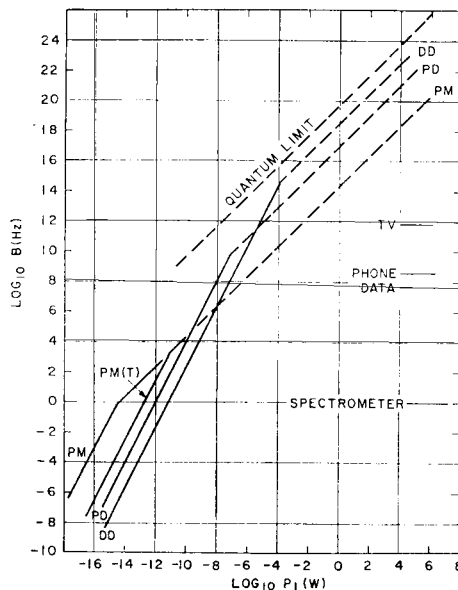


FIG. 6.12. System noise performance $B = (S/N)\Delta f$ versus signal power P_1 for direct detection (DD) with Ge : Hg, sum-mixing with an S-1 photomultiplier (PM), or sum-mixing with an avalanche photodiode (PD). PM(T) includes thermal background noise. (Boyd *et al.*, 1971c.)

The full phase-matched aperture for a crystal 1 cm long is 0.55° in ZnGeP_2 versus 0.038° in Ag_3AsS_3 . When $\theta = 90^\circ$ in ZnGeP_2 , the full width is 3.6° .

Boyd *et al.* (1971c) have also considered the system noise performance of upconversion in ZnGeP_2 and compared such a system with the noise performance of a Ge:Hg photoconductor. As a measure of system performance they have used the parameter $B = (S/N)f$ where S/N is the required signal-to-noise ratio and f is the required system bandwidth. Using an upconversion efficiency of 0.014, we show in Fig. 6.12 the calculations of Boyd *et al.* for three systems: direct detection (DD) with a Ge:Hg photoconductor, avalanche photodiode (PD) detection following sum-mixing with the 1.064μ laser, and photomultiplier (PM) detection following sum-mixing with the 1.064μ laser.

Figure 6.12 indicates that room-temperature detection by optical sum-mixing and a PD is superior to cooled DD for $B < 4 \times 10^{11} \text{ Hz}$. When a PM is used, upconversion is superior to DD for $B < 2.5 \times 10^6 \text{ Hz}$. Since the upconversion quantum efficiency is 0.014, this system will still not be as sensitive as a good heterodyne detector at 10.6μ , whose overall quantum efficiency can approach that of the photoconductive detector. Heterodyne detection has the disadvantages, however, of requiring cooled detectors and good frequency stability.

Boyd *et al.* (1971b) have also considered a scheme for upconverting 10.6μ radiation using AgGaS_2 and a xenon ion laser (0.597μ). Phase-matching is achieved for $\theta = 86^\circ$, which is near normal to the optic axis. Using the experimentally determined nonlinear coefficient for AgGaS_2 , they calculate an upconversion quantum efficiency

$$\eta_{13} = (\omega_1 P_3 / \omega_3 P_1) = 0.0023 IP_2, \quad (6.8)$$

which is 6 times smaller than in ZnGeP_2 . This deficit is more than compensated for by the increased photomultiplier efficiency of 18% at $0.565\ \mu$ (S-20) as opposed to a quantum efficiency of 0.15% for an S-1 photomultiplier at $0.967\ \mu$ using ZnGeP_2 . Both AgGaS_2 and ZnGeP_2 are very promising, and the material to be selected depends upon the system requirements and the availability of high optical quality material.

6.4 Difference Frequency Generation of Submillimeter Waves

In the generation of submillimeter radiation by the nonlinear difference frequency mixing of optical radiation from two powerful gas laser sources, the source frequencies lie above and the difference frequency lies below the lattice absorption band of the nonlinear material. Boyd *et al.* (1972c) have recently reported phase-matched generation of frequencies between 70 and $110\ \text{cm}^{-1}$ by nonlinear mixing of two step-tunable CO_2 lasers in a crystal of ZnGeP_2 . The refractive index and absorption data for ZnGeP_2 in this frequency range are shown in Fig. 6.13. The refractive index of the ordinary wave in the submillimeter range ($\nu < 150\ \text{cm}^{-1}$) is given by

$$(n^o)^2 = 9.723 + \frac{1.615}{1 - (\nu/264)^2}, \quad (6.9)$$

where 9.723 is a single oscillator extrapolation of the optical dielectric constant. The absorption data show that useful difference frequency-mixing can be obtained up to $\sim 110\ \text{cm}^{-1}$.

The optimum geometry for collinear phase-matched difference mixing in ZnGeP_2 is illustrated in Fig. 6.14 (lower inset). x , y , and z are the crystallographic axes; u and v are perpendicular bisectors of the x - and y -axes. The direction of propagation \mathbf{k} lies in the $v-z$ plane at the phase-matching angle θ to the optic axis z . The difference frequency ω_1 and the lower source frequency ω_2 propagate as ordinary waves, and the higher source frequency ω_3 propagates as an extraordinary wave. Figure 6.13 shows a typical disposition of the frequencies when CO_2 lasers are used as mixing sources. The phase-matching angles calculated from Fig. 6.13 are shown as the solid line in Fig. 6.14 including a small correction ($\sim -2^\circ$ at $100\ \text{cm}^{-1}$) for the tight focusing of the Gaussian beam.

Fifteen separate difference frequencies between 70 and $107\ \text{cm}^{-1}$ were selected using two single mode, single frequency, Q -switched CO_2 lasers. A typical trace in Fig. 6.14 (upper inset) shows the relative power output as a function of internal angle of propagation. The observed trace agrees well with the expected $\sin^2 \phi/\phi^2$ behavior. The width at half power points is 3.56° , which agrees with the calculated value of 3.55° for a crystal of length 0.36 cm. The agreement between the experimental phase-matching angles (solid points in Fig. 6.14) and the calculated curve is within experimental error.

The measured peak power external to the crystal was $1.7\ \mu\text{W}$ at $83\ \text{cm}^{-1}$ for peak powers of 360 W at ω_2 and 55 W at ω_3 . Since this power is adequate to produce a signal-to-noise ratio of $\sim 1000:1$ using a Ge:Ga detector, this source of far infrared radiation should find practical application. If one of the lasers at ω_2 or ω_3 were replaced by a tunable laser, such as the spin-flip Raman laser, or a parametric oscillator with comparable power, a tunable source of radiation in the submillimeter wave region suitable for high resolution spectroscopy would be possible.

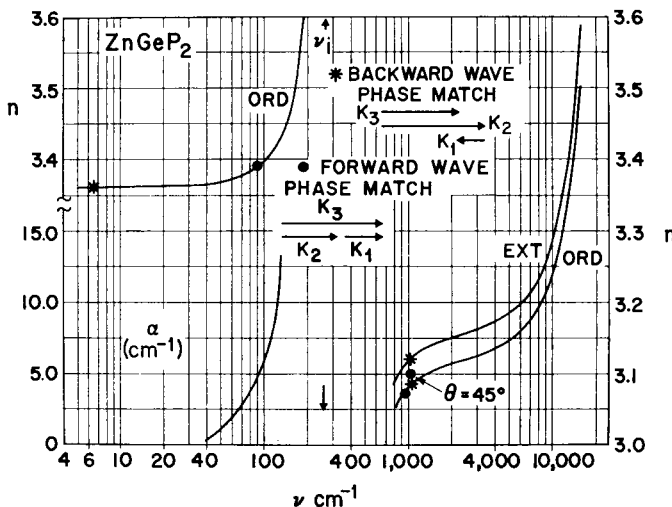


FIG. 6.13. Refractive index versus wavenumber for ZnGeP_2 . Phase-matching examples are given assuming $\nu_1 + \nu_2 = \nu_3$. Also shown is the absorption coefficient in the submillimeter region. (Boyd *et al.*, 1972c.)

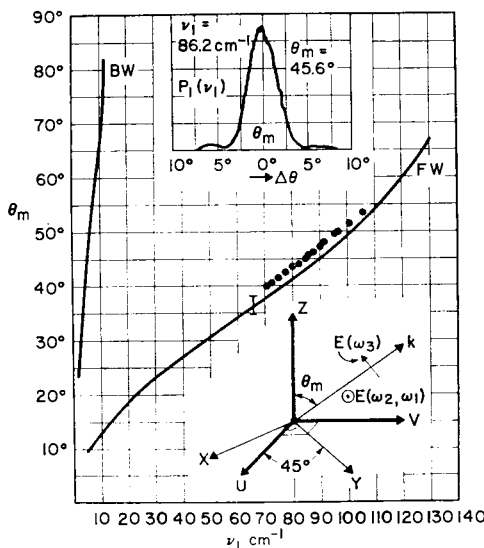


FIG. 6.14. Internal phase-matching angle θ_m versus ν_1 for forward wave (FW) and backward wave (BW) difference-mixing. The solid points are the experimental data; the solid line is calculated from the refractive index data in Fig. 6.13. The upper inset shows the difference mixing power $P_1(\nu_1)$ versus internal angle $\Delta\theta$ near θ_m . The lower inset shows the geometry for FW difference mixing. For BW mixing, the labels " ω_2 " and " ω_3 " should be interchanged. (Boyd *et al.*, 1972c.)

References

- BORN, M., and WOLF, E. (1964) *Principles of Optics*, Pergamon Press, London.
- BOYD, G. D., BUEHLER, E., and STORZ, F. G. (1971a) *Appl. Phys. Lett.* **18**, 301.
- BOYD, G. D., KASPER, H. M., and MCFEE, J. H. (1971b) *IEEE J. Quantum Electr.* QE **7**, 563.
- BOYD, G. D., GANDRUD, W. B., and BUEHLER, E. (1971c) *Appl. Phys. Lett.* **18**, 446.
- BOYD, G. D., BUEHLER, E., STORZ, F. G., and WERNICK, J. H. (1972a) *IEEE J. Quantum Electr.* QE **8**, 419.
- BOYD, G. D., KASPER, H. M., MCFEE, J. H., and STORZ, F. G. (1972b) *IEEE J. Quantum Electr.* QE **8**, 900.
- BOYD, G. D., BRIDGES, T. J., BUEHLER, E., and PATEL, C. K. N. (1972c) *Appl. Phys. Lett.* **21**, 553.
- BYER, R. L., KILDAL, H., and FEIGELSON, R. S. (1971) *Appl. Phys. Lett.* **19**, 237.
- CHEMLA, D. S., KUPECEK, P. J., ROBERTSON, D. S., and SMITH, R. C. (1971) *Optics Commun.* **3**, 29.
- GIORDMAINE, J. A. (1962) *Phys. Rev. Lett.* **8**, 19.
- HERBST, R. L., and BYER, R. L. (1971) *Appl. Phys. Lett.* **19**, 527.
- LEVINE, B. F. (1973) *Phys. Rev.* **7**, 2591; **7**, 2600; *J. Chem. Phys.* (1 August issue).
- LEVINE, B. F., and BETHEA, C. G. (1972) *Appl. Phys. Lett.* **20**, 272; **21**, 76.
- MAKER, P. D., TERHUNE, R. W., NISENHOFF, M., and SAVAGE, C. M. (1962) *Phys. Rev. Lett.* **8**, 21.
- MIDWINTER, J. E. and WARNER, J. (1965) *Br. J. Appl. Phys.* **16**, 1135.
- MILTON, A. F. (1972) *Appl. Optics* **11**, 2311.
- PHILLIPS, J. C. (1970) *Rev. Mod. Phys.* **42**, 317.

CHAPTER 7

ELECTRICAL PROPERTIES

7.1 Electrical Properties of II-IV-V₂ Compounds

In this chapter we review studies of the electrical properties of chalcopyrite crystals. It has been suggested that the electrical properties of II-IV-V₂ compounds are dominated by electrically active native defects resulting from deviations from a stoichiometric composition. The existence of these electrically active native defects has not been well documented for any compound, although highly suggestive results have been found in the case of CdSiAs₂. It has been found that the hole concentration in crystals grown from dilute solutions of Si in Cd + As is a strong function of the Cd to As ratio. The hole concentrations varied from $6 \times 10^{16} \text{ cm}^{-3}$ to $7 \times 10^{14} \text{ cm}^{-3}$ as the Cd to As ratio varied from 1.5 to 0.5 (Averkieva, 1970). The observed correlation between the composition of the solution and the resulting hole concentration strongly suggests the existence of an electrically active native defect.

Typical room temperature electrical properties for II-IV-V₂ crystals are listed in Table 7.1. Where available, the activation energies of the defects or impurities responsible for the conductivity are included. Due to the possibility of strong compensation in these compounds, there is some uncertainty as to whether or not the thermal activation energy should be doubled to obtain the impurity ionization energy.

7.1.1 CdSnAs₂

The temperature dependence of the conductivity and Hall coefficient of *n*-type CdSnAs₂ is shown in Fig. 7.1a for a sample with an electron concentration of $6 \times 10^{16} \text{ cm}^{-3}$ at room temperature. The electron mobility calculated from these data is shown in Fig. 7.1b and can be divided into three parts: $\mu \sim T^{0.25}$, $\mu(T) \sim T^2$, and $\mu \sim T^{-1.67}$. In the third region the mobility is dominated by electron-scattering by thermal lattice vibrations. Although the simple theory for this type of scattering predicts $\mu \sim T^{-1.5}$, the experimental exponent, -1.67, is close to the values observed in other semiconducting compounds with covalent bonding, e.g. InSb. The maximum electron mobility at 500 K is 25,000 cm²/V-s. The mobility obtained by extrapolating $\mu \sim T^{-1.67}$ to room temperature is of the same order of magnitude as observed in InSb.

The temperature dependences of the Hall constant and resistivity of a *p*-type crystal of CdSnAs₂ ($p = 3.4 \times 10^{16} \text{ cm}^{-3}$ at 300 K) are shown in Fig. 7.2. The behavior of these data have been attributed to a two-carrier conductivity mechanism. The electron-to-hole mobility ratio was estimated to be ~ 83 .

7.1.2 CdGeAs₂

It has been found that the electron mobility in CdGeAs₂ having $n \sim 4 \times 10^{18} \text{ cm}^{-3}$ remains constant at $\sim 1600 \text{ cm}^2/\text{V-s}$ within the range 100–500 K (Emelyanenko and Polushina, 1969). This suggests that the number of scattering defects is so large that

TERNARY CHALCOPYRITE SEMICONDUCTORS

TABLE 7.1. Room-temperature electrical properties of II-IV-V₂ crystals

Crystal	Energy gap (eV)	Growth method	Dopant	Carrier conc. (cm ⁻³)	Mobility (cm ² /V-s)	Resistivity	E_a (eV)
ZnSiP ₂	~2.2	I_2 transp. ^a	Cu, Te, or Se	$n \sim 10^{17}$ – 10^{18}	100	10^4 – 10^6 10^6	0.08
		I_2 transp. ^a					
ZnSiAs ₂	1.74	Zn solution ^a				0.12, 0.28	0.08
		Zn solution ^a	Te	$n \sim 4 \times 10^{17}$	100		
ZnGeP ₂	1.99	Unknown ^b		$n \sim 10^{17}$	100	10^4 10^2 – 10^5	0.35 0.05, 0.31
		Melt ^c		$p \sim 10^{15}$	140		
ZnGeAs ₂	1.15	Bi solution ^{d,e}		$p \sim 10^{13}$	20	4×10^6	0.55
		Melt ^f					
ZnSnP ₂	1.66	Melt ^g				0.11	0.11
		Sn solution ⁱ					
ZnSnAs ₂	0.73	Melt ^h		$p \sim 10^{17}$ – 10^{21}	40–200	$\sim 10^6$	0.48
		Sn solution ^j		$p \sim 10^{20}$	70		
CdSiP ₂	~2.4	I_2 transp. ^k		$n \sim 10^{14}$ – 10^{15}	80–150	10^4	0.2
		I_2 transp. ^l		$n \sim 10^{15}$	150		
CdSiAs ₂	1.55	Sn solution ⁱ				10^3 – 10^4	0.2
		Sn solution ^g					
CdGeP ₂	1.72	CdAs solution ⁿ		$p \sim 6 \times 10^{15}$ – 4×10^{16}	300–500	$\sim 10^6$	0.2
		Melt ^a	In, Sb Bi	$n \sim 10^{15}$ $p \sim 10^{15}$	~ 100 25		
CdGeAs ₂	0.57	Melt ^o		$p \sim 7 \times 10^{15}$	700–1500	10^3 – 10^4	0.2
		Melt ^p	In, Te	$n \sim 10^{16}$ – 10^{18}	2500		
CdSnP ₂	1.17	Sn solution ^q		$n \sim 10^{15}$ – 10^{18}	2000	10^3 – 10^4	0.2
		Sn solution ^r	Cu	p -type			
CdSnAs ₂	0.26	Melt ^s		$n \sim 10^{18}$	11000	10^3 – 10^4	0.2
		(Unknown) ^t		$p \sim 6 \times 10^{17}$	190		

^a Alekperova *et al.* (1969).

^b Goryunova *et al.* (1965).

^c Snell *et al.* (1968).

^d Bertotti and Somogyi (1971).

^e Somogyi and Bertotti (1972).

^f Ray *et al.* (1969).

^g Isomura and Masumoto (1971, 1972).

^h Borshchevskii *et al.* (1967).

ⁱ Goryunova *et al.* (1967a).

^j Kradinova and Voronina (1969); Ivakhno *et al.* (1969).

^k Bychkov *et al.* (1971).

^l Bychkov *et al.* (1966).

^m Averkieva *et al.* (1971).

ⁿ Goryunova *et al.* (1967b); Wiley *et al.* (1973).

^o Vaipolin *et al.* (1964); Kildal (1972).

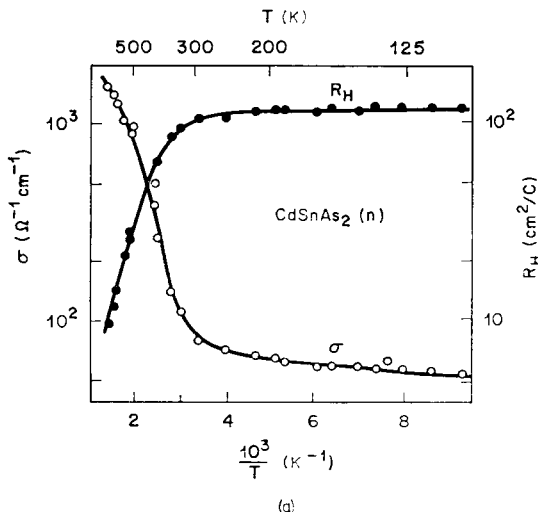
^p Emelyanenko and Polushina (1969).

^q Knight *et al.* (1972); Akimchenko *et al.* (1972).

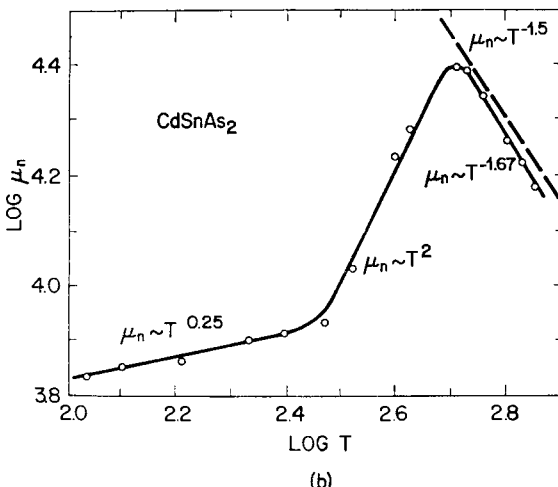
^r Leonov *et al.* (1971).

^s Strauss and Rosenberg (1961); Spitzer *et al.* (1961).

^t Polyanskaya *et al.* (1966).



(a)



(b)

FIG. 7.1. Electrical properties of n -type CdSnAs₂. (Matyas and Höschl, 1962.) (a) Conductivity and Hall coefficient. (b) Electron mobility.

scattering by thermal vibrations does not dominate even at 500 K. From these data it is estimated that the mobility for scattering by lattice vibrations is at least $18,000 \text{ cm}^2/\text{V}\cdot\text{s}$ at 500 K and even higher at room temperature. No appreciable change of the mobility with the electron concentration was observed over the range 4×10^{16} to $3 \times 10^{18} \text{ cm}^{-3}$, whereas the values of mobility for samples with similar concentrations can differ markedly. Both of these results indicate that either a strong compensation of impurities takes place (perhaps by deviations from stoichiometry) or there are a large number of strongly scattering defects such as microcracks, which are frequently observed during growth of CdGeAs₂ from the melt (Chapter 2).

In p -type samples of CdGeAs₂ ($p \sim 10^{16} \text{ cm}^{-3}$) the conductivity increases with increasing temperature in the entire range 90–750 K (Fig. 7.3). The Hall coefficient

TERNARY CHALCOPYRITE SEMICONDUCTORS

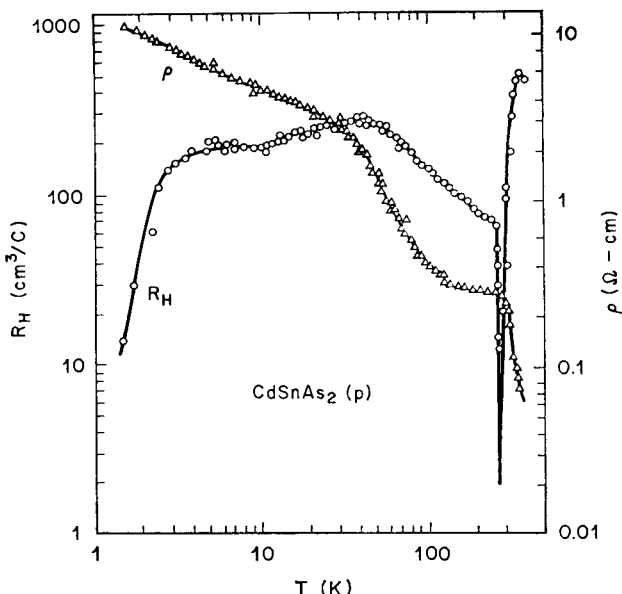


FIG. 7.2. Temperature dependence of the resistivity Δ and Hall coefficient (\circ) of p -type CdSnAs_2 . (Polyanskaya *et al.*, 1966.)

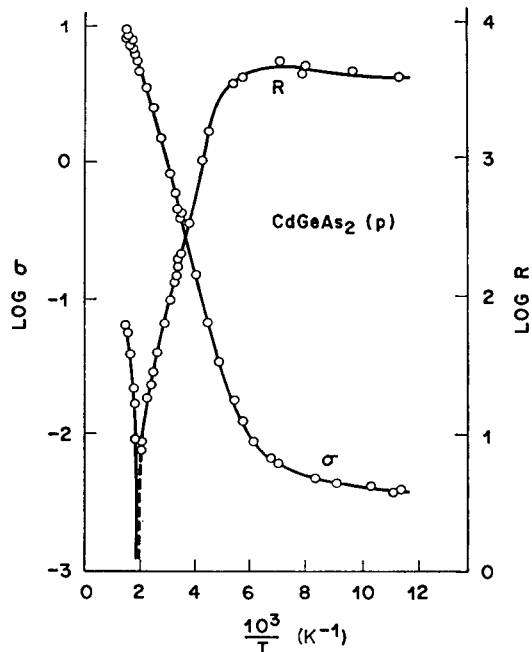


FIG. 7.3. Temperature dependence of the Hall coefficient and conductivity of p -type CdGeAs_2 . (Vaipolin *et al.*, 1964.)

decreases above 150 K and changes sign at about 500 K. From these data it is concluded that the conductivity remains extrinsic up to 150 K, then the mixed conductivity range begins, and above 650 K intrinsic conductivity dominates.

7.1.3 ZnSiAs₂ and ZnGeP₂

The temperature dependence of the electrical properties of *p*-type ZnSiAs₂ and ZnGeP₂ are shown in Figs. 7.4 and 7.5. In the high-temperature region the conductivity increases exponentially with activation energies of 0.28 and 0.35 eV respectively. Somogyi and Bertoti (1972) argue that since ZnGeP₂ is likely to be heavily compensated, the activation energy of 0.35 eV is equal to the acceptor binding energy. The temperature independence of the mobility (Fig. 7.5) is consistent with this suggestion. Snell *et al.* (1968) have emphasized that since the mobility drops rapidly for $T < 210$ K in ZnSiAs₂, low-temperature resistivity measurements should be used with caution in the derivation of ionization energies. The mobility data of Siegel *et al.* (1973) in Fig. 7.6 make this point very nicely.

7.1.4 ZnSiP₂

In Fig. 7.7 we show the temperature dependence of the conductivity and Hall coefficient for a sample of ZnSiP₂ having a room-temperature electron density of $\sim 10^{17}$ cm⁻³ and a Hall mobility of ~ 100 cm²/V-s. The conductivity decreases with cooling throughout the whole temperature range 80–500 K. Such behavior, together with the low electron mobility, suggests the possibility of strong compensation of impurities. The ionization energy of the donor impurities estimated from the temperature dependence of the conductivity is 0.08 eV. In the temperature range 350–670 K the electron mobility varies with temperature as $\sim T^{-1}$.

7.1.5 ZnSnP₂ and ZnSnAs₂

ZnSnP₂ and ZnSnAs₂ are unique among II–IV–V₂ compounds in that they crystallize with vanishing tetragonal compressions, i.e. $c/a = 2.00$. These compounds also crystallize in both the chalcopyrite and sphalerite structures. The crystals with chalcopyrite structure have an ordered distribution of Zn and Sn on the cation sites. However, large single crystals have not been obtained due to the existence of small domains in which the x -, y - and z -axes of various domains are aligned, at random, parallel to each other. The sphalerite modification differs from the chalcopyrite form only by a random distribution of atoms in the cation sublattice.

The temperature dependences of the Hall coefficient and conductivity of crystals of ZnSnP₂ having the chalcopyrite and sphalerite structures respectively, and room temperature hole concentrations of $\sim 7 \times 10^{16}$ cm⁻³, are shown in Fig. 7.8. The temperature dependences of the hole mobility for crystals of both structures are shown in Fig. 7.9. The low value of the hole mobility in crystals with the sphalerite structure is perhaps explained by the additional scattering by defects associated with the disordered crystal structure. At low temperatures, scattering by defects or impurities dominates in crystals of both modifications. This scattering mechanism remains dominant in sphalerite crystals up to higher temperatures. At temperatures above 200 K scattering by lattice vibrations dominates the hole mobility in chalcopyrite crystals.

ZnSnAs₂ crystals having the chalcopyrite structure are only obtained *p*-type with room temperature hole concentrations of 10^{17} – 10^{21} cm⁻³. Crystals with the disordered

TERNARY CHALCOPYRITE SEMICONDUCTORS

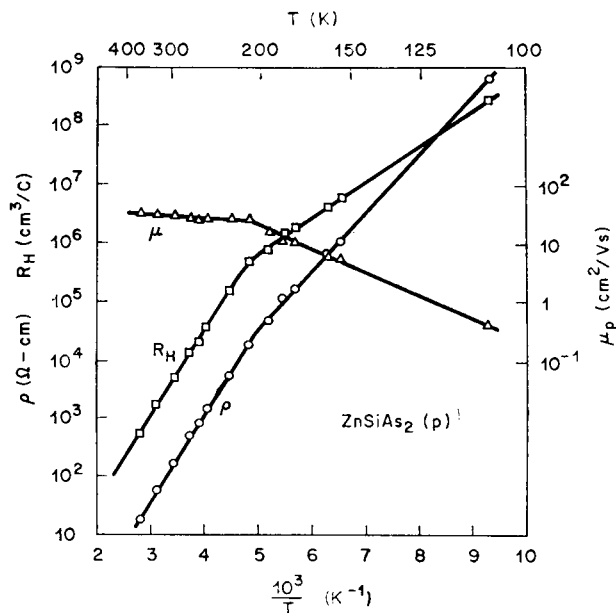


FIG. 7.4. Electrical properties of *p*-type ZnSiAs_2 . (Snell *et al.*, 1968.)

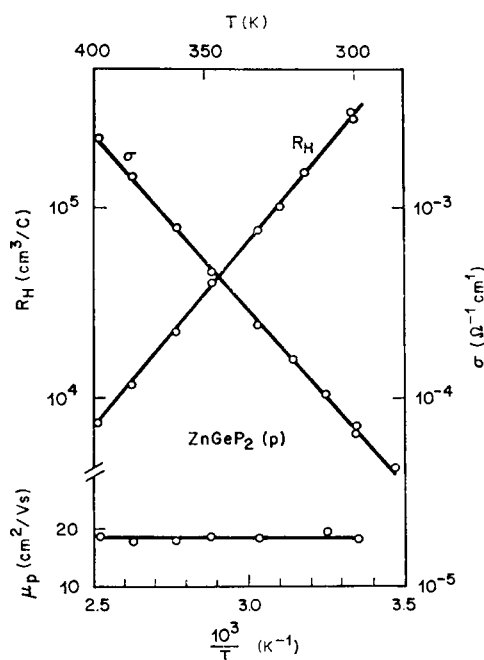


FIG. 7.5. Electrical properties of *p*-type ZnGeP_2 . (Bertoti and Somogyi, 1971.)

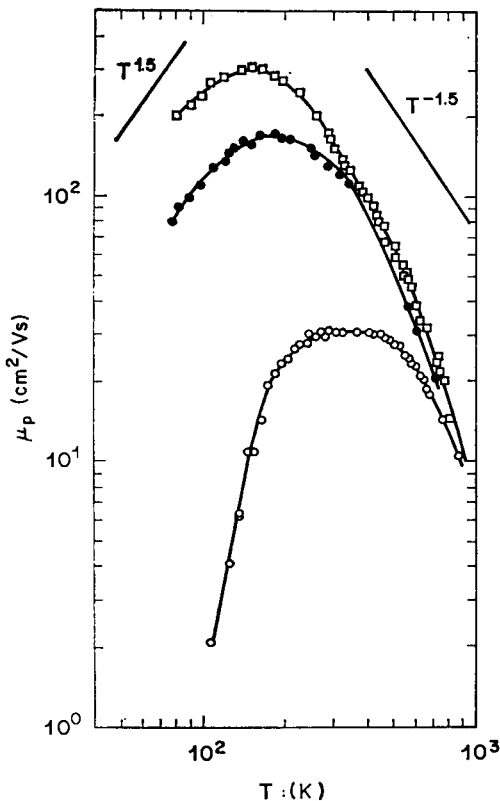


FIG. 7.6. Temperature dependence of the mobility of various samples of ZnSiAs₂ with room temperature hole concentrations $p = 2 \times 10^{15}$ (\circ), 2.3×10^{17} (\bullet), and 2.6×10^{17} (\square). (Siegel *et al.*, 1973.)

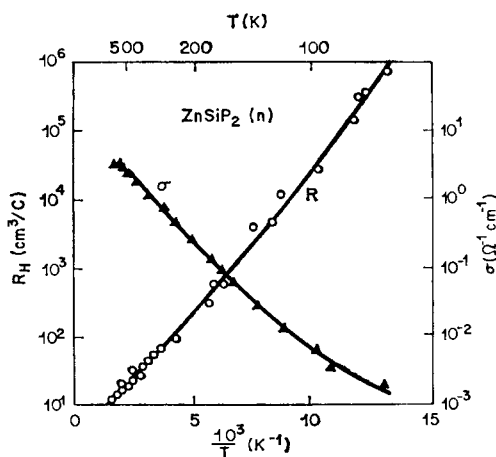


FIG. 7.7. Electrical properties of *n*-type ZnSiP₂. (Goryunova *et al.*, 1965.)

TERNARY CHALCOPYRITE SEMICONDUCTORS

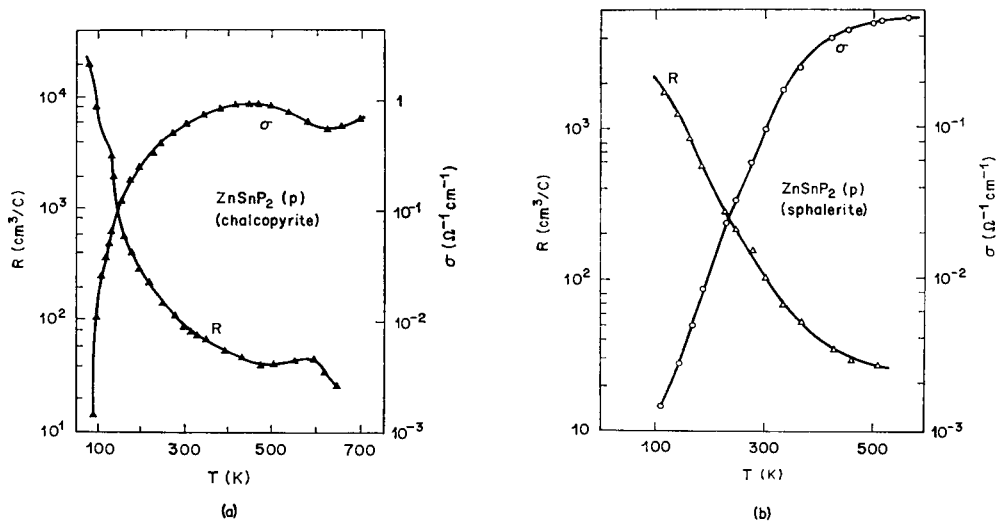


FIG. 7.8. Electrical properties of p -type $ZnSnP_2$ in the chalcopyrite (a) and sphalerite (b) structures. (Goryunova *et al.*, 1967a.)

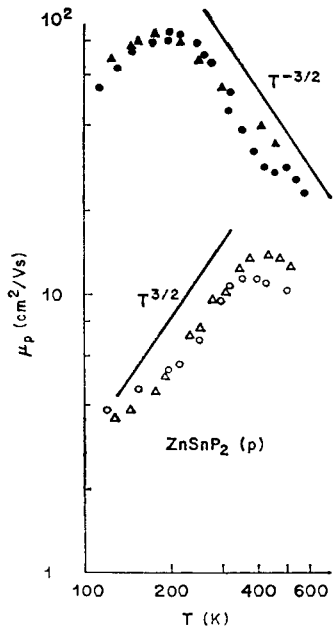


FIG. 7.9. Temperature dependence of the hole mobility in p -type $ZnSnP_2$ in the sphalerite (\circ , \triangle) and chalcopyrite (\bullet , \blacktriangle) structures. (Goryunova *et al.*, 1967a.)

zincblende structure are only obtained with hole concentrations $\sim 10^{20} \text{ cm}^{-3}$ and very low mobilities. In Fig. 7.10 we show the temperature dependence of the Hall coefficient and mobility between 80 and 825 K for crystals having the chalcopyrite structure. The interesting feature of this figure is that the Hall coefficient reverses sign at about 675 K and reaches a higher value in the intrinsic range than in the extrinsic region. From these data a mobility ratio μ_n/μ_p of ~ 10 is determined. The room temperature hole mobility in relatively pure *p*-type ZnSnAs₂ crystals having the chalcopyrite structure has the value $190 \text{ cm}^2/\text{V}\cdot\text{s}$. The hole mobility decreases rapidly with increasing hole concentration (Fig. 7.11).

The electrical properties of a single crystal of ZnSnAs₂ having the disordered zincblende structure are shown in Fig. 7.12. The temperature independence of these properties is characteristic of a degenerate semiconductor.

7.2 Band Parameters of II-IV-V₂ Compounds

Band parameters are available for a few compounds and are summarized in Table 7.2. The band edge structure of CdSnAs₂ has been studied the most extensively, and the model proposed to explain the observed electrical and optical behavior is shown in Fig. 7.13, and its band parameters are listed in Table 7.3 (Karymshakov *et al.*, 1971). The ordering of the valence bands shown in Fig. 7.13 agrees with the electroreflectance studies discussed in Section 3.2 although the hole effective masses do not agree with the values in Table 3.2 (p. 90). In addition, the proposed conduction band structure is very unusual. The Γ_3 and ($T_1 + T_2$) minima are derived from the X points in the binary analog InAs. Although in InAs the lowest X minimum is ~ 1.5 eV above the lowest Γ minimum, Fig. 7.13 suggests that in CdSnAs₂, Γ_3 and $T_1 + T_2$ are only 0.07 and 0.19 eV above Γ_1 , respectively. A theoretical calculation predicting the energy separations between Γ_1 , Γ_3 , and $T_1 + T_2$ minima is not yet available.

Values of the effective mass of conduction electrons in CdGeAs₂ have been determined from a study of the plasma reflection spectra in crystals of various electron concentrations. Taking into account the damping of plasma oscillations, the effective mass is determined from the following equation:

$$\left(\frac{m^*}{m_0}\right)^2 - \frac{3\epsilon_\infty - 1}{4\epsilon_\infty(\epsilon_\infty - 1)} \left[\frac{(1/\Omega^2) + 5 + 8\Omega^2}{1 + 3\Omega^2} \right] C \frac{m^*}{m_0} + \frac{3\epsilon_\infty - 2}{2\epsilon_\infty(\epsilon_\infty - 1)} \left[\frac{1 + 2\Omega^2}{1 + 3\Omega^2} \right] C^2 = 0, \quad (7.1)$$

where $\Omega = \omega_{\min}\tau$, $C = ne^2/(m_0\epsilon_0\omega_{\min}^2)$, ϵ_0 is the permittivity of vacuum, ω_{\min} is the frequency at the plasma minimum of the reflection curve, and τ is the average time between collisions found from the relationship $\mu_n = e\tau/m^*$. The high-frequency permittivity $\epsilon_\infty = 14.3$ was determined from reflection measurements on a nondegenerate *p*-type crystal. Plasma reflection spectra for three *n*-type crystals and one *p*-type crystal of CdGeAs₂ are shown in Fig. 7.14. Values of the electron effective mass determined from eq. (7.1) are shown in Fig. 7.15 as a function of electron concentration. Although the increase in m^* for $n \geq 10^{18} \text{ cm}^{-3}$ probably results from conduction band non-parabolicity, it may also result from the existence of a second conduction band.

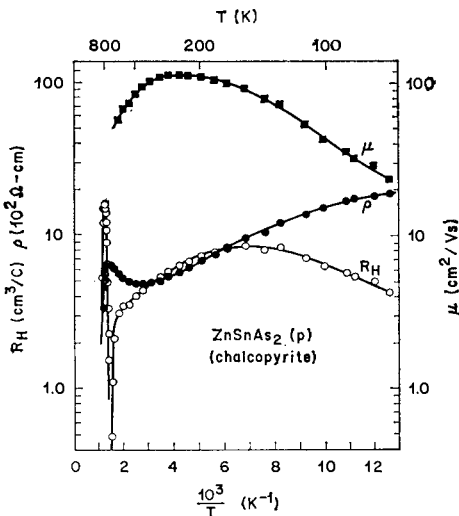


FIG. 7.10. Electrical properties of *p*-type ZnSnAs_2 in the chalcopyrite structure. (Masumoto and Isomura, 1965.)

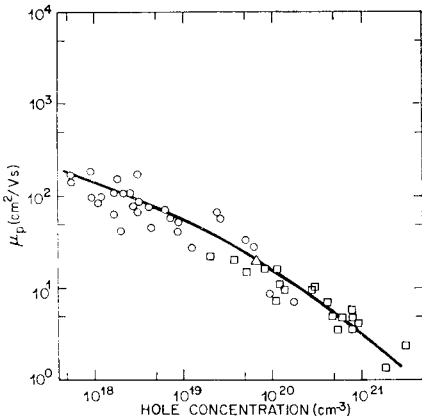


FIG. 7.11. Dependence of the hole mobility in ZnSnAs_2 on hole concentration. (Borshchevskii *et al.*, 1967.)

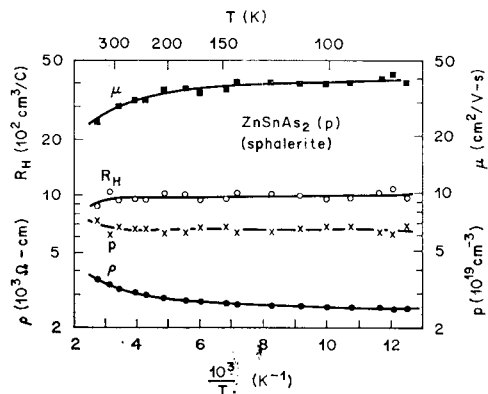


FIG. 7.12. Electrical properties of *p*-type ZnSnAs_2 in the zincblende structure. (Masumoto and Isomura, 1965.)

TABLE 7.2. Band parameters for II-IV-V₂ Compounds

Crystal	Energy gap (eV)	m_e	m_h	Reference
ZnSiP ₂	~2.1	0.07–0.13		a
ZnSiAs ₂	1.74		0.07	b
ZnGeP ₂	1.99		0.5	c
ZnGeAs ₂	1.15		0.4–0.7	d
ZnSnAs ₂	0.73		0.35	e
			0.4–0.6	f
ZnSnSb ₂	0.30		0.25	g
CdSiP ₂	~2.2	0.09		b
CdGeAs ₂	0.57	0.035		h
CdSnP ₂	1.17	0.036	0.3	i
				j

^a Goryunova *et al.* (1966a).^b Vaipolin *et al.* (1964).^c Somogyi and Bertoti (1972).^d Leroux-Hugon (1963); Kesamanly *et al.* (1965).^e Korneev *et al.* (1971).^f Borshchevskii *et al.* (1967); Masumoto and Isomura (1965).^g Kradinova and Voronina (1969).^h Zlatkin *et al.* (1969).ⁱ Emelyanenko *et al.* (1971).^j Sokolova *et al.* (1968).TABLE 7.3. Band parameters of CdSnAs₂
(energies in eV, masses in units of the free electron mass)

Band parameter	Values
Energy gap	0.23
Δ_{12}	0.07
Δ_{23}	0.12 ± 0.02
Δ_c	0.03 ± 0.01
Δ_{so}	0.5 ± 0.1
g^* (electrons)	$-(42 \pm 10)$
$m_n^* 1$	0.015 ± 0.005
$m_n^* 2$	0.035
$m_n^* 3$	0.056 ± 0.002
$m_p^* 1$	1.0 ± 0.3
$m_p^* 2$	0.020 ± 0.005
$m_p^* 3$	0.10 ± 0.05

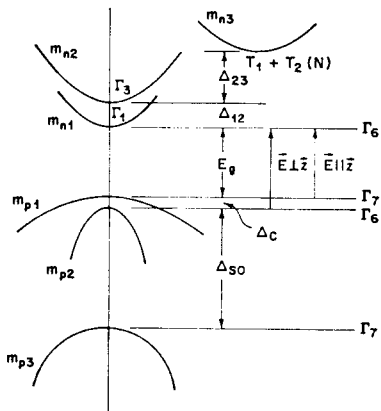


FIG. 7.13. Band structure of CdSnAs₂ near the direct energy gap. (Karymshakov *et al.*, 1971.) The relevant band parameters are listed in Table 7.3.

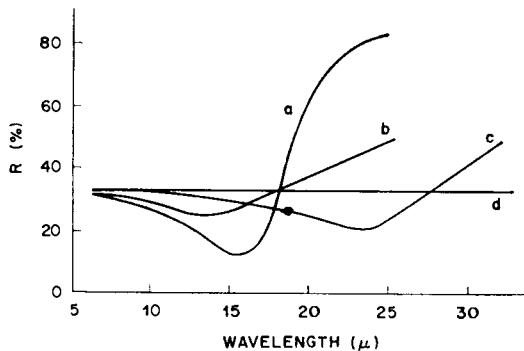


FIG. 7.14. Plasma reflection of *n*-type CdGeAs₂ at 295 K. (a) $n = 2.6 \times 10^{18} \text{ cm}^{-3}$; (b) $n = 5 \times 10^{18} \text{ cm}^{-3}$; (c) $n = 0.8 \times 10^{18} \text{ cm}^{-3}$; (d) *p*-type crystal with $p = 4 \times 10^{16} \text{ cm}^{-3}$. (Zlatkin *et al.*, 1969.)

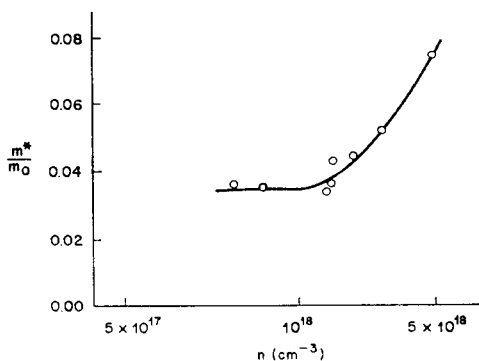


FIG. 7.15. Dependence of the effective mass of the conduction electrons on the electron density in CdGeAs₂. (Zlatkin *et al.*, 1969.)

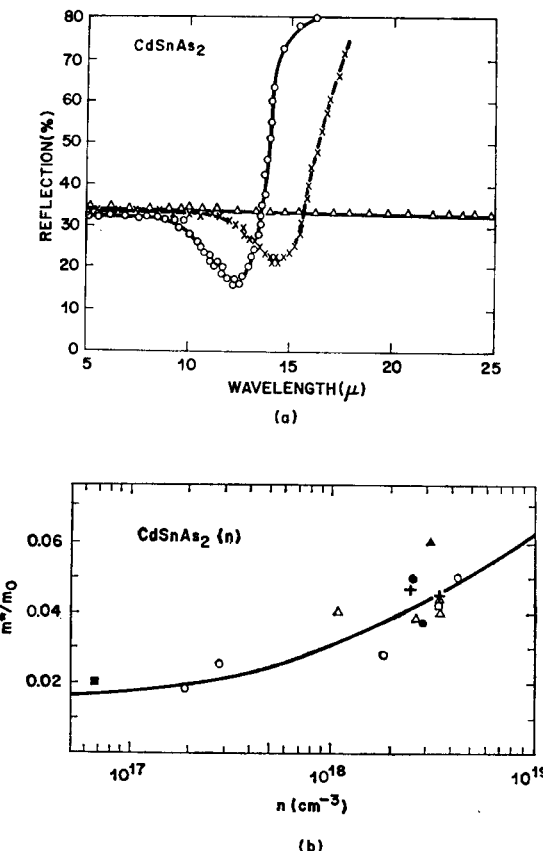


FIG. 7.16. (a) Plasma reflection spectrum of CdSnAs₂ at room temperature: (○) $n = 3.5 \times 10^{18} \text{ cm}^{-3}$; (X) $n = 2.6 \times 10^{18} \text{ cm}^{-3}$; (Δ) $n = 6.2 \times 10^{16} \text{ cm}^{-3}$. (Sikharulidze *et al.*, 1966.) (b) Electron effective mass in CdSnAs₂ as a function of the free electron concentration. (Borshchevskii *et al.*, 1967; Goryunova *et al.*, 1966 b.)

Results of similar measurements of the plasma reflection spectra of *n*-type CdSnAs₂ are shown in Fig. 7.16a. Using a dielectric constant $\epsilon = 13.7$, effective masses between 0.04 and 0.06 m_0 have been determined. The electron effective mass in CdSnAs₂ crystals of various concentrations has also been determined from measurements of the thermal e.m.f. in magnetic fields (Fig. 7.16b).

7.3 Electrical Properties of I-III-VI₂ Compounds

7.3.1 Sulfides and Selenides — Annealing Characteristics

It has been found that the electrical properties of I-III-VI₂ compounds containing S or Se can readily be controlled by suitable annealing conditions (Tell *et al.*, 1972). Electrical characteristics of a series of melt-grown Cu and Ag compounds which have been annealed under maximum or minimum chalcogen pressures are given in Table 7.4. The values given in the table are typical, since significant changes in resistivity and

TERNARY CHALCOPYRITE SEMICONDUCTORS

TABLE 7.4. Room-temperature electrical properties of annealed I-III-VI₂ Compounds (after Tell et al., 1972).

Compound	Energy gap (eV)	Annealed under maximum S or Se pressure				Annealed under minimum S or Se pressure			
		Type	ρ ($\Omega \text{ cm}$)	p (cm^{-3})	μ ($\text{cm}^2/\text{V}\cdot\text{s}$)	Type	ρ ($\Omega \text{ cm}$)	n (cm^{-3})	μ ($\text{cm}^2/\text{V}\cdot\text{s}$)
CuAlS ₂	3.5	<i>p</i>	$10^2\text{--}10^3$	3×10^{15}	<2			$>10^5$	
CuAlSe ₂	2.7	<i>p</i>	$10^2\text{--}10^3$	1×10^{16}	~ 1			$>10^5$	
CuGaS ₂	2.4	<i>p</i>	1	4×10^{17}	15			$>10^5$	
CuGaSe ₂	1.7	<i>p</i>	0.05	5×10^{18}	20			$>10^5$	
CuInS ₂	1.5	<i>p</i>	5	1×10^{17}	15	<i>n</i>	1	3×10^{16}	200
CuInSe ₂	1.0	<i>p</i>	0.5	1×10^{18}	10	<i>n</i>	0.05	4×10^{17}	320
AgGaS ₂	2.7		$>10^5$					$>10^5$	
AgInS ₂	1.9		$>10^5$			<i>n</i>	10	4×10^{15}	150
AgGaSe ₂	1.8		$>10^5$					$>10^5$	
AgInSe ₂	1.2	<i>n</i>	10^4	8×10^{11}	750	<i>n</i>	0.02	5×10^{17}	600

mobility can be obtained by annealing at different temperatures. The Cu compounds are readily made *p*-type by annealing at temperatures in the range 600–800°C for 24 hr under maximum S or Se pressure, and quenching to room temperature. On the other hand, annealing under minimum S or Se pressure renders the crystals highly resistive (wide-bandgap members) or *n*-type (narrow-gap members). It is also seen from Table 7.4 that there is a moderately sharp energy boundary between those Cu compounds which can be made both *p*- and *n*-type, and those which are only *p*-type. CuInS₂ with a direct gap of 1.5 eV has been made *n*-type by annealing under minimum S pressure at temperatures as low as 650°C for as short as 15 min. CuGaSe₂, with a direct gap of 1.7 eV, exhibits only high resistivity after being annealed under minimum Se pressure at 800°C for 24 hr, and even the addition of donor impurities such as Cl or Zn has failed to make this compound usefully *n*-type.

AgInS₂ and AgInSe₂ have been made usefully *n*-type, whereas AgGaS₂ and AgGaSe₂ are not appreciably affected by these annealing procedures. Appreciable bulk conductivity has never been obtained by various doping experiments (diffusion and during growth) on the latter two Ag compounds.

The *p*-type conductivity observed in the Cu I-III-VI₂ compounds is surprising, since it is a characteristic flaw of the analogous II-VI sulfides and selenides that they cannot be made usefully *p*-type. While it seems clear that intrinsic defects are playing a major role in determining the conductivity, it is not certain whether annealing in S vapor creates shallow intrinsic acceptors (i.e. Cu vacancies or S interstitials) or removes intrinsic donors (i.e. Cu interstitials or S vacancies). In the latter case, the acceptors would be extrinsic (e.g. P or Zn), and the respective anneals under minimum or maximum S pressure would compensate or uncompensate the foreign acceptors.

Likely extrinsic acceptors can probably be ruled out, since it has been found that the group II atoms Cd and Zn, which are possible donors on the Cu site and acceptors on the group III site, act primarily as donors. The group V atoms are not normally present in undoped II-VI compounds and are probably also unimportant in undoped I-III-VI₂ compounds. Spectrochemical analysis usually indicates the major contaminant to be Si, which should be a donor. The most likely acceptor is therefore the Cu vacancy.

It is expected that Cu does not participate in the covalent bonding to any great extent. That is, most of the covalent nature of the bonding is due to the group III and group VI atoms. Therefore, the energy of formation of Cu vacancy acceptors should be considerably smaller, and their concentration considerably larger, than the corresponding quantities for Zn vacancies in ZnS. Although Cu is also expected to readily go into interstitial positions, thereby compensating the Cu vacancy acceptors, the experimental observation of low-resistivity *p*-type material shows that this compensation is not complete. In addition, the reduction in the energy gaps of the Cu compounds by ~ 1.5 eV relative to their binary analogs reduces the likelihood of self-compensation by S vacancies, since the energy to be gained by spontaneous formation of a S vacancy is ~ 1.5 eV less than in the binary analog. In contrast to the Cu compounds, none of the Ag compounds studied has been made usefully *p*-type. This indicates that either the Ag vacancy acceptor is deep, or else the vacancy formation energy is considerably larger than for the Cu vacancy.

We mentioned above that two of the Ag compounds are readily made *n*-type, while the other two are semi-insulating. The ability to achieve *n*-type conductivity does not decrease smoothly with increasing bandgap in the Ag compounds, since AgInS_2 which is readily made *n*-type has a slightly larger energy gap than AgGaSe_2 which is always semi-insulating. It is interesting that every ternary containing In has been made *n*-type, whereas every ternary containing Cu has been made *p*-type. The role of In, if any, in the ability to achieve *n*-type conductivity is not clear, nor is the nature of the donors. The donors may well be extrinsic, since the crystals often contain significant amounts of Si and, to less extent, group II impurities such as Mg.

Thus far we have been considering exclusively I-III-VI₂ crystals grown from the melt. An alternate means for growing single crystals of these compounds is by halogen transport. It is likely that such crystals contain an appreciable halogen concentration, perhaps residing on the chalcogen site and acting as donors. Honeyman (1969) reports that iodine transported CuAlS_2 is *n*-type with a room temperature resistivity of $10^5\text{--}10^7 \Omega\text{-cm}$. With increasing temperature up to 400°C, the resistivity decreases with an activation energy of 0.35 eV. Irreversible changes in the crystal's resistance prevented the measurements from being extended to higher temperatures. Honeyman (1969) also reports that the room temperature resistivity of iodine transported CuAlSe_2 is $10^4\text{--}10^5 \Omega\text{-cm}$ *p*-type.

7.3.2 Sulfides and Selenides — Transport Measurements

7.3.2.1. CuGaSe_2

Measurements of the transport properties of I-III-VI₂ compounds as a function of temperature are much less extensive than for II-IV-V₂ compounds. The resistivity and Hall coefficients of one high-resistivity sample ($1.9 \times 10^5 \Omega\text{-cm}$ at 300 K) and one low-resistivity sample ($1.6 \times 10^3 \Omega\text{-cm}$) of CuGaSe_2 are shown in Fig. 7.17. The high-temperature segments of the two resistivity curves are almost identical, and are dominated by intrinsic carriers thermally generated across a bandgap of ~ 1.63 eV. This value is close to the room temperature bandgap of 1.68 eV determined from electroreflectance measurements (Table 4.1, p. 118).

The middle segments of the resistivity curves in Fig. 7.17 display activation energies of 0.27 eV, suggesting the excitation of carriers from a prominent impurity level. Lerner

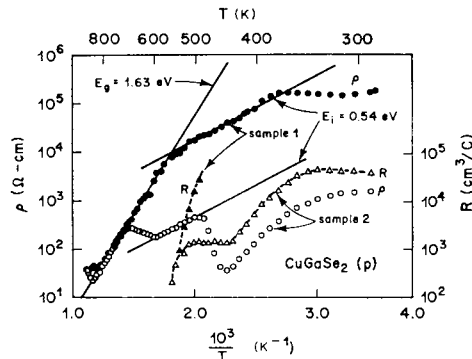


FIG. 7.17. Resistivity (\circ , \bullet) and Hall coefficient (Δ , \blacktriangle) as a function of $1/T$ for samples 1 (\bullet) and 2 (\circ) of CuGaSe_2 . (Lerner, 1966.)

has speculated that the level results from the presence of an excess of copper. Later work described earlier in this section indicates that the likely dominant acceptor is a copper vacancy.

Hall measurements were obtained from sample 1 in a limited temperature range (Fig. 7.17). In this range, the Hall coefficient falls much faster than one would expect simply on the basis of thermal activation of holes from the 0.27 eV impurity level. The contribution of intrinsic carriers to the conductivity, estimated by extrapolation of the resistivity curve from the high temperature region, is not negligible here. The presence of intrinsic electrons decreases the Hall voltage; hence the highest value of R plotted ($27.5 \times 10^3 \text{ cm}^3/\text{C}$) must be regarded as a lower limit on the true one-carrier value. Likewise, the derived values of hole concentration, $p = 3.3 \times 10^{11} \text{ cm}^{-3}$, and hole mobility, $\mu = 1.3 \text{ cm}^2/\text{V-s}$, are to be taken as upper and lower limits, respectively.

In the case of sample 2, it was possible to obtain Hall data over the entire extrinsic region (Fig. 7.17). The Hall voltage again drops precipitously in the high-temperature region, presumably due to the onset of intrinsic conduction. At temperatures below $\sim 500 \text{ K}$, however, one may safely assume hole conduction. The mobilities and hole concentrations derived on this assumption are plotted in Fig. 7.18. The room temperature hole mobility is $\sim 30 \text{ cm}^2/\text{V-s}$.

7.3.2.2. AgInSe_2

Figure 7.19 depicts the resistivity and Hall coefficient for a single crystal of n -type AgInSe_2 . The slope of the resistivity curve in the intrinsic region gives a bandgap of 1.15 eV, close to the value of 1.24 eV deduced from room temperature electroreflectance measurements (Table 4.1). A prominent impurity level with an activation energy of 0.11 eV dominates the electrical conductivity in the intermediate temperature range. In the intrinsic region Lerner obtains the quantities

$$\frac{R}{q} = \mu_n(1 - b^{-1}) \quad \text{and} \quad \frac{1}{Re} = n_i \left(\frac{b + 1}{b - 1} \right), \quad (7.2)$$

where $b \equiv \mu_n/\mu_p$. These quantities are plotted in Fig. 7.20, and both are fairly smooth curves up to $\sim 800 \text{ K}$.

Lerner observed an irregularity in the Hall coefficient of AgInSe_2 at temperatures above $\sim 800 \text{ K}$ at about the same temperature at which the resistivity deviates from the intrinsic curve. Below that point, recycling the temperature resulted in reproducible

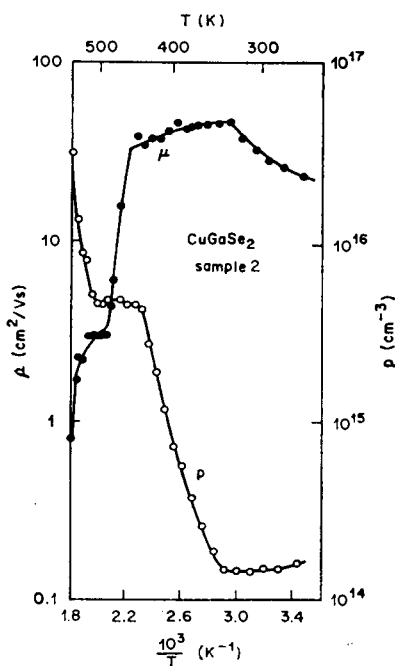


FIG. 7.18. Hall mobility and hole concentration computed from data for CuGaSe₂ sample 2 (Fig. 7.17). (Lerner, 1966.)

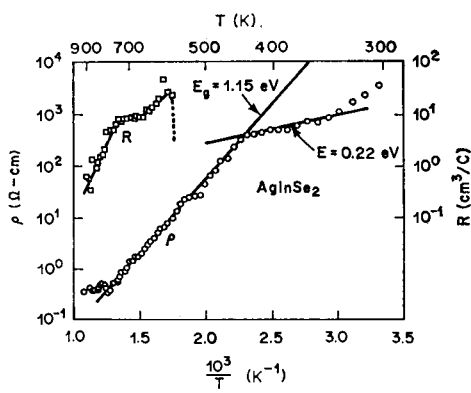


FIG. 7.19. Electrical properties of AgInSe₂. (Lerner, 1966.)

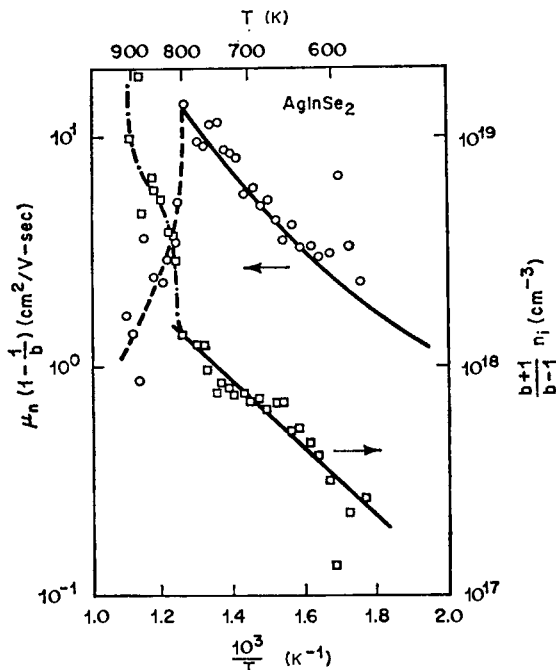


FIG. 7.20. Two-carrier Hall mobility, $\mu_n(1 - b^{-1})$ and $n_i(b + 1)(b - 1)^{-1}$, for a sample of AgInSe_2 , deduced from data in Fig. 7.19. (Lerner, 1966.)

data. Once the temperature was raised above 800 K, however, the resistivity and Hall coefficient both changed by 10–20% on recycling. Lerner correctly attributed these irregularities to small, but irreversible, chemical changes above $T \sim 800$ K. We now know that these irregularities result from native defects, the number of which depends upon the annealing temperature and chalcogen overpressure.

7.3.2.3. CuGaSe_2 , CuInSe_2 , and CuAsSe_2

The electrical conductivities and thermoelectric powers of the compounds CuGaSe_2 , CuInSe_2 , and CuAsSe_2 have been measured at temperatures below and above the respective melting points (Mal'sagov, 1970). As shown in Fig. 7.21, up to a temperature of ~ 800 °C these samples of CuGaSe_2 exhibit impurity conduction: the electrical conductivity decreases monotonically, and the thermoelectric power increases slowly at first and then rapidly. As the temperature is further increased, intrinsic conduction predominates. Near the melting point, the electrical conductivity increases abruptly apparently due to an increase in the carrier density and change in the electron–hole ratio. The carrier activation energy for the solid state (1.68 eV) is surprisingly high since the energy gap determined from room temperature electroreflectance measurements is only 1.68 eV.

The electrical conductivity and the thermoelectric power of CuInSe_2 (Fig. 7.22) change abruptly in the temperature range 810–820°C evidently due to the structural changes revealed in the X-ray and thermographic studies of Austin *et al.* (1956) and Palatnik and Rogachev (1966). The abrupt decrease in the magnitude of the thermoelectric power at the melting point and the reversal of its sign from negative to positive

as well as the increase of the electrical conductivity have been explained by Mal'sagov (1970) as the result of dissociation of CuInSe_2 . He suggests that ionic conduction predominates in the melt, and the bonding is mainly of the "ionic-covalent" type. The electrical conductivity of CuInSe_2 measured by Zhuze *et al.* (1958) is shown in Fig. 7.23.

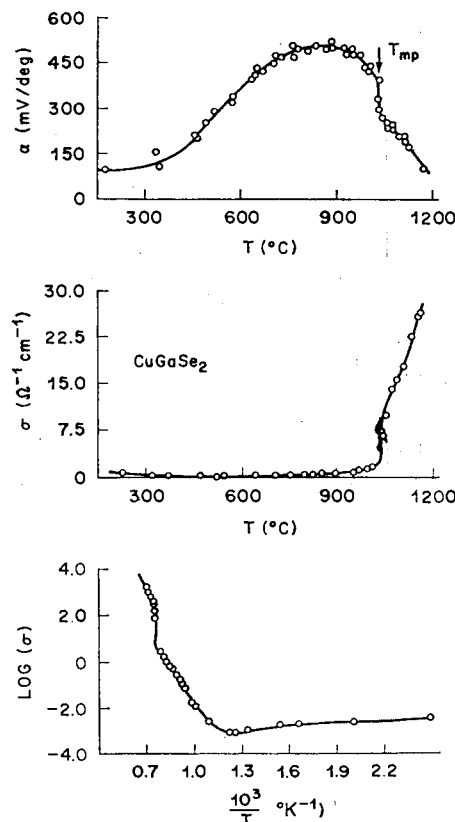


FIG. 7.21. Electrical conductivity and thermoelectric power of CuGaSe_2 .
(Mal'sagov, 1970.)

From the slope of the curve in the intrinsic region a bandgap of 1.07 eV is determined. For comparison, the optical energy gap at room temperature is 1.00 eV (Chapter 4).

The temperature dependences of the thermoelectric power and electrical conductivity of CuAsSe_2 shown in Fig. 7.24 indicate that CuAsSe_2 is an extrinsic semiconductor which exhibits quasimetallic behavior right up to the melting point. At the melting point the electrical conductivity falls by a factor of 10 and the thermoelectric power increases by the corresponding amount. Mal'sagov (1970) attributes these effects to a disappearance of impurity levels associated with vacancies or interstitials due to the high mobility of atoms and the disruption of short-range order. Nonetheless, the constancy of the thermoelectric power and the slow variation of the electrical conductivity in the range 415–470°C above the melting point are attributed to the influences of impurities. There follows at higher temperatures a well-defined region of intrinsic conduction with a carrier activation energy of 1 eV. CuAsSe_2 exhibits *p*-type conduction in the whole temperature range investigated.

TERNARY CHALCOPYRITE SEMICONDUCTORS

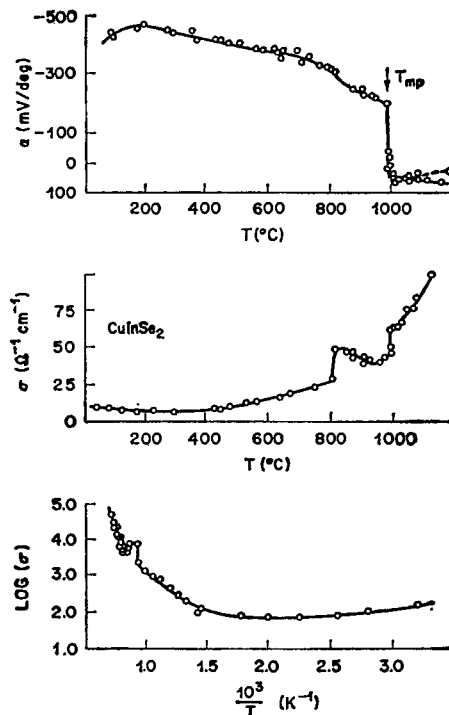


FIG. 7.22. Electrical conductivity and thermoelectric power of CuInSe_2 .
(Mal'sagov, 1970.)

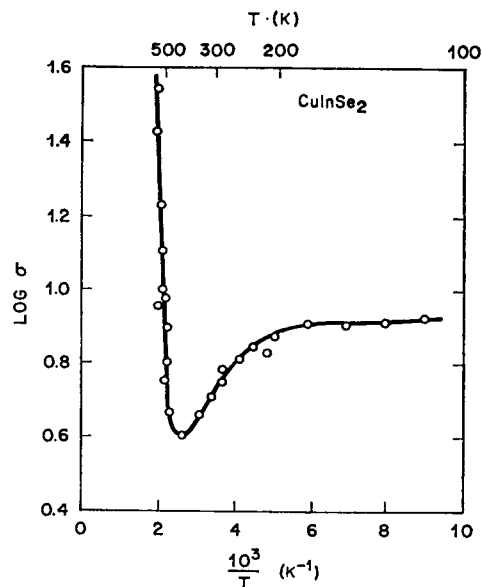


FIG. 7.23. Temperature dependence of the electrical conductivity of CuInSe_2 . (Zhuze *et al.*, 1958.)

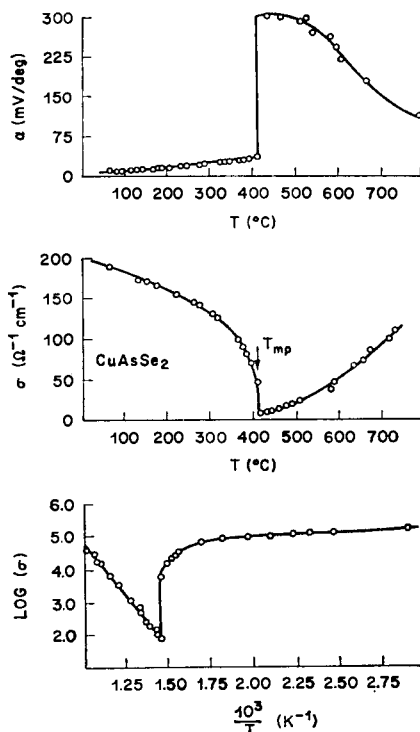


FIG. 7.24. Electrical conductivity and thermoelectric power of CuAsSe_2 .
(Mal'sagov, 1970.)

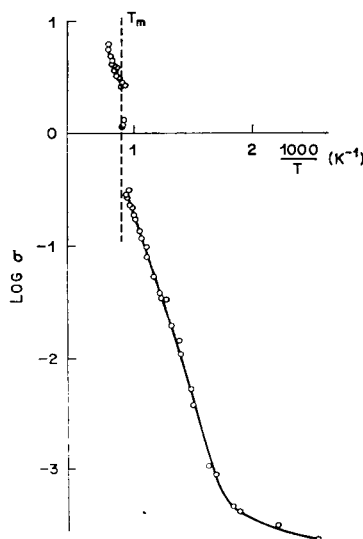


FIG. 7.25. Electrical conductivity of AgGaSe_2 . (Balanevskaya *et al.*, 1971.)

If a liquid semiconductor is used in a multistage thermoelectric energy converter, it must be in contact with a solid semiconductor. Thermoelectric effects can arise at the solid-liquid interface and can make an important contribution to the heat balance of the converter. Mal'sagov (1970) has pointed out that of the three materials just described, the CuAsSe₂ melt is the most promising for applications in thermoelectric converters. In this compound the change in the Peltier coefficient on melting can only improve the total heat balance of the thermoelectric converter. Exploitation of the other two, which exhibit an appreciable decrease of the thermoelectric power when they melt in the presence of a phase interface, is not recommended because the liberation of Peltier heat would lower the efficiency of a thermoelectric energy converter.

7.3.2.4. *AgGaSe₂*

The electrical conductivity and thermo-e.m.f. of AgGaSe₂ have been measured in the range 20–1000°C (Figs. 7.25 and 7.26) by Balanovskaya (1971). In the range 780 to 820°C the electrical conductivity displays anomalies associated with structural changes (thermograms exhibit two effects at 665° and 785°C). The activation energy of the conductivity in the liquid and the solid phases is 1.3 eV which is to be compared with an energy gap of 1.8 eV (Table 4.1). At the melting point, there is a jump in the thermo-e.m.f. and a change from *n*-type to *p*-type conductivity.

7.3.2.5. *CuGaS₂*

Tell and Kasper (1973) have measured the temperature dependence of the resistivity of CuGaS₂ samples of various room-temperature hole concentrations. As shown in Fig. 7.27a, the room-temperature hole concentration is determined solely by the temperature *T* of the anneal in a saturated sulfur vapor. The annealing times varied from ~40 hr (*T* > 600°C) to ~200 hr at the lowest temperatures. Each crystal annealed at *T* < 400°C had previously been annealed at 750°C, for it was found that otherwise the approach to equilibrium was so slow as to require much longer annealing times. The data in Fig. 7.27a fit an Arrhenius plot of the form $p \propto e^{(-E/kT)}$ with $E = 0.55\text{eV}$. This energy may be the energy of formation of Cu vacancies. It can be seen in Fig. 7.27b that the activation energy associated with freeze-out of holes onto acceptors increases with decreasing room-temperature hole concentration, and approaches 70 meV.

7.3.3 Tellurides—Transport Measurements

The electrical and optical properties of the tellurides have been studied in much less detail than those of the other I-III-VI₂ chalcogenides. Vapor-grown CuAlTe₂ has an absorption edge near 2.06 eV but no electrical properties have been reported (Honeyman and Wilkinson, 1971). The bandgap of melt-grown AgAlTe₂ has been reported at 1.8 eV from photoconductivity measurements, but this value is considered unreliable since similar measurements lead to a bandgap of 1.2 eV for CuAlTe₂ (Berger and Petrov, 1970). The bandgap of AgInTe₂ has been reported to be ~0.97 eV (Woolley and Williams, 1966). Very recent electroreflectance measurements locate the direct energy gaps in AgGaTe₂ and AgAlTe₂ at 1.32 and 2.27 eV respectively (Tell *et al.*, 1974).

Large, single crystals of CuGaTe₂ and CuInTe₂ can be prepared by melt growth. For CuInTe₂, room-temperature hole concentrations of $\sim 10^{17}\text{ cm}^{-3}$ and mobilities of $\sim 16\text{ cm}^{-2}/\text{V}\cdot\text{s}$ have been reported (Berger and Petrov, 1970). The bandgaps of CuGaTe₂ (Woolley and Williams, 1966) and CuInTe₂ (Austin *et al.*, 1956), have been reported to be ~1.2 and ~1.0 eV respectively.

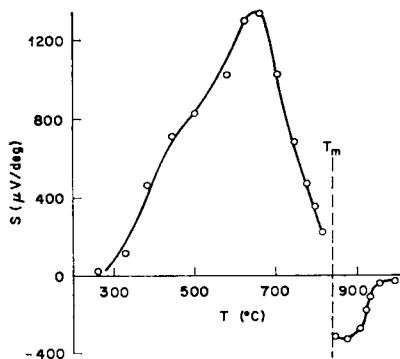


FIG. 7.26. Thermo-e.m.f. of AgGaSe_2 . (Balanevskaya *et al.*, 1971.)

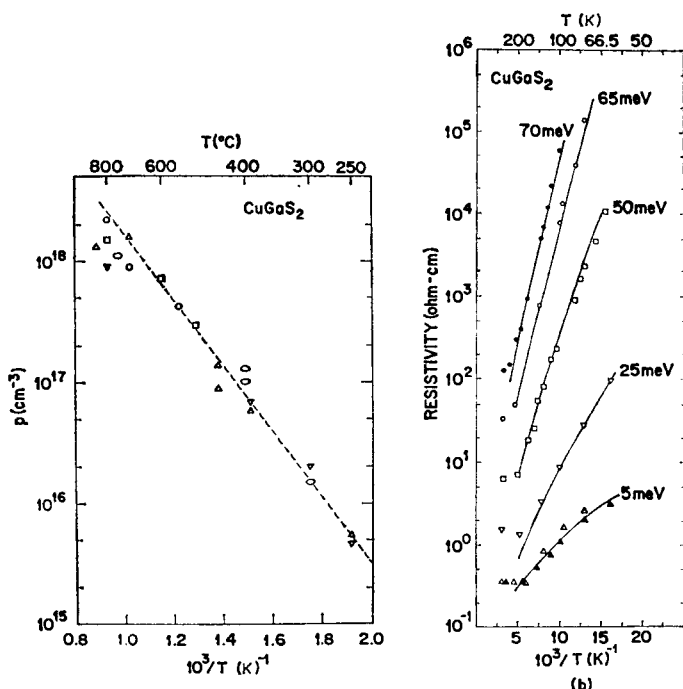


FIG. 7.27. (a) Room-temperature hole concentrations for CuGaS_2 crystals annealed at temperature T in saturated sulfur vapor. (b) Temperature dependence of the electrical resistivity of CuGaS_2 samples having various room temperature hole concentrations. The activation energies determined from the slopes are indicated. (Tell and Kasper, 1973.)

TERNARY CHALCOPYRITE SEMICONDUCTORS

7.3.3.1. *CuInTe₂* and *CuGaTe₂*

Zalar (1966) has investigated the high-temperature electrical behavior of CuInTe₂ in some detail. These high-temperature studies (to 800°C) required a method which would suppress evaporation of Te, thus maintaining the original composition. This was achieved in the following way. Thin platinum wires of 0.005 in. diameter were electrically welded onto the surface of the sample. The specimen was then dipped repeatedly into a pot of diluted, liquid porcelain (Savereisen No. 1). After each dip, thin porcelain layers were left to dry under infrared illumination. Typically, five to eight coatings were applied.

The temperature dependence of the resistivity of a sample of CuInTe₂ annealed for 24 hr at 400°C is shown in Fig. 7.28. Zalar has suggested that the sharp drop of resistivity above 455°C may be due to a precipitation of a more conductive secondary phase, such as InTe. At higher temperatures the carrier mobility in this secondary phase decreases and the resistivity climbs again until it joins the original curve. Other evidence for the existence of a second phase is the observation, microscopically, of precipitates in samples annealed at 650°C for 15 hr. This has been taken as supporting the hypothesis that CuInTe₂ is a supersaturated solid solution. These resistivity "pockets" near 450°C are much more pronounced in as-grown crystals than in samples annealed at 400°C. In all samples a well-defined and reproducible intrinsic region is observed from 710°C to the melting point (779.8°C). The energy gap determined from the intrinsic region is 1.04 ± 0.02 eV.

The temperature dependence of the hole mobilities in CuInTe₂ and CuGaTe₂ are shown in Fig. 7.29. The room temperature values are 80 and 50 cm²/V-s respectively. The room-temperature hole concentrations are 7×10^{18} cm⁻³ (CuInTe₂) and 10^{18} cm⁻³ (CuGaTe₂). Above room temperature, the mobilities vary as $T^{-1.6}$ and $T^{-1.3}$ for CuInTe₂ and CuGaTe₂ respectively, suggesting that the mobility is dominated by acoustic lattice vibrations.

7.3.3.2. *AgInTe₂*

The temperature dependence of the electrical conductivity of AgInTe₂ is shown in Fig. 7.30. From the slope of the conductivity in the intrinsic region, Zhuze *et al.* (1958) estimate that the bandgap of AgInTe₂ is ~ 0.95 eV.

7.3.4 Other Ternary Compounds

The electrical properties of some ternary compounds containing Tl or Fe are summarized in Table 7.5. The compound AgFeTe₂ exhibits a very high electron mobility. For example, in samples with carrier densities of $\sim 10^{18}$ cm⁻³, the electron mobility exceeds 2000 cm²/V-s. AgFeTe₂ is dimorphous and undergoes an isothermal increase in volume near 145°C. The volume change is large and amounts to 0.55 %. The activation energy of current carriers also changes greatly in this region. Up to the transition region it is 0.28 eV; above the transition temperature it approximately doubles to 0.58 eV. Wernick and Wolfe (1961) have questioned the existence of single-phase AgFeTe₂.

The sign of conduction of some of the compounds in Table 7.5 can be reversed by a partial replacement of one of the metal atoms by some other atom. For example, partial replacement of iron by Tl in AgFeSe₂ and AgFeTe₂ alters the conductivity from *n*- to *p*-type. It is therefore possible to produce *p-n* junctions in these compounds.

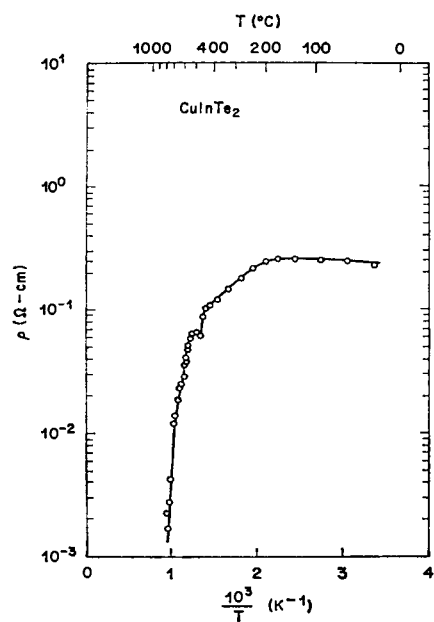


FIG. 7.28. Temperature dependence of the resistivity of CuInTe_2 .
(Zalar, 1966.)

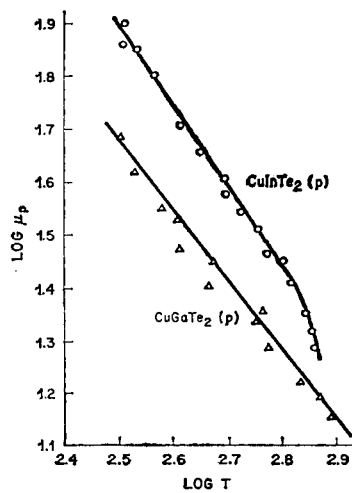


FIG. 7.29. Temperature dependence of the hole mobility in CuInTe_2 and CuGaTe_2 . (Zhuze *et al.*, 1958.)

TERNARY CHALCOPYRITE SEMICONDUCTORS

TABLE 7.5. Electrical properties of other ternary compounds (Zhuze et al., 1958)

Compound	Melting point (°C)	Conductivity ($\Omega^{-1} \text{ cm}^{-1}$)	μ_n (cm 2 /V-s)	μ_p (cm 2 /V-s)
CuSbSe ₂	452	4		5
CuSbTe ₂	530	3000		
CuBiSe ₂	585	1200		
CuBiTe ₂	520	2000		
AgSbSe ₂	636	10^{-3}		1500
AgSbTe ₂	556	160		75
AgBiSe ₂	762	180		
AgBiTe ₂	520	1300		
CuTlSe ₂	405	6000		
CuTlTe ₂	375	2800		
AgTlSe ₂	328	10^{-5}		
AgTlTe ₂	290	410		
CuFeS ₂	875	100		30
CuFeSe ₂	574	700		20
CuFeTe ₂	740	400		50
AgFeSe ₂	736	1500	250	
AgFeTe ₂	680	700	2000	

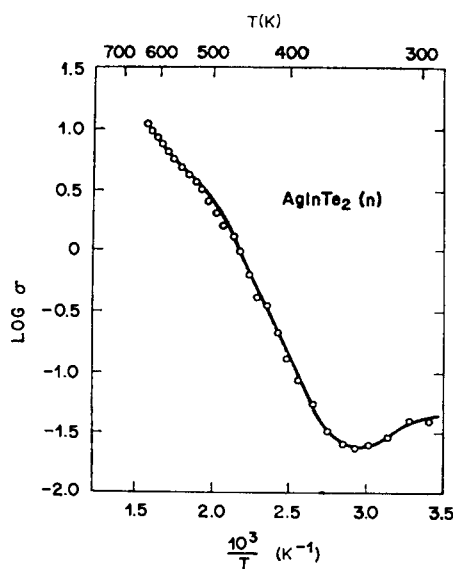
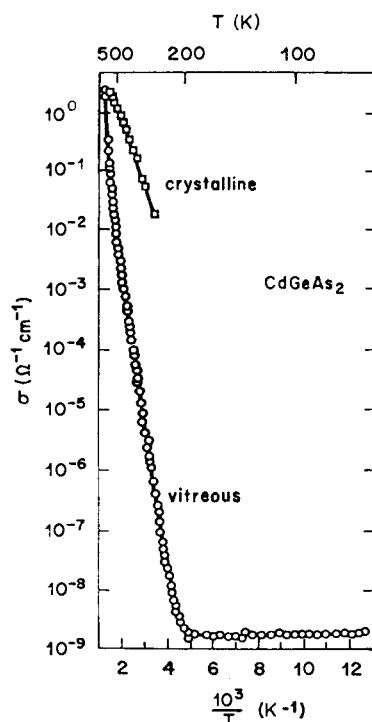


FIG. 7.30. Temperature dependence of the electrical conductivity of AgInTe₂. (Zhuze et al., 1958.)

TABLE 7.6. Properties of amorphous and crystalline II-IV-V₂ Compounds

State	Refractive index at 2.5 μ	Density (g/cm ³)	E_g^{el} (eV)	E_g^{op} (eV)
<i>a</i> -CdGeAs ₂	3.9 ^a	5.72 ^a	1.1 ^b	0.73, ^c 0.77 ^d
<i>c</i> -CdGeAs ₂	3.6 ^h	5.61		0.53, ^d 0.57 ^e
<i>a</i> -CdGeP ₂		4.86 ^f	0.95 ^g	0.95 ^g
<i>c</i> -CdGeP ₂	3.2 ^h	4.54 ^f		1.72 ^e
<i>a</i> -CdSiAs ₂			1.4 ^l	1.05 ^l
<i>c</i> -CdSiAs ₂				1.55 ^e

^a Avetikyan *et al.* (1969).^b Vaipolin *et al.* (1965).^c Borisova *et al.* (1968).^d Aksenov (1970a).^e Table 3.1.^f Serednii *et al.* (1971).^g Fedotov *et al.* (1969).^h Appendix.ⁱ Aksenov (1970b).FIG. 7.31. Temperature dependence of the electrical conductivity of vitreous CdGeAs₂ before (○) and after (□) crystallization. (Vaipolin *et al.*, 1965.)

7.4 Glassy II-IV-V₂ Compounds

7.4.1 CdGeAs₂, CdGeP₂, and CdSiAs₂

There is considerable interest in vitreous substances for possible applications in memory and switching devices. It has been found that the ternary compounds CdGeAs₂, CdGeP₂, and CdSiAs₂ can be prepared in a glassy state by rapid quenching of the melts. Vitrification of CdSiAs₂ requires far greater cooling rates than for the other two compounds.

Some properties of vitreous and crystalline II-IV-V₂ compounds are summarized in Table 7.6. The energy gaps E_g^{el} have been determined from measurements of the electrical conductivity. The sign of the thermal e.m.f. of vitreous CdGeAs₂ obtained by quenching indicates *n*-type conductivity. The magnitude of conductivity is practically temperature independent between 80 and 200 K (Fig. 7.31); above 200 K the conductivity increases exponentially,

$$\sigma = \sigma_0 \exp\left(\frac{-E_g^{el}}{2 kT}\right) \quad (7.3)$$

with $E_g^{el} = 1.1$ eV. However, the optical energy gap E_g^{op} of vitreous CdGeAs₂ determined from the absorption edge is considerably smaller (~ 0.75 eV). On the other hand, the optical energy gap obtained from the spectral dependence of the Faraday rotation in vitreous CdGeAs₂ is ~ 1.3 eV (Vorlicek and Zvara, 1971). The reason for the differences among these values is not understood. In any case the energy gap in amorphous CdGeAs₂ is 0.2 to 0.8 eV larger than in crystalline CdGeAs₂. Multiple heating to 670 K does not change the properties of vitreous CdGeAs₂. However, when samples are heated to higher temperatures, the electrical conductivity sharply increases, the sample crystallizes, and the properties change irreversibly (Fig. 7.31).

The electrical conductivity of glassy CdGeP₂ depends exponentially on $1/T$ in the temperature range 295–750 K (Fig. 7.32). Assuming that the conductivity is intrinsic in this range, E_g^{el} is found to be 0.95 eV. The optical energy gap E_g^{op} of vitreous CdGeP₂ (estimated as the photon energy for which $\alpha \approx 10^3$ cm⁻¹) is also 0.95 eV (Fig. 7.33). The energy gap of amorphous CdGeP₂ is thus ~ 0.8 eV less than the energy gap of its crystalline counterpart (1.72 eV).

Electrical and optical properties of glassy alloys of CdGe(As_xP_{1-x})₂ have been studied by Borisova *et al.* (1968). The optical energy gap varies monotonically between 0.73 and 0.95 eV as x varies from 1 to 0, increasing slightly more rapidly with decreasing x for low phosphorus concentrations. Samples of all compositions exhibited *n*-type conduction with an electrical energy gap $E_g^{el} \sim 1.2$ eV. The dark conductivity at room temperature decreased with increasing phosphorus concentration.

The electrical energy gap E_g^{el} of amorphous CdSiAs₂ (1.4 eV) is considerably larger than the optical gap E_g^{op} (1.05 eV) estimated from photoconductivity measurements. Both values are less than the direct energy gap of crystalline CdSiAs₂ (1.55 eV).

The absorption spectra of ZnSnP₂ crystals in the sphalerite and chalcopyrite structures respectively are compared in Fig. 7.34. It is apparent that the disorder on the cation sites reduces the energy gap ~ 0.2 eV relative to the ordered phase. A comparison of the electroreflectance spectra appropriate to the two modifications of ZnSnP₂ would be very interesting.

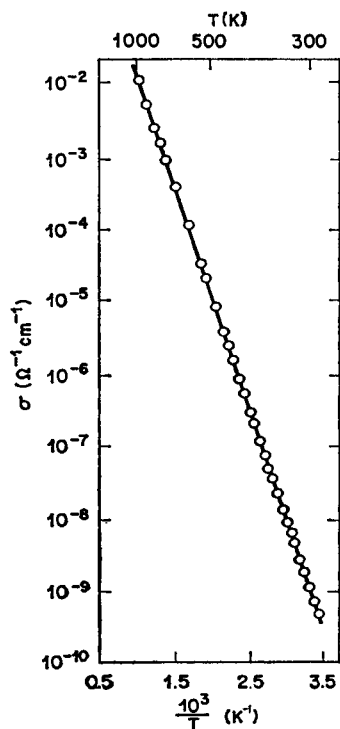


FIG. 7.32. Temperature dependence of the electrical conductivity of glassy CdGeP_2 . (Fedotov *et al.*, 1969.)

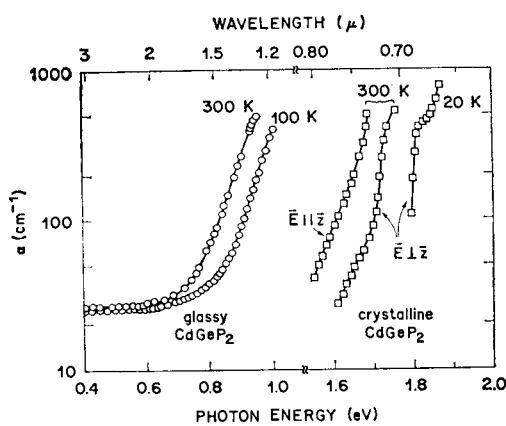


FIG. 7.33. Absorption spectra of glassy (Fedotov *et al.*, 1969) and crystalline (Shay *et al.*, 1971) CdGeP_2 .

7.4.2 Memory and Switching Devices

A switching device based on glassy CdGeAs₂ has been studied by Baryshev *et al.* (1970a). Samples in the form of irregular beads ~1 mm diameter were obtained by mechanical cleaving and crushing of glassy ingots prepared by the quenching of melts sealed in quartz ampoules. Platinum wire electrodes of ~0.1 mm diameter were attached ~0.1 mm apart.

The static current–voltage characteristics of a typical device is shown in Fig. 7.35. When the external load resistor R_2 was of the order of 500 kΩ (Fig. 7.35a), an element could be switched to the off-state without a change in the voltage polarity. When R_2 was reduced to 50 kΩ (Fig. 7.35b) and the maximum current through the element was increased to ~3 mA, the transition to the off-state could be achieved only by reducing the bias voltage to zero and by reversing its polarity. The switching voltage increased with increasing distance between the electrodes and was within the range 80–500 V. The switching current was ~10 μA and the residual (holding) voltage was 5–30 V.

When the current–voltage characteristics were recorded using a low load-resistance, the transition to the on-state was accompanied by a memory effect in which the device remained in the on-state. This effect was governed by the value of the current and the duration of its flow through the element in its on state. The passage of currents over 2 mA produced a strong memory effect. The element remained in the on-state even when it was disconnected from the measuring circuit. The transition to the off-state required a stimulating pulse.

The stability of the electrical parameters of the elements under dynamic conditions depended on the applied voltage and the load resistance. Typical elements withstood over 10^6 switching cycles without an appreciable change in the switching voltage. The switching times of the elements were less than 100 ns.

At certain values of the load resistance and bias voltage, electrical oscillations were generated in the negative resistance region. The amplitude and frequency of the pulses generated were governed by the bias voltage: when the voltage was increased the frequency increased. The tendency to generate such oscillations was enhanced by an increase in the load resistance.

In view of the current activity in amorphous materials for memory and switching applications, the short switching times, the memory effect, and the stability of the characteristics of bulk CdGeAs₂ devices may be of interest in computer applications.

7.4.3 Thin-film Devices

Any large-scale application of amorphous memory or switching devices would certainly be cheaper and simpler if thin-film devices could be employed. It has been found that evaporated films of amorphous CdGeAs₂, ZnGeAs₂, and CdGeP₂ can be prepared by explosion in vacuum onto room-temperature substrates (Baryshev *et al.*, 1970b). Microstructure and X-ray diffraction analyses showed that the films obtained were amorphous and essentially free of crystalline inclusions. It was found that the chemical composition of the films did not agree with the compositions of the original compounds. The films were deficient in Ge, the least volatile element. Thus in the case of CdGeAs₂, the composition of the films was 40 atm %Cd, 10% Ge, and 50% As; in the case of ZnGeAs₂ the composition of the films was 38 atm %Zn, 12% Ge, and 50% As.

Current–voltage characteristics of 2–6 μ thick films using evaporated Sb or Pb con-

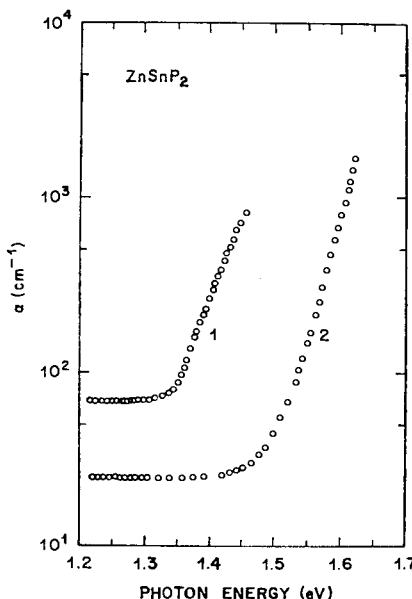


FIG. 7.34. Absorption coefficient of ZnSnP_2 at 295 K (Goryunova *et al.*, 1968): (1) sphalerite structure; (2) chalcopyrite structure.

tacts displayed switching and memory effects. The current-voltage characteristic in the nonconducting state could be linear or it could have a narrow negative resistance region. The shape of the characteristic was independent of the measuring frequency over the range 0.3–300 Hz. The transition to the nonconducting state was easily achieved by means of an additional stimulating pulse. The electric fields at the onset of the negative resistance regions for these films ($2\text{--}6 \mu$) were similar to those measured for relatively thick (80μ) plates of stoichiometric glassy CdGeAs_2 , $\sim 2 \times 10^4 \text{ V/cm}$.

Under pulse conditions the films exhibited memory effects when the applied pulse duration was longer than $4 \mu\text{s}$. When the duration of the pulse was reduced, the turnover (switching) voltage increased. For example, in a Zn-Ge-As element 5.6μ thick, the turnover voltage under dynamic conditions was 8 V for a load resistance $R_2 = 12 \text{ k}\Omega$. When pulses of 0.5 ms duration were applied at a repetition frequency of 50 Hz, the turnover voltage was found to be 12 V, and when the pulse duration was reduced to $0.5 \mu\text{s}$, the turnover voltage increased to 25 V.

Figure 7.36 shows the response of a 5.6μ thick Zn-Ge-As film for different amplitude voltage pulses. Switching from the nonconducting to the conducting state occurred after a delay caused by the charge accumulation time τ_1 , which depended upon the pulse amplitude. Similar characteristics were also observed for Cd-Ge-As and Cd-Ge-P elements. The rise time of the avalanche current τ_2 , which followed the charge accumulation process, was at least an order of magnitude shorter than τ_1 . The time for switching back to the nonconducting state was also very fast, and was of the same order of magnitude as τ_2 .

Although the investigated ternary systems yielded nonstoichiometric films, the devices made from these films have a negative resistance region and could be switched from the nonconducting to the conducting state, and conversely. The short switching times suggest that these devices may have practical applications.

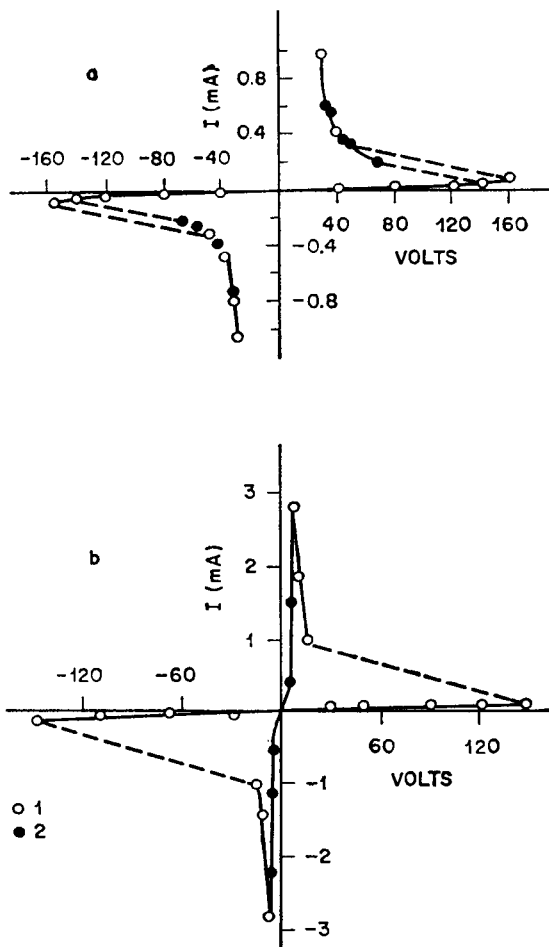


FIG. 7.35. Forward (1) and reverse (2) static current-voltage characteristics (a) $R_L = 430 \text{ k}\Omega$, (b) $R_L = 50 \text{ k}\Omega$. (Baryshev *et al.*, 1970a.)

7.5 Current Oscillations

Low- and high-frequency current oscillations have been observed in CdSnP_2 , the ternary analog of InP. Although CdSnP_2 is usually *n*-type with a free electron concentration $n \sim 10^{15}\text{--}10^{17} \text{ cm}^{-3}$ and a mobility of 1000–2000 $\text{cm}^2/\text{V}\cdot\text{s}$ (Table 7.1), current oscillations were first observed in the photocurrent of high resistivity samples doped with Cu to increase the resistivity to $\sim 10^3 \Omega\cdot\text{cm}$ at 300 K and $10^7\text{--}10^8 \Omega\cdot\text{cm}$ at 80 K. The photocurrent was excited by multiphoton processes using a Nd:YAG *Q*-switched laser (output energy 0.5 J, pulse duration 35 ns).

Figure 7.37 shows the kinetics of the nonequilibrium-carrier relaxation at different sample temperatures for an electric field of 80 V/cm and laser intensity of 2×10^{26} photons/cm. Several oscillations of the photocurrent are observed, and their number and amplitude increase with decreasing temperature. The appearance of the oscillations is not connected with any threshold value of the electric field. The amplitude of the

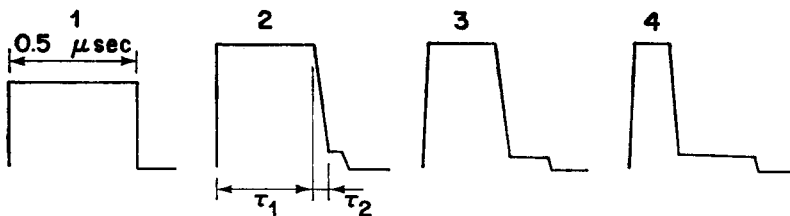


FIG. 7.36. Schematic representation of the oscilloscope for a film element: (1) single pulse before turnover; (2-4) switching pulses obtained at increasing values of the applied voltage pulse (150, 200, 300 V). (Baryshev *et al.*, 1970b.)

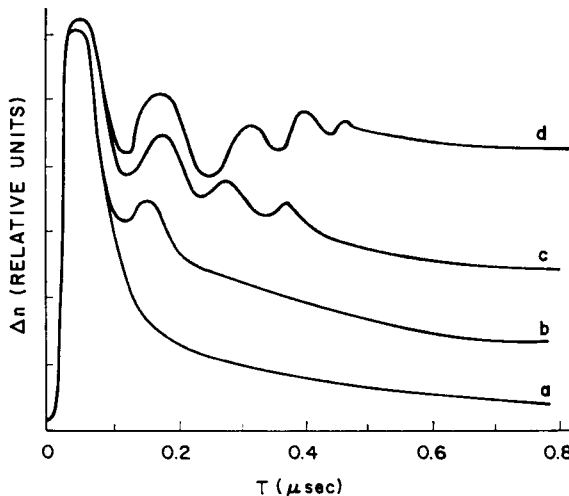


FIG. 7.37. Oscillations of the photocurrent in high-resistivity Cu-doped CdSnP₂ for high intensity laser excitation: (a) 300 K; (b) 240 K; (c) 170 K; (d) 90 K. (Koval'skaya *et al.*, 1970.)

oscillations is proportional to both the electric field E and light intensity I , and the number of oscillations also increases with increasing I and E . The oscillation frequency is independent of I and E , and amounts to $\sim 8\text{--}12$ MHz for a series of thirty samples investigated. The decay time of the nonequilibrium current is ~ 80 ns at 300 K and ~ 20 μ s at 80 K.

It was concluded that the observed oscillations were not connected with the classical Gunn effect or with generation of acousto-electric domains in piezoelectric crystals. Rather it was speculated that Cerenkov emission of phonons by electrons takes place in the field of the powerful light wave.

Low-frequency photocurrent oscillations have been observed in high resistivity samples of Cu-doped CdSnP₂ in strong electric fields by Goryunova *et al.* (1970). The investigations were carried out at 77 K on samples of various lengths illuminated with white light. Figure 7.38 shows current-voltage characteristics of a CdSnP₂ sample 1 mm long at two different illumination intensities. Under weak illumination (curve 1) there is a sublinear region for electron fields above 0.5 kV/cm, and a current saturation region that persists to 7 kV/cm. For an illumination intensity above a certain threshold

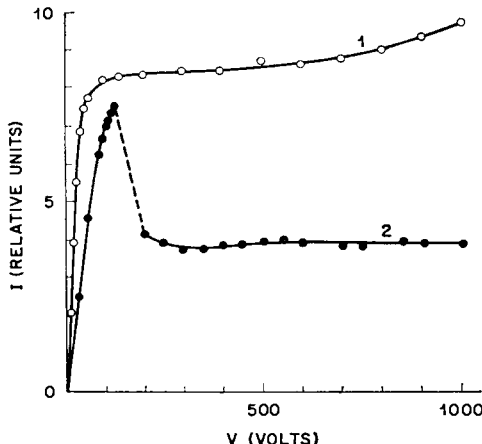


FIG. 7.38. Current-voltage characteristics of a CdSnP_2 sample 1 mm long at low (1) and high (2) illumination levels. The ordinate scales are 10^{-7} A/div for (1) and 10^{-5} A/div for (2). (Goryunova *et al.*, 1970.)

value (curve 2), the current-voltage characteristic changes significantly, and low-frequency, large-amplitude current oscillations set in for fields stronger than $\sim 1 \text{ kV/cm}$.

The amplitude of the oscillations and the mean value of the current remain constant when the voltage increases to fields of $\sim 1 \text{ kV/cm}$. The current oscillations have a relaxation character, and their period decreases in the field interval 2–6 kV/cm from 56 to 16 ms, without changing in stronger fields, and also decreases with increasing illumination intensity. The threshold field corresponding to the start of the oscillations does not depend on the illumination level. Probe investigations and the study of the kinetics of the formation of the “current jump” in the current-voltage curve have shown that a region of negative volume differential conductivity appears in these samples for fields exceeding $\sim 1 \text{ kV/cm}$, and a high field domain moving through the sample is produced. The spectral dependence of the photoconductivity of $\text{CdSnP}_2:\text{Cu}$ suggests the existence of multiply charged impurity centers. The observed low-frequency instabilities have been attributed to the capture of hot electrons by these centers, although it is possible that higher lying conduction bands play an important role.

Current oscillations have also been observed in conducting CdSnP_2 under an applied electric field at room temperature (Knight *et al.*, 1972). These studies with conducting samples have concluded that the observed oscillations are due to the intervalley transfer of carriers as originally proposed by Ridley and Watkins (1961) and Hilsum (1962), and originally observed in GaAs and InP by Gunn (1963).

The current voltage characteristic of a typical device 0.1 mm thick and 10^{-4} cm^2 area is shown in Fig. 7.39. Current saturation is observed for both bias polarities at about 40 V. For positive bias coherent oscillations are observed at 450 MHz; for negative bias incoherent microwave noise is observed. The average threshold field in all samples was between 4 and 8 kV/cm.

7.6 Thermoelectric Properties

The Seebeck coefficient relates the thermal e.m.f. generated in a crystal to the temperature difference impressed. Its value is of interest in connection with applications in

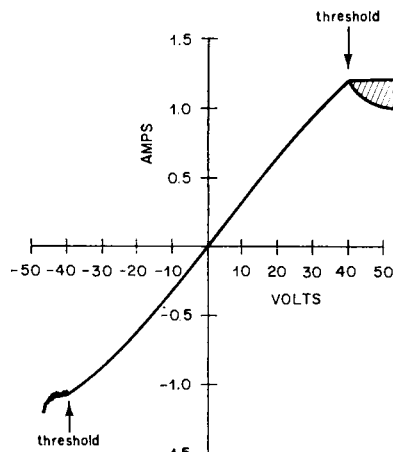


FIG. 7.39. Current-voltage characteristic for a conducting, unintentionally doped sample of CdSnP_2 . (Knight *et al.*, 1972.)

thermoelectric coolers, and since it permits a crude estimate of the free carrier effective mass m^* . For ellipsoidal energy surfaces, m^* can be obtained from the equation

$$S = \frac{k}{e} \left[\left(\frac{1}{2} - s \right) + \ln \left(\frac{2(2m^*kT)^{3/2}}{nh^3} \right) \right], \quad (7.4)$$

where n is the carrier concentration, h is Planck's constant, T is the absolute temperature, and s is a parameter determined by the dependence of the relaxation time τ on the energy of the charge carriers:

$$\tau = aE^{-s}. \quad (7.5)$$

Frequently s is assumed equal to $\frac{1}{2}$ corresponding to the simplified case of lattice scattering.

In Table 7.7 we summarize thermal conductivity and Seebeck coefficient data for several compounds, and in Fig. 7.40 we show the temperature dependence of the thermal conductivity in CdGeAs_2 , ZnGeAs_2 , and CdSnAs_2 . Several of the effective mass values in Table 7.2 have been deduced from the Seebeck coefficients in Table 7.7. A typical dependence of the Seebeck coefficient upon carrier concentration is shown in Fig. 7.41 for ZnSnAs_2 .

Although the lattice thermal conductivity of CdSnAs_2 is about 4 times smaller than that of InAs , its binary analog, the thermoelectric "figure of merit", $z = S^2/k\varrho$, of CdSnAs_2 is low at room temperature ($z \sim 10^{-4}/^\circ\text{C}$). However, it has been suggested that alloys of CdSnAs_2 with InAs might have electrical properties similar to the end members, but their thermal conductivities should be greatly reduced. The thermoelectric figure of merit would therefore be considerably higher than either of the compounds.

The thermoelectric properties measured by Zhuze *et al.* (1958) on several polycrystalline I-III-VI₂ compounds are listed in Table 7.8. All of these compounds were prepared by direct melting of components taken in stoichiometric proportions. Although X-ray analysis did not reveal any secondary phase in any of these compounds, notice that AgGaSe_2 is reported to have a conductivity of $8.8 \Omega^{-1} \text{ cm}^{-1}$. As discussed earlier, Tell *et al.* (1972) find that the resistivity of relatively pure, single crystal AgGaSe_2 is always greater than $10^5 \Omega\text{-cm}$.

TERNARY CHALCOPYRITE SEMICONDUCTORS

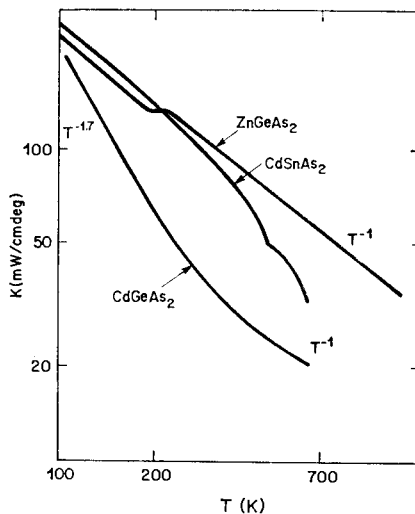


FIG. 7.40. Temperature dependence of the thermal conductivity of CdSnAs_2 , CdGeAs_2 , and ZnGeAs_2 crystals. (Leroux-Hugon, 1963.)

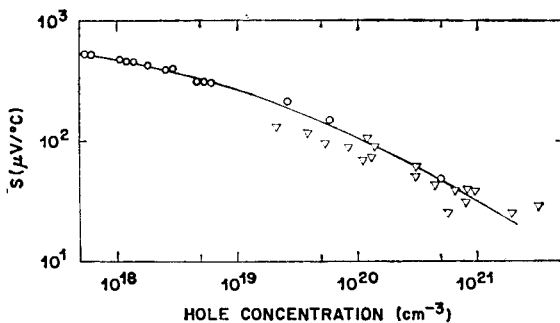


FIG. 7.41. Dependence of the differential thermal e.m.f. at 300 K in p -type ZnSnAs_2 on hole concentration. (Borshchevskii *et al.*, 1967.)

TABLE 7.7 *Thermoelectric properties of II-IV-V₂ Crystals*

Crystal	Thermal conductivity (W/cm-deg)	Seebeck coefficient (μV/deg)	Carrier concentration (cm ⁻³)	References
ZnSiAs ₂	0.14	1100		a
ZnGeAs ₂	0.11	250		b
ZnGeP ₂	0.18	1200		a, c
ZnSnAs ₂	0.15	500-40	$p = 10^{17}-10^{21}$	d
ZnSnSb ₂		36×10^6		e
CdGeAs ₂	0.42	-190	$n = 10^{17}$	b, f
CdGeP ₂	0.11	-1200		a
CdSnAs ₂	0.092	-85	$n \sim 10^{18}$	g

^a Masumoto *et al.* (1966).^b Bin-Si *et al.* (1963).^c Somogyi and Bertoti (1972).^d Vaipolin *et al.* (1967).^e Kradanova and Voronina (1969).^f Vaipolin *et al.* (1964).^g Spitzer *et al.* (1961).TABLE 7.8. *Thermoelectric properties of I-III-VI₂ compounds*

Crystal	Electrical conductivity (Ω ⁻¹ cm ⁻¹)	Thermoelectric power (mV/°C)
CuGaSe ₂	0.02	75
CuGaTe ₂	11	270
CuInSe ₂	0.14	480
CuInTe ₂	200	140
CuTlSe ₂	6000	10
CuTlTe ₂	2800	80
AgGaSe ₂	8.8	-70
AgGaTe ₂	1.7×10^{-4}	700
AgInSe ₂	0.48	-140
AgInTe ₂	0.78	-70
AgTlSe ₂	10^{-5}	800
AgTlTe ₂	4.0	60

TERNARY CHALCOPYRITE SEMICONDUCTORS

References

- AKIMCHENKO, I. P., LEONOV, E. I., ORLOV, V. M., and SOKOLOVA, V. I. (1972) *J. Phys. Chem. Solids* **33**, 1565.
- AKSENOV, V. V., PETROV, V. M., KHARAKHORIN, F. F., and YURUSHKIN, B. I. (1970a) *Izv. Akad. Nauk SSSR, Neorgan. Mater.* **6**, 826 [*Inorganic Materials* **6**, 725 (1970)].
- AKSENOV, V. V., PETROV, V. M., and KHARAKHORIN, F. F. (1970b) *Izv. Akad. Nauk SSSR, Neorgan. Mater.* **6**, 1881 [*Inorganic Materials* **6**, 1657 (1970)].
- ALEKPEROVA, E. E., VALOV, Yu. A., GORYUNOVA, N. A., RYVKIN, S. M., and SHPENKOV, G. P. (1969) *Phys. Status Solidi* **32**, 49.
- AUSTIN, I. G., GOODMAN, C. H., and PENGELLY, A. E. (1956) *J. Electrochem. Soc.* **103**, 609.
- AVERKIEVA, G. K., GORYUNOVA, N. A., PROCHUKHAN, V. D., and SERGINOV, M. (1970) *Dokl. Akad. Nauk. SSSR, Tekh. Fiz.* **191**, 811 [*Soviet Phys. Doklady* **15**, 386 (1970)].
- AVERKIEVA, G. K., GORYUNOVA, N. A., PROCHUKHAN, V. D., RYVKIN, S. M., SERGINOV, M., and SHRETER, Yu. G. (1971) *Fizika tekhn. Pol.* **5**, 174 [*Soviet Phys. Semiconductors* **5**, 151 (1971)].
- AVETIKYAN, G. A., BAIDAKOV, L. A., GORYUNOVA, N. A., KOZUZOVA, N. I., and OSMANOV, E. O. (1969) *Zh. prikl. Khim.* **42**, 2345 [*J. Appl. Chem. USSR* **42**, 2201 (1969)].
- BALANEVSKAYA, A. E., BERGER, L. I., and ISAEV, Z. A. (1971) *Izv. Akad. Nauk SSSR, Neorgan. Mater.* **7**, 2084 [*Inorganic Materials* **7**, 1857 (1971)].
- BARYSHEV, V. G., BOLTIVETS, N. S., and BORSHCHEVSKII, A. S. (1970a) *Fizika tekhn. Pol.* **4**, 1164 [*Soviet Phys. Semiconductors* **4**, 983 (1970)].
- BARYSHEV, V. G., BOLTIVETS, N. S., BORSCHHEVSKII, A. S., GORYUNOVA, N. A., and ORESHKIN, P. T. (1970b) *Fizika tekhn. Pol.* **4**, 372 [*Soviet Phys. Semiconductors* **4**, 308 (1970)].
- BERGER, L. I., and PETROV, V. M. (1970) *Izv. Akad. Nauk. SSSR, Neorgan. Mater.* **6**, 1348 [*Inorganic Materials* **6**, 1185 (1970)].
- BERTOTTI, I., and SOMOGYI, K. (1971) *Phys. Status Solidi* (a) **6**, 439.
- BIN-SI, T., TYCHINA, I. I., OSMANOV, E. O., and GORYUNOVA, N. A. (1963) *Physics—Reports of the 21st Conference LISI, Leningrad*, p. 8.
- BORISOVA, Z. U., GORYUNOVA, N. A., KOZUZOVA, N. I., OSMANOV, E. O., and RUD', Yu. V. (1968) *Fizika tekhn. Pol.* **2**, 1548 [*Soviet Phys. Semiconductors* **2**, 1292 (1969)].
- BORSHCHEVSKII, A. S., GORYUNOVA, N. A., KESAMANLY, F. P., and NASLEDOV, D. N. (1967) *Phys. Status Solidi* **21**, 9.
- BYCHKOV, A. G., PLECHKO, R. L., VALOV, Yu. A., and GORYUNOVA, N. A. (1966) *Izv. Akad. Nauk SSSR, Neorgan. Mater.* **2**, 2078 [*Inorganic Materials* **2**, 1798 (1966)].
- BYCHKOV, A. G., POPLAVNOI, A. S., RADZIVIL, V. P., TYCHINA, I. I., and SHARENKO, V. E. (1971) *Fizika tekhn. Pol.* **5**, 2197 [*Soviet Phys. Semiconductors* **5**, 1912 (1972)].
- EMELYANENKO, O. V., and POLUSHINA, I. K. (1969) *Phys. Status Solidi* **36**, K13.
- EMELYANENKO, O. V., KESAMANLY, F. P., POLUSHINA, I. K., and SKRIPKIN, V. A. (1971) *Fizika tekhn. Pol.* **5**, 351 [*Soviet Phys. Semiconductors* **5**, 304 (1971)].
- FEDOTOV, V. G., LEONOV, E. I., IVEKHNO, V. N., GORYUNOVA, N. A., and TYCHINA, I. I. (1969) *Fizika tekhn. Pol.* **3**, 1739 [*Soviet Phys. Semiconductors* **3**, 1470 (1970)].
- GORYUNOVA, N. A., KESAMANLY, F. P., NASLEDOV, D. N., NEGRESKUL, V. V., RUD', Yu. V., and SLOBODCHIKOV, S. V. (1965) *Fizika tverd. Tela* **7**, 1312 [*Soviet Phys. Solid State* **7**, 1060 (1965)].
- GORYUNOVA, N. A., GRIGORYAN, S. S., and ZLATKIN, L. B. (1966a) *Izv. Akad. Nauk SSSR, Neorgan. Mater.* **2**, 2125 [*Inorganic Materials* **2**, 1838 (1966)].
- GORYUNOVA, N. A., KESAMANLY, F. P., and KORSHAK, N. M. (1966b) *Physics, Reports of the 24th Conference of LISI, Leningrad*, p. 15.
- GORYUNOVA, N. A., KESAMANLY, F. P., and LOSHAKOVA, G. V. (1967a) *Fizika tekhn. Pol.* **1**, 1010 [*Soviet Phys. Semiconductors* **1**, 844 (1968)].
- GORYUNOVA, N. A., TYCHINA, I. I., and KHANSEVAROV, R. Yu. (1967b) *Fizika tekhn. Pol.* **1**, 141 [*Soviet Phys. Semiconductors* **1**, 110 (1967)].
- GORYUNOVA, N. A., BELLE, M. L., ZLATKIN, L. B., LOSHAKOVA, G. V., POPLAVNOI, A. S., and CHALDYSHEV, V. A. (1968) *Fizika tekhn. Pol.* **2**, 1344 [*Soviet Phys. Semiconductors* **2**, 1126 (1969)].
- GORYUNOVA, N. A., LEONOV, E. I., ORLOV, V. M., RODIONOV, L. F., and SONDAEVSKII, V. P. (1970) *Zh. eksp. teor. Fiz. Pis. Red.* **12** 459 [*JETP Lett.* **12**, 459 (1970)],

- GUNN, J. B. (1963) *Solid State Commun.* **1**, 88.
- HILSUM, C. (1962) *Proc. IRE* **50**, 185.
- HONEYMAN, W. N. (1969) *J. Phys. Chem. Solids* **30**, 1935.
- HONEYMAN, W. N., and WILKINSON, K. H. (1971) *J. Phys. D, Appl. Phys.* **4**, 1182.
- ISOMURA, S., and MASUMOTO, K. (1971) *Phys. Status Solidi (a)* **6**, K139.
- ISOMURA, S., and MASUMOTO, K. (1972) *Phys. Status Solidi (a)* **13**, 223.
- IVAKHNO, V. N., KRADINOVA, L. V., and PROCHUKHAN, V. D. (1969) *Fizika tekhn. Pol.* **3**, 1083 [Soviet Phys. Semiconductors **3**, 913 (1970)].
- KARYMSHAKOV, R. K., UKHANOV, YU. I., and SHMARTSEV, YU. V. (1971) *Fizika tekhn. Pol.* **5**, 514 [Soviet Phys. Semiconductors **5**, 450 (1971)].
- KESAMANLY, F. P., NASLEDOV, D. N., and RUD', YU. V. (1965) *Physics, Reports of the 23rd Conference of LISI, Leningrad*, p. 51.
- KILDAL, H. (1972) Ph. D. thesis, Stanford University, Technical Report AFML-TR-72-277 Wright Patterson Air Force Base, Ohio.
- KNIGHT, S., BUEHLER, E., and CAMTIBEL, I. (1972) *J. Appl. Phys.* **43**, 3422.
- KORNEEV, E. F., REMENYUK, A. D., and SHMARTSEV, YU. V. (1971) *Fizika tekhn. Pol.* **5**, 1669 [Soviet Phys. Semiconductors **5**, 1465 (1972)].
- KOVAL'SKAYA, V. A., FERDMAN, N. A., LEONOV, E. I., ORLOV, V. M., GORYUNOVA, N. A., RYVKIN, S. M., and RADAUTSAN, S. I. (1970) *Zh. eksp. teor. Fiz. Pis. Red.* **12**, 399 [JETP Lett. **12**, 275 (1970)].
- KRADINOVA, L. V., and VORONINA, T. I. (1969) *Phys. Status Solidi* **32**, K173.
- LERNER, L. S. (1966) *J. Phys. Chem. Solids* **27**, 1.
- LEONOV, E. I., ORLOV, V. M., SOKOLOVA, V. I., and SHRETER, YU. G. (1971) *Phys. Status Solidi (a)* **8**, 387.
- LEROUX-HUGON, P. (1963) *C. r. hebd. Seanc. Acad. Sci. (Paris)* **256**, 118.
- MAL'SAGOV, A. U. (1970) *Fizika tekhn. Pol.* **4**, 1417 [Soviet Phys. Semiconductors **4**, 1213 (1971)].
- MASUMOTO, K., and ISOMURA, S. (1965) *J. Phys. Chem. Solids* **26**, 163.
- MASUMOTO, K., ISOMURA, S., and GOTO, W. (1966) *J. Phys. Chem. Solids* **27**, 1939.
- MATYAS, M., and HÖSCHL, P. (1962) *Czech. J. Phys.* **12**, 788.
- PALATNIK, L. S., and ROGACHEV, E. I. (1966) *Izv. Akad. Nauk SSSR, Neorgan. Mater.* **2**, 659 [Inorganic Materials **2**, 568 (1966)].
- POLYANSKAYA, T. A., SIKHARULIDZE, G. A., TUCHKEVICH, V. M., and SMARTSEV, YU. V. (1966) *Fizika tverd. Tela* **8**, 1851 [Soviet Phys. Solid State **8**, 1468 (1966)].
- RAY, B., PAYNE, A. J., and BURRELL, G. J. (1969) *Phys. Status Solidi* **35**, 197.
- RIDLEY, B. K., and WATKINS, T. B. (1961) *Proc. Phys. Soc. (London)* **78**, 293.
- SEREDNII, A. P., KIRILENKO, M. M., MENYAILOV, N. E., TYCHINA, I. I., RADZIVIL, V. P., and FEDOTOV, V. G. (1971) *Izv. Akad. Nauk SSSR, Neorgan. Mater.* **7**, 2086 [Inorganic Materials **7**, 1859 (1971)].
- SHAY, J. L., BUEHLER, E., and WERNICK, J. H. (1971) *Phys. Rev. B*, **4**, 2479.
- SIEGEL, W., ZIEGLER, E., and KÜHNEI, G. (1973) *Phys. Status Solidi (a)* **15**, 521.
- SIKHARULIDZE, G. A., TUCHKEVICH, V. M., UKHANOV, YU. I., and SHMARTSEV, YU. V. (1966) *Fizika tverd. Tela* **8**, 1159 [Soviet Phys. Solid State **8**, 924 (1966)].
- SNELL, J. E., BURRELL, G. J., MOSS, T. S., and MABBERLEY, J. C. (1968) In *Proceedings of the 9th International Conference on the Physics of Semiconductors, Moscow*, p. 1227.
- SOKOLOVA, V. I., ORLOV, V. M., SHPENKOV, G. P., TSVETKOVA, S. V., POLUSHINA, I. K., RADUL, V. A., and GORYUNOVA, N. A. (1968) *Fizika (LISI, Leningrad)*, p. 14.
- SOMOGYI, K., and BERTOTI, I. (1972) *Jap. J. Appl. Phys.* **11**, 103.
- SPITZER, W. G., WERNICK, J. H., and WOLFE, R. (1961) *Solid State Electr.* **2**, 96.
- STRAUSS, A. J., and ROSENBERG, A. J. (1961) *J. Phys. Chem. Solids* **17**, 278.
- TELL, B., and KASPER, H. M. (1973) *J. Appl. Phys.* **44**, 4988.
- TELL, B., SHAY, J. L., and KASPER, H. M. (1972) *J. Appl. Phys.* **43**, 2469.
- TELL, B., SHAY, J. L., and KASPER, H. M. (1974) To be published.
- VAIPOLIN, A. A., GASHIMZADE, F. M., GORYUNOVA, N. A., KESAMANLY, F. P., NASLEDOV, D. N., OSMANOV, E. O., and RUD', YU. V. (1964) *Izv. Akad. Nauk SSSR, Fiz.* **28**, 1085 [Bull. Acad. Sci. USSR, Physical Series (USA) **28**, 984 (1964)].
- VAIPOLIN, A. A., OSMANOV, E. O., and RUD', YU. V. (1965) *Fizika tverd. Tela* **7**, 2266 [Soviet Phys. Solid State **7**, 1833 (1966)].
- VAIPOLIN, A. A., KESAMANLY, F. P., and RUD', YU. V. (1967) *Izv. Akad. Nauk SSSR, Neorg. Mater.* **3**, 974 [Inorganic Materials **3**, 871 (1967)].

TERNARY CHALCOPYRITE SEMICONDUCTORS

- VORLICEK, V., and ZVARA, M. (1971) *Phys. Status Solidi (b)* **48**, 93.
WERNICK, J. H., and WOLFE, R. (1961) *J. Appl. Phys.* **32**, 149.
WILEY, J. D., BUEHLER, E., SHAY, J. L., and WERNICK, J. H. (1973) *J. Electronic Materials* **2**, 601.
WOOLLEY, J. C., and WILLIAMS, E. W. (1966) *J. Electrochem. Soc.* **113**, 899.
ZALAR, S. M. (1966) *J. Electrochem. Soc.* **113**, 230.
ZHUZE, V. P., SERGEEVA, V. M., and SHTRUM, E. L. (1958) *J. Tech. Phys.* **28**, 2093 [*Soviet Phys. Technical Physics* **3**, 1925 (1958)].
ZLATKIN, L. B., MARKOV, Yu. F., and POLUSHINA, I. K. (1969) *Fizika tekhn. Pol.* **3**, 1590 [*Soviet Phys. Semiconductors* **3**, 1336 (1970)].

CHAPTER 8

MISCELLANEOUS PHYSICAL PROPERTIES

8.1 Lattice Vibrational Spectra

The restructuring of the Brillouin zone of chalcopyrite relative to zincblende that proved so important in the electronic structure of ternary compounds (cf. Fig. 3.4, p. 83) is equally as important with regard to the lattice vibrations. Whereas there are two zone-center optic modes in a binary zincblende crystal, there are fifteen such modes in a ternary chalcopyrite crystal. Of these, four are Raman active, two are inactive, and nine are both Raman and infrared active. Whereas the lattice reflectivity spectrum (Reststrahlen) of a binary zincblende crystal is independent of the polarization of the electric field, in a ternary chalcopyrite crystal there is a very large optical anisotropy, since only three modes are active for $\mathbf{E} \parallel \mathbf{z}$ but six modes are active for $\mathbf{E} \perp \mathbf{z}$.

We list in Table 8.1 the character table and transformation properties of $\bar{4}2m(D_{2d})$, the point group for the chalcopyrite structure ($I\bar{4}2d$). Using this information the number of zone center Γ' vibrational modes belonging to a particular symmetry type (or irreducible representation Γ_i') can be calculated (Kaminow *et al.*, 1970). The results are summarized in Table 8.1, where it can be seen that all but the A_2 modes are Raman active.

The unit cell of minimal volume is spanned by the translation vectors $(-a/2, a/2, c/2)$, $(a/2, -a/2, c/2)$, and $(a/2, a/2, -c/2)$, and contains eight atoms (2 Cu, 2 Ga, 4 S) which give rise to 24 vibrational modes ignoring degeneracies. The distribution of the 24 modes over the 5 representations in Table 8.1 is as follows: $1\Gamma_1'$, $2\Gamma_2'$, $3\Gamma_3'$, $4\Gamma_4'$, and $7\Gamma_5'$. Since Γ_1' through Γ_4' are nondegenerate and Γ_5' is twofold degenerate, this distribution sums to 24 modes as required. Three of the modes are acoustic, one Γ_4' and one Γ_5' . Since the electric dipole operator transforms like a vector, only those Γ_i' which transform as coordinates (x , y , or z) correspond to infrared active vibrations. (x, y) transforms as Γ_5' , and z transforms as Γ_4' , where z is parallel to the tetragonal axis. Consequently there are $3\Gamma_4'$ and $6\Gamma_5'$ optic modes infrared active for electric fields polarized respectively parallel and perpendicular to the optic axis.

The infrared optical properties due to lattice vibrations can be approximated by a model consisting of independent harmonic oscillators with frequency-independent damping. The complex dielectric function for such a system may be written

$$\epsilon(\nu) = \epsilon'(\nu) + i\epsilon''(\nu) = \epsilon_\infty + \sum_{j=1}^n \frac{S_j \nu_j^2}{\nu_j^2 - \nu^2 - i\Gamma_j \nu} \quad (8.1)$$

It follows from our previous discussion that $n = 3$ for $\mathbf{E} \parallel \mathbf{z}$ (B_2 modes) and $n = 6$ for $\mathbf{E} \perp \mathbf{z}$ (E modes).

TERNARY CHALCOPYRITE SEMICONDUCTORS

TABLE 8.1. *Character table for the point group $\bar{4}2m$*

	<i>E</i>	$2S_4$	C_2	$2C'_2$	$2\sigma_d$	Symmetry	Activity	Optic	Acoustic
$A_1(\Gamma_1)$	1	1	1	1	1	$x^2 + y^2, z^2$	R	1	
$A_2(\Gamma_2)$	1	1	1	-1	-1	—	Inactive	2	
$B_1(\Gamma_3)$	1	-1	1	1	-1	$x^2 - y^2$	R	3	
$B_2(\Gamma_4)$	1	-1	1	-1	1	$xy; z$	R, IR	3	1
$E(\Gamma_5)$	2	0	-2	0	0	$xz, yz; x, y$	R, IR	6	1

TABLE 8.2. *Mode Parameters for E and B_2 Modes of $ZnSiP_2$ (Holah, 1972)*

	ν_{TO} (cm $^{-1}$)	ν_{LO} (cm $^{-1}$)	<i>S</i>	Γ (cm $^{-1}$)
B_2 modes				
1	491	509	1.02	21.9
2	347	360	1.04	2.3
E modes				
1	500	516	0.63	6.7
2	320	328	0.53	13.2
3	260	265	0.50	10.9
4	185	188	0.67	9.7

8.1.1 Infrared and Raman Spectra of $ZnSiP_2$

$ZnSiP_2$ is the only chalcopyrite crystal for which both Raman and Reststrahlen spectra are available. It is interesting to compare these two studies since they are complementary and lead to a fuller understanding of the vibrational properties. The results of reflectivity measurements using polarized light are shown in Fig. 8.1. Four of the six B_2 modes expected are observed, and two of the three E modes are observed. The dashed curves represent least-squares fits to the data using eq. (8.1) and the parameters listed in Table 8.2. The optical constants n and k , and the dielectric functions ϵ' and ϵ'' , calculated from these parameters are shown in Figs. 8.2 and 8.3 respectively. Using these parameters, Holah (1972) finds the following values for the dielectric constants:

$$\left. \begin{aligned} E \text{ modes: } & \epsilon_\infty = 9.26, \quad \epsilon_0 = 11.1, \\ & \epsilon_0/\epsilon_\infty = 1.1994; \\ B \text{ modes: } & \epsilon_\infty = 9.68, \quad \epsilon_0 = 11.2, \\ & \epsilon_0/\epsilon_\infty = 1.157. \end{aligned} \right\} \quad (8.2)$$

The values of the resonance frequency, ν_j in eq. (8.1), are associated with transverse optical (TO) frequencies. The maximum in the conductivity gives exactly the TO frequency when damping is present. The value of the related longitudinal optical frequency is given by $\epsilon'(\nu) = 0$. When $\epsilon'(\nu)$ does not reach zero, the frequency at the minimum value is usually taken.

The vibrational modes observed in the Raman spectra of $ZnSiP_2$ are shown in Fig. 8.4 together with the phonon dispersion curves for the [001] direction in GaP. Kaminow *et al.* (1970) and Holah (1972) conclude that there are three groups of zone

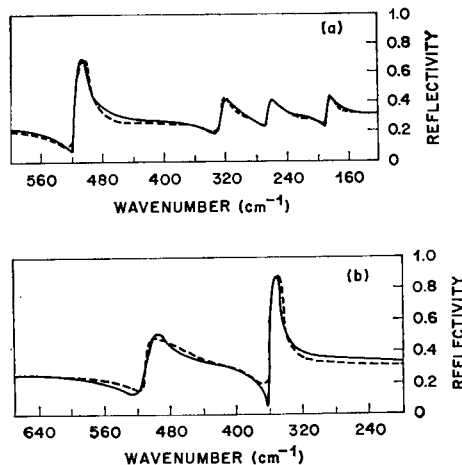


FIG. 8.1. Experimental and calculated reflectivity of (a) the E modes ($\mathbf{E} \perp \mathbf{z}$), and (b) the B_2 modes ($\mathbf{E} \parallel \mathbf{z}$) of ZnSiP_2 . Full line, experiment; broken line, theory. (Holah, 1972.)

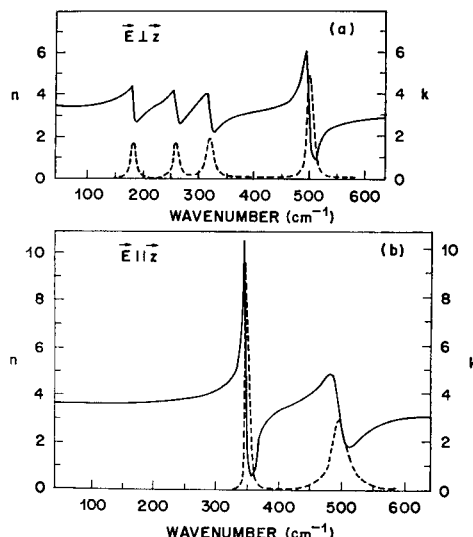


FIG. 8.2. Optical constants n and k for (a) E modes ($\mathbf{E} \perp \mathbf{z}$), and (b) B_2 modes ($\mathbf{E} \parallel \mathbf{z}$) of ZnSiP_2 . Full line, n ; broken line, k . (Holah, 1972.)

TERNARY CHALCOPYRITE SEMICONDUCTORS

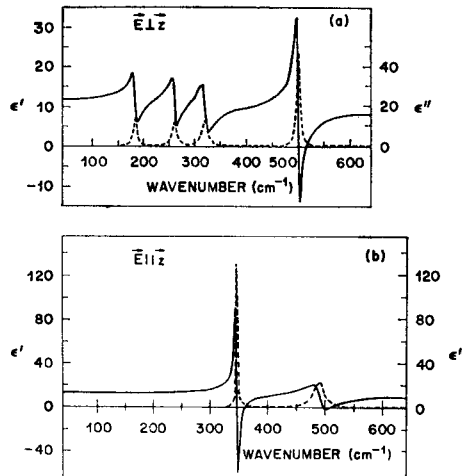


FIG. 8.3. Real and imaginary parts of the dielectric function for (a) the E modes ($E \perp z$), and (b) the B_2 modes ($E \parallel z$) of ZnSiP_2 . Full line, ϵ' ; broken line, ϵ'' . (Holah, 1972.)

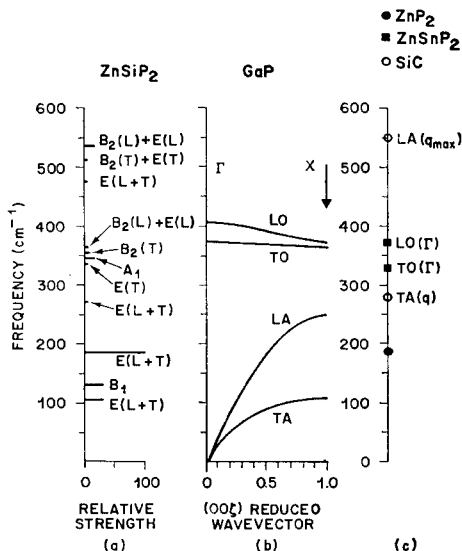
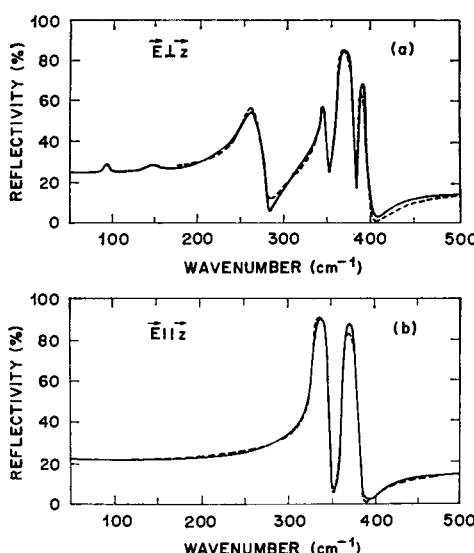


FIG. 8.4. (a) Raman modes observed in ZnSiP_2 indicating relative strengths, (b) GaP dispersion curves in [001] direction, and (c) mode frequencies in ZnP_2 , ZnSnP_2 , and SiC . (Kaminow *et al.*, 1970.)

center modes in ZnSiP_2 corresponding to zone center and zone boundary modes in GaP. There is a low frequency group corresponding to transverse acoustic zone-boundary modes in GaP, an intermediate frequency group corresponding to zone boundary longitudinal acoustic modes, and a high frequency group corresponding to zone-boundary and zone-center optic modes. The identifications of all of the observed B_2 and E modes are given in Table 8.3.

TABLE 8.3. Assignments of Vibrational Modes in $ZnSiP_2$ (frequencies in cm^{-1})

	Kaminow <i>et al.</i> (1970)	Holah (1972)	Symmetry Species
Zn-P	105	—	$E(T)$ $E(L + T)$ X_5
	185	185	$E(T)$
	—	188	$E(L)$
	270	260	$E(T)$
	—	265	$E(L)$
	335	320	$E(T)$
	—	328	$E(L)$
	362	—	$E(L)$
	477	—	$E(L)$
Si-P	511	500	$E(T)$
	535	516	$E(L)$
			X_5
Zn-P	352	347	$B_2(T)$
Si-P	362	360	$B_2(L)$
	511	491	$B_2(T)$
	535	509	$B_2(L)$
			Γ_{15}
			W_2

FIG. 8.5. Reflectivity of CuGaS_2 for (a) E modes ($E \perp z$), and (b) B_2 modes ($E \parallel z$). The dashed curves are the fits obtained using the parameters in Tables 8.4 and 8.5. (Baars and Koschel, 1972.)

TERNARY CHALCOPYRITE SEMICONDUCTORS

8.1.2 Infrared Spectra of CuGaS₂ and AgGaS₂

A complete infrared reflectivity analysis using polarized radiation is available for only two other chalcopyrite crystals, CuGaS₂ and AgGaS₂. All six of the *E* modes expected have been observed in CuGaS₂, but only two of the three *B* modes were observed (Fig. 8.5). The parameters leading to the best fits to the data are listed in Tables 8.4 and 8.5 for *E* modes and *B*₂ modes respectively. Using these parameters, Baars and Koschel (1972) find:

$$\left. \begin{aligned} E \text{ modes: } & \varepsilon_{\infty} = 6.2, \quad \varepsilon_0 = 8.9, \\ & \varepsilon_0/\varepsilon_{\infty} = 1.44; \\ B_2 \text{ modes: } & \varepsilon_{\infty} = 6.1, \quad \varepsilon_0 = 7.6, \\ & \varepsilon_0/\varepsilon_{\infty} = 1.25. \end{aligned} \right\} \quad (8.3)$$

Baars and Koschel (1972) have attempted to relate the vibrational modes observed in CuGaS₂ to those observed in ZnS, the binary analog. These authors point out that the TO frequency of the strongest mode (mode 4 in Table 8.4) is closest to the TO frequency of ZnS (272 cm⁻¹). The weak modes 1, 5, and 6 of Table 8.4 may be related to phonons at the boundary of the cubic Brillouin zone, $X(0, 0, \pm 2\pi/a)$, which corresponds to Γ in the chalcopyrite Brillouin zone. The TA and TO modes at X of the zincblende Brillouin zone belong to the $\Gamma_5(E)$ representation in the chalcopyrite structure. Since for a point charge lattice the dipole moments of these *E* modes are zero, they are expected to be weak in the real lattice. The modes at 93 and 148 cm⁻¹ may correspond to the TA mode at 90 cm⁻¹ in ZnS (Bergsma, 1970). The weak mode at 387 cm⁻¹ may be related to the TO mode of ZnS.

Ditzenberger (1974) has measured the infrared optical properties of AgGaS₂ using polarized radiation (Fig. 8.6). The classical oscillator fits to the data were obtained using the values in Table 8.6. From these data Ditzenberger finds:

$$\left. \begin{aligned} E \text{ modes: } & \varepsilon_{\infty} = 5.90, \quad \varepsilon_0 = 8.51, \\ & \varepsilon_0/\varepsilon_{\infty} = 1.442; \\ B_2 \text{ modes: } & \varepsilon_{\infty} = 5.50, \quad \varepsilon_0 = 8.23, \\ & \varepsilon_0/\varepsilon_{\infty} = 1.497. \end{aligned} \right\} \quad (8.4)$$

8.1.3 Other Chalcopyrite Crystals

For CuAlS₂ a single well-defined Reststrahl band has been observed in reflection from a natural growth surface in unpolarized light (Bhar and Smith, 1972). Only one mode is observed in the region 300–700 cm⁻¹. A good fit to the data was obtained using a single oscillator with the following parameters: $\nu_{TO} = 463$ cm⁻¹, $S = 0.75$, and $\Gamma = 11.1$ cm⁻¹. For comparison, parameters for the nearest binary equivalent, ZnS, are $\nu_{TO} = 272$ cm⁻¹, $S = 1.38$, and $\Gamma = 2.72$ cm⁻¹.

It has been suggested (Karavaev *et al.*, 1970) that the chalcopyrite mode with the largest dipole moment corresponds to the motion of the whole cation sublattice with respect to the anion sublattice, and is therefore directly equivalent to the TO mode of zincblende. Experimental confirmation of this prediction has been provided by measurements of Zlatkin *et al.* (1969) on ZnSnP₂ with the chalcopyrite and the quasi-zincblende (cations randomly distributed over the two chalcopyrite sites) structures. In each case

TABLE 8.4. *E modes of CuGaS₂ observed for E ⊥ z from Kramers-Kronig analysis compared to parameters of the least-squares fit to eq. (8.1) (after Baars and Koschel, 1972)*

Kramers-Kronig			Least-squares fit		
Mode	ν_{TO} (cm ⁻¹)	ν_{LO} (cm ⁻¹)	ν (cm ⁻¹)	S	Γ (cm ⁻¹)
1	387	399	387	0.04	3.60
2	364	383	364	0.56	3.44
3	346	350	345	0.55	6.85
4	259	279	259	1.54	15.02
5	148	—	—	—	—
6	93	—	—	—	—

TABLE 8.5. *B₂ modes of CuGaS₂ observed for E || z from Kramers-Kronig analysis compared to parameters of the least-squares fit to eq. (8.1) (after Baars and Koschel, 1972)*

Kramers-Kronig			Least-squares fit		
Mode	ν_{LO} (cm ⁻¹)	ν_{TO} (cm ⁻¹)	ν (cm ⁻¹)	S	Γ (cm ⁻¹)
1	365	384	364	0.27	2.70
2	331	350	330	1.20	2.49

TABLE 8.6. *Mode parameters for E and B₂ Modes of AgGaS₂ (Ditzengerger, 1974)*

	ν_{TO} (cm ⁻¹)	ν_{LO} (cm ⁻¹)	S	Γ (cm ⁻¹)
<i>B₂ modes</i>				
1	365	400	0.94	9.1
2	216	238	1.45	12.6
3	193	195	0.3	24.0
4	128	130	0.04	17.8
<i>E modes</i>				
1	368	390	0.32	5.34
2	323	346	1.35	6.78
3	223	230	0.40	15.8
4	157	160	0.28	9.7
5	90	93	0.26	13.5

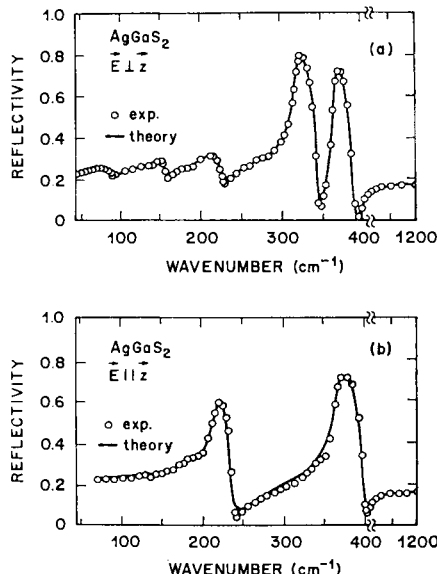


FIG. 8.6. Reflectivity of AgGaS_2 for (a) E modes ($E \perp z$), and (b) B_2 modes ($E \parallel z$). (Ditzengerger, 1974.)

a single Reststrahl band was observed which could be described by very similar parameters:

$$\left. \begin{array}{l} \text{Chalcopyrite: } \varepsilon_{\infty} = 8.08, \quad \varepsilon_0 = 10.0, \\ \quad \nu_{\text{TO}} = 327, \quad S = 1.90, \quad \Gamma = 20.0; \\ \text{Zincblende: } \varepsilon_{\infty} = 8.30, \quad \varepsilon_0 = 10.8, \\ \quad \nu_{\text{TO}} = 322, \quad S = 2.51, \quad \Gamma = 35.4. \end{array} \right\} \quad (8.5)$$

The infrared reflectivity of CdSnP_2 has been measured by Zlatkin *et al.* (1970) using unpolarized radiation. The results of a classical oscillator fit to the data are listed in Table 8.7. These authors find that $\varepsilon_{\infty} = 10.0$ and $\varepsilon_0 = 11.8$.

LO and TO frequencies have been determined for several crystals from an analysis of sum bands observed in absorption spectra. These results are listed in Table 8.8. The sum bands in CdSiP_2 (Isomura and Masumoto, 1971) are more complicated and lead to the following results: $\text{TO}_1 = 505 \text{ cm}^{-1}$, $\text{TO}_2 = 490$, $\text{LO} = 458$, $\text{LA} = 335$, and $\text{TA} = 150$.

8.2 Optical Activity in AgGaS_2

In the absence of birefringence, optical activity gives two contra-rotating circularly polarized modes of propagation with a small difference of refractive index, causing a rotation of the plane of polarization when the crystal is examined with linearly polarized light. The directional properties of this rotation can be described in terms of the gyration tensor. For crystals of class $42m$, the rotary power, the rotation of the plane of polarization in radians per unit length, is

$$\varrho = \frac{\pi G}{\lambda_0 \bar{n}} = \frac{\pi g_{11}(l_x^2 - l_y^2)}{\lambda_0 \bar{n}} \quad (8.6)$$

TABLE 8.7. *Vibrational Frequencies of CdSnP₂ and its Iso-electronic Analog InP (Zlatkin et al., 1970)*

	ν_{TO} (cm ⁻¹)	ν_{LO} (cm ⁻¹)	S	Γ (cm ⁻¹)
CdSnP ₂	339.5	353.5	0.87	7.5
	318	327	0.58	7.6
	295	—	—	9.1
	280	285	0.50	6.1
InP	307.2	348.5	2.77	3.1

TABLE 8.8. *Vibrational modes (in cm⁻¹) estimated from sum band absorption peaks (Boltivets et al., 1970; Isomura and Masumoto, 1971)*

Mode	ZnSiAs ₂	CdGeAs ₂	CdGeP ₂	ZnGeP ₂	ZnSnP ₂
TO	394	260	359	377	330
LO	409	273	376	397	350

where g_{11} is the only independent nonzero element of the gyration tensor, and l_x and l_y are direction cosines of the direction of propagation relative to the x - and y -axes. It follows from (8.6) that $\varrho = 0$ for propagation along the optic axis, and for all directions in the symmetry plane, and that ϱ is a maximum $\pm \pi g_{11}/\lambda_0 \bar{n}$ along the two diad axes.

The optical properties of crystals exhibiting birefringence and optical activity can be obtained by combining the two effects using a principle of superposition. A concise exposition of the theory has been given by Nye (1964). The effects of optical activity are difficult to observe in the presence of birefringence, for optical activity is a weak effect easily overwhelmed by birefringence. The theory predicts that there are two elliptically polarized modes of propagation with a phase retardation per unit length of

$$\Delta = 2\pi\{(n_e - n_o)^2 + (G/\bar{n})^2\}^{1/2}/\lambda_o. \quad (8.7)$$

From the data in Fig. 6.1 (p. 155) it can be seen that for each of the crystals AgGaSe₂, CuGaS₂, CuAlSe₂, and AgGaSe₂ there is a wavelength at which the birefringence vanishes. The wavelength is 4974 Å for AgGaS₂, and therefore AgGaS₂ is optically isotropic at 4974 Å although structurally it is tetragonal ($42m$). This accidental optical isotropy allows the observation of optical activity in all directions as pure optical rotation without the complications of birefringence. By measuring the rotation of the plane of polarization in AgGaS₂ plates of various thicknesses, Hobden (1968) has shown that the rotary power is 522 deg/mm. It was verified that there is no rotation along the z -axis. This rotary power for AgGaS₂ is very much greater than that of quartz but is comparable to that of cinnabar.

The appearance of AgGaS₂ under the polarizing microscope is somewhat unusual. With monochromatic light at 4974 Å there is no conoscopic figure owing to the absence of birefringence. Orthoscopic examination with white light illumination shows an incomplete extinction due to a band of blue radiation transmitted in the region of 4974 Å. The conoscopic figure in white light shows pale blue fringes on a yellow-orange background. These arise from the fact that in the orange and red parts of the visible spec-

trum, the birefringence is approximately proportional to the wavelength, which gives an achromatic conoscopic figure of dark fringes on a yellow-orange background. These dark fringes appear pale blue owing to the light transmitted at about 4974 Å. The appearance of this crystal under the polarizing microscope with monochromatic green, yellow, or red illumination is indistinguishable from that of a uniaxial crystal with no optical activity.

The principle of superposition of optical rotation and birefringence at wavelengths close to 4974 Å was demonstrated by Hobden (1968) by passing linearly polarized white light normally through a 0.61 mm thick *y*-cut plate of AgGaS₂, oriented with the *z*-axis in the plane of polarization. The emerging light was passed through a crossed analyzer and focused on the slit of a spectrograph. Had the crystal been birefringent but not optically active, the light would have propagated in the crystal as an extraordinary wave and would have been rejected by the analyzer. The simultaneous presence of optical activity and birefringence led to the appearance of dark fringes ~10 Å apart. The experimental spectra was consistent with the theoretical form

$$I/I_0 = \{(G/\bar{n})^2/((n_e - n_o)^2 + (G/\bar{n})^2)\} \sin^2(L\Delta/2), \quad (8.8)$$

where Δ is given by eq. (8.7) and L is the thickness of the crystalline slab. The second term shows that there will be dark fringes when $L\Delta = 2\pi N$.

The wavelength for optical isotropy in AgGaS₂ is 4974 Å at 20°C. As the temperature rises this wavelength increases initially at the rate of 0.2 Å/°C. At higher temperatures the rate of increase is greater, and by 200°C the wavelength for isotropy is 5030 Å.

8.3 E.S.R. of Fe³⁺ in I-III-VI₂ Crystals

The e.s.r. spectrum of Fe³⁺ impurity ions has been observed in the ternary compound CuGaS₂ by Schneider *et al.* (1973). The spin Hamiltonian appropriate to a Fe³⁺ ion in tetragonal symmetry is

$$H = g\beta\mathbf{H} \cdot \mathbf{S} + D(\mathbf{S}_z^2 - 35/12) + (7/36)F(\mathbf{S}_z^4 - (95/14)\mathbf{S}_z^2 + 81/16) + (a/6)(\mathbf{S}_{\xi}^4 + \mathbf{S}_{\eta}^4 + \mathbf{S}_z^4 - 707/16). \quad \left. \right\} \quad (8.9)$$

The first term represents the electronic Zeeman energy, the operators proportional to D and F correspond to the second- and fourth-order axial terms of the crystalline potential, and a corresponds to the cubic symmetric part. The parameters observed experimentally are as follows: $g = 2.024$, $a = 69$, $D = 1885$, and $F = 50$. Schneider *et al.* (1973) remark that the linewidths of the fine structure transition $\pm 5/2 \leftrightarrow \pm 3/2$, which are very sensitive to random crystalline fields, do not greatly exceed that of the central fine structure line. This indicates that the degree of crystalline perfection in the vapor transported crystals is good and that deviations from stoichiometry are small.

Brandt *et al.* (1973) have recently reported the ESR of Fe³⁺ in CuAlS₂, CuInS₂, and AgGaS₂. Their results are summarized in Table 8.9. These authors point out that the trends indicated for some of the parameters in Table 8.9 do not agree with expectations based on the crystallographic data. For example, the unusually large value of the axial field parameter D in AgGaS₂ is surprising in view of the almost ideal tetrahedral sulfur arrangement around the gallium site.

TABLE 8.9 E.S.R. parameters of Fe^{3+} in chalcopyrite hosts at 77° K. Crystal field parameters are given in units of 10^{-4} cm^{-1} . Their sign is positive as is that of the cubic parameter a .

	CuAlS ₂	CuGaS ₂	CuInS ₂	AgGaS ₂
g_{11}	2.020	2.024	2.022	2.019
D	900	1886	990	4871
$a + 2/3F$	90	103	66	71

8.4 N.M.R. of Cu⁶³ and Ga⁶⁹

Peterson and Kasper (1974) have studied the n.m.r. of Cu⁶³ and Ga⁶⁹ in variously colored crystals of CuGaS₂ in an attempt to identify the stoichiometric variety. The yellow-orange crystals grew at a higher temperature and their lattice parameters are $a = 5.328 \text{ \AA}$, $c = 10.462 \text{ \AA}$. The dark crystals grow at a lower temperature and their lattice parameters are $a = 5.351 \text{ \AA}$, and $c = 10.484 \text{ \AA}$. Previously, Belova *et al.* (1967) measured the lattice constants of Cu_{1-x}Ga_{1+x/3}S₂ samples ($0 < x < 1$) sintered at 1100°C and quenched to room temperature. Using Belova's values as a calibration for the lattice constants (Chapter 2, Fig. 2.10, p. 21) the yellow-orange crystals studied by Peterson and Kasper correspond to a composition Cu_{0.88}Ga_{1.04}S₂ and the dark crystals correspond to stoichiometric CuGaS₂.

The n.m.r. studies find that the Cu⁶³ resonance at 5609 kHz and the Ga⁶⁹ resonance at 8700 kHz are much broader and weaker in the yellow-orange crystals than in the dark crystals, but the resonance frequencies did not seem to vary. The signal strength is about one order of magnitude weaker in the yellow-orange crystals. From these results Peterson and Kasper conclude that the dark crystals are closer to ideal stoichiometry than the yellow-orange crystals in agreement with Belova's results.

Peterson (1970) has measured the Cu⁶³ nuclear quadrupole coupling constants for six chalcopyrite compounds prepared as powders. He finds that the coupling constant decreases with increasing electronegativity of the trivalent metal (Fig. 8.7a), and the coupling constant increases with increasing electronegativity of the chalcogen (Fig. 8.7b).

8.5 Properties of Quaternary Alloys

8.5.1 Electrical Properties of CdSnAs₂-InAs Solid Solutions

Mamaev *et al.* (1961) have studied the electrical properties of (CdSnAs₂)_x(2InAs)_{1-x} solid solutions prepared by alloying together the components in evacuated quartz capsules. For $x \lesssim 0.25$ the samples were *p*-type, whereas for $x > 0.25$ the samples were *n*-type. The concentration of current carriers at 300K was 0.44 to $1 \times 10^{19} \text{ cm}^{-3}$ for all compositions except CdSnAs₂, which was purified by zone melting to $4.4 \times 10^{17} \text{ cm}^{-3}$.

The electrical conductivity of all samples is practically independent of temperature in the region 77–280 K. In the high-temperature region beginning at approximately 350 K, an exponential increase is observed for all compositions. The energy gaps determined in this high-temperature region assuming intrinsic conductivity are shown in Fig. 8.8. The “bowing” of the energy gap below the value obtained from a straight line interpolation is quite a bit larger than usually observed in alloys such as (In_xGa_{1-x})As

TERNARY CHALCOPYRITE SEMICONDUCTORS

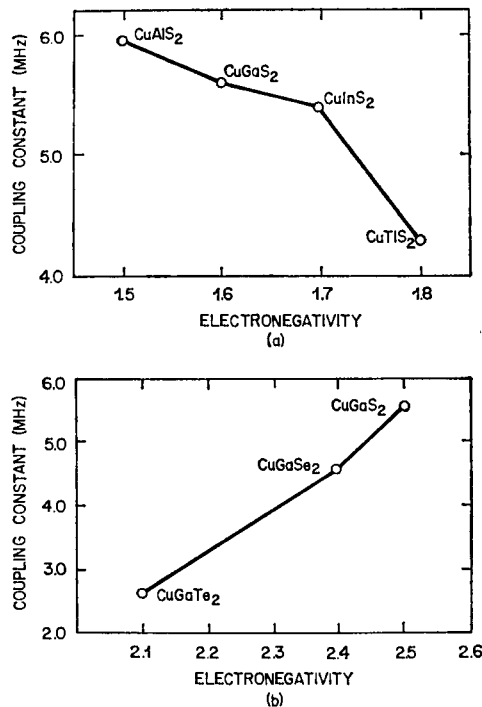


FIG. 8.7. Nuclear quadrupole coupling constant of Cu^{63} in chalcopyrites plotted against (a) the electronegativity of the trivalent metal, and (b) the electronegativity of the chalcogen. (Peterson, 1970.)

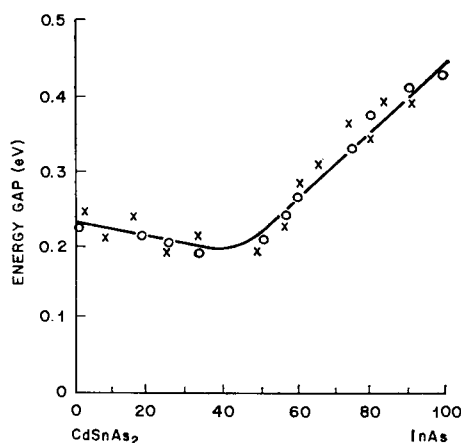


FIG. 8.8. Dependences of the energy gap upon the composition of CdSnAs_2 - InAs solid solutions. (Mamaev *et al.*, 1961.)

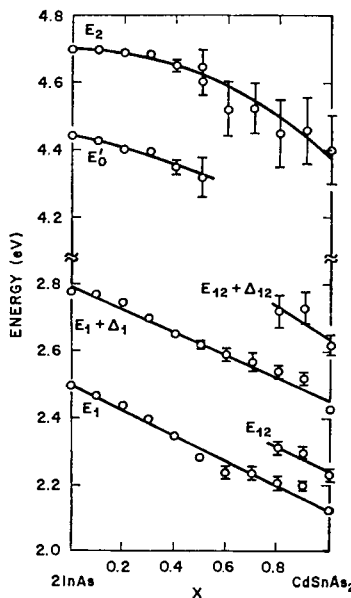


FIG. 8.9. Variation with composition of the energies of E_1 , $E_1 + \Delta_1$, E_{12} , $E_{12} + \Delta_{12}$, E'_0 , and E_2 peaks in the electroreflectance spectra of $(\text{CdSnAs}_2)_x(2\text{InAs})_{1-x}$ alloys. (Kwan and Woolley, 1970.)

in which the substitutions are isoelectronic. Since the substitution of In atoms on Cd and Sn sites produces strong coulombic potentials, perhaps the bowing manifest in Fig. 8.8 results in large measure from "band tails" in the alloys.

Kwan and Woolley (1970) have measured the electroreflectance spectra of $(\text{CdSnAs}_2)_x \times (2\text{InAs})_{1-x}$ alloys. They found that alloys with $x \leq 0.7$ had the zincblende structure, and alloys with $x > 0.7$ had the chalcopyrite structure. The energies of characteristic structures in the electroreflectance spectra are shown in Fig. 8.9 as a function of composition. Despite the change in the alloys from zincblende to chalcopyrite structure at $x \approx 0.7$, it is found that the E_1 and $E_1 + \Delta_1$ energies vary smoothly with x . For compositions having the chalcopyrite structure, extra components labeled E_{12} and $E_{12} + \Delta_{12}$ are observed.

Alloys of the form $(\text{ZnSnAs}_2)_x(2\text{InAs})_{1-x}$ were also studied by Kwan and Woolley (1970), but the spectra were very broad for $x \gtrsim 0.5$. The spectrum for ZnSnAs_2 consisted of one peak ~ 0.5 eV below the average energy of the E_1 and $E_1 + \Delta_1$ peaks in InAs.

8.5.2 CdTe–AgInTe₂ and CdTe–CuGaTe₂ Solid Solutions

Woolley and Williams (1966) have studied alloys of CdTe with AgInTe₂ or CuGaTe₂. The dependences of lattice constants upon composition were given in Chapter 2 (Figs. 2.20 and 2.21, p. 32). The ternary compounds were produced by melting components and then quenching in water. With these quenched samples, CuGaTe₂ and AgInTe₂ were found to have optical energy gaps of 1.17 and 0.97 eV respectively.

It was found that when CuGaTe₂ (m.p. 870°C) was annealed at 750°C a second phase began to appear. Although it was difficult to detect the presence of this phase with

TERNARY CHALCOPYRITE SEMICONDUCTORS

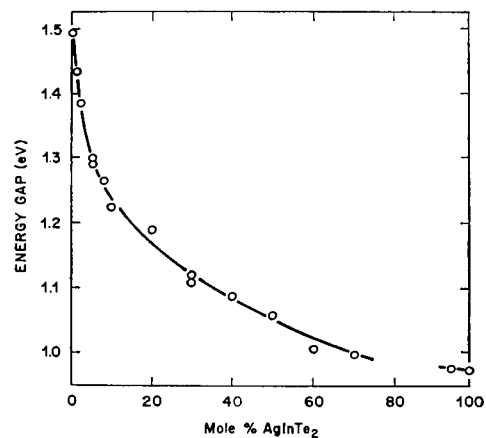


FIG. 8.10. Variation of optical energy gap E_g with composition for CdTe-AgInTe₂ alloys. (Woolley and Williams, 1966.)

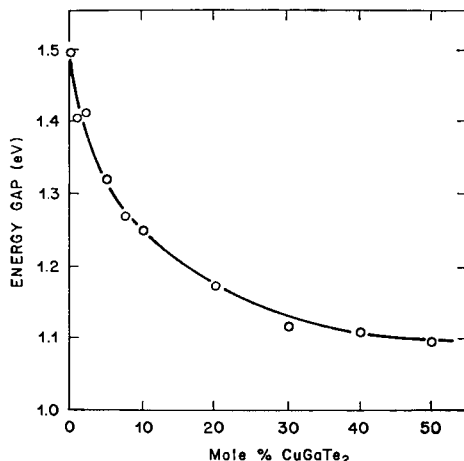


FIG. 8.11. Variation of optical energy gap E_g with composition for CdTe-CuGaTe₂ alloys. (Woolley and Williams, 1966.)

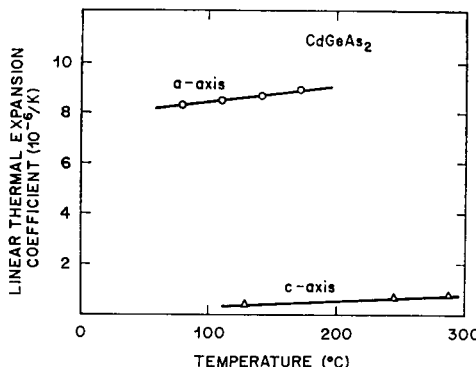


FIG. 8.12. Linear thermal expansion coefficient for CdGeAs_2 . (Kildal, 1972.)

X-ray powder photographs, the results of both photomicrographic analysis and optical absorption measurements showed its presence. Even in the quenched state, a number of small needle-like inclusions were observed. On annealing at 750°C these inclusions grew, and then the second phase was observed to segregate out at the grain boundaries and to cause large cracks. Correspondingly, the quenched sample gave a normal absorption curve with an absorption edge at an energy of 1.17 eV, but after the sample was annealed at 750°C , a broad absorption peak appeared on the low energy side of the absorption edge at photon energies of about 0.7–0.9 eV, and the magnitude of this peak increased with continued annealing. When the CuGaTe_2 was annealed at lower temperatures (e.g. 400°C), no growth of a second phase was observed in the photomicrographs beyond the small inclusions of the quenched state, and the optical absorption curve did not change with annealing from that for the quenched material.

When AgInTe_2 (m.p. 680°C) was annealed at 600°C , no changes in behavior could be detected from that for the quenched material. However, when samples were annealed at 400°C for 10 days, photomicrographs showed the appearance of a second phase (possibly tellurium) at the grain boundaries. In an X-ray photograph of this material the value of the lattice parameter a_0 (6.455 Å) was found to be a little higher than that for the samples annealed at 600°C (6.446 Å).

Alloys were prepared by melting together the appropriate amounts of CdTe and the ternary compound concerned, and then quenching in water. Such samples showed blurred X-ray lines, were generally in nonequilibrium condition, and needed annealing to give equilibrium. The variation of the energy gaps in annealed alloys of $\text{CdTe}-\text{AgInTe}_2$ and $\text{CdTe}-\text{CuGaTe}_2$ is shown in Figs. 8.10 and 8.11. For both systems the energy gap drops rapidly as ternary compound is added to CdTe , and then the E_g versus composition curve levels out. Perhaps this variation is associated with the strong coulomb potentials resulting when Cu and Ga (or Ag and In) substitute for Cd in CdTe .

8.6 Linear Thermal Expansion of CdGeAs_2

Kildal (1972) has measured the linear thermal expansion coefficient of CdGeAs_2 as a function of temperature using an optical interference technique. As can be seen in Fig. 8.12, CdGeAs_2 has a very anisotropic linear thermal expansion, with α_{\perp} more than 10 times larger than α_{\parallel} . It is interesting to note that the built-in compressive distortion $2 - c/a$ increases with increasing temperature, at least for $T \lesssim 300^\circ\text{C}$.

TERNARY CHALCOPYRITE SEMICONDUCTORS

References

- BAARS, J., and KOSCHEL, W. H. (1972) *Solid State Commun.* **11**, 1513.
- BELOVA, C. K., KOSHKIN, V. M., PALATNIK, L. S. (1967) *Izv. Akad. Nauk SSSR, Neorgan. Mater.* **3**, 617 [*Inorganic Materials* **3**, 543 (1967)].
- BERGSMA, J. (1970) *Phys. Lett.* **32A**, 324.
- BHAR, G. C., and SMITH, R. C. (1972) *Phys. Status Solidi (a)* **13**, 157.
- BOLIVETS, N. S., MAMEDOV, B. K.H., and OSMANOV, E. O. (1970) *Fizika tekhn. Pol.* **4**, 596 [*Soviet Phys. Semiconductors* **4**, 499 (1970)].
- BRANDT, G., RAUBER, A., and SCHNEIDER, J. (1973) *Solid State Commun.* **12**, 481.
- DITZENBERGER, J. A. (1974). To be published.
- HOBDEN, M. V. (1968) *Acta Crystallogr. A*, **24**, 676.
- HOLAH, G. D. (1972) *J. Phys. C.: Solid State Phys.* **5**, 1893.
- ISOMURA, S., and MASUMOTO, K. (1971) *Phys. Status Solidi (a)* **6**, K139.
- KAMINOW, I. P., BUEHLER, E., and WERNICK, J. H. (1970) *Phys. Rev. B*, **2**, 960.
- KARAVAEV, G. F., POPLAVNOI, A. C., and TYUTEREV, B. G. (1970) *Izv. vyssh. ucheb. Zaved. Fiz.* **13**(10), 42 [*Soviet Phys. J.* **13**, 1292 (1970)].
- KILDAL, H. (1972) Ph. D. thesis, Stanford University, Technical Report AFML-TR-72-277, Wright Patterson Air Force Base, Ohio.
- KWAN, C. C. Y., and WOOLLEY, J. C. (1970) *Can. J. Phys.* **48**, 2085.
- MAMAEV, S., NASLEDOV, D. N., and GALAVANOV, V. V. (1961) *Fizika tverd. Tela* **3**, 3405 [*Soviet Phys. Solid State* **3**, 2473 (1962)].
- NYE, J. F. (1964) *Physical Properties of Crystals*, London, Oxford Univ. Press.
- PETERSON, G. E. (1970) *Magnetic Resonance*, Plenum Press.
- PETERSON, G. E. and KASPER, H. M. (1974) To be published.
- SCHNEIDER, J., RÄUBER, A., and BRANDT, G. (1973) *J. Phys. Chem. Solids* **34**, 443.
- WOOLLEY, J. C., and WILLIAMS, E. W. (1966) *J. Electrochem. Soc.* **113**, 899.
- ZLATKIN, L. B., MARKOV, Y. F., STEKHANOV, A. I., and SHUR, M. S. (1969) *Phys. Status Solidi* **32**, 473.
- ZLATKIN, L. B., MARKOV, YU. F., ORLOV, V. M., SOKOLOVA, V. I., and SHUR, M. S. (1970) *Fiz. tekhn. Pol.* **4**, 1387 (1970) [*Soviet Phys. Semiconductors* **4**, 1181 (1970)].

APPENDIX

TABULATED REFRACTIVE INDEX DATA

IN THIS appendix we tabulate the room temperature refractive index data of Boyd and coworkers from four II-IV-V₂ crystals and seven I-III-VI₂ crystals.

TABLE A1.1. *Refractive indices of ZnGeP₂ (Boyd et al., 1971a)*

λ (μ)	$\nu = \lambda^{-1}$ (μ^{-1})	n^o	n^e	$n^e - n^o$	$10^5 \times dn^o/dT$	$10^5 \times dn^e/dT$	$10^5 \times dB/dT$
0.64	1.5625	3.5052	3.5802	0.0750	35.94	37.58	3.54
0.66	1.5152	3.4756	3.5467	0.0710	31.23	37.34	3.32
0.68	1.4706	3.4477	3.5160	0.0684	29.52	32.53	3.13
0.70	1.4286	3.4233	3.4885	0.0652	28.63	31.82	2.97
0.75	1.3333	3.3730	3.4324	0.0595	26.22	28.26	2.66
0.80	1.2500	3.3357	3.3915	0.0558	24.69	26.43	2.44
0.85	1.1765	3.3063	3.3593	0.0530	24.12	25.39	2.27
0.90	1.1111	3.2830	3.3336	0.0506	22.34	24.61	2.14
0.95	1.0526	3.2638	3.3124	0.0486	21.32	24.26	2.04
1.00	1.0000	3.2478	3.2954	0.0476	21.18	23.01	1.95
1.10	0.9091	3.2232	3.2688	0.0456	20.11	22.08	1.82
1.20	0.8333	3.2054	3.2493	0.0438	18.63	20.51	1.73
1.30	0.7692	3.1924	3.2346	0.0423	16.84	20.12	1.66
1.40	0.7143	3.1820	3.2244	0.0423	15.34	16.55	1.60
1.60	0.6250	3.1666	3.2077	0.0411	15.10	16.75	1.53
1.80	0.5556	3.1562	3.1965	0.0403	13.20	14.40	1.47
2.00	0.5000	3.1490	3.1889	0.0399	14.19	15.29	1.44
2.20	0.4545	3.1433	3.1829	0.0396	14.60	15.28	1.41
2.40	0.4167	3.1388	3.1780	0.0391	14.14	15.49	1.39
2.60	0.3846	3.1357	3.1745	0.0388	15.13	16.80	1.37
2.80	0.3571	3.1327	3.1717	0.0390	15.48	16.05	1.36
3.00	0.3333	3.1304	3.1693	0.0388	13.26	13.96	1.35
3.20	0.3125	3.1284	3.1671	0.0386	14.94	16.28	1.34
3.40	0.2941	3.1263	3.1647	0.0384	14.40	15.46	1.34
3.60	0.2778	3.1257	3.1632	0.0376	15.58	16.29	1.33
3.60	0.2632	3.1237	3.1616	0.0380	14.58	16.53	1.33
4.00	0.2500	3.1223	3.1608	0.0386	14.26	15.02	1.33
4.20	0.2381	3.1209	3.1595	0.0386	13.57	15.14	1.33
4.50	0.2222	3.1186	3.1561	0.0374	15.31	16.60	1.32
4.70	0.2128	3.1174	3.1549	0.0375	15.51	16.71	1.32
5.00	0.2000	3.1149	3.1533	0.0383	15.05	16.43	1.32
5.50	0.1818	3.1131	3.1518	0.0387	14.49	15.42	1.32
6.00	0.1667	3.1101	3.1480	0.0379	14.58	16.30	1.32
6.50	0.1538	3.1057	3.1445	0.0387	15.60	16.13	1.32
7.00	0.1429	3.1040	3.1420	0.0380	12.85	15.01	1.33
7.50	0.1333	3.0994	3.1378	0.0384	18.15	18.59	1.33
8.00	0.1250	3.0961	3.1350	0.0389	16.10	17.43	1.33
8.50	0.1176	3.0919	3.1311	0.0392	15.16	17.37	1.33
9.00	0.1111	3.0880	3.1272	0.0392	15.56	17.50	1.34
9.50	0.1053	3.0836	3.1231	0.0395	16.27	17.11	1.34
10.00	0.1000	3.0788	3.1183	0.0396	16.53	18.41	1.34
10.50	0.0952	3.0738	3.1137	0.0399	15.40	16.84	1.34
11.00	0.0909	3.0689	3.1087	0.0398	15.25	16.34	1.34
11.50	0.0870	3.0623	3.1008	0.0386	14.74	18.32	1.34
12.00	0.0833	3.0552	3.0949	0.0397	14.24	16.59	1.34

TERNARY CHALCOPYRITE SEMICONDUCTORS

 TABLE A1.2. *Refractive indices of CdGeAs₂ (Boyd et al., 1972a)*

λ (μ)	$\nu = \lambda^{-1}$ (μ^{-1})	n^o	n^e	$n^e - n^o$
2.3	0.4348	3.6076		
2.4	0.4167	3.5973	3.7545	0.1572
2.5	0.4000	3.5895	3.7316	0.1420
2.6	0.3846	3.5823	3.7156	0.1333
2.7	0.3704	3.5773	3.7030	0.1257
2.8	0.3571	3.5721	3.6926	0.1206
2.9	0.3448	3.5684	3.6846	0.1162
3.0	0.3333	3.5645	3.6775	0.1131
3.1	0.3226	3.5615	3.6714	0.1099
3.2	0.3125	3.5581	3.6661	0.1080
3.4	0.2941	3.5536	3.6574	0.1038
3.6	0.2778	3.5503	3.6508	0.1005
3.8	0.2632	3.5468	3.6454	0.0986
4.0	0.2500	3.5448	3.6402	0.0962
4.2	0.2381	3.5415	3.6368	0.0954
4.4	0.2273	3.5391	3.6329	0.0938
4.6	0.2174	3.5372	3.6299	0.0928
4.8	0.2083	3.5354	3.6373	0.0919
5.0	0.2000	3.5336	3.6249	0.0914
5.5	0.1818	3.5285	3.6178	0.0893
6.0	0.1667	3.5251	3.6134	0.0883
6.5	0.1538	3.5223	3.6104	0.0881
7.0	0.1429	3.5200	3.6073	0.0873
7.5	0.1333	3.5175	3.6050	0.0875
8.0	0.1250	3.5157	3.6030	0.0873
8.5	0.1176	3.5140	3.6009	0.0869
9.0	0.1111	3.5120	3.5988	0.0868
9.5	0.1053	3.5098	3.5966	0.0867
10.0	0.1000	3.5078	3.5942	0.0864
10.5	0.0952	3.5054	3.5922	0.0868
11.0	0.0909	3.5031	3.5896	0.0865
11.5	0.0870	3.5004	3.5871	0.0868
12.0	0.0833	3.4977		
12.5	0.0800	3.4950		

TABULATED REFRACTIVE INDEX DATA

TABLE A1.3. *Refractive indices of CdGeP₂ (Boyd et al., 1972a)*

λ (μ)	$\nu = \lambda^{-1}$ (μ^{-1})	n^o	n^e	$n^e - n^o$	$10^5 \times dn^o/dT$	$10^5 \times dn^e/dT$	$10^5 \times dB/dT$
0.80	1.2500	3.4833			35.56		
0.85	1.1765	3.4403	3.4942	0.0539	29.11	43.35	14.24
0.90	1.1111	3.4059	3.4505	0.0445	53.72	61.38	7.66
0.95	1.0526	3.3789	3.4167	0.0378	25.55	26.16	0.61
1.00	1.0000	3.3560	3.3902	0.0342	24.80	28.75	2.95
1.10	0.9091	3.3232	3.3505	0.0272	23.60	26.37	2.76
1.20	0.8333	3.2990	3.3222	0.0231	22.25	25.08	2.83
1.30	0.7692	3.2811	3.3025	0.0214	20.71	22.52	1.81
1.40	0.7143	3.2669	3.2867	0.0198	20.20	21.42	1.22
1.60	0.6250	3.2470	3.2643	0.0173	18.68	20.57	1.89
1.80	0.5556	3.2342	3.2502	0.0161	20.56	21.75	1.19
2.00	0.5000	3.2255	3.2406	0.0151	18.11	19.31	1.20
2.20	0.4545	3.2202	3.2340	0.0138	17.12	18.25	1.13
2.40	0.4167	3.2159	3.2287	0.0128	18.70	19.61	0.91
2.60	0.3846	3.2128	3.2243	0.0115	17.77	19.31	1.55
2.80	0.3571	3.2096	3.2206	0.0110	17.30	18.96	1.66
3.00	0.3333	3.2065	3.2175	0.0110	17.69	19.22	1.53
3.20	0.3125	3.2049	3.2156	0.0106	16.61	18.24	1.63
3.40	0.2941	3.2026	3.2132	0.0106	16.10	17.65	1.55
3.60	0.2778	3.2003	3.2108	0.0104	16.39	17.94	1.56
3.80	0.2632	3.1981	3.2083	0.0102	17.19	18.72	1.53
4.00	0.2500	3.1963	3.2063	0.0100	17.04	18.61	1.57
4.50	0.2222	3.1924	3.2026	0.0102	17.44	18.49	1.05
5.00	0.2000	3.1887	3.1991	0.0103	17.86	18.75	0.89
5.50	0.1818	3.1830	3.1934	0.0105	17.71	18.51	0.80
6.00	0.1667	3.1800	3.1906	0.0106	18.08	19.03	0.95
6.50	0.1538	3.1768	3.1876	0.0108	18.38	19.56	1.18
7.00	0.1429	3.1735	3.1846	0.0112	17.69	19.02	1.33
7.50	0.1333	3.1703	3.1816	0.0113	17.12	18.52	1.40
8.00	0.1250	3.1669	3.1785	0.0116	15.51	16.73	1.23
8.50	0.1176	3.1624	3.1743	0.0119	16.58	17.92	1.34
9.00	0.1111	3.1585	3.1707	0.0122	16.20	17.28	1.08
9.50	0.1053	3.1547	3.1672	0.0125	14.75	16.69	1.94
10.00	0.1000	3.1508	3.1636	0.0128	12.88	14.72	1.84
10.50	0.0952	3.1435	3.1574	0.0139	16.14	16.98	0.84
11.00	0.0909	3.1372	3.1517	0.0145	16.59	17.62	1.03
11.50	0.0870	3.1321	3.1470	0.0149	15.93	17.02	1.09
12.00	0.0833	3.1241	3.1402	0.0151	17.14	17.85	0.70
12.50	0.0800	3.1165	3.1332	0.0167	15.48	16.11	0.63

TABLE A1.4. *Refractive indices of ZnSiAs₂* (Boyd et al., 1972a)

λ (μ)	$\nu = \lambda^{-1}$ (μ^{-1})	n^o	n^e	$n^e - n^o$
0.70	1.4286	3.5579	3.6201	0.0621
0.75	1.3333	3.5002	3.5539	0.0537
0.80	1.2500	3.4570	3.5050	0.0480
0.85	1.1765	3.4210	3.4655	0.0445
0.90	1.1111	3.3946	3.4362	0.0416
0.95	1.0526	3.3722	3.4116	0.0393
1.00	1.0000	3.3551	3.3928	0.0377
1.10	0.9091	3.3266	3.3618	0.0352
1.20	0.8333	3.3061	3.3394	0.0333
1.30	0.7692	3.2900	3.3221	0.0320
1.40	0.7143	3.2782	3.3093	0.0311
1.60	0.6250	3.2593	3.2889	0.0296
1.80	0.5556	3.2485	3.2771	0.0286
2.00	0.5000	3.2405	3.2692	0.0287
2.20	0.4545	3.2346	3.2620	0.0274
2.40	0.4167	3.2296	3.2572	0.0276
2.60	0.3846	3.2268	3.2539	0.0272
2.80	0.3571	3.2233	3.2506	0.0272
3.00	0.3333	3.2210	3.2481	0.0271
3.20	0.3125	3.2197	3.2464	0.0267
3.40	0.2941	3.2178	3.2447	0.0269
3.60	0.2778	3.2162	3.2426	0.0264
3.80	0.2632	3.2146	3.2413	0.0268
4.00	0.2500	3.2133	3.2402	0.0268
4.50	0.2222	3.2106	3.2372	0.0266
5.00	0.2000	3.2081	3.2345	0.0265
5.50	0.1818	3.2053	3.2317	0.0264
6.00	0.1667	3.2025	3.2287	0.0262
6.50	0.1538	3.2002	3.2263	0.0261
7.00	0.1429	3.1979	3.2241	0.0263
7.50	0.1333	3.1956	3.2220	0.0264
8.00	0.1250	3.1930	3.2195	0.0265
8.50	0.1176	3.1905	3.2168	0.0264
9.00	0.1111	3.1874	3.2138	0.0263
10.00	0.1000	3.1810	3.2074	0.0264
10.50	0.0952	3.1772	3.2037	0.0264
11.00	0.0909	3.1733	3.1996	0.0263
11.50	0.0870	3.1685	3.1953	0.0268
12.00	0.0833	3.1626		

TABULATED REFRACTIVE INDEX DATA

TABLE A 1.5. *Refractive indices of AgGaS₂ (Boyd et al., 1971b)*

λ (μ)	$\nu = \lambda^{-1}$ (μ^{-1})	n^o	n^e	$n^e - n^o$
0.490	2.0408	2.7148	2.7287	0.0138
0.500	2.0000	2.6916	2.6867	-0.0049
0.525	1.9048	2.6503	2.6239	-0.0264
0.550	1.8182	2.6190	2.5834	-0.0356
0.575	1.7391	2.5944	2.5537	-0.0407
0.600	1.6667	2.5748	2.5303	-0.0444
0.625	1.6000	2.5577	2.5116	-0.0461
0.650	1.5385	1.5437	2.4961	-0.0476
0.675	1.4815	2.5310	2.4824	-0.0486
0.700	1.4286	2.5205	2.4706	-0.0499
0.750	1.3333	2.5049	2.4540	-0.0509
0.800	1.2500	2.4989	2.4395	-0.0514
0.850	1.1765	2.4802	2.4279	-0.0522
0.900	1.1111	2.4716	2.4192	-0.0525
0.950	1.0526	2.4644	2.4118	-0.0526
1.000	1.0000	2.4582	2.4053	-0.0529
1.100	0.9891	2.4486	2.3954	-0.0532
1.200	0.8333	2.4414	2.3881	-0.0533
1.300	0.7692	2.4359	2.3819	-0.0548
1.400	0.7143	2.4315	2.3781	-0.0534
1.500	0.6667	2.4280	2.3745	-0.0535
1.600	0.6258	2.4252	2.3716	-0.0535
1.800	0.5556	2.4206	2.3670	-0.0536
2.000	0.5000	2.4164	2.3637	-0.0527
2.200	0.4545	2.4142	2.3604	-0.0537
2.400	0.4167	2.4119	2.3583	-0.0535
2.600	0.3846	2.4182	2.3567	-0.0535
2.800	0.3571	2.4094	2.3559	-0.0535
3.000	0.3333	2.4080	2.3545	-0.0535
3.200	0.3125	2.4068	2.3534	-0.0534
3.400	0.2941	2.4062	2.3522	-0.0540
3.600	0.2778	2.4046	2.3511	-0.0535
3.800	0.2632	2.4024	2.3491	-0.0533
4.000	0.2500	2.4024	2.3488	-0.0536
4.500	0.2222	2.4003	2.3461	-0.0542
5.000	0.2000	2.3953	2.3419	-0.0536
5.500	0.1818	2.3938	2.3401	-0.0537
6.000	0.1667	2.3908	2.3369	-0.0539
6.500	0.1538	2.3874	2.3334	-0.0540
7.000	0.1429	2.3827	2.3291	-0.0536
7.500	0.1333	2.3787	2.3252	-0.0535
8.000	0.1258	2.3757	2.3219	-0.0538
8.500	0.1176	2.3699	2.3163	-0.0536
9.000	0.1111	2.3663	2.3121	-0.0542
9.500	0.1053	2.3606	2.3064	-0.0542
10.000	0.1000	2.3548	2.3012	-0.0536
10.500	0.0952	2.3486	2.2948	-0.0538
11.000	0.0969	2.3417	2.2880	-0.0537
11.500	0.0870	2.3329	2.2789	-0.0540
12.000	0.0833	2.3266	2.2716	-0.0550
12.500	0.0800	2.3177		
13.000	0.0769	2.3076		

TERNARY CHALCOPYRITE SEMICONDUCTORS

 TABLE A1.6. Refractive indices of $CuGaS_2$ (Boyd et al., 1971b)

λ (μ)	$\nu = \lambda^{-1}$ (μ^{-1})	n^o	n^e	$n^e - n^o$	$10^5 \times dn^o/dT$	$10^5 \times dn^e/dT$	$10^5 \times dB/dT$
0.55	1.8182	2.7630	2.7813	0.0183	12.95	17.32	4.37
0.59	1.6949	2.7091	2.7141	0.0050			
0.60	1.6667	2.6983	2.7019	0.0036	9.72	10.57	0.84
0.61	1.6393	2.6890	2.6914	0.0024			
0.62	1.6129	2.6804	2.6818	0.0014			
0.63	1.5873	2.6724	2.6731	0.0007			
0.64	1.5625	2.6649	2.6649	-0.0001			
0.65	1.5385	2.6577	2.6570	-0.0007	8.08	8.61	0.53
0.70	1.4286	2.6293	2.6266	-0.0027	6.37	7.64	1.27
0.75	1.3333	2.6100	2.6056	-0.0044	4.64	5.89	1.26
0.80	1.2500	2.5925	2.5886	-0.0040	5.26	6.22	0.96
0.85	1.1765	2.5786	2.5737	-0.0049	6.06	6.51	0.45
0.90	1.1111	2.5681	2.5630	-0.0051	5.64	5.94	0.29
0.95	1.0526	2.5591	2.5538	-0.0053	5.87	6.08	0.21
1.00	1.0000	2.5517	2.5464	-0.0053	5.86	5.98	0.13
1.10	0.9091	2.5406	2.5349	-0.0058	5.75	6.03	0.28
1.20	0.8333	2.5322	2.5265	-0.0058	5.44	5.57	0.13
1.30	0.7692	2.5259	2.5199	-0.0060	5.48	5.74	0.27
1.40	0.7143	2.5209	2.5148	-0.0061	5.44	5.75	0.31
1.60	0.6250	2.5135	2.5073	-0.0062	5.32	5.62	0.30
1.80	0.5556	2.5092	2.5028	-0.0063	4.49	4.82	0.34
2.00	0.5000	2.5051	2.4991	-0.0061	4.52	4.73	0.21
2.20	0.4545	2.5019	2.4956	-0.0063	4.95	5.20	0.24
2.40	0.4167	2.4993	2.4931	-0.0062	5.29	5.64	0.35
2.60	0.3846	2.4975	2.4913	-0.0063	5.08	5.41	0.33
2.80	0.3571	2.4959	2.4894	-0.0065	5.15	5.73	0.58
3.00	0.3333	2.4945	2.4880	-0.0065	4.99	5.44	0.44
3.20	0.3125	2.4932	2.4871	-0.0061	5.16	5.35	0.19
3.40	0.2941	2.4922	2.4853	-0.0069	5.09	5.66	0.57
3.60	0.2778	2.4910	2.4841	-0.0069	5.63	6.00	0.37
3.60	0.2632	2.4897	2.4831	-0.0066	5.33	5.56	0.22
4.00	0.2500	2.4884	2.4816	-0.0068	5.76	6.29	0.53
4.50	0.2222	2.4869	2.4801	-0.0068	4.53	4.99	0.46
5.00	0.2000	2.4843	2.4772	-0.0071	4.39	5.12	0.73
5.50	0.1818	2.4803	2.4728	-0.0075	5.68	6.12	0.44
6.00	0.1667	2.4774	2.4694	-0.0080	5.62	6.08	0.46
6.50	0.1538	2.4744	2.4657	-0.0087	5.44	6.24	0.80
7.00	0.1429	2.4714	2.4621	-0.0094	5.11	5.52	0.40
7.50	0.1333	2.4674	2.4582	-0.0092	6.67	6.95	0.28
8.00	0.1250	2.4639	2.4539	-0.0100	4.91	5.52	0.62
8.50	0.1176	2.4589	2.4490	-0.0099	4.70	4.94	0.25
9.00	0.1111	2.4539	2.4435	-0.0103	5.68	6.21	0.54
9.50	0.1053	2.4491	2.4376	-0.0115	4.93	5.44	0.51
10.00	0.1000	2.4429	2.4311	-0.0119	5.19	5.50	0.13
10.50	0.0952	2.4372	2.4234	-0.0138	5.66	6.73	1.07
11.00	0.0909	2.4311	2.4179	-0.0132	5.61	5.72	0.10
11.50	0.0870	2.4275	2.4121	-0.0154	1.26	2.58	1.32
12.00	0.0833	2.4171			4.81		
12.50	0.0800	2.4094			4.80		
13.00	0.0769	2.3999			3.49		

TABULATED REFRACTIVE INDEX DATA

TABLE A 1.7. *Refractive indices of CuInS₂* (Boyd et al., 1971b)

λ (μ)	$\nu = \lambda^{-1}$ (μ^{-1})	n^o	n^e	$n^e - n^o$
0.90	1.1111	2.7907	2.7713	-0.0194
0.92	1.0870	2.7718	2.7536	-0.0182
0.94	1.0638	2.7567	2.7392	-0.0174
0.96	1.0417	2.7437	2.7268	-0.0168
0.98	1.0204	2.7324	2.7162	-0.0162
1.00	1.0000	2.7225	2.7067	-0.0158
1.10	0.9091	2.6861	2.6727	-0.0134
1.20	0.8333	2.6638	2.6510	-0.0129
1.30	0.7692	2.6478	2.6357	-0.0121
1.40	0.7143	2.6359	2.6243	-0.0115
1.50	0.6667	2.6267	2.6156	-0.0112
1.60	0.6250	2.6195	2.6087	-0.0108
1.80	0.5556	2.6089	2.5985	-0.0104
2.00	0.5000	2.6020	2.5918	-0.0103
2.20	0.4545	2.5961	2.5860	-0.0100
2.40	0.4167	2.5915	2.5821	-0.0095
2.60	0.3846	2.5886	2.5789	-0.0097
2.80	0.3571	2.5860	2.5765	-0.0096
3.00	0.3333	2.5838	2.5741	-0.0097
3.50	0.2857	2.5802	2.5707	-0.0095
4.00	0.2500	2.5760	2.5663	-0.0097
4.50	0.2222	2.5729	2.5630	-0.0099
5.00	0.2000	2.5699	2.5598	-0.0101
5.50	0.1818	2.5673	2.5571	-0.0102
6.00	0.1667	2.5645	2.5539	-0.0106
7.00	0.1429	2.5587	2.5474	-0.0113
8.00	0.1250	2.5522	2.5401	-0.0121
9.00	0.1111	2.5448	2.5311	-0.0137
10.00	0.1000	2.5366	2.5225	-0.0141
11.00	0.0909	2.5274	2.5112	-0.0162
12.00	0.0833	2.5166	2.4987	-0.0179
12.50	0.0800	2.5108		

TERNARY CHALCOPYRITE SEMICONDUCTORS

 TABLE A 1.8. Refractive indices of CuAlSe₂ (Boyd et al., 1972b)

λ (μ)	$v = \lambda^{-1}$ (μ^{-1})	n^o	n^e	$n^e - n^o$
0.50	2.0000	2.7797	2.7886	0.0089
0.55	1.8182	2.7038	2.7005	-0.0033
0.60	1.6667	2.6560	2.6489	-0.0071
0.65	1.5385	2.6230	2.6145	-0.0085
0.70	1.4286	2.5973	2.5886	-0.0087
0.75	1.3333	2.5789	2.5699	-0.0090
0.80	1.2500	2.5650	2.5556	-0.0094
0.85	1.1765	2.5536	2.5428	-0.0109
0.90	1.1111	2.5437	2.5327	-0.0110
0.95	1.0526	2.5364	2.5252	-0.0112
1.00	1.0000	2.5293	2.5179	-0.0115
1.10	0.9091	2.5189	2.5075	-0.0115
1.20	0.8333	2.5113	2.4997	-0.0115
1.30	0.7692	2.5053	2.4937	-0.0116
1.40	0.7143	2.5007	2.4889	-0.0117
1.50	0.6667	2.4969	2.4852	-0.0117
1.60	0.6250	2.4938	2.4821	-0.0117
1.70	0.5882	2.4913	2.4794	-0.0118
1.80	0.5556	2.4892	2.4773	-0.0119
1.90	0.5263	2.4872	2.4753	-0.0119
2.00	0.5000	2.4851	2.4734	-0.0117
2.10	0.4762	2.4832	2.4714	-0.0119
2.20	0.4545	2.4820	2.4700	-0.0120
2.30	0.4348	2.4807	2.4689	-0.0119
2.40	0.4167	2.4802	2.4683	-0.0119
2.50	0.4000	2.4795	2.4676	-0.0118
2.60	0.3846	2.4786	2.4665	-0.0120
2.80	0.3571	2.4771	2.4651	-0.0121
3.00	0.3333	2.4759	2.4638	-0.0122
3.50	0.2857	2.4733	2.4609	-0.0125
4.00	0.2500	2.4712	2.4586	-0.0126
4.50	0.2222	2.4685	2.4559	-0.0126
5.00	0.2000	2.4659	2.4533	-0.0126

TABULATED REFRACTIVE INDEX DATA

TABLE A 1.9. *Refractive indices of AgGaSe₂ (Boyd et al., 1972b)*

λ (μ)	$\nu = \lambda^{-1}$ (μ^{-1})	n^o	n^e	$n^e - n^o$
0.725	1.3793	2.8452	2.8932	0.0480
0.750	1.3333	2.8191	2.8415	0.0224
0.800	1.2500	2.7849	2.7866	0.0017
0.850	1.1765	2.7598	2.7522	-0.0077
0.900	1.1111	2.7406	2.7275	-0.0130
0.950	1.0526	2.7252	2.7085	-0.0167
1.000	1.0000	2.7132	2.6934	-0.0198
1.100	0.9091	2.6942	2.6712	-0.0230
1.200	0.8333	2.6806	2.6554	-0.0253
1.300	0.7692	2.6705	2.6438	-0.0267
1.400	0.7143	2.6624	2.6357	-0.0277
1.600	0.6250	2.6516	2.6224	-0.0292
1.800	0.5556	2.6432	2.6131	-0.0301
2.000	0.5000	2.6376	2.6071	-0.0305
2.200	0.4545	2.6336	2.6027	-0.0309
2.400	0.4167	2.6304	2.5992	-0.0313
2.600	0.3846	2.6286	2.5968	-0.0317
2.800	0.3571	2.6261	2.5943	-0.0318
3.000	0.3333	2.6245	2.5925	-0.0320
3.200	0.3125	2.6231	2.5912	-0.0319
3.400	0.2941	2.6221	2.5899	-0.0321
3.600	0.2778	2.6213	2.5889	-0.0324
3.800	0.2632	2.6200	2.5876	-0.0324
4.000	0.2500	2.6189	2.5863	-0.0325
4.500	0.2222	2.6166	2.5840	-0.0325
5.000	0.2000	2.6144	2.5819	-0.0326
5.500	0.1818	2.6128	2.5800	-0.0328
6.000	0.1667	2.6113	2.5784	-0.0329
6.500	0.1538	2.6094	2.5765	-0.0329
7.000	0.1429	2.6070	2.5743	-0.0327
7.500	0.1333	2.6049	2.5723	-0.0326
8.000	0.1250	2.6032	2.5704	-0.0328
8.500	0.1176	2.6009	2.5681	-0.0329
9.000	0.1111	2.5988	2.5659	-0.0329
9.500	0.1053	2.5964	2.5635	-0.0329
10.000	0.1000	2.5939	2.5608	-0.0331
10.500	0.0952	2.5917	2.5585	-0.0332
11.000	0.0909	2.5890	2.5555	-0.0335
11.500	0.0870	2.5868	2.5536	-0.0332
12.000	0.0833	2.5837	2.5505	-0.0332
12.500	0.0800	2.5805	2.5473	-0.0333
13.000	0.0769	2.5771	2.5439	-0.0331
13.500	0.0741	2.5731	2.5404	-0.0327

TABLE A 1.10. *Refractive indices of CuGaSe₂ (Boyd et al., 1972b)*

λ (μ)	$\nu = \lambda^{-1}$ (μ^{-1})	n^o	n^e	$n^e - n^o$
0.78	1.2821	2.9580	3.0093	0.0513
0.80	1.2500	2.9365	2.9759	0.0394
0.85	1.1765	2.8984	2.9197	0.0214
0.90	1.1111	2.8716	2.8925	0.0209
0.95	1.0526	2.8513	2.8690	0.0176
1.00	1.0000	2.8358	2.8513	0.0154
1.10	0.9091	2.8115	2.8245	0.0130
1.20	0.8333	2.7951	2.8066	0.0115
1.30	0.7692	2.7823	2.7928	0.0105
1.40	0.7143	2.7725	2.7825	0.0099
1.60	0.6250	2.7587	2.7677	0.0090
1.80	0.5556	2.7496	2.7579	0.0084
2.00	0.5000	2.7430	2.7510	0.0080
2.20	0.4545	2.7377	2.7456	0.0079
2.40	0.4167	2.7344	2.7419	0.0074
2.60	0.3846	2.7315	2.7388	0.0073
2.80	0.3571	2.7293	2.7363	0.0071
3.00	0.3333	2.7273	2.7344	0.0071
3.20	0.3125	2.7256	2.7328	0.0070
3.40	0.2941	2.7242	2.7311	0.0069
3.60	0.2778	2.7232	2.7300	0.0068
3.80	0.2632	2.7220	2.7287	0.0067
4.00	0.2500	2.7211	2.7276	0.0066
4.50	0.2222	2.7188	2.7252	0.0064
5.00	0.2000	2.7170	2.7232	0.0062
5.50	0.1818	2.7152	2.7212	0.0060
6.00	0.1667	2.7133	2.7192	0.0059
6.50	0.1538	2.7116	2.7174	0.0058
7.00	0.1429	2.7101	2.7158	0.0058
7.50	0.1333	2.7082	2.7136	0.0054
8.00	0.1250	2.7060	2.7111	0.0051
8.50	0.1176	2.7042	2.7089	0.0047
9.00	0.1111	2.7021	2.7065	0.0044
10.00	0.1000	2.6974	2.7014	0.0040
11.00	0.0909	2.6926	2.6981	0.0034
12.00	0.0833	2.6872	2.6898	0.0026

TABLE A 1.11. *Refractive indices of AgInSe₂* (Boyd et al., 1972b)

λ (μ)	$\nu = \lambda^{-1}$ (μ^{-1})	n^o	n^e	$n^e - n^o$
1.05	0.9524	2.8265		
1.10	0.9091	2.7971	2.8453	0.0483
1.20	0.8333	2.7608	2.7906	0.0298
1.30	0.7692	2.7376	2.7595	0.0218
1.40	0.7143	2.7211	2.7385	0.0174
1.60	0.6250	2.6992	2.7116	0.0125
1.80	0.5556	2.6856	2.6949	0.0094
2.00	0.5000	2.6761	2.6838	0.0076
2.20	0.4545	2.6694	2.6758	0.0065
2.40	0.4167	2.6643	2.6702	0.0060
2.60	0.3846	2.6601	2.6658	0.0057
2.80	0.3571	2.6568	2.6623	0.0055
3.00	0.3333	2.6542	2.6592	0.0050
3.20	0.3125	2.6521	2.6570	0.0049
3.40	0.2941	2.6503	2.6551	0.0048
3.60	0.2778	2.6488	2.6533	0.0045
3.80	0.2632	2.6474	2.6516	0.0042
4.00	0.2500	2.6463	2.6504	0.0041
4.50	0.2222	2.6436	2.6475	0.0038
5.00	0.2000	2.6416	2.6451	0.0035
5.50	0.1818	2.6399	2.6431	0.0033
6.00	0.1667	2.6381	2.6414	0.0032
6.50	0.1538	2.6366	2.6398	0.0032
7.00	0.1429	2.6352	2.6379	0.0027
7.50	0.1333	2.6335	2.6361	0.0026
8.00	0.1250	2.6318	2.6343	0.0025
8.50	0.1176	2.6302	2.6327	0.0025
9.00	0.1111	2.6286	2.6310	0.0025
9.50	0.1053	2.6266	2.6290	0.0024
10.00	0.1000	2.6251	2.6274	0.0023
10.50	0.0952	2.6233	2.6254	0.0021
11.00	0.0909	2.6210	2.6229	0.0019
11.50	0.0870	2.6187	2.6204	0.0017
12.00	0.0833	2.6167	2.6183	0.0017

References

- BOYD, G. D., BUEHLER, E., and STORZ, F. G. (1971a) *Appl. Phys. Lett.* **18**, 307.
 BOYD, G. D., KASPER, H. M., and McFEE, J. H. (1971b) *IEEE J. Quantum Electr.* QE**7**, 563.
 BOYD, G. D., BUEHLER, E., STORZ, F. G., and WERNICK, J. H. (1972a) *IEEE J. Quantum Electr.* QE**8**, 419.
 BOYD, G. D., KASPER, H. M., McFEE, J. H., and STORZ, F. G. (1972b) *IEEE J. Quantum Electr.* QE**8**, 900.

INDEX

- Anisotropic thermal expansion 229
- Band structure
I–III–VI₂ compounds 110–128
II–IV–V₂ compounds 79–109
effective mass 183
effective mass values 89
pseudodirect energy gaps 90–96
quasicubic model 85–87
- Birefringence 99–100, 153–155
physical origin 157–159
- Brillouin zone structure
chalcopyrite lattice 79–80
zincblende lattice 79–80
- Cathodoluminescence 133–135, 141–142
- Chalcopyrite crystals
dissociation pressures 15–19
growth of single crystals 49–71
hardness 72–73
mechanical properties 72–74
melting points 11–12, 72
phase transitions 10–11
short range order 72
structure 3–10
- Chalcopyrite glasses 71–72
- Chalcopyrite structure 3–10
- Chemical vapour deposition (CVD) 50–51
- Conductivity 175–182, 192–198
- Crystal growth 49–71
I–III–VI₂ compounds 51–55
II–IV–V₂ compounds 55–66
- Bridgman technique 52
crucibles 50–51
epitaxial layers 66–71
Stockberger method 52
- Defect tetrahedral phases 13
- Direct energy gap
temperature dependence 116–117
- Electrical properties 175–213
I–III–VI₂ compounds 187–213
II–IV–V₂ compounds 175–186
amorphous II–IV–V₂ compounds 201
annealing characteristics 187–189
band parameters 183–187
Cerenkov emission 207
- conductivity 175–182
crystalline II–IV–V₂ compounds 201
current oscillations 206–208
classy II–IV–V₂ compounds 202–205
Hall coefficient 175–178, 190–192
transport measurements 189
- Electroluminescence 148–151
- Electroluminescent diodes 148–151
- Electron spin resonance 224
- Electronic structure
I–III–VI₂ compounds 110–128
II–IV–V₂ compounds 79–109
exciton optical properties 121–127
high energy gaps 103–105
p–d hybridization 116–120
spin-orbit interactions 120
theoretical crystal field parameters 120
- Electroreflectance spectra 82–85, 91–94, 105–115
- Energy gaps in chalcopyrite crystals
experimental results 82–85
- Epitaxial layers 66–71
- Exciton optical properties 121–127
- Exciton reflectance spectra 121–127
- Glass formation in chalcopyrite systems 71–72
- Glassy II–IV–V₂ compounds 202–205
absorbtion spectra 202–203
conductivity 202
memory devices 204
switching devices 204
thin film devices 204
- Hall coefficient 175–178, 190–192
temperature dependence 177–178
- Heterodiodes 145–146
electroluminescence 145
- Infrared detection 169–172
- Infrared optical properties 215–216
- Infrared spectra 216–222
- Interface dislocations 66
- Ion implantation 66
- Ioniccovalent bonding 193
- Lattice parameters
I–III–VI₂ compounds 4–5
II–IV–V₂ compounds 7–8

TERNARY CHALCOPYRITE SEMICONDUCTORS

- Lattice vibrational spectra 215–222
Liquid phase epitaxy 66
Luminescence 129–151
 heterodiodes 145–146
- Memory devices 204
Mixed I–III–VI₂ systems 24
Mixed II–IV–V₂ systems 44
- Nonlinear optical materials 60–61
Nonlinear optical properties 152–174
 birefringence 153–155
 optical parametric oscillator 161–169
 parametric upconversion 169–172
 refractive index 154, 159
 three frequency phase matching 161–169
Nuclear magnetic resonance 225
- Optical absorption coefficients 96–102
Optical absorption spectra 96–102, 121–123,
 202–203
Optical activity 222–224
Optical anisotropy
 II–IV–V₂ compounds 96–103
Optical birefringence 99–100, 153–159
Optical parametric oscillator 161–169
Optical transmission spectra 96–99
- Phase relationships
 I–III–VI₂ systems 19–25
 (I–III–VI₂)–(II–VI) systems 25–37
 (I–III–VI₂)–(III–V) systems 25–37
 II–IV–V₂ systems 38–45
- (II–IV–V₂)–(III–V) systems 45–49
Photoluminescence 129–144
 band to band transitions 131
 exciton-exciton scattering 142
Photoluminescence spectra
 I–III–VI₂ compounds 136–140
 II–IV–V₂ compounds 129–135
 stimulated emission 131–132, 142–144
Pressure induced transformations 72
Pseudodirect energy gaps 90–96
 selection rules 91
- Quaternary alloys
 electrical properties 225–229
 energy gap 226–227
 optical energy gap 228–229
- Raman spectra 216–218
Refractive index 154, 159, 172–173, 231–241
Reststrahlen spectra 216–222
- Seebeck coefficient 208–211
Stimulated emission spectra
 I–III–VI₂ compounds 142–144
Switching devices 204
- Thermal conductivity 209–211
Thermoelectric materials 45
Thermoelectric power 192–197
Thermoelectric properties 208–211
- Zincblende structure 3, 6, 10–13